MEASUREMENTS OF νN CHARGED CURRENT CROSS SECTIONS FROM E_ν = 25 GEV TO E_ν = 260 GEV

Thesis by

James Roy Lee

In Partial Fulfillment of the Requirements

for the Degree of

Doctor of Philosophy

California Institute of Technology

Pasadena, California

1981

(Submitted October 13, 1980)

ACKNOWLEDGEMENTS

This experiment was made possible by the efforts of a great many people. At the time these data were taken, the CFRR collaboration included B. Barish, R. Blair, P. Linsay, J. Ludwig, R. Messner, F. Sciulli, and M. Shaevitz of Caltech; F. Bartlett, D. Edwards, E. Fisk, G. Krafczyk, Y. Fukushima, Q. Kerns, T. Kondo, D. Nease, S. Segler, and D. Theriot of Fermilab; A. Bodek and W. Marsh of the University of Rochester; and O. Fackler and K. Jenkins of Rockefeller University.

In particular, I would like to thank Barry Barish for critically reading this thesis, and Frank Sciulli, Mike Shaevitz, Jens Ludwig, and Orrin Fackler for a great many useful discussions during the past several years.

Most of the beam monitoring data discussed in this thesis, including the Cherenkov counter data, were analyzed by Keith Jenkins and Orrin Fackler.

I wish to thank Caltech for financial support of my graduate studies.

I am very grateful to my wife, Kathleen, for much

patience and understanding during the time I was working on this experiment and writing this thesis.

Most of all, I wish to thank my parents for enthusiastic support of my education far beyond what a son has any right to expect.

ABSTRACT

The primary objective of this experiment was to measure normalized cross sections for the interaction $\nu N \rightarrow \mu^- X$ at energies up to E_ν=260 GEV.

The Fermilab dichromatic neutrino beam is made by focusing 400 GEV protons onto a BeO target to produce a secondary beam containing pions and kaons. Pions and kaons decay into neutrinos in a 340m evacuated decay pipe. The absolute π and K flux was determined by measuring the total flux of secondary particles with an ionization chamber and by measuring relative particle composition with a Cherenkov counter. The decay of pions and kaons into neutrinos was calculated to obtain the normalized ν flux at the detector.

We observed 6500 charged current interactions in an 1100 ton iron ν target. Hadron energy deposited in the detector was measured with calorimetric techniques. Muon trajectories were measured with spark chambers. Muon momenta were measured with an iron toroidal magnet.

The total charged current cross section was measured to be $\sigma/E_\nu=(.700\pm.038)X10^{-38}$ cm^2/GEV independent of energy

from E_ν=25 GEV to E_ν=260 GEV. This sets a lower bound on the mass of the W boson of M_W>27 GEV at the 90% confidence level. The mean inelasticity is <y>=.484±.012 independent of energy. The antiquark fraction of the nucleon is α =.21±.07 at a mean neutrino energy of E_ν=226 GEV. The x distributions were measured in the region .1<y<.4 at E_ν=67 GEV and at E_ν=226 GEV. Scaling violations were found at low x, but they can be removed by using the scaling variable $x'=x/(1+M_N^2/Q^2)$.

These results are in good agreement with a simple quark-parton model of deep inelastic scattering.

To Brian

TABLE OF CONTENTS

CHAPTER 1

INTRODUCTION

1.1 A BRIEF HISTORY

This thesis describes a neutrino experiment done at Fermi National Accelerator Laboratory in the summer of 1978. The experiment was a collaboration of 23 physicists from Caltech, Fermilab, University of Rochester, and Rockefeller University. The results presented here are the first to come from a second generation neutrino detector that we started building in 1976. This detector will be used for a variety of interesting experiments over the next several years.

The study of neutrino interactions entered a new era when the Fermilab 400 GEV proton accelerator began operation in 1971. It became possible there and later at CERN to study neutrinos with energies in the range from 20 to 200 GEV. A Caltech-Fermilab-Rockefeller group, including several members of the present CFRR collaboration, built a neutrino counter detector and

conducted several experiments from 1971 to 1975. Important discoveries included the observation of neutral current interactions[1] and multimuon events[2,3,4]. Normalized charged current cross sections were measured to $\pm$10% for both neutrinos and antineutrinos[5,6], and charge symmetry was tested by measuring cross sections at y near 0[7]. The mean inelasticity of charged current interactions was found not to vary dramatically with energy[8]. The neutral current coupling was found to be consistent with the Weinberg-Salam model of weak interactions[9].

By 1975 the limitations of the first experiment were clear, and it was decided to build a new experiment. The neutrino beam line was redesigned to get a cleaner dichromatic beam at higher energies. Beam monitors were built that would contain the entire secondary beam and could measure the important parameters of the beam while running at normal intensities. Finally, a larger and more sophisticated neutrino detector was built in Lab E.

Construction of the new apparatus was completed in the spring of 1978, and the first experiment (E356) took data for 3 months during the summer. Despite problems with beam transmission and accelerator reliability, we collected about 6500 usable neutrino interactions. More than 70% of

the events were taken with the secondary beam tuned to 300 GEV and represent the highest energy neutrino data to date. Since then another experiment (E616) already has run, collecting well over 100,000 neutrino interactions at somewhat lower energies. The analysis of the E616 data currently is under way. In this thesis I will report only on the E356 charged current data.

1.2 INTRODUCTION TO CHARGED CURRENT INTERACTIONS

Neutrino and antineutrino charged current interactions are interactions of the form

$$\nu N \rightarrow \mu^- + \text{hadrons}, \qquad (1\text{-}1a)$$

$$\bar{\nu} N \rightarrow \mu^+ + \text{hadrons}. \qquad (1\text{-}1b)$$

These interactions are believed to be mediated by a heavy charged W boson, as shown in figure 1-1(a). The W^+ and W^- are the charged members of a triplet of W bosons. The neutral W mediates neutral current interactions, which have the form

$$\nu N \rightarrow \nu + \text{hadrons}. \qquad (1\text{-}2)$$

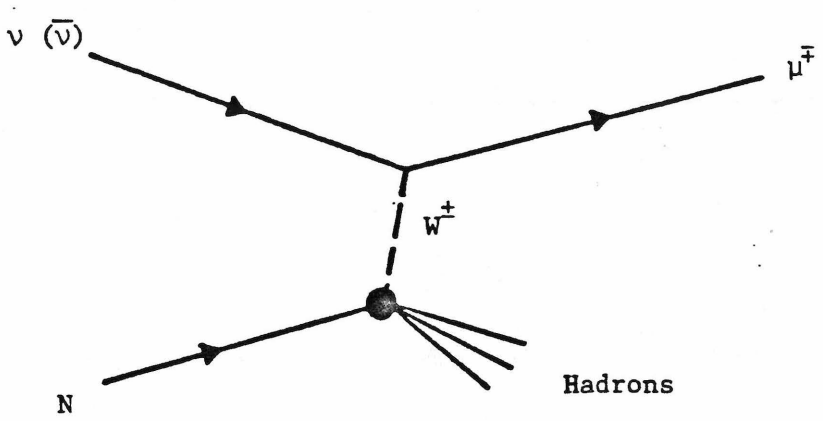

(a)

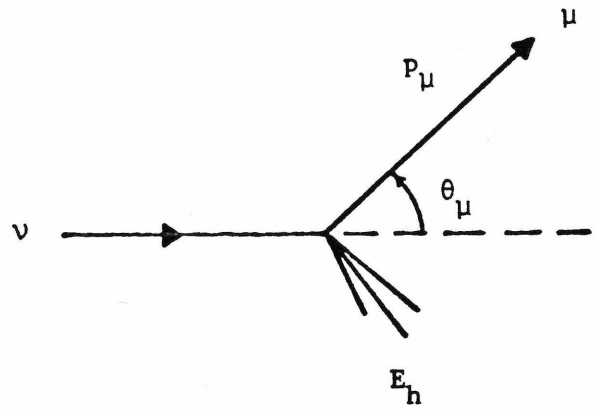

(b)

Figure 1-1: (a) Neutrino charged current interaction.
(b) Measured quantities are the muon momentum and production angle and the total hadron energy.

For a charged current interaction, we measure the angle θ_μ and momentum p_μ of the outgoing muon and the total energy E_h of the hadron shower (see figure 1-1(b)). The sum of the muon energy and the hadron energy gives the incident neutrino energy E_ν. The momentum transfer is given by

$$Q^2 = 2E_\nu p_\mu \sin^2(\theta_\mu/2). \qquad (1\text{-}3)$$

We measure three parameters of each interaction, and so we can characterize the interaction by three independent kinematic variables. These conventionally are chosen to be E_ν, x, and y, where

$$x = \frac{Q^2}{2M_N E_h}, \qquad (1\text{-}4a)$$

and

$$y = \frac{E_h}{E_\nu}. \qquad (1\text{-}4b)$$

1.3 OUTLINE OF PRESENTATION

We measure normalized cross sections by determining both the number of neutrino interactions in the detector and the incident neutrino flux. These are two distinct

measurements and are discussed in different sections of this thesis.

The characteristics of the neutrino beam are discussed in chapter 2. This includes a description of the neutrino beam, the beam line monitors, and pion and kaon decay calculations needed to determine neutrino fluxes.

The neutrino detector is described in chapter 3. This includes a description of the hadron calorimeter and its calibration in a hadron beam, a description of the muon spectrometer, and a discussion of how muon momenta are determined.

The neutrino event analysis is discussed in chapter 4. The acceptance of the apparatus is determined and the data are corrected for missing acceptance. Pion neutrino events are separated from kaon neutrino events, and our procedures for extracting cross sections are explained in detail. The energy calibration of the detector is checked by comparing data with monte carlo predictions based on our knowledge of the neutrino beam.

The results of this experiment are presented in chapter 5. In chapter 6 the CFRR measurements are compared

with previous results. Chapter 6 includes a discussion of how our data can be interpreted.

CHAPTER 2

DICHROMATIC NEUTRINO BEAM

2.1 EXPERIMENTAL LAYOUT

The CFRR experiment uses a sign selected dichromatic neutrino beam. A diagram of the E356 neutrino beam line is shown in figure 2-1. A 400 GEV primary proton beam is focused onto a BeO target at the front of the N30 train. The N30 train is a string of magnets that selects the sign and momentum of secondary particles produced at the target and focuses them toward Lab E. These secondary particles travel through a 340 meter decay pipe, where some of the pions and kaons decay into neutrinos. At a fixed secondary energy and decay angle, neutrinos from pion decays have lower momenta than neutrinos from kaon decays, resulting in a dichromatic neutrino energy spectrum.

At the end of the decay pipe is a beam dump to absorb the remaining hadrons and a 910 meter berm to range out the muons in the secondary beam. The neutrino target is located in Lab E, directly behind the berm. Any muons from

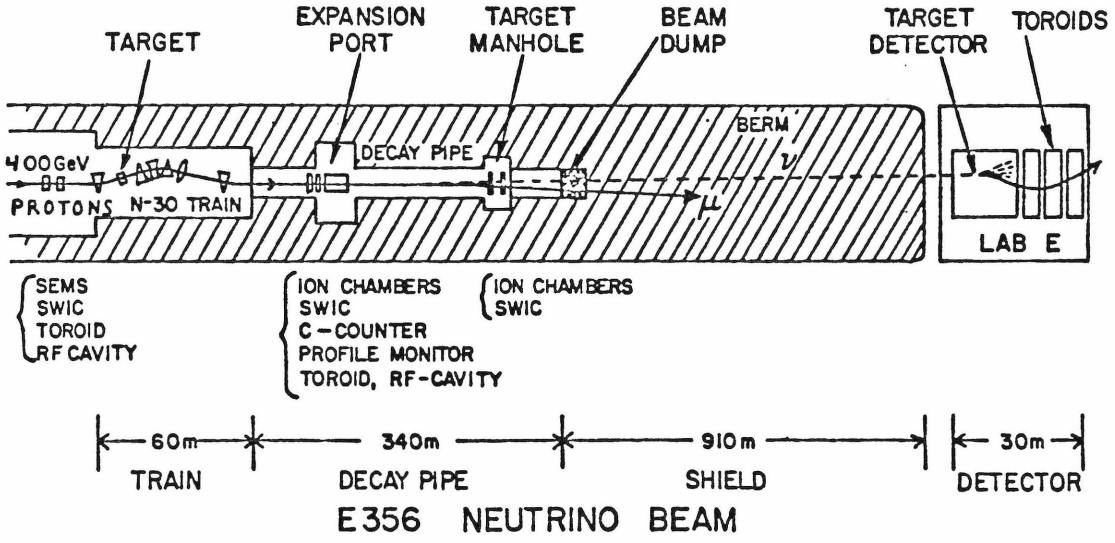

Figure 2-1: Experimental layout of E356.

neutrino interactions in the berm that penetrate into Lab E are vetoed at the front of the neutrino detector.

The neutrino flux at the detector must be determined to measure normalized cross sections. A detailed knowledge of the neutrino spectrum at Lab E depends on knowing the intensity, particle composition, momentum spectrum, transverse size, and angular divergence of the secondary beam. There are two places in the decay pipe where equipment to monitor the secondary beam may be placed, the expansion port and the target manhole. We measure the total number of particles in the decay pipe with an ion chamber located in the expansion port. The fraction of pions, kaons, and protons in the secondary beam is measured with a Cherenkov counter. The Cherenkov counter also measures the momentum spectra of the protons and kaons. The vertical and horizontal extent of the beam is mapped with a profile monitor. Both the Cherenkov counter and the profile monitor are located in the expansion port. After measuring the secondary flux, the neutrino flux is determined by calculating the probability that a pion or kaon in the decay pipe will decay into a neutrino that hits the detector.

To provide redundancy in measuring the secondary beam

intensity, a toroid and an RF cavity were installed in the expansion port, and a second ion chamber was installed in the target manhole. These devices were not available when we took the E356 data.

When running the experiment, the steering of the primary proton beam is monitored with segmented wire ion chambers (SWICs) located upstream of the target. We monitor the secondary beam steering with SWICs and split plate ion chambers in the expansion port and target manhole. The intensity of the primary proton beam is measured with a secondary emission monitor (SEM), a toroid, and an RF cavity.

2.2 DICHROMATIC TRAIN

Neutrino beams at Fermilab are made by producing an intermediate beam containing pions and kaons that are allowed to decay into neutrinos. A primary proton beam is focused onto a fixed target. The thickness of the target is approximately one collision length of material to maximize the production of hadrons. Both positively and negatively charged pions and kaons are produced at the target with energies ranging nearly up to the energy of the primary protons. If all of the hadrons produced at the

target are allowed to decay, they will produce both neutrinos and antineutrinos with a broad energy spectrum.

It is desirable to study neutrino interactions in a beam of monoenergetic neutrinos (or antineutrinos). The closest practical approximation to this is a sign selected, narrow band dichromatic beam. The neutrino spectrum from such a beam is much simpler and less uncertain than the spectrum from a wide band beam. The principles of a dichromatic beam line are shown schematically in figure 2-2.

Secondary hadrons are sign and momentum selected by bending the particles with a dipole magnet and accepting particles in a narrow momentum band with a momentum slit. The central momentum of the hadrons that make it through the momentum slit can be selected by adjusting the current in the dipole. Reversing the polarity of the dipole selects hadrons of opposite sign. A positive secondary beam produces a neutrino beam (from $\pi^+, K^+ \rightarrow \mu^+ + \nu$), while a negative secondary beam produces an antineutrino beam (from $\pi^-, K^- \rightarrow \mu^- + \bar{\nu}$). A monochromatic secondary hadron beam produces a dichromatic neutrino beam since pions and kaons have different masses and decay into neutrinos of different energies.

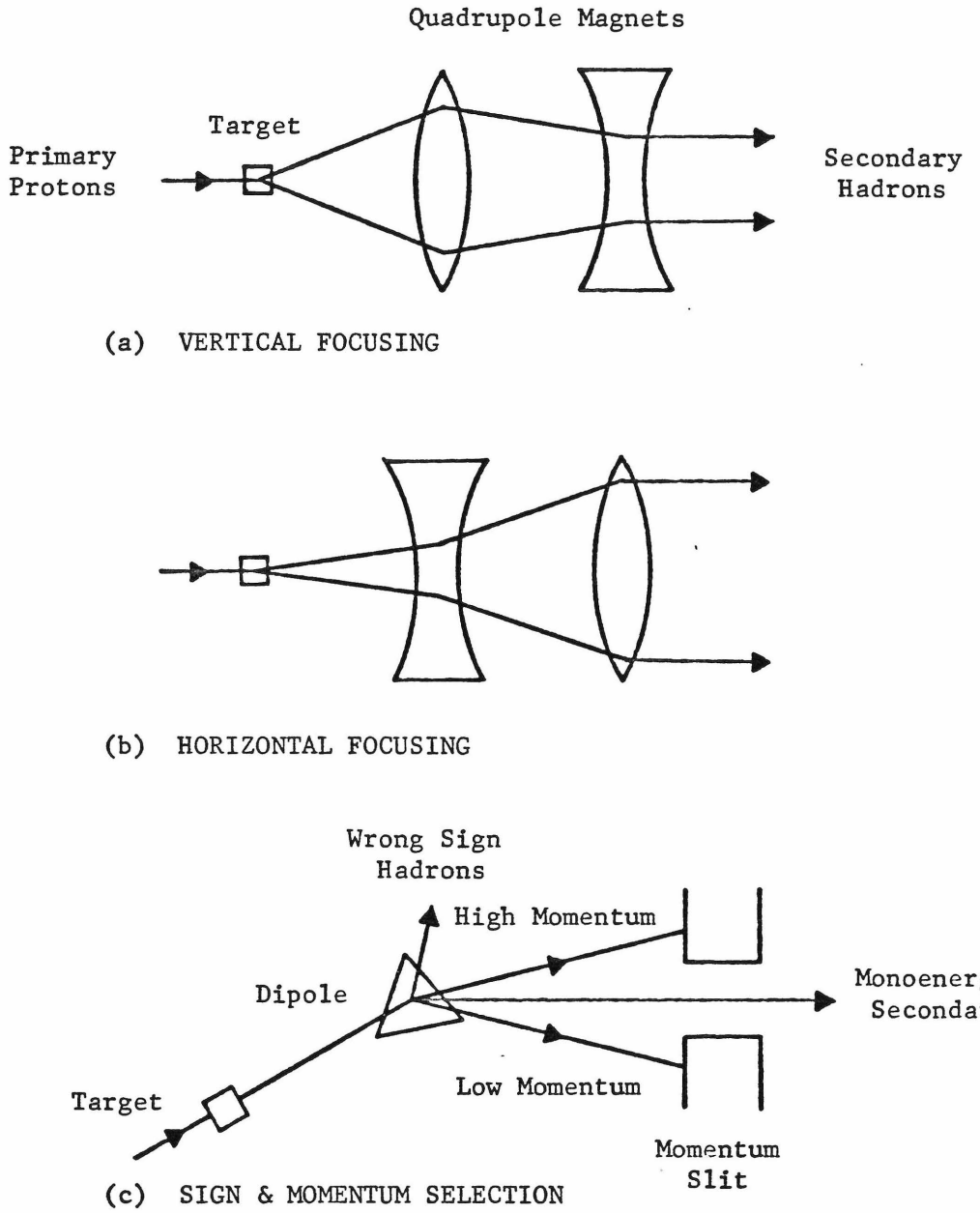

Figure 2-2: Principles of a narrow band dichromatic neutrino beam.

The forward production cone of hadrons with the desired momentum is captured with a quadrupole doublet that forms a point to parallel focusing system. A quadrupole magnet focuses a beam in one transverse dimension and defocuses it in the other. A pair of quadrupole magnets can be designed to provide point to parallel focusing in both dimensions. The production target sits at the focus of the doublet.

A schematic of the CFRR beamline (the N30 train) is shown in figure 2-3. Point to parallel focusing is accomplished with five vertically focusing (horizontally defocusing) quadrupole magnets labelled QV1-5, and two horizontally focusing (vertically defocusing) quadrupole magnets labelled QH1-2. The momentum selection is done with three dipole magnets, D1-3, and a momentum slit in front of D4. The designed momentum acceptance of $\pm 9\%$ is the minimum practical with a point to parallel focusing system. E356 took data in a neutrino beam only at two separate secondary beam energy settings, 200 GEV and 300 GEV.

Hadrons that decay before the momentum selection is done produce a background of neutrinos with a broad momentum spectrum. The wideband background is minimized by

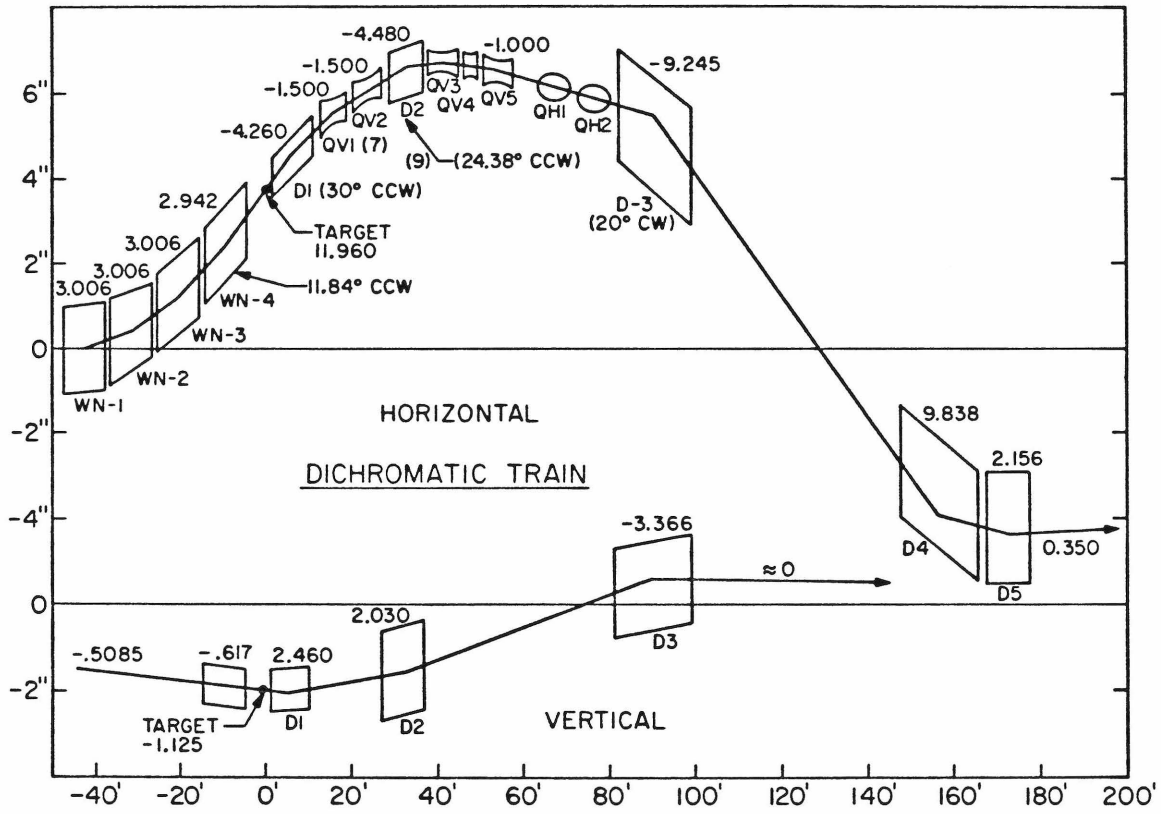

Figure 2-3: E356 dichromatic beam line. The beam deflection imparted by each beam element is given in miliradians.

pointing the secondary beam away from Lab E until the momentum selection is complete. The primary proton beam is bent away from the beam line by 12 mrad horizontally and 1 mrad vertically before hitting the target. Dipoles D1-3 are tilted to bend both horizontally and vertically. When the secondary beam points toward Lab E horizontally, it points away vertically. After the momentum slit, two dipole magnets (D4-5) bend the beam back toward Lab E. The wideband background is measured experimentally by taking neutrino data with the momentum slit closed. The wideband neutrino spectrum peaks at low energy since the neutrinos come either from hadrons produced at large production angles or from wide angle decays. A significant subtraction must be made to obtain cross sections at low neutrino energies.

The characteristics of the dichromatic train are summarized in table 2-1. The design of the CFRR dichromatic beam is discussed elsewhere[10,11,12] in greater detail.

2.3 FLUX MONITORS

The primary device used in E356 to determine the total number of charged particles in the secondary beam is the

TABLE 2-1: DICHROMATIC NEUTRINO BEAM PARAMETERS

Incoming proton energy	400 GEV
Intensity	$>10^{13}$ protons/pulse
Target	10.5" BeO
Spot size	2.0X.5 mm^2
Targeting angles	
Horizontal	11.96 mrad
Vertical	1.125 mrad
Solid angle acceptance at central momentum	11.5 μsr
Momentum acceptance	±9%
Angular divergence of secondary beam	
Horizontal	±.15 mrad
Vertical	±.18 mrad
Secondary energy	50-300 GEV

ionization chamber located in the expansion port. The location of the ion chamber is shown in figure 2-4.

The expansion port ion chamber consists of three separate ion chambers in one unit (see figure 2-5). The first is an ion chamber with two 1/4" gaps between the signal plates and the high voltage plate. This is the chamber used to measure the total flux of charged particles in the decay pipe. The second is an ion chamber with 1" gaps. This is intended to be used when calibrating the chamber in a beam with sufficiently low intensity that it is possible to use particle counting techniques. The third is a split plate ion chamber. Each signal plate is composed of two separate halves. One is split horizontally and the other is split vertically. The signals from this chamber are very sensitive to the position of a beam going through the ion chamber, and they are used to monitor the steering of the beam. All three chambers are 18" in diameter and contain the entire secondary beam. The signals from the ion chambers are split and sent to livetime and deadtime integrators. Livetime particles are particles in the decay pipe when the detector is ready to accept a trigger. Deadtime particles are in the decay pipe when the detector will not trigger on an interaction, and so the livetime and deadtime fluxes must be measured

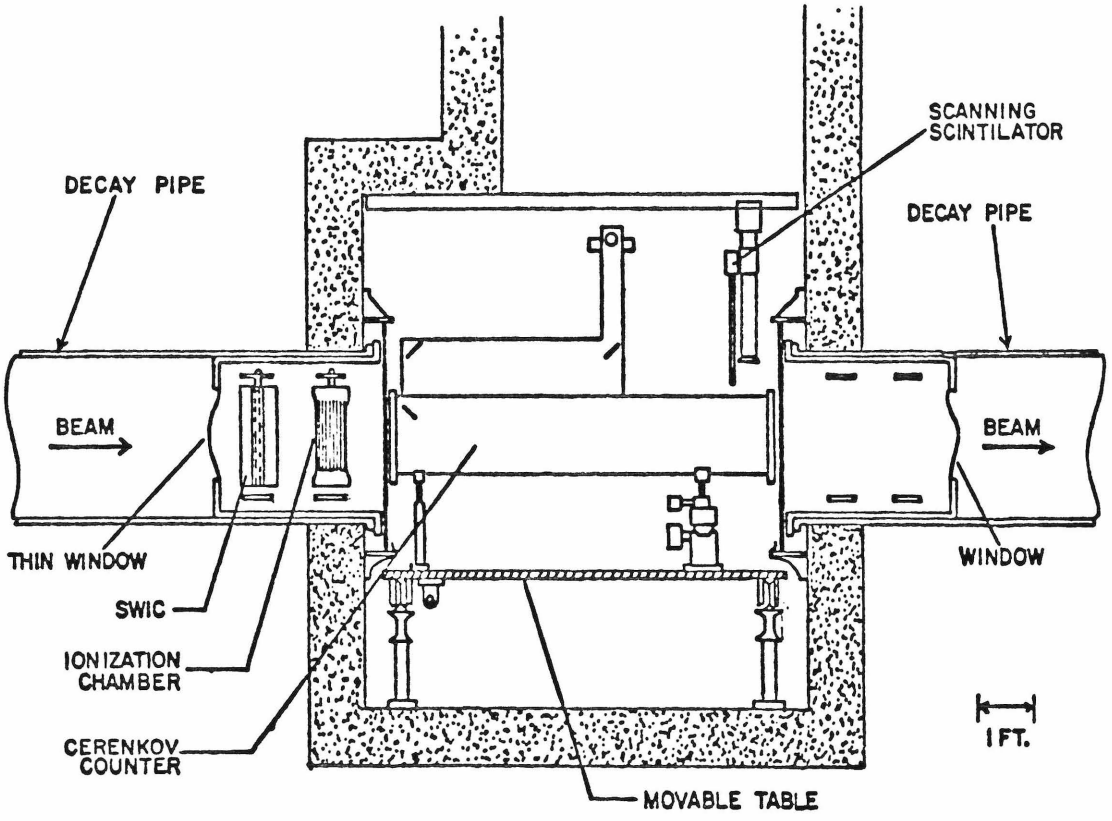

Figure 2-4: Expansion port instrumentation.

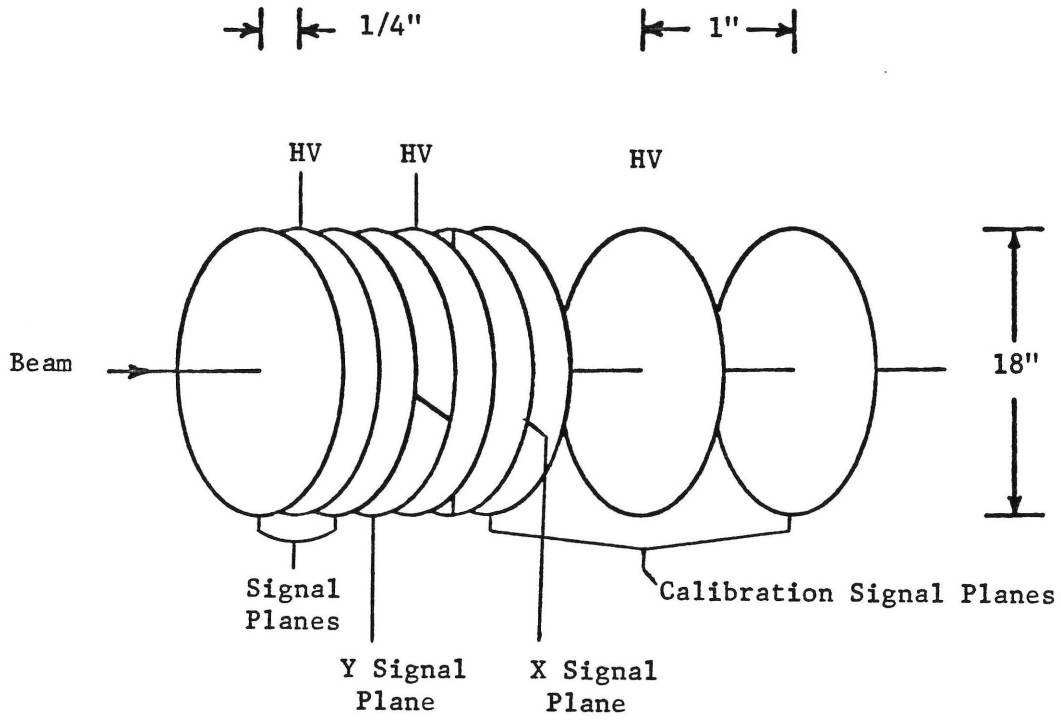

Figure 2-5: Schematic of the expansion port ion chamber.

separately to measure normalized cross sections. The integrators must switch on a time scale much shorter than the duration of the 1 msec beam spill. The livetime integrator starts integrating charge before the start of the beam spill. If an event trigger occurs at Lab E, a signal sent via a fast cable stops the livetime integrator and starts the deadtime integrator. Both integrators are stopped at the end of the beam spill. Deadtime introduced by the veto at the detector must be measured separately. The total flux for a particular spill is determined by summing the livetime and deadtime integrators.

The linearity of the ion chamber is tested by comparing its signal with signals from beam monitors located upstream of the target. This cannot be done on a long time scale because the transmission of the train is very sensitive to the tune of the primary proton beam and varies by a few percent over the course of the run. However, the beam typically remains stable for periods up to a few hours, which is adequate to study the linearity of the ion chamber. Figure 2-6 compares the total ion chamber response with the primary beam SEM and toroid.

The total ion chamber response is linear to within ± 0.5%, but we encountered a problem in switching from the

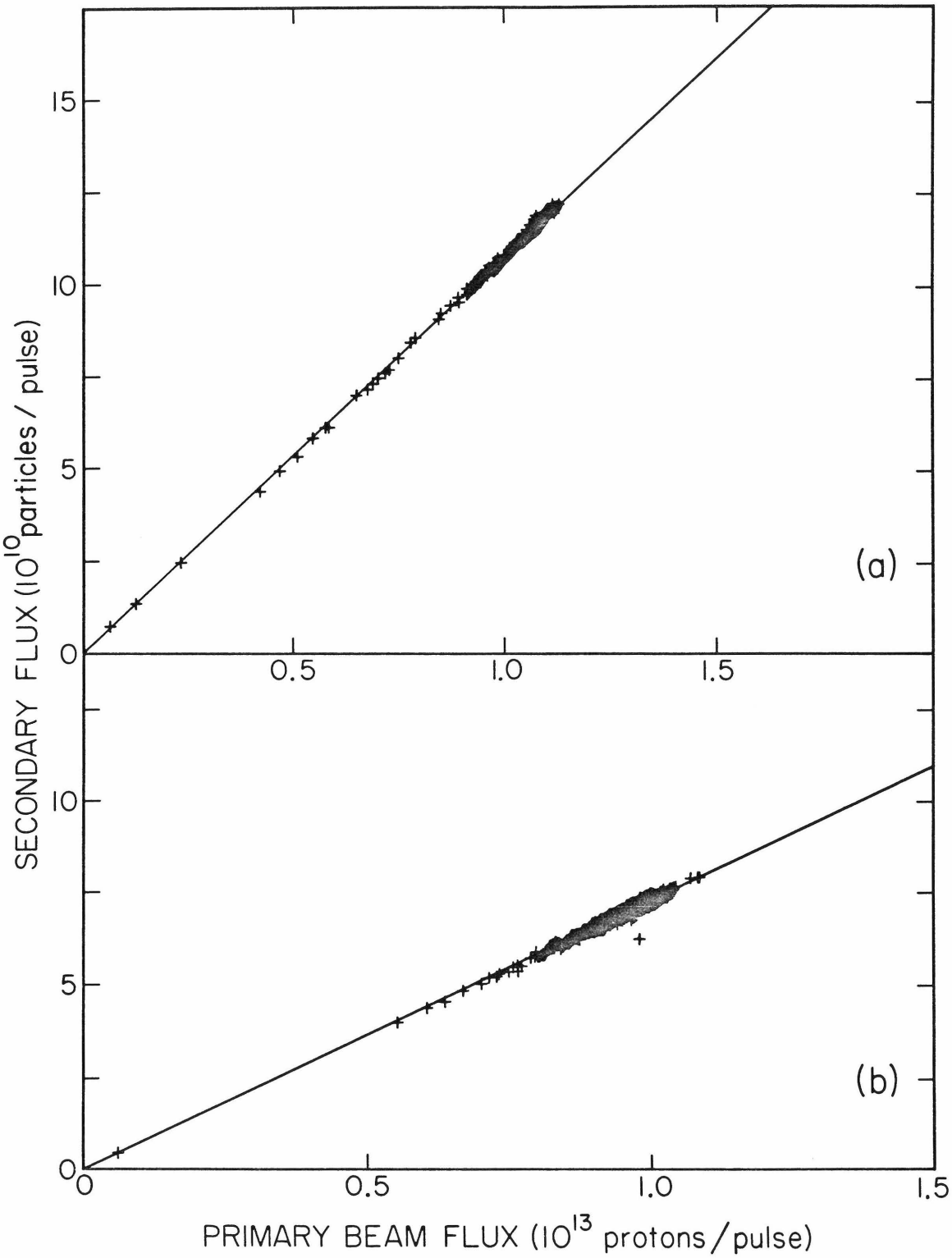

Figure 2-6: Linearity of ion chamber response
(a) with respect to primary beam SEM
(b) with respect to primary beam toroid.

livetime integrator to the deadtime integrator. Figure 2-7 compares the livetime flux measured by the ion chamber with the livetime flux measured by the SEM. This problem has been corrected by redesigning the integrators, but for the E356 data we have to correct for the switching problem by using the toroid. The total flux for a given beam spill is measured with the ion chamber. The fraction of the spill contained in the experimental livetime is measured with the toroid.

The ion chamber is calibrated by a foil activation technique. Copper foils are placed in the decay pipe, and a 200 GEV proton beam is run through the train with the target out. After the foil is irradiated, the intensity of ^{24}Na decay is measured. The ion chamber is calibrated assuming a cross section of 4.0 mb for the production of ^{24}Na in copper. This method has systematic uncertainties of $\pm$5%, but is reproducible to better than 2%.

Recently we attempted to obtain a calibration using the toroid and RF cavity in the expansion port. The toroid was calibrated with a current carrying wire. The RF cavity was calibrated with an internal antenna. Preliminary results with the RF cavity give a calibration that is equivalent to using a 4.06 mb ^{24}Na production cross

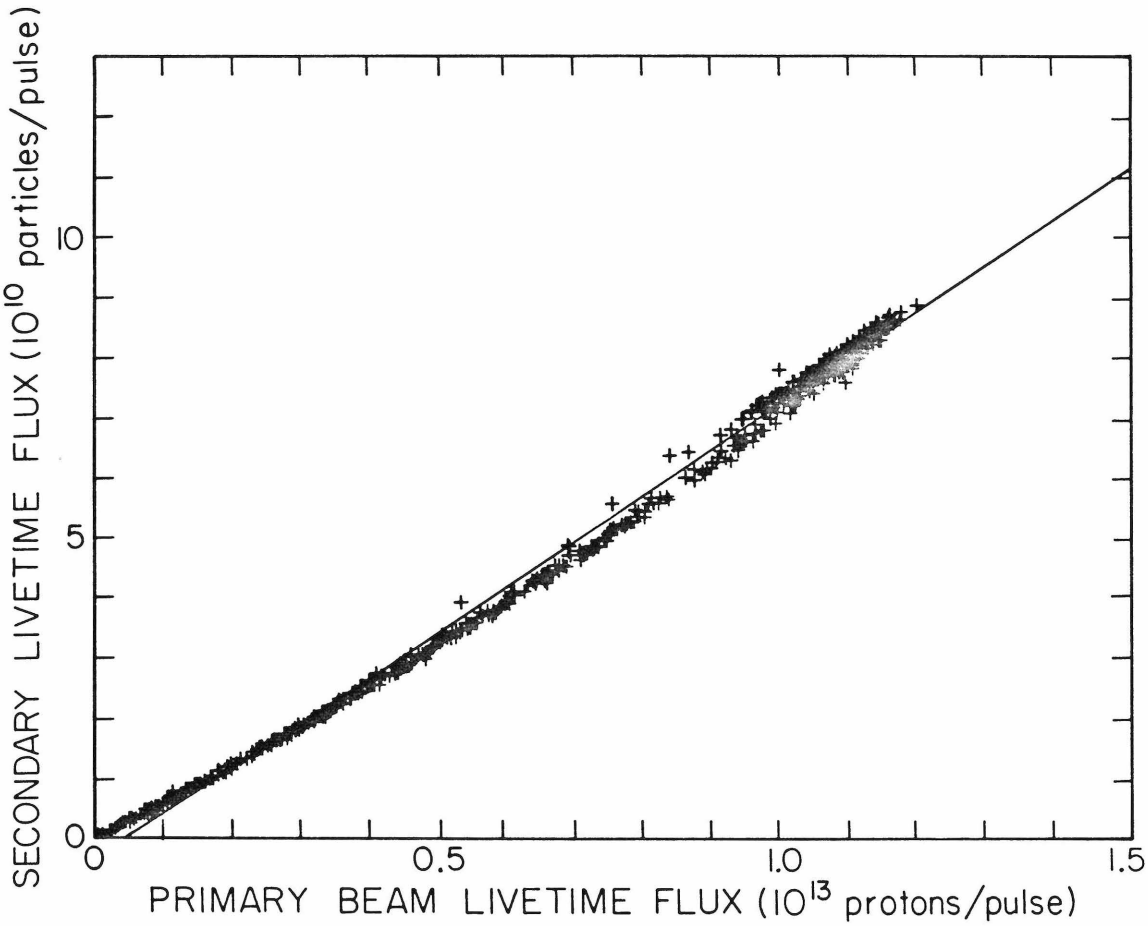

Figure 2-7: Ion chamber livetime versus SEM livetime. The lack of linearity reflects a switching problem between the ion chamber livetime and deadtime integrators.

section. Early results with the toroid give a 4.18 mb cross section.

2.4 BEAM PROFILE MONITOR

The beam profile monitor is a small scanniing scintillation counter of transverse dimension 1/4"X1/4". It can be moved both vertically and horizontally to map out the profile of the secondary beam at the expansion port (see figure 2-4).

The vertical profile of the beam is shown in figure 2-8 at various horizontal positions. It can be seen from these profiles that the beam is contained completely by the ion chamber (diameter 18") and by the Cherenkov counter (diameter 10").

2.5 CHERENKOV COUNTER

A. CONSTRUCTION

We determine particle fractions in the secondary beam with an integrating Cherenkov counter in the expansion port (see figure 2-4). The Cherenkov counter is mounted on a

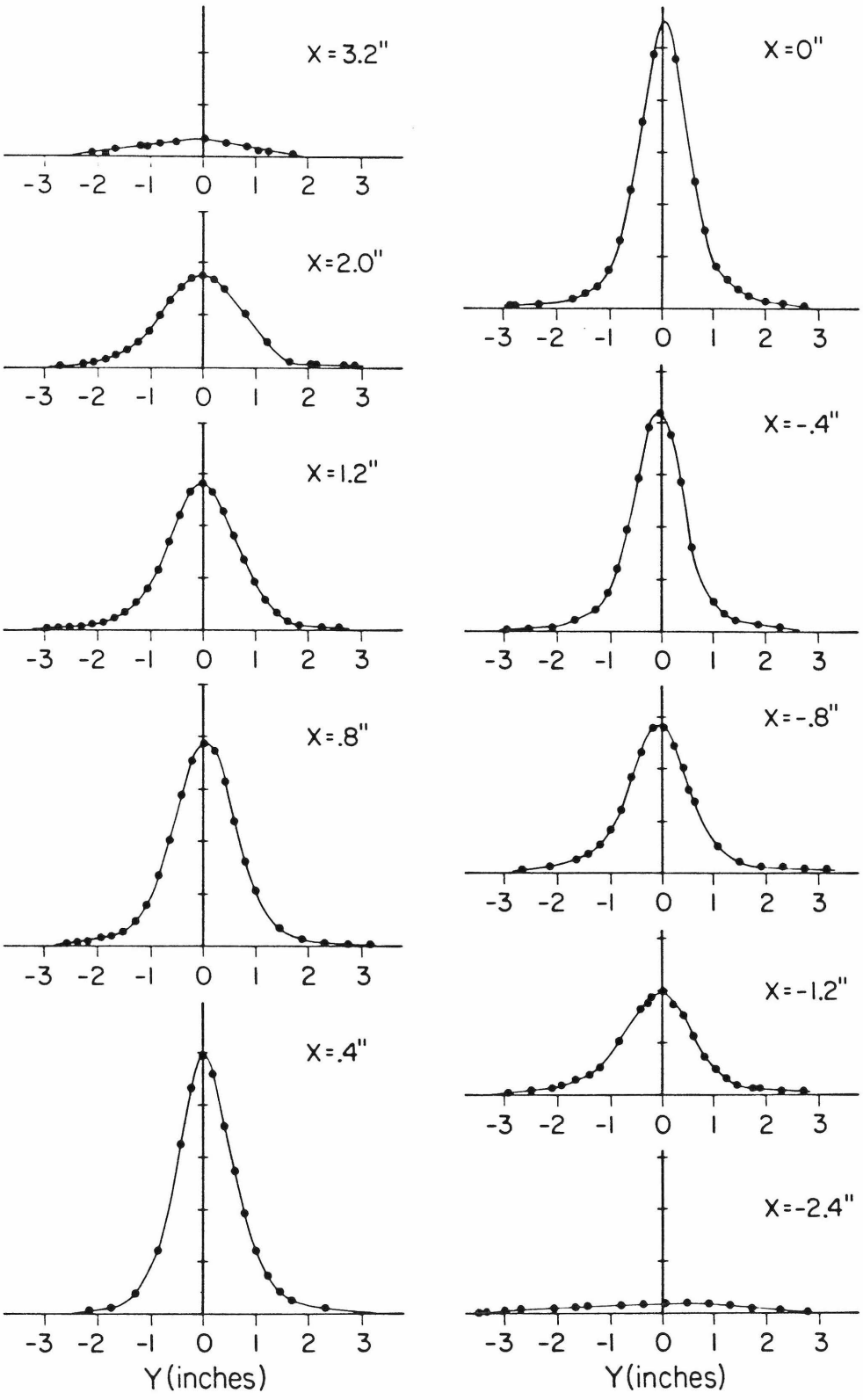

Figure 2-8: Secondary beam profiles at the expansion port.

movable table so that it may be moved out of the beam when taking neutrino data, minimizing the amount of material in the secondary beam.

A diagram of the Cherenkov counter is shown in figure 2-9. The main vessel of the counter is filled with helium. Cherenkov light produced in the gas is collected by a parabolic mirror (M1). A movable iris plate containing a variety of apertures sits at the focal point of M1. A lens focuses the light onto a phototube. The signal from the phototube is integrated over each beam pulse and then digitized. A shutter (CHS1) may be closed to isolate light produced outside of the helium containing part of the counter. The counter may be tilted to center the Cherenkov cone on the iris.

A schematic of the gas system is shown in figure 2-10. A controlled amount of gas can be added to the Cherenkov counter by filling the gas line between valves CH1 and CH2 to a known pressure and then opening CH2.

B. LINEARITY TESTS

The linearity of the phototube-integrator-digitizer system can be tested by comparing the Cherenkov counter

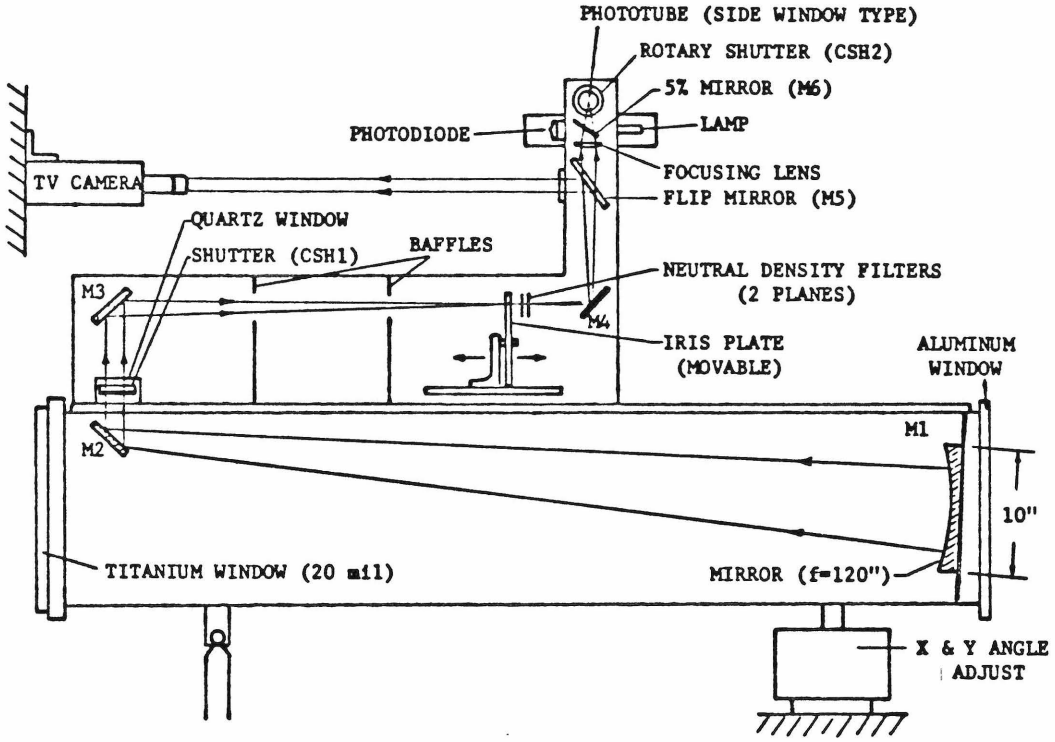

Figure 2-9: E356 Cherenkov counter.

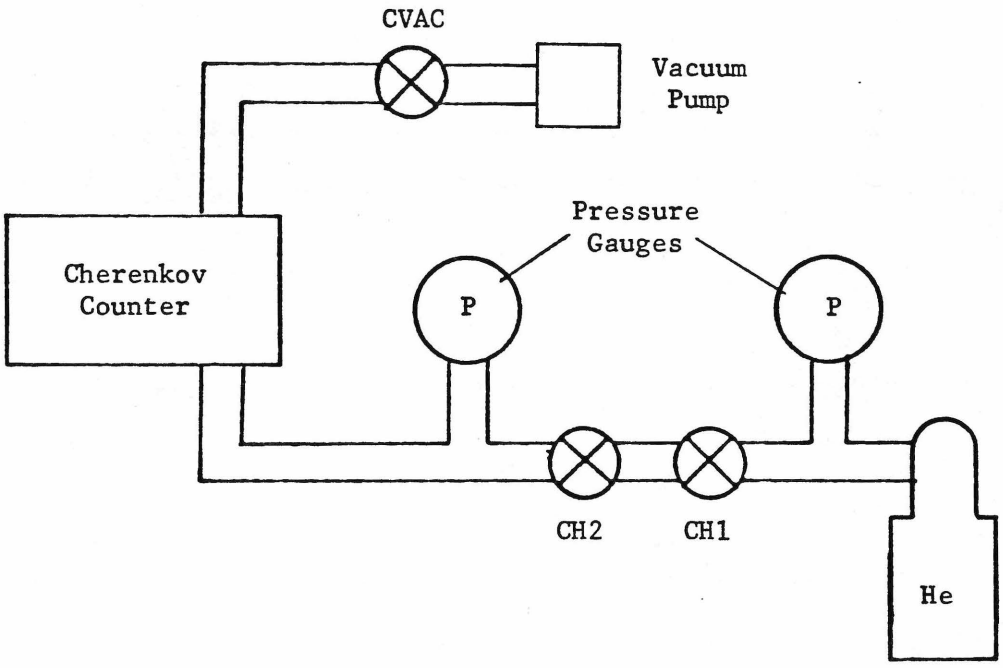

Figure 2-10: Cherenkov counter gas system. CVAC, CH1, and CH2 are valves.

signal with the ion chamber. A beam of 200 GEV protons was steered through the train with the target out. The aperture at the iris was set to a hole that corresponds to a 2 mrad Cherenkov angle. The gas pressure in the Cherenkov counter was set to 285 mm Hg. At this pressure the Cherenkov angle is 1.7 mrad, making the measurement insensitive to small changes in beam steering. The response of the Cherenkov counter was measured by varying the beam intensity. Figure 2-11(a) shows the Cherenkov counter response versus the ion chamber signal. Nonlinearities of about 10% are present. The nonlinearities are parameterized to correct the Cherenkov counter response. Figure 2-11(b) shows the result of the correction.

The linearity of the pressure gauge was checked by evacuating the counter and putting in one fill of gas at a time. If the fill line is kept at constant pressure, the pressure in the counter after n fills should have the functional form

$$P_n = a(1-b^n). \qquad (2-1)$$

The pressure, measured after every fill, was fit to this function to determine a and b. Figure 2-12 shows the

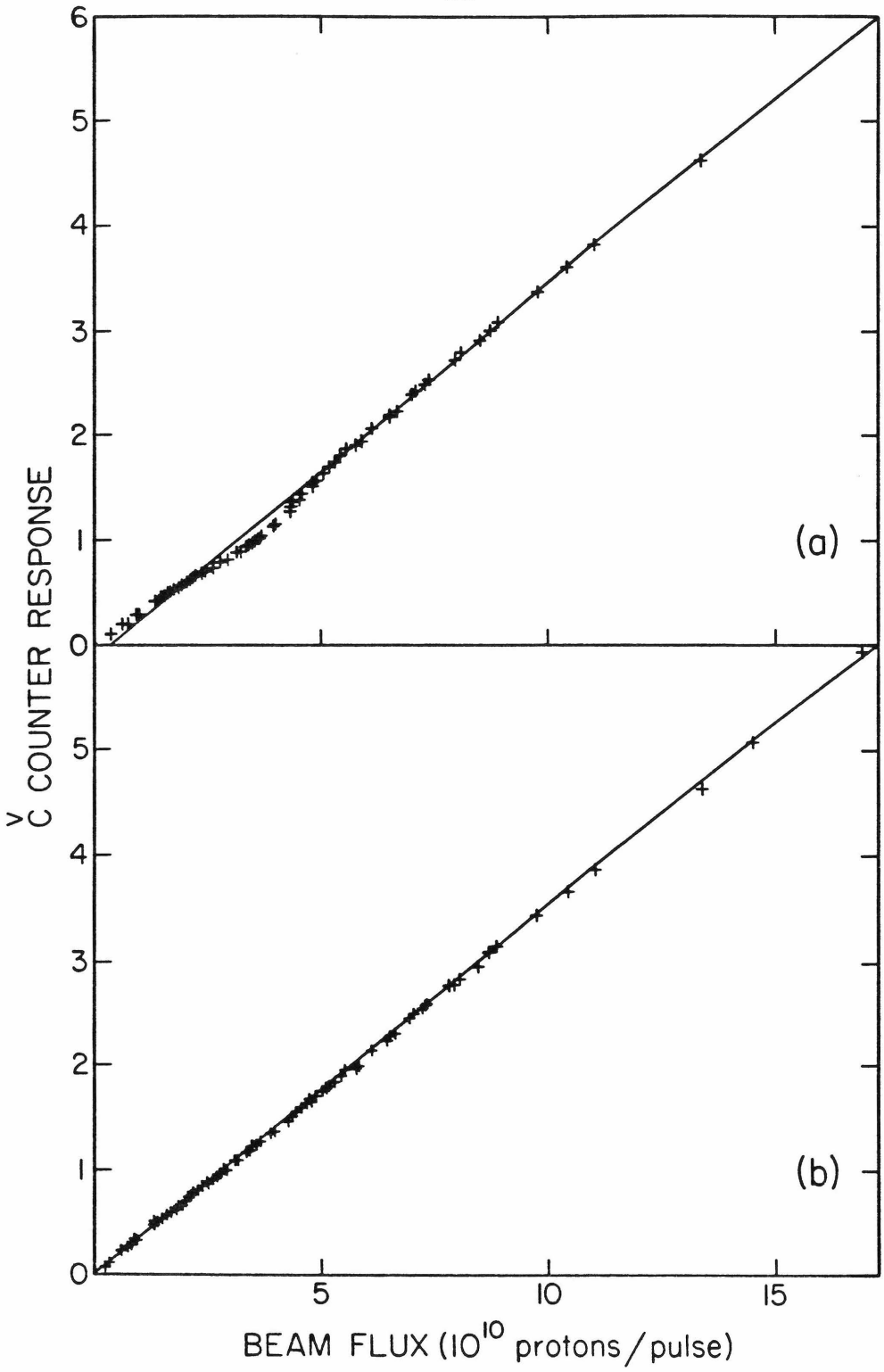

Figure 2-11: Linearity of Cherenkov counter response
(a) before correction
(b) after correction

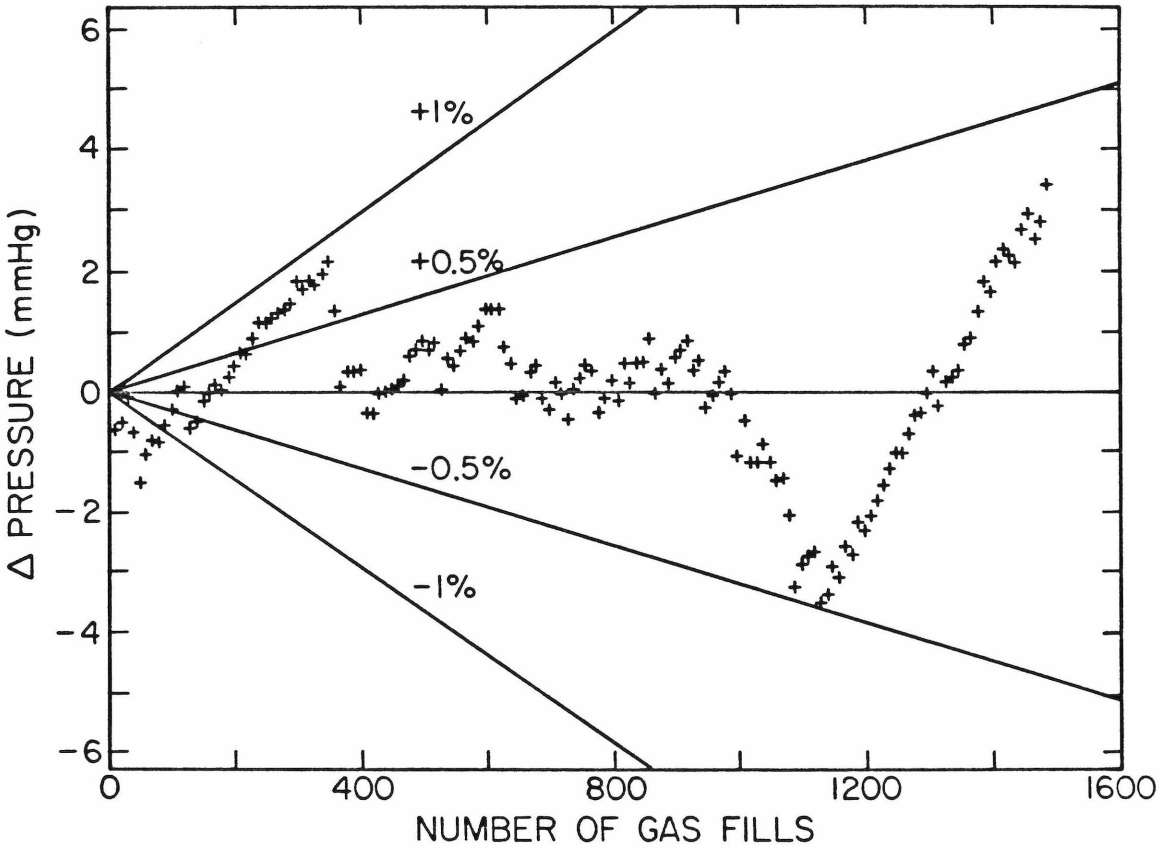

Figure 2-12: Linearity of Cherenkov counter pressure gauge.

difference between the measured pressure and the fit as a function of number of fills. The jitter in the pressure gauge is less than 1%. The pressure curves have not been corrected for this jitter.

C. PRINCIPLES OF OPERATION

A charged particle traveling with velocity v (c=1) greater than the local speed of light in a medium with index of refraction n produces Cherenkov light at an angle θ given by

$$\cos\theta = 1/nv. \qquad (2\text{-}2)$$

The index of refraction of a gas is a function of its pressure P,

$$n = 1+\kappa P. \qquad (2\text{-}3)$$

The gas constant κ can be measured directly (see section 2.5G). For small angles and low pressures, a particle of mass m and momentum p produces light at an angle θ at a pressure given by

$$P = \frac{1}{2\kappa}\left[\theta^2+(m/p)^2\right]. \qquad (2\text{-}4)$$

The energy radiated by such a particle at a frequency ω over a distance L is

$$I(\omega) = e^2 \omega L \theta^2. \qquad (2\text{-}5)$$

If the Cherenkov counter accepts light produced between angles θ_1 and θ_2, and if the pressure is varied and the signal integrated over pressure, the integrated result is

$$\int I \, dP = \frac{e^2 \omega L}{4 K} (\theta_1^4 - \theta_2^4), \qquad (2\text{-}6)$$

which is independent of mass and momentum. In general the acceptance is a function of θ and ω, but the signal integrated over momentum is independent of particle type and momentum.

In this experiment we need to know the relative fraction of pions, kaons, and protons in the secondary beam. At a given Cherenkov angle, particles of different masses produce light at different pressures. Figure 2-13 shows the Cherenkov angle as a function of pressure for pions, kaons, and protons of momentum 200±20 GEV. Good separation between particle types is achieved by accepting light at Cherenkov angles between .7 mrad and 1.0 mrad. Figure 2-14 is a pressure curve taken at the 300 GEV beam

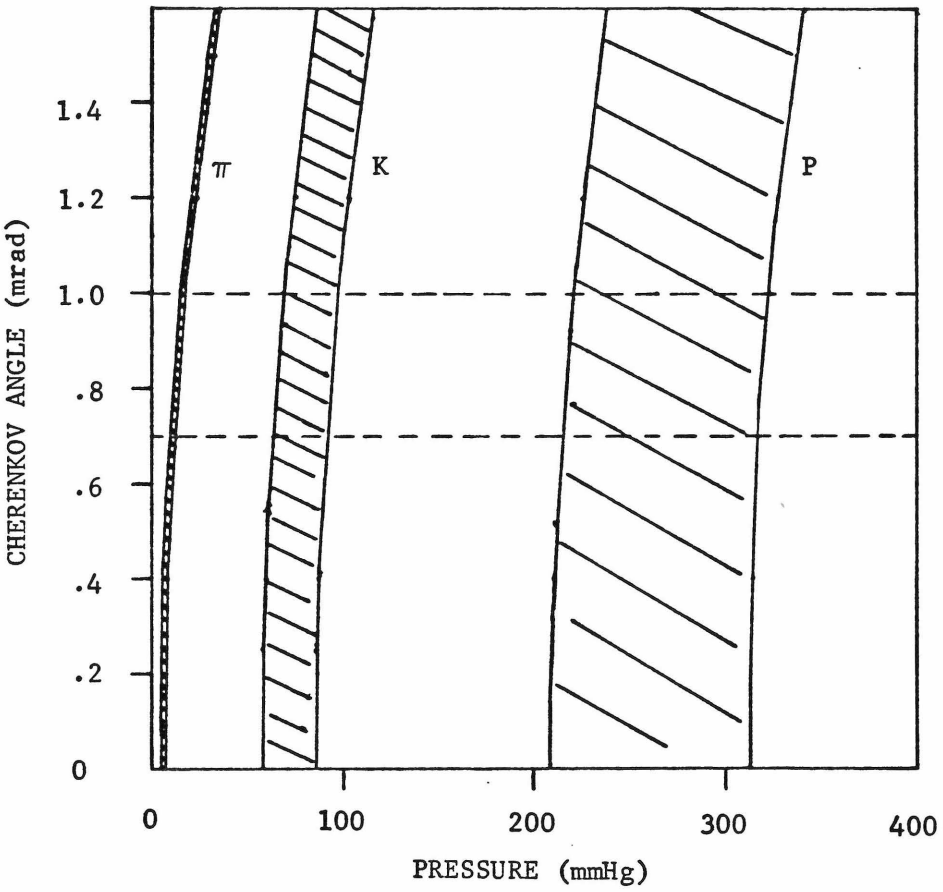

Figure 2-13: Cherenkov angle versus pressure for hadrons of momentum 200±20 GEV.

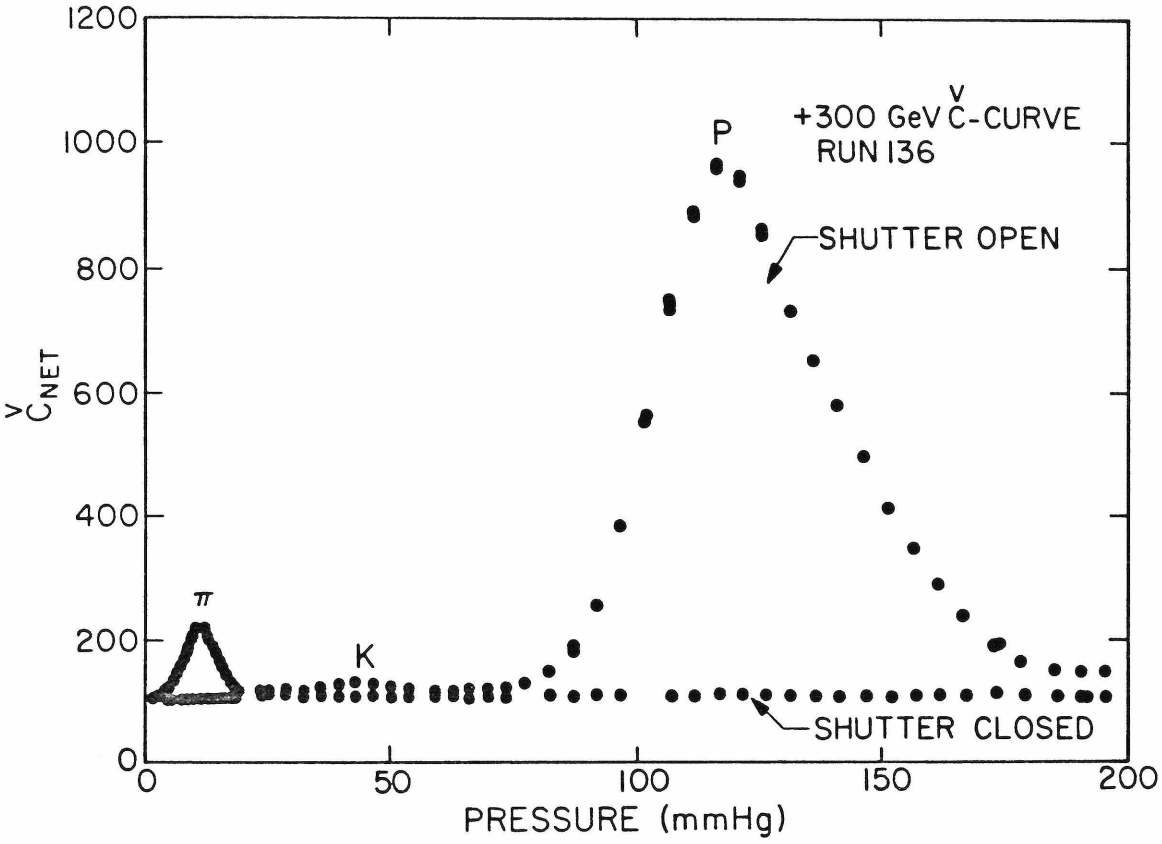

Figure 2-14: Cherenkov counter pressure curve with the secondary beam tuned to 300 GEV positives.

setting. Each point is normalized to the total intensity of that beam pulse by dividing the Cherenkov counter signal by the ion chamber signal. The aperture at the iris is an annulus with an inside diameter that corresponds to a .7 mrad Cherenkov angle and an outside diameter that corresponds to a 1.0 mrad Cherenkov angle. The shutter closed curve was taken with shutter CSH1 closed (see figure 2-9). This signal comes from light produced outside the gas container and is subtracted from the shutter open signal. The background curve is the sum of the backgrounds discussed in the next section and also is subtracted. Since each particle contributes equally to the integrated signal independant of its mass and momentum, the fractional pion/kaon/proton composition of the beam is proportional to the areas under the respective peaks in the pressure curve.

D. BACKGROUNDS

It became apparent while running this experiment that a significant background exists under the particle peaks and that the background is not simple, but has more than one component. During a later run (E616) a series of studies was done to isolate and measure the various backgrounds. For the latter experiment the transmission and momentum bite of the train were increased

significantly, and minor modifications were made to the Cherenkov counter, but the background studies proved invaluable in understanding the E356 particle fractions.

There are four different backgrounds in these pressure curves. Two are caused by beam interactions in the small amount of material in the beam line upstream of the Cherenkov counter. Particles produced off axis by beam-material interactions can produce a great deal of light because light production varies linearly with θ^2 (see equation 2-5). Pions, kaons, and protons produce a significant background from scattered pions. In addition, protons in the beam that get deflected produce a background at pressures above that of the proton peak. A third background is caused by light that is scattered by the optics of the counter. The primary source of the scattered light eventually was found to be mirror M2 (see figure 2-9). The final background is not well understood. It causes a signal that has a maximum at zero pressure and decreases as the pressure is increased. All four backgrounds have been measured.

We can isolate the backgrounds caused by interactions in material by putting additional material in the beam to magnify the effect. The scattered pion background can be

extracted best by studying a beam tuned to negatives, where the kaon/pion ratio is small and the antiproton peak is tiny. Pressure curves were taken with the beam tuned to 120 GEV negative secondaries and to 250 GEV negative secondaries. First a pressure curve was taken with the normal beam configuration, and then a curve was taken with 1/2" of aluminum placed upstream of the Cherenkov counter. The aluminum increases the total amount of material in front of the Cherenkov counter by a factor of 4.9. The increase in the signal at each pressure equals 4.9 times the background from beam-material interactions. The rest of the background comes from scattered light. The 120 GEV curve with aluminum in the beam is shown in figure 2-15, and the 250 GEV curve with aluminum in the beam is shown in figure 2-16. The scattered light background has been subtracted from these curves. The signal from the material background is drawn under the pressure curve.

In subtracting the scattered pion background from other pressure curves it is assumed that secondary pions and kaons contribute equally to the background and that the background is proportional to the total number of pions and kaons. The background depends on the secondary energy. At each pressure, a linear interpolation (or extrapolation) is done using the two points at 120 GEV and 250 GEV.

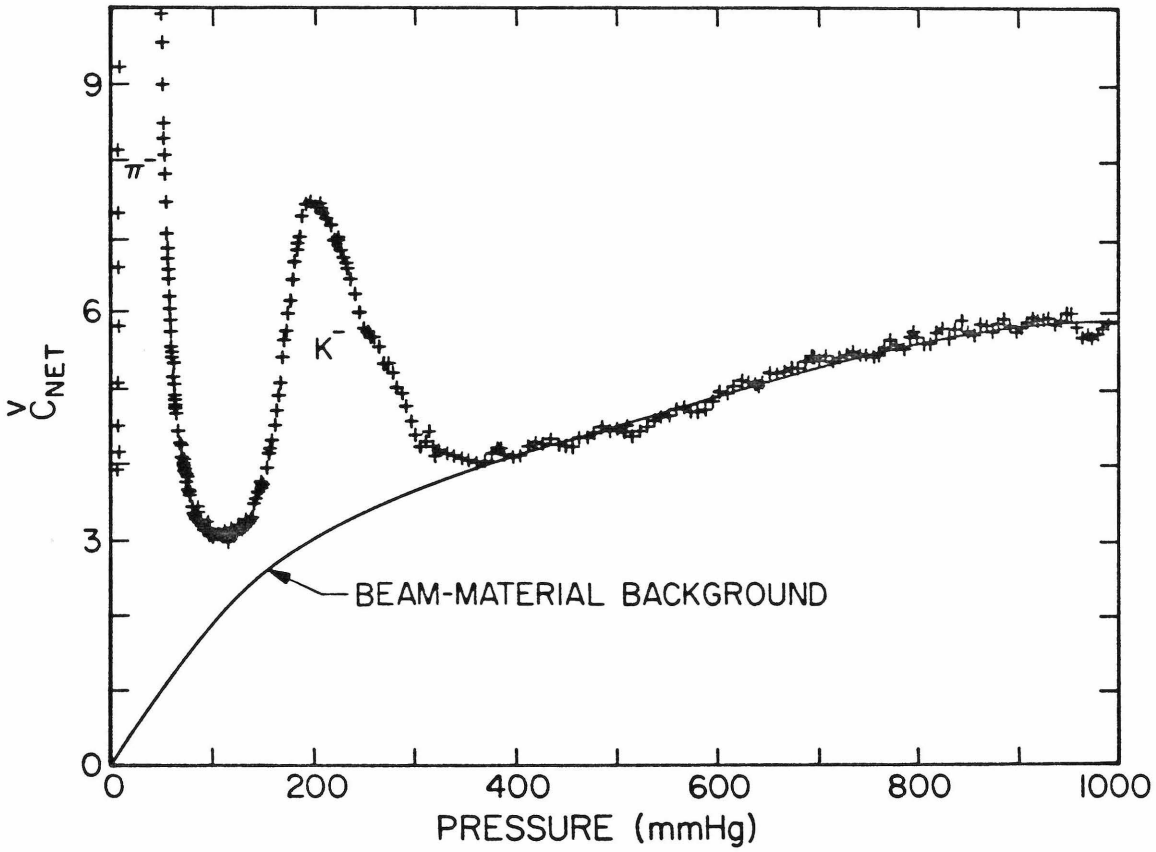

Figure 2-15: Pressure curve of 120 GEV negative secondaries with 1/2" Al in beam.

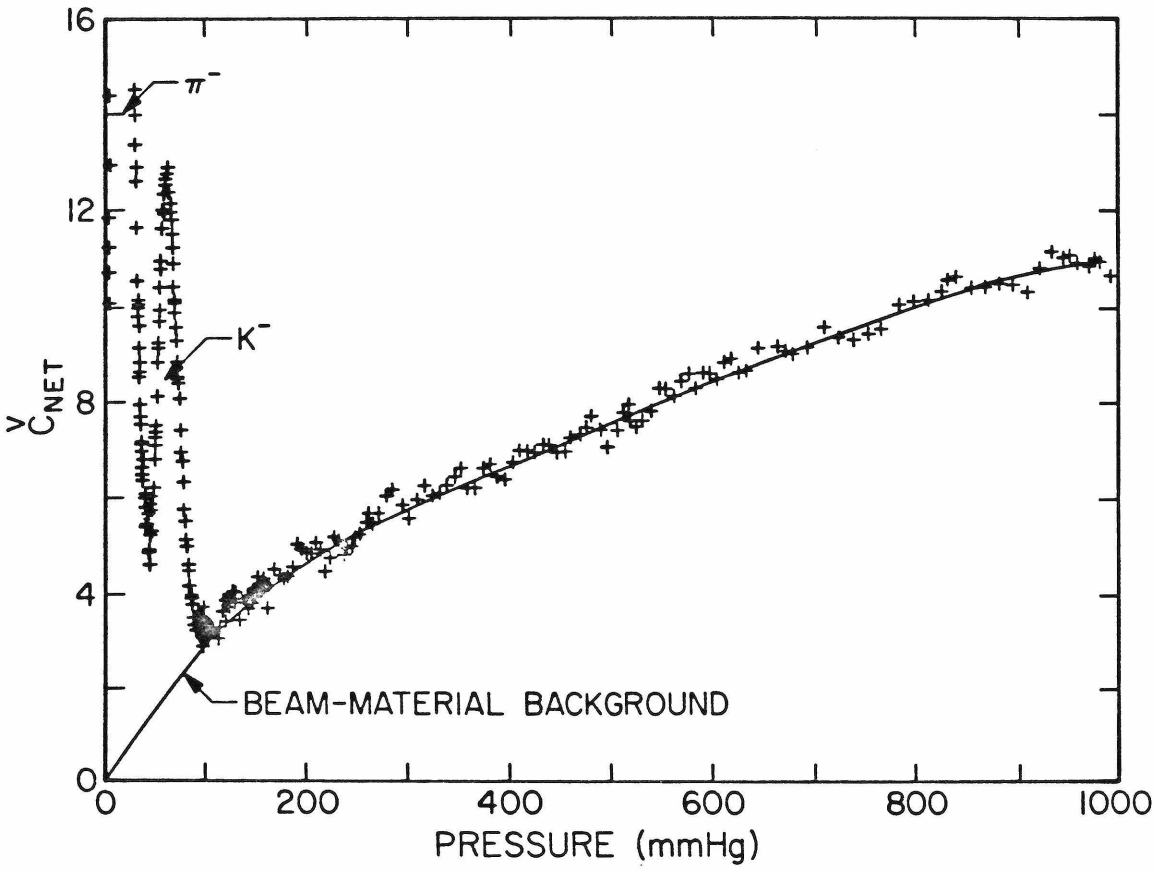

Figure 2-16: Pressure curve of 250 GEV negative secondaries with 1/2" Al in beam.

Pressure curves taken with a 200 GEV primary proton beam are shown in figure 2-17. Figure 2-17(a) was taken with no additional material in the beam, and figure 2-17(b) was taken with 1/2" Al in the beam. The scattered pion background is consistent with the background produced by a pion beam with 1/3 the momentum of the proton beam on the low pressure side of the peak. The curves drawn under the pressure curves represent extrapolations on the high pressure side of the peak.

The remaining background from proton-material interactions comes from scattered protons, and this background is on the high pressure side of the peak. Subtracting all of the material background from the pressure curve leaves the background from scattered light. Figure 2-18 shows a 200 GEV primary proton pressure curve with all three backgrounds indicated.

The last background we have to deal with occurs at low pressures. The Cherenkov counter gives a signal even at zero gas pressure. The magnitude of this signal relative to the pion flux is shown in figure 2-19 at different beam settings. We can measure the pressure dependence of this background because in many cases we expect clean separation between particle peaks. In figure 2-20 the signal

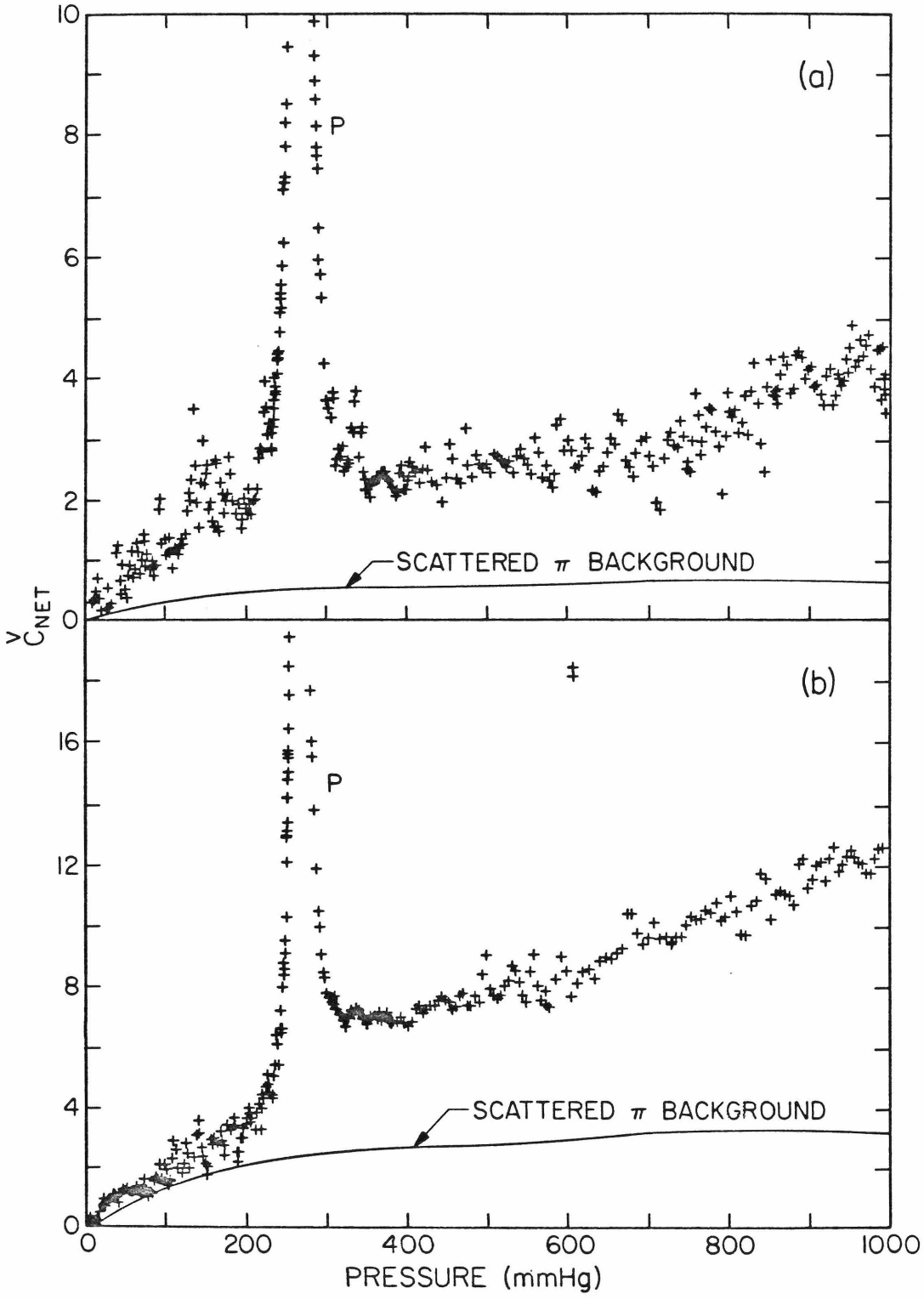

Figure 2-17: Pressure curve of 200 GEV primary protons
(a) no additional material in beam
(b) 1/2" Al in beam.

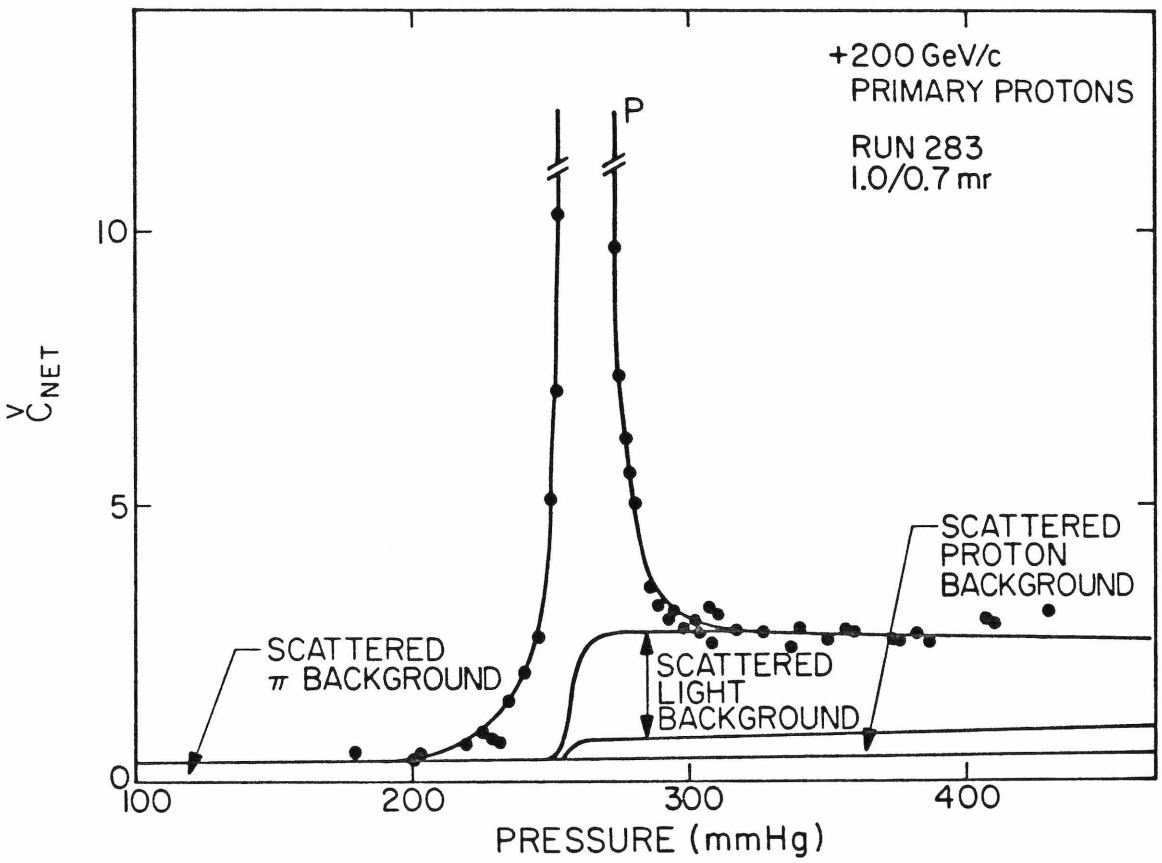

Figure 2-18: Backgrounds under a 200 GEV primary proton pressure curve.

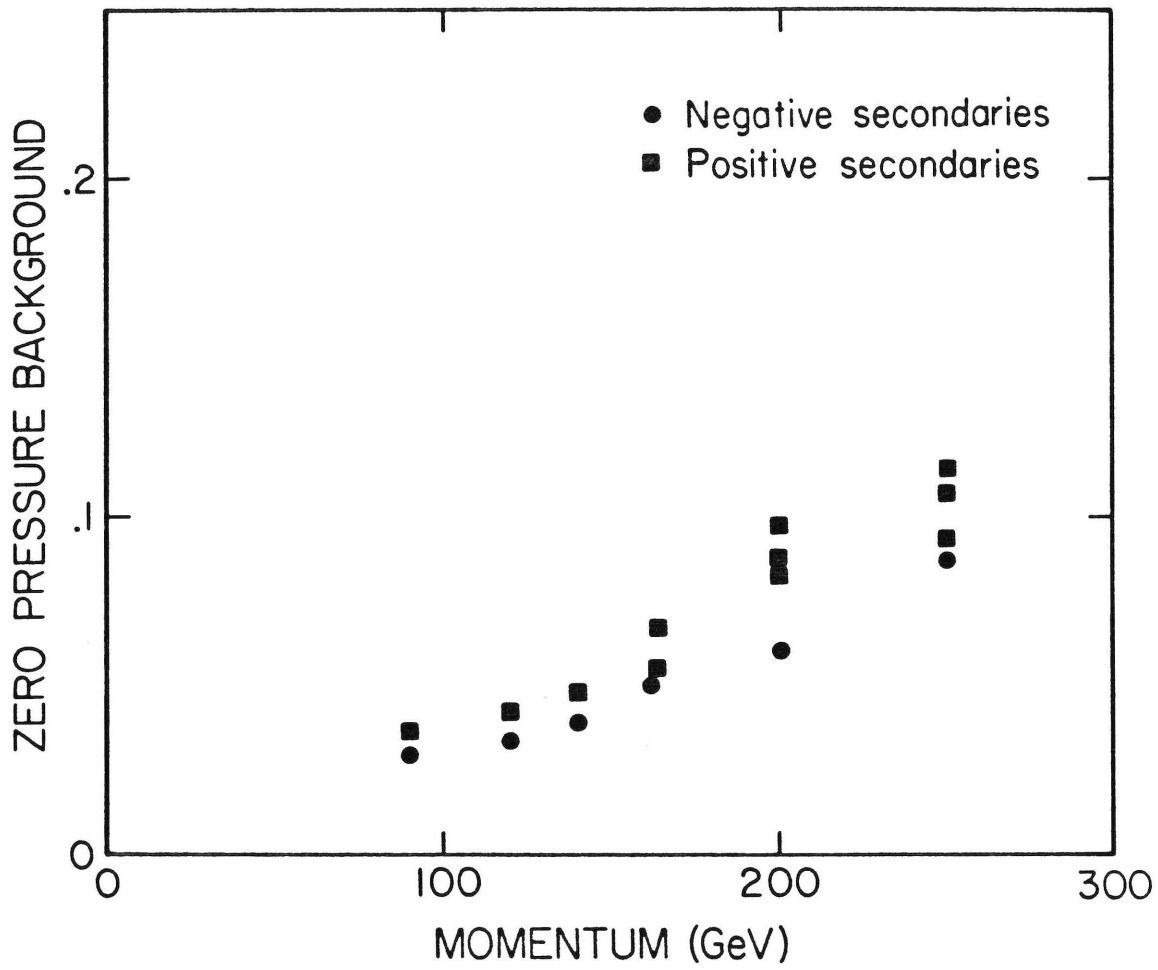

Figure 2-19: Zero pressure signal relative to pion flux.

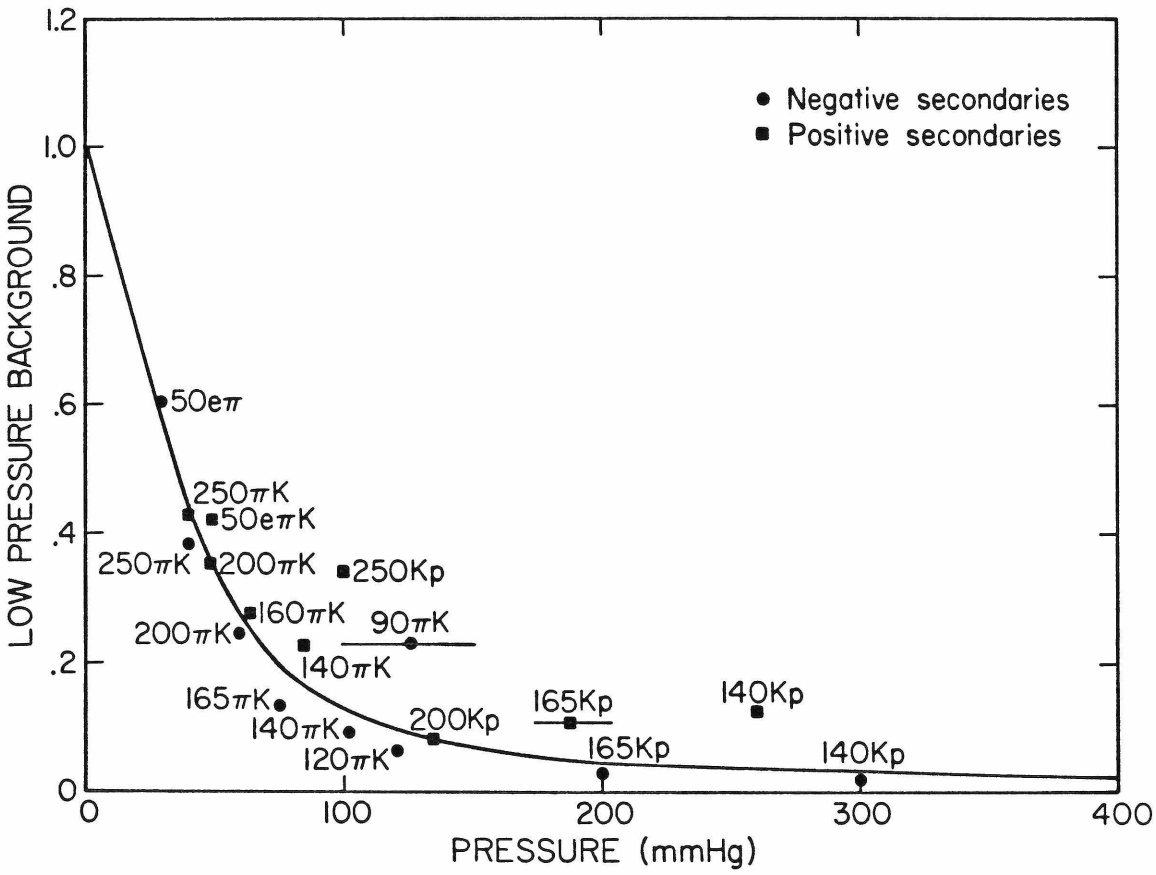

Figure 2-20: Low pressure background normalized to signal at zero pressure.

normalized to the zero pressure signal is shown at various pressures where we expect no signal. The beam setting for each point is shown in the graph. The backgrounds discussed previously have been subtracted from the pressure curves before determining this signal.

The origin of the zero pressure background is not understood, but it varies roughly like the secondary momentum times the pion flux, which would be the expected dependence if muons from pion decay were interacting with the counter in some way to produce light. The light must be at a wavelength that is attenuated by the gas to explain the pressure dependence.

The subtraction of each of these backgrounds from the pressure curves used to extract particle fractions for this experiment is shown in detail in section 2.5F.

E. POSITRON COMPONENT OF SECONDARY BEAM

Positive secondary beams at low momentum settings contain a significant positron component. In principle there are two methods of measuring the e^+/π^+ ratio with the Cherenkov counter.

Pressure curves taken at 90 GEV and 120 GEV with a .7/1.0 mrad aperture show a distinct e^+ peak. At these momenta the positron peak and pion peak can be integrated separately to determine the e^+/π^+ ratio. Figure 2-21(a) shows the pressure curve taken at 90 GEV.

Another method is to take a pressure curve with a 2 mrad aperture. Operated in this mode, the slope of the pressure curve below the pion threshold is proportional to the positron flux, while the slope just above the pion threshold is proportional to the sum of the positron flux and the pion flux. Figure 2-21(b) shows an example of this differential method taken at a beam setting of 120 GEV.

Preliminary E616 data are shown in figure 2-22. The two methods give results differing by a factor of 2 at 90 GEV. The reason for the discrepancy is not understood at present, but we have more confidence in the integral method.

A crude calculation was made to determine the energy dependence of the e^+/π^+ ratio. It was assumed that the source of positrons is $\pi^0 \rightarrow \gamma\gamma$, with the photons converting into e^+e^- pairs. It also was assumed that π^0 production at the target is the average of π^+ and π^- production, for

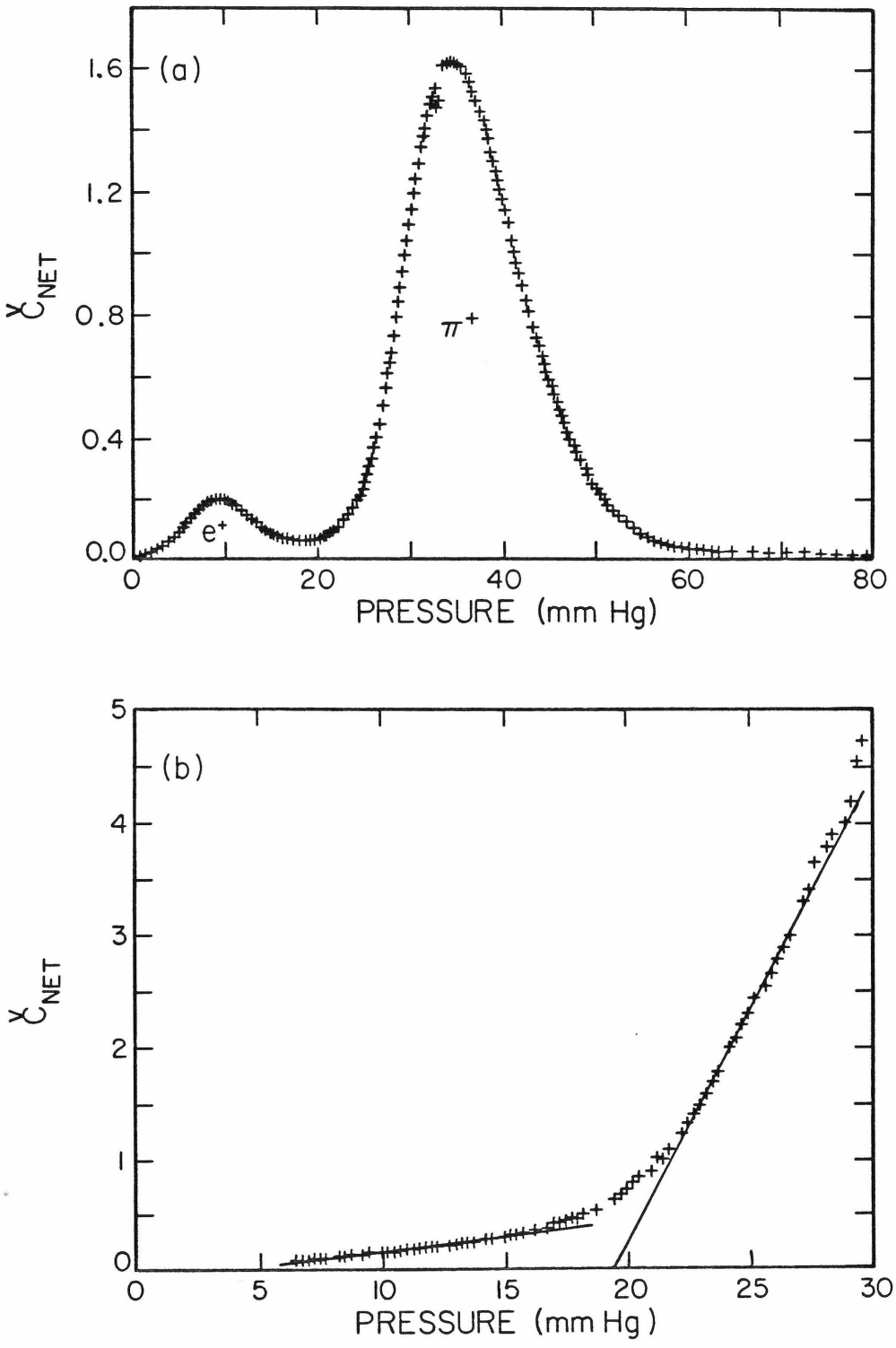

Figure 2-21: Extracting the e^+/π^+ ratio.
(a) Integral method at 90 GEV
(b) Differential method at 120 GEV

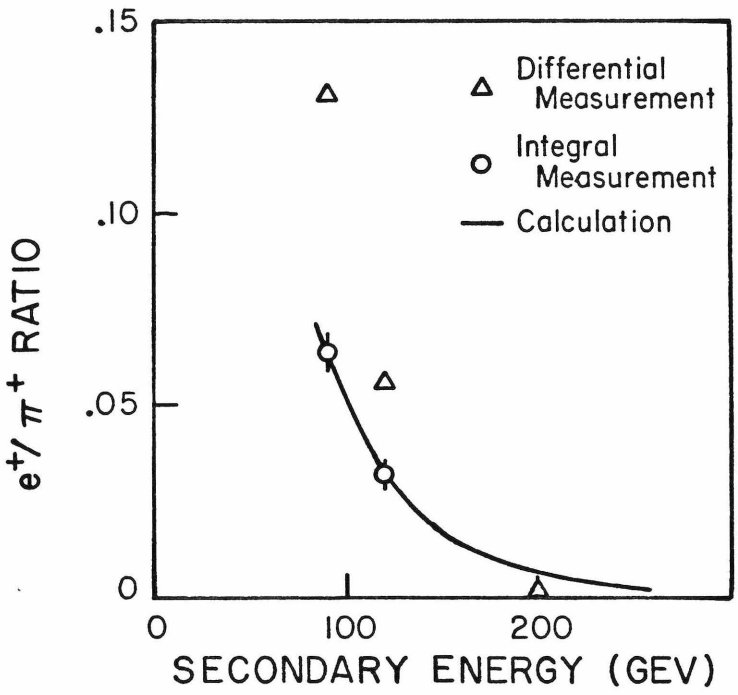

Figure 2-22: e^+/π^+ ratio as a function of beam setting.

which the Stefansky-White[13] parameterization was used. The overall level was adjusted by a constant factor to agree with the measurement at 90 GEV made by the integral method. The result is the curve shown in figure 2-22.

The positron component still is very uncertain at low momenta, but the indication is that the e^+/π^+ ratio is negligible at the E356 energy settings (200 GEV and 300 GEV). In this analysis we assume that the positron component of our beam is zero.

F. PARTICLE RATIOS

The particle fractions in the secondary beam are determined from pressure curves taken with a .7/1.0 mrad annular aperture.

The raw pressure curve at 200 GEV is shown in figure 2-23. The backgrounds discussed in section 2.5D are shown in figure 2-24. Figure 2-25 shows the final pressure curve after all backgrounds are subtracted. The pion, kaon, and proton peaks are well separated, and the relative areas determine the particle fractions.

The raw pressure curve at 300 GEV is shown in figure

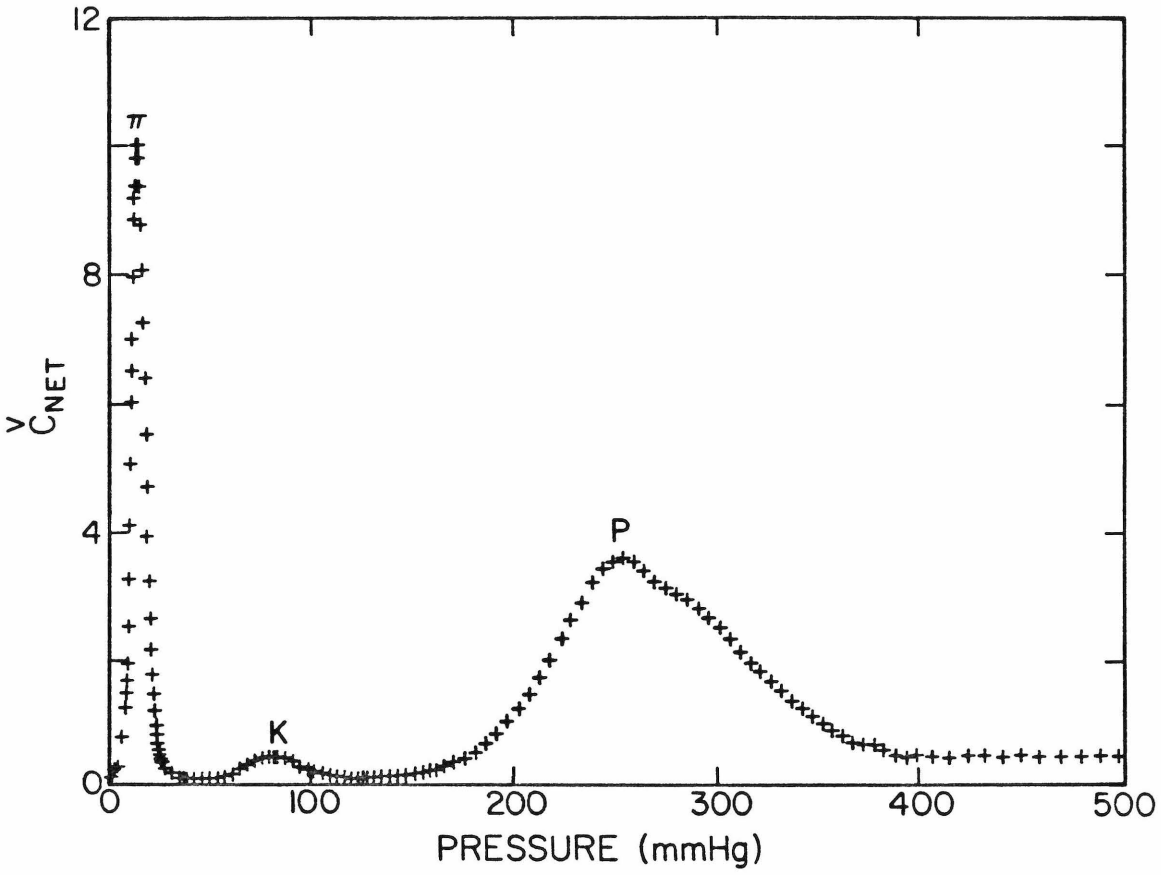

Figure 2-23: Raw pressure curve for 200 GEV positive secondaries.

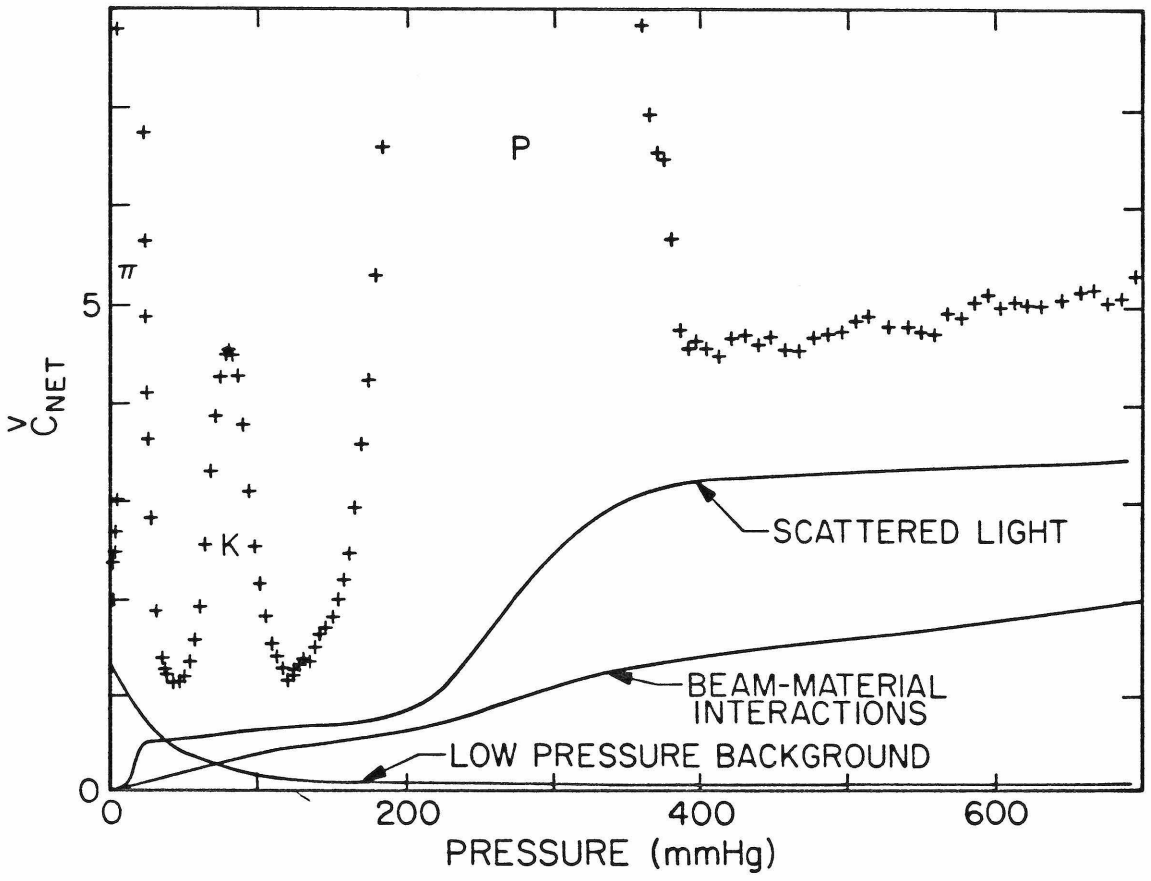

Figure 2-24: Background subtraction at 200 GEV.

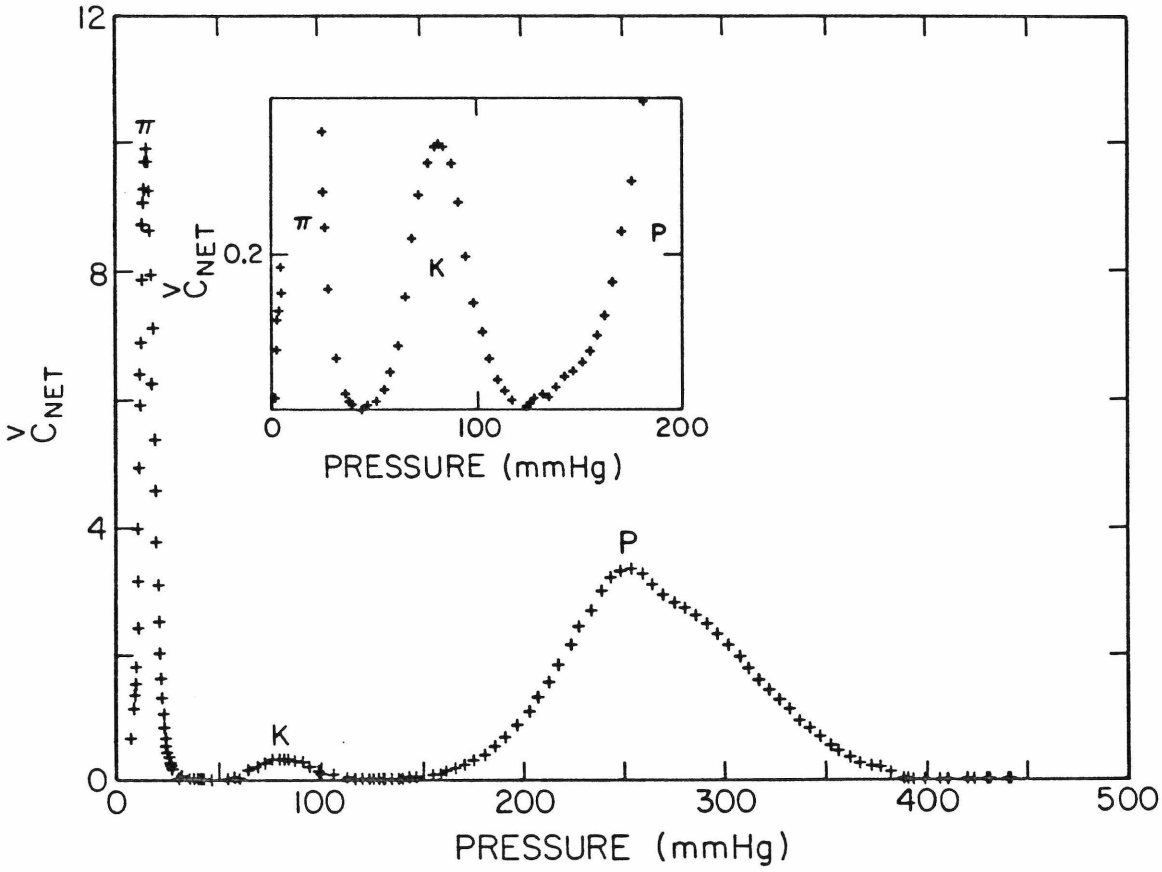

Figure 2-25: 200 GEV pressure curve after background subtraction.

2-26. The background levels are shown in figure 2-27, and the curve after background subtraction is shown in figure 2-28. This time the pion and kaon peaks are not completely separated. However, the shape of the pion peak above 200 GEV is dominated by the counter resolution, so it is possible to determine the shape of the high pressure side of the pion peak at 200 GEV where the pion and kaon separation is good. Figure 2-29 compares the 300 GEV pion peak with the 200 GEV pion peak, where the 200 GEV peak has been rescaled to match the trailing edge of the 300 GEV peak. The high pressure tail on the rescaled 200 GEV curve then is used to extrapolate the pion peak under the kaon peak at 300 GEV. This extrapolation is shown in figure 2-30.

The particle fractions at the Cherenkov counter determined by these curves are listed in table 2-2. The uncertainties come from the background subtractions. The most severe systematic uncertainty is in subtracting the tail of the pion peak at 300 GEV. The uncertainties in the pion neutrino cross sections and the 200 GEV kaon neutrino cross sections are dominated by statistical errors.

The particle fractions measured at the Cherenkov counter must be corrected for pion and kaon decays upstream

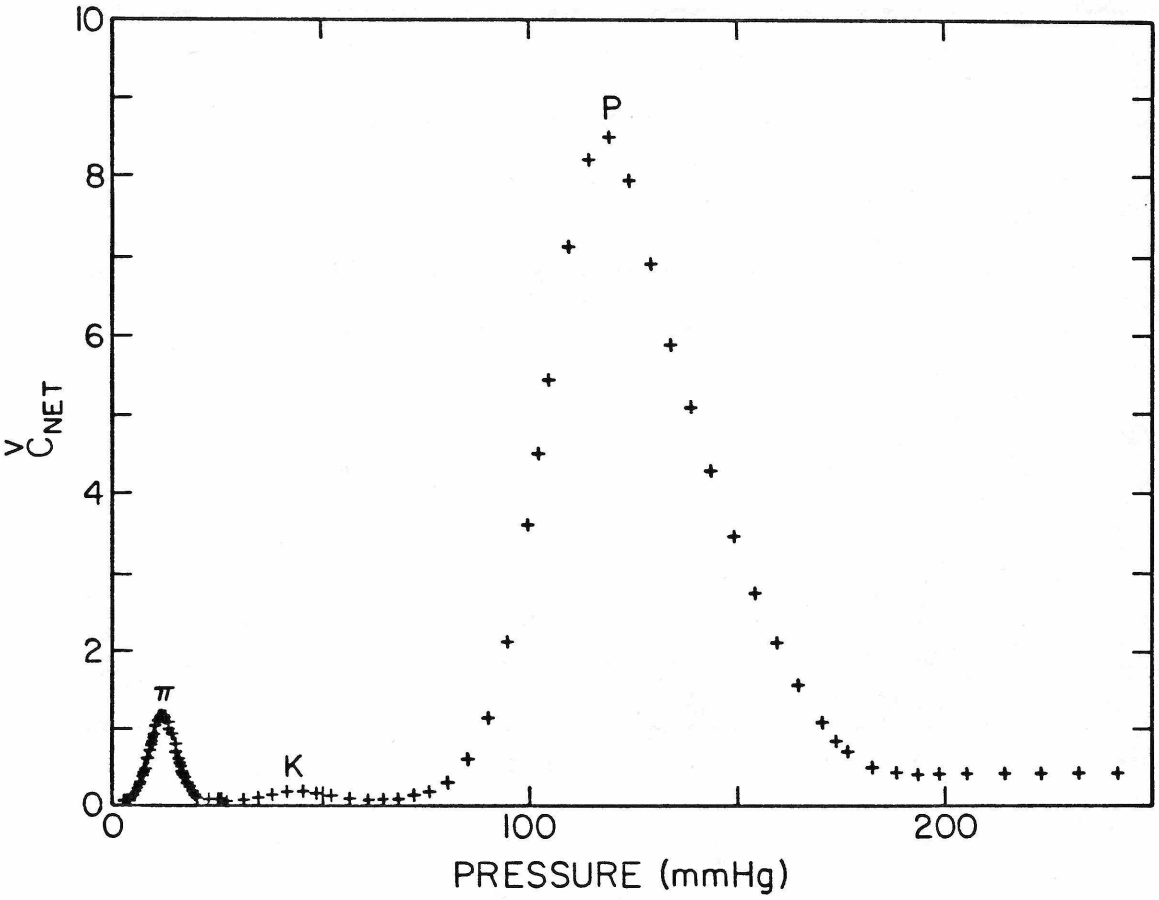

Figure 2-26: Raw pressure curve for 300 GEV positive secondaries.

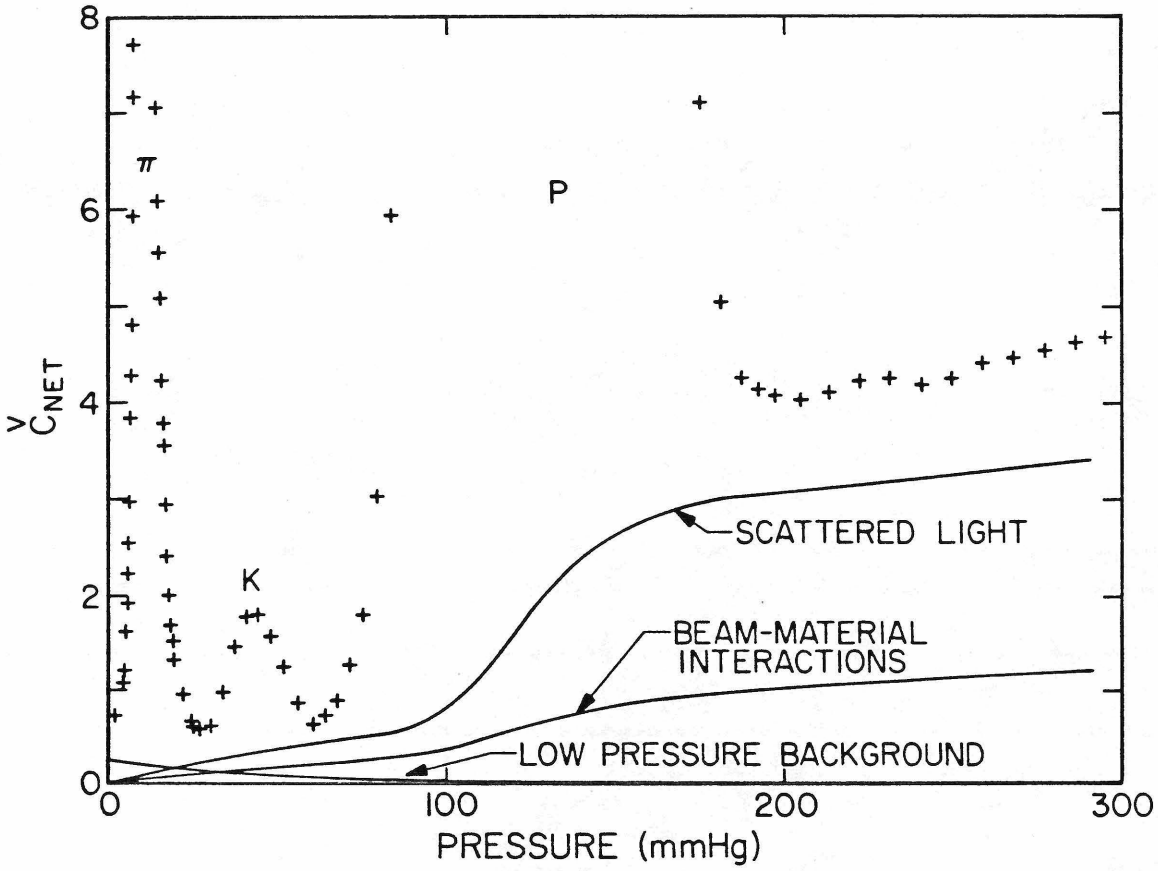

Figure 2-27: Background subtraction at 300 GEV.

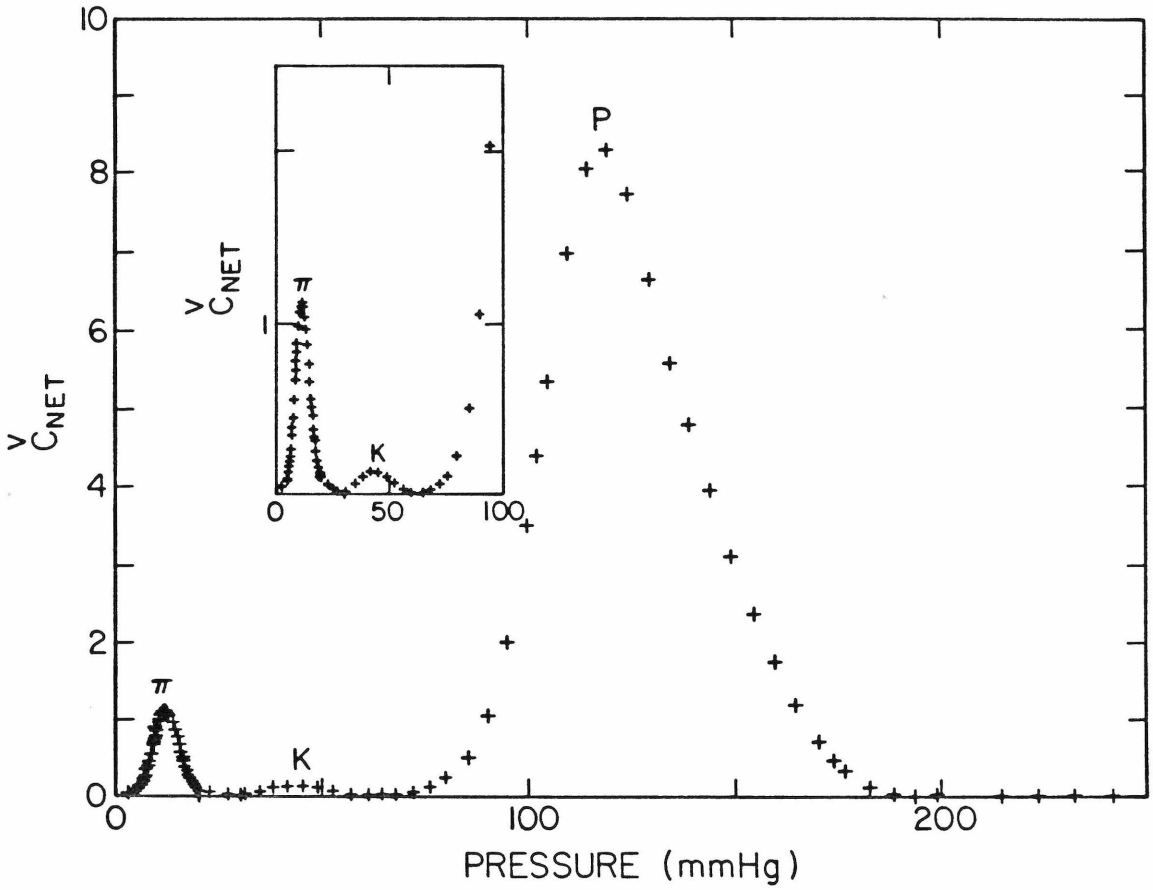

Figure 2-28: 300 GEV pressure curve after background subtraction.

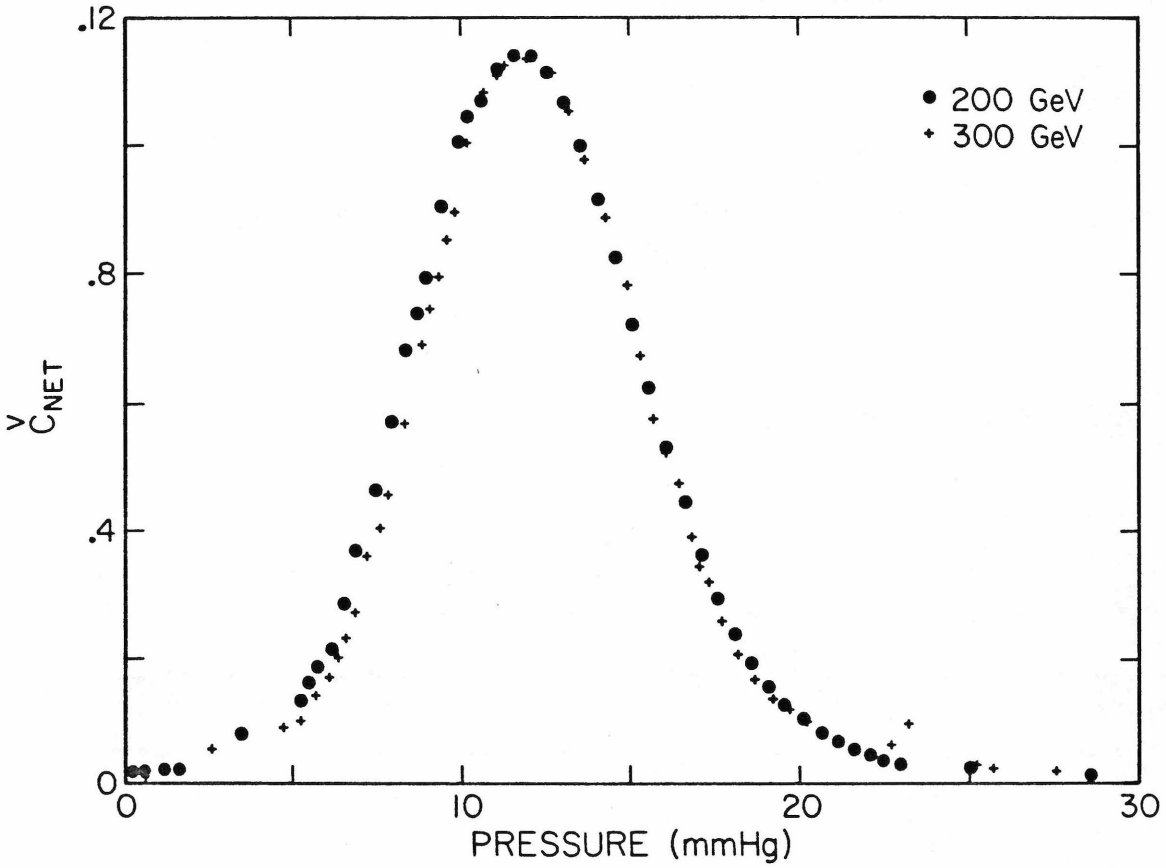

Figure 2-29: Comparison of 300 GEV pion peak with rescaled 200 GEV pion peak.

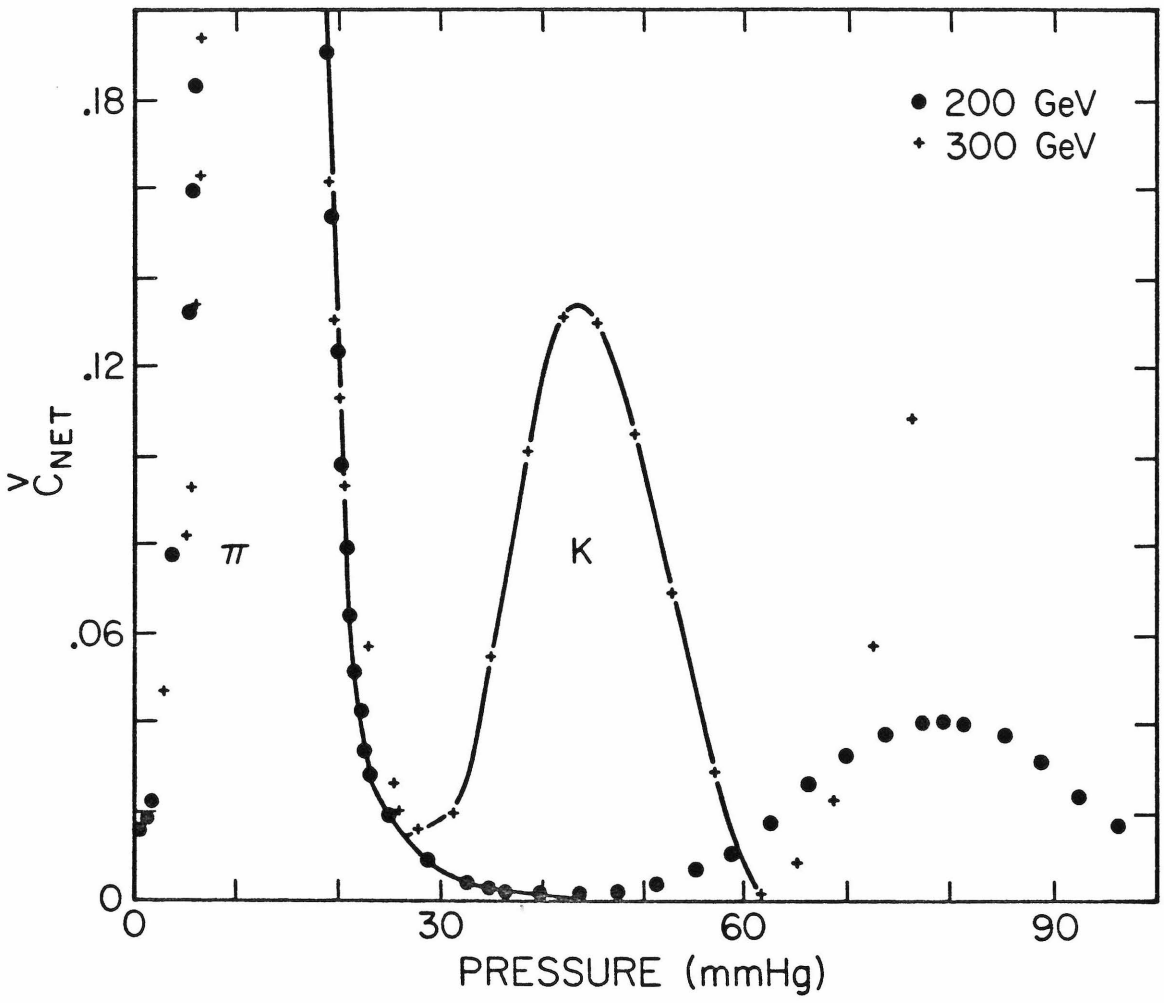

Figure 2-30: Subtraction of pions from 300 GEV kaon peak.

TABLE 2-2: SECONDARY BEAM PARTICLE FRACTIONS AT THE CHERENKOV COUNTER

200 GEV secondary energy setting	
Protons	78.51±.30%
Pions	19.05±.29%
Kaons	2.44±.07%
300 GEV secondary energy setting	
Protons	96.88±.05%
Pions	2.52±.04%
Kaons	.59±.03%

of the Cherenkov counter to obtain relative particle production at the target. The π/K and K/p production ratios are shown in figure 2-31. These particle ratios are compared with results from other experiments that produced hadrons by hitting a thick target with a 400 GEV proton beam. The CFR[14], CDHS[15], and CHARM[16] measurements were made in dichromatic neutrino beams. The CFRR target is 10.5" BeO. The CFR target was 12" Al. CDHS and CHARM use a 19.7" Be target. Dichromatic neutrino beams accept particles produced in the forward direction. The maximum production angles accepted by these beams is about 2 mrad. The BFR[17] experiment measured relative particle production with an 8" beryllium target at production angles between 2 and 3.5 mrad. These five experiments are not strictly comparable because of different acceptances and production targets. The particle fractions are relatively insensitive to these differences. The curves shown are exponentials determined by the E356 measurements.

Comparing our absolute particle yields with other experiments is difficult because absolute particle production varies rapidly as a function of production angle and of target thickness. We had difficulty determining the acceptance of the dichromatic train as it existed for the E356 run (see section 2.6C), and it must be known quite

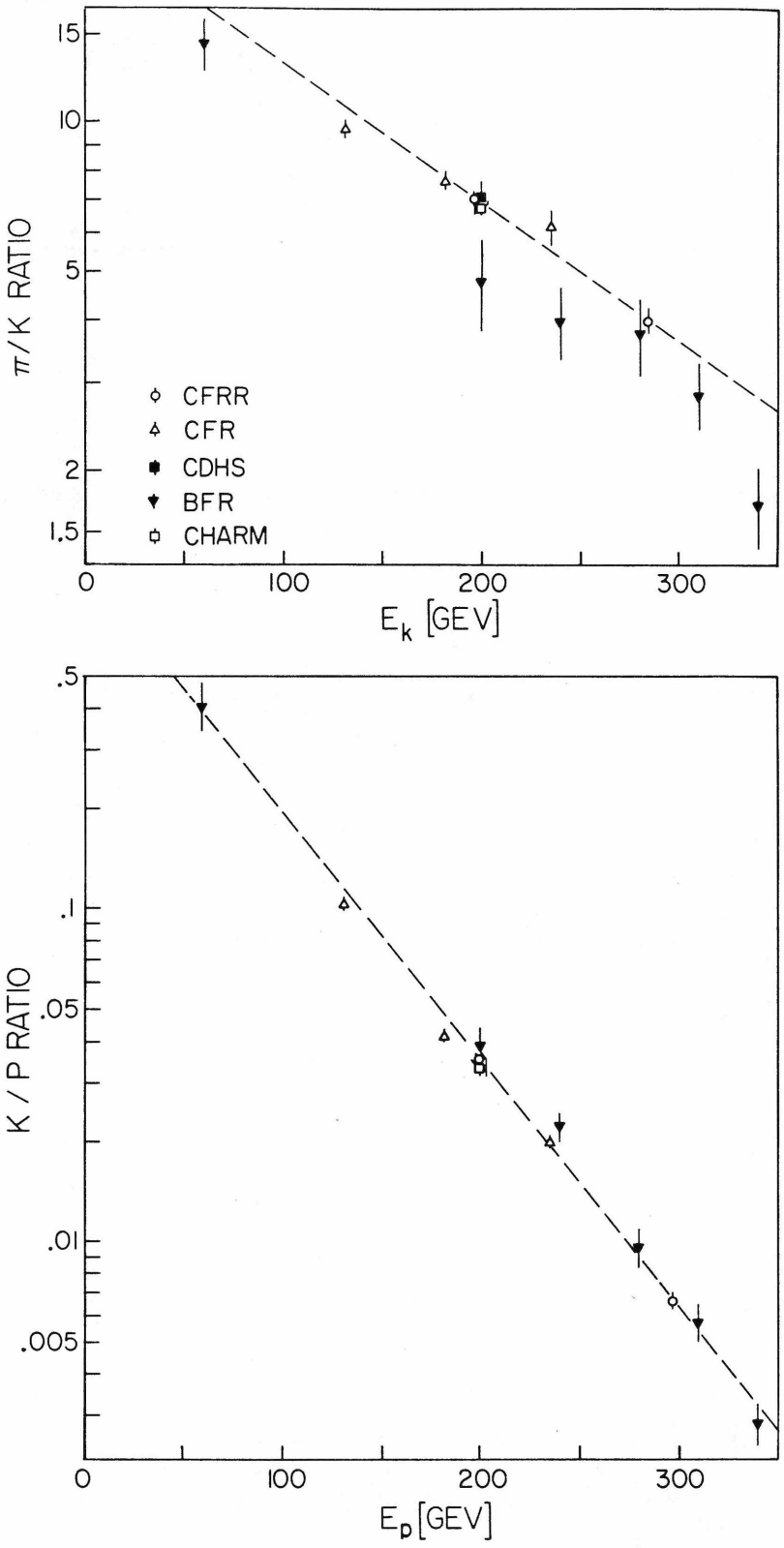

Figure 2-31: π^+/K^+ **&** K^+/P **ratios at the target.**

accurately to meaningfully compare absolute yields. Also, significant uncertainties exist in comparing targets of different thickness. We must rely on the ion chamber to determine the absolute particle flux in the decay pipe.

G. DETERMINATION OF THE GAS CONSTANT

The gas constant of the Cherenkov counter can be determined by looking at a beam of 200 GEV primary protons, which has a very small momentum dispersion (±0.1%). Equation 2-4 can be solved for K to give

$$K = \frac{1}{2P}\left(\frac{m}{p}\right)^2\left[1+\left(\frac{\theta p}{m}\right)^2\right]. \qquad (2\text{-}7)$$

There are two methods of extracting K which give results consistent to within 0.5%.

The first method uses a pressure curve taken with a .7/1.0 mrad annular aperture. The mean angle is .86 mrad, and K is determined from the pressure at the peak of the curve (see figure 2-32(a)).

The second method uses a pressure curve taken with a 2 mrad circular aperture. The pressure at which protons start producing Cherenkov light at 0 degrees is used to

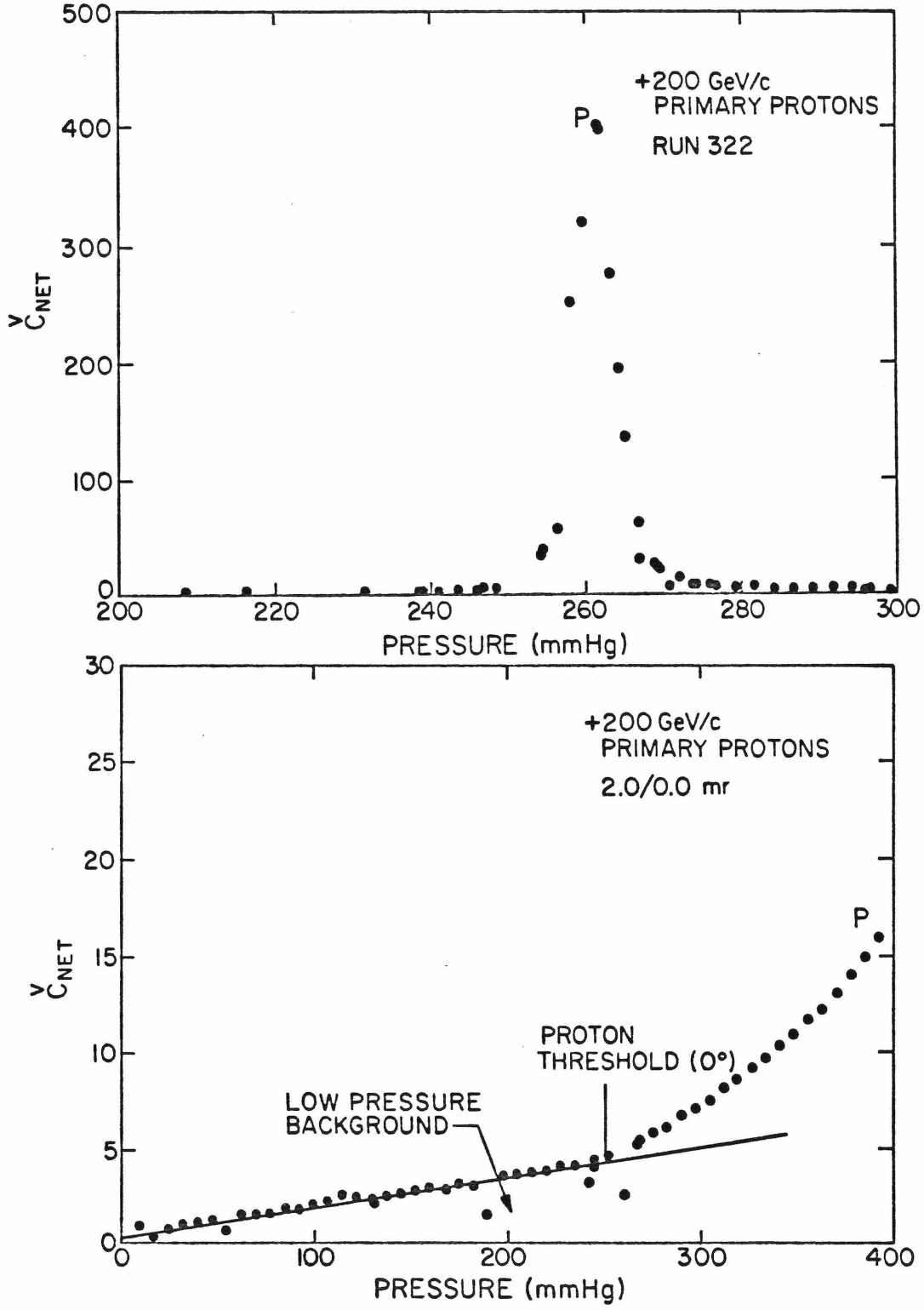

Figure 2-32: Pressure curves of 200 GEV primary protons
(a) .7/1.0 mrad annular aperture
(b) 2.0 mrad circular aperture

determine κ (see figure 2-32(b)).

The values of κ determined from three separate pressure curves were averaged to give a best value for κ of $(4.36\pm.02)X10^{-8}$/mmHg.

H. PROTON AND KAON MOMENTUM DISTRIBUTIONS

The shapes of the proton peaks in the 200 GEV and 300 GEV secondary beam pressure curves are dominated by the momentum spectra of the protons. The proton peaks are broadened by less than 1% by the Cherenkov counter resolution, which is determined by the angular acceptance of the iris and the aberrations in the optics. The kaon peaks also are dominated by momentum dispersion. Counter resolution broadens the 200 GEV kaon peak by about 2% and the 300 GEV peak by about 8%. Since we have determined the gas constant with protons of known momenta, it is possible to determine the momentum distributions of the kaons and protons in the secondary beam from the pressure curves.

Each pressure is converted to a momentum by the relation

$$p = \frac{M}{\sqrt{2\kappa P - \theta^2}} \quad , \qquad (2\text{-}8)$$

where θ = .86 mrad, the mean value for a .7/1.0 mrad annular aperture. Differentiating equation 2-4 gives

$$dP/dp = -m^2/(\kappa p^3) \quad . \qquad (2\text{-}9)$$

The signal at each pressure is weighted by $1/p^3$ to convert a pressure distribution into a momentum distribution. The resulting distributions are shown in figure 2-33 and figure 2-34. The means and standard deviations of the distributions are tabulated in table 2-3.

2.6 NEUTRINO FLUX CALCULATIONS

A. IDEAL BEAM

Before discussing the monte carlo beam program we use to calculate neutrino fluxes, it is useful to consider the simpler case of an ideal secondary beam. An ideal beam would consist of a parallel beam of monoenergetic secondaries. The spectrum of neutrinos incident on our target from such a beam is very easy to calculate, and in fact is a close approximation to the real beam. For this reason it is useful to use an ideal beam to estimate the sensitivity of the flux calculation to uncertainties in the secondary momentum spectrum.

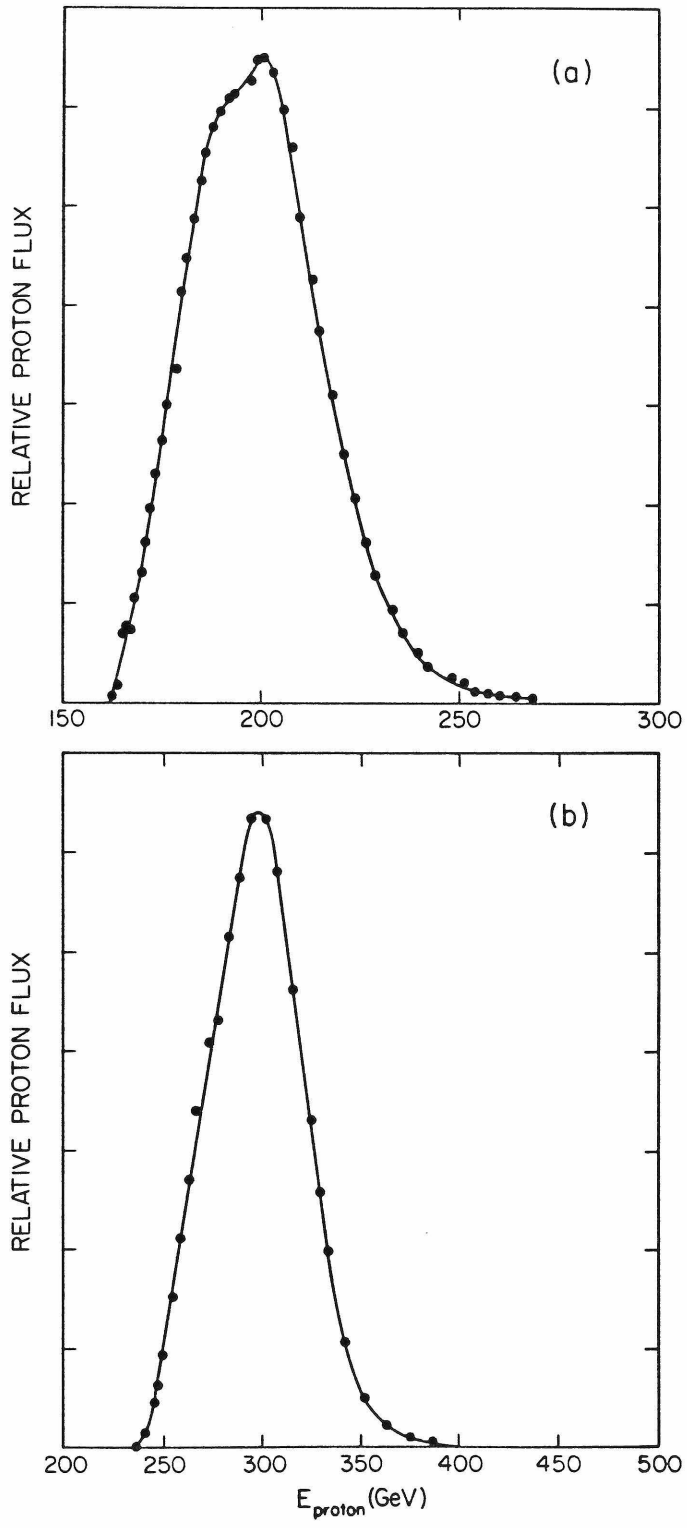

Figure 2-33: Secondary proton momentum spectra
(a) 200 GEV
(b) 300 GEV

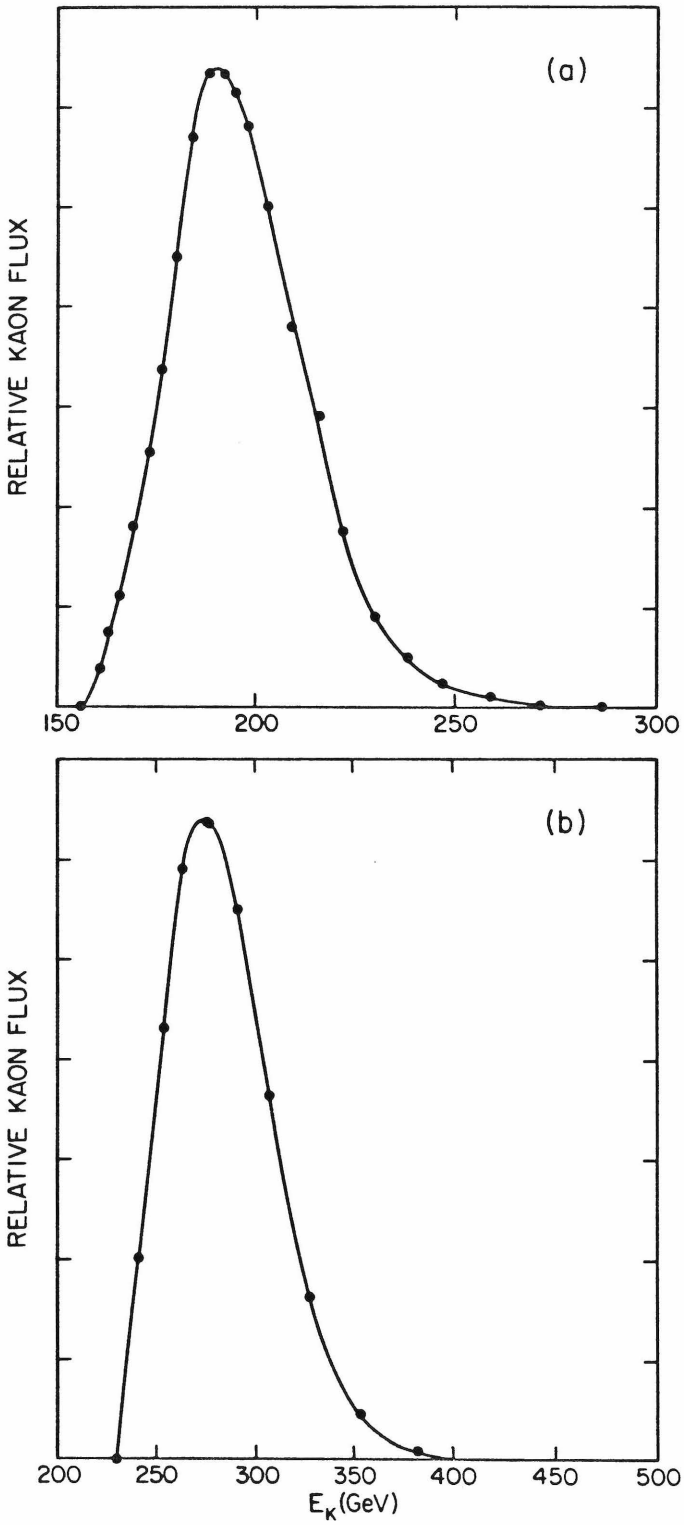

Figure 2-34: Secondary kaon momentum spectra
(a) 200 GEV
(b) 300 GEV

TABLE 2-3: SECONDARY PROTON & KAON MOMENTA

Beam Setting	Proton momentum Mean	σ /p	Kaon momentum Mean	σ /p
200 GEV	199.5	8.4%	196.6	8.8%
300 GEV	297.2	8.2%	284.4	9.6%

About 98% of the neutrino flux comes from 2-body decays of pions and kaons, $\pi, K \rightarrow \mu\nu$. This is the only decay considered in this chapter. A small correction later will be made to account for $K_{\mu 3}$ decays (see section 4.7D).

We want to calculate the neutrino density at the target for a particular type of secondary particle (see figure 2-35). The number of secondaries decaying into neutrinos within solid angle $d\Omega$ in distance dz trivially can be written down in the center of mass coordinates of the decaying particle,

$$dN_\nu = BN_s e^{(z-z_2)/\lambda} dz d\frac{\Omega_{cm}}{4\pi}, \qquad (2\text{-}10)$$

where N_s is the number of secondaries at the beginning of the decay pipe, B is the $\mu\nu$ branching ratio, and $\lambda = (p/M)\lambda_0$ for a particle of mass M, momentum p, and decay length λ_0. In the lab frame, the differential solid angle becomes

$$d\Omega_{cm} = \frac{(E+p\cos\theta)^2}{M^2\left[1+\left(\frac{p\sin\theta}{M}\right)^2\right]^2} d\Omega . \qquad (2\text{-}11)$$

Using the small angle approximation $\theta = r/z$, and writing the differential area at the target as $dA = z^2 d\Omega$, equation 2-11

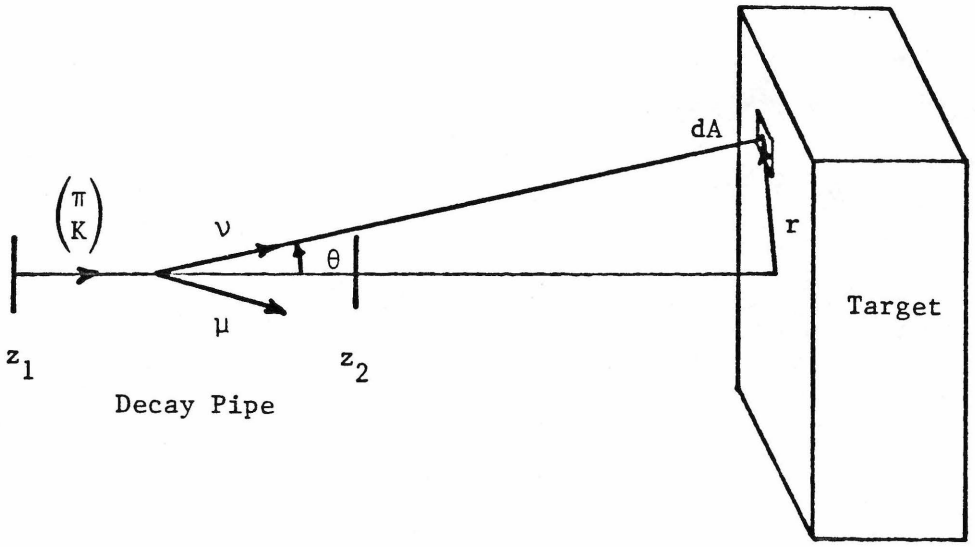

Figure 2-35: Pion and kaon decay.

becomes

$$d\Omega_{cm} = \frac{4(p/M)}{z^2\left[1+\left(\frac{pr}{Mz}\right)^2\right]^2} dA. \qquad (2\text{-}12)$$

Substituting into equation 2-10 and integrating over the decay pipe gives

$$\frac{dN_\nu}{dA} = \frac{BN_s p}{\pi\lambda_0 M}\int_{z_1}^{z_2} \frac{e^{(z-z_2)/\lambda}}{z^2\left[1+\left(\frac{pr}{Mz}\right)^2\right]^2} dz. \qquad (2\text{-}13)$$

The flux per secondary f_ν into a circle of radius R centered at the target is obtained by integrating dN_ν/dA over area,

$$f_\nu = (1/N_s)\int_0^R (dN_\nu/dA)2\pi r dr \qquad (2\text{-}14a)$$

$$= \frac{BpR}{\lambda_0 M}\int_{z_1}^{z_2} \frac{e^{(z-z_2)/\lambda}}{z^2+(pr/M)^2} dz. \qquad (2\text{-}14b)$$

The integration can be done numerically for a given momentum and decay length.

The energy of a neutrino striking the target at radius r from a decay at distance z from the target is

$$E_\nu = \frac{p[1-(m_\mu/M)^2]}{1 + \left(\frac{pr}{Mz}\right)^2} . \qquad (2\text{-}15)$$

E_ν does not depend strongly on z because the length of the decay pipe is small compared with its distance from the target. At each value of r the energy spectrum is dichromatic, because pions and kaons have different masses. Because E_ν depends on r, it is possible to measure cross sections at several different neutrino energies with a single beam setting by dividing the target into annular bins of different radius.

The neutrino flux per unit area as a function of radius is shown in figure 2-36 for four different secondary momenta. The mean neutrino energy is shown in figure 2-37. The flux calculations for an ideal beam are summarized in table 2-4, where the kaon momenta are the mean momenta measured with the Cherenkov counter. The mean pion momenta are adjusted slightly to take into account the relative production of pions and kaons at the target. The sensitivity of $1/(f_\nu E_\nu)$ to small changes in secondary momentum is shown in the last column.

A real neutrino beam differs from the ideal case in two respects. First, a real secondary beam has a finite

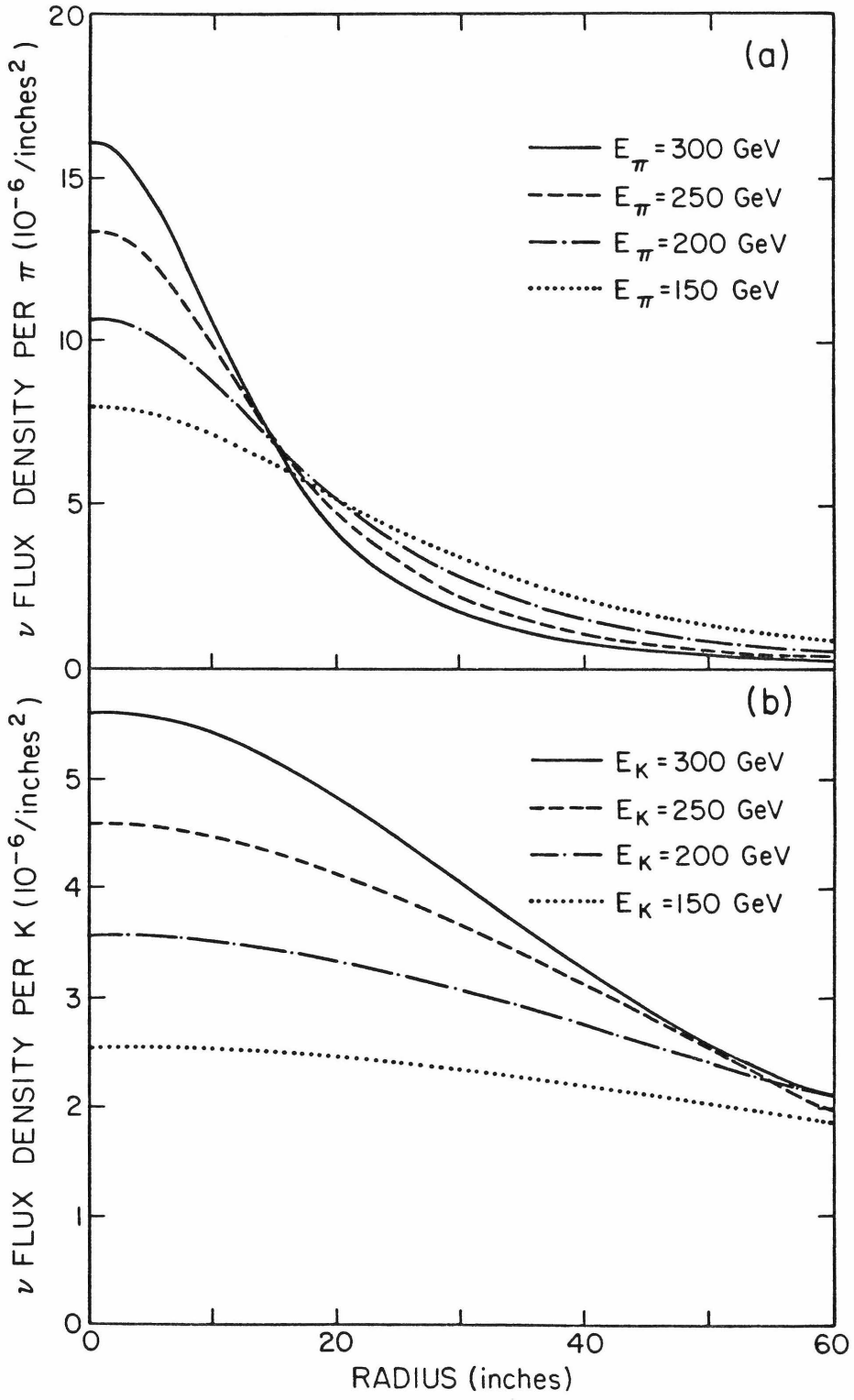

Figure 2-36: Neutrino flux density at the detector
(a) pion neutrinos
(b) kaon neutrinos

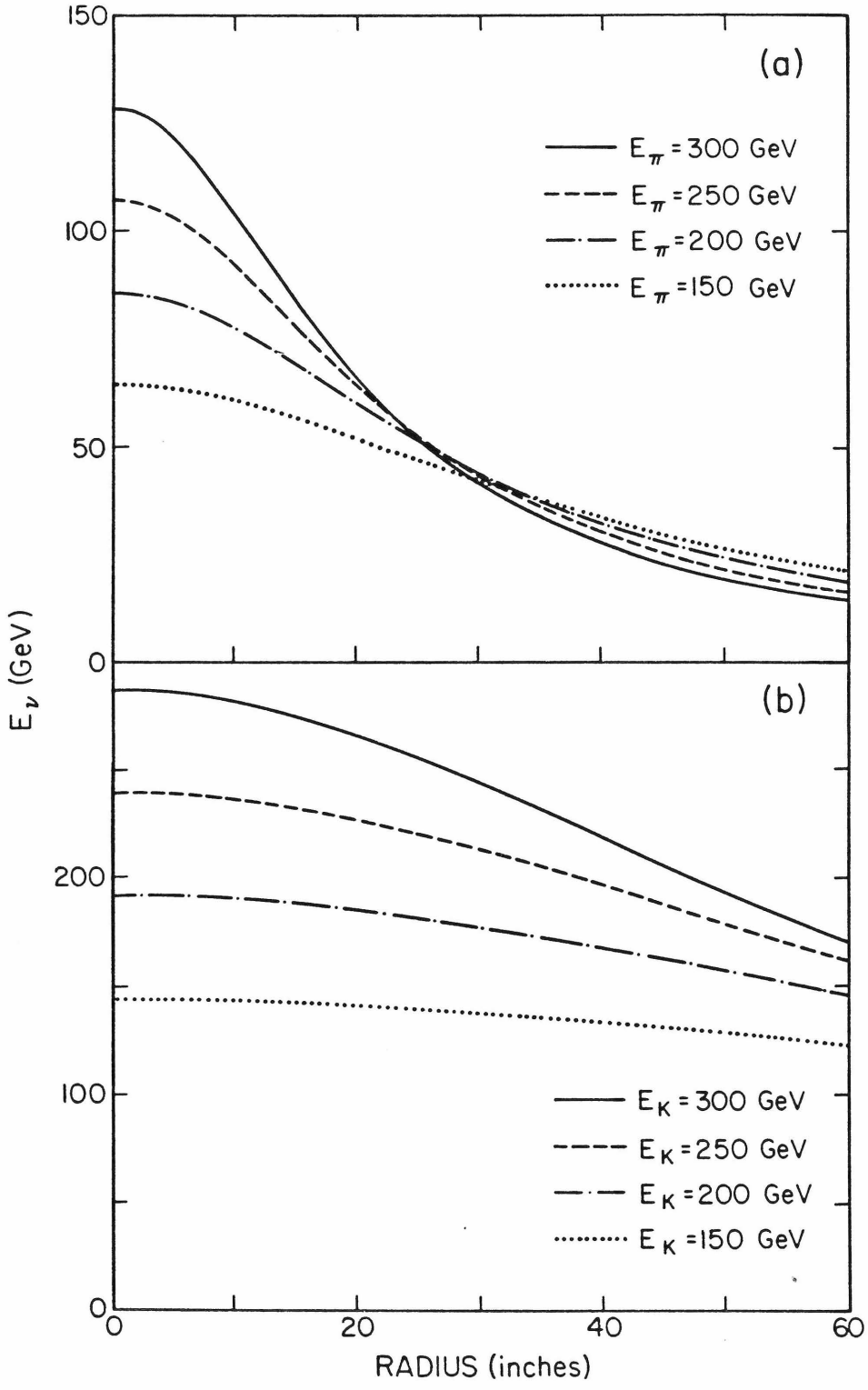

Figure 2-37: Neutrino energy at the target
(a) pion neutrinos
(b) kaon neutrinos

TABLE 2-4: NEUTRINO FLUXES FROM AN IDEAL BEAM

A. KAON NEUTRINOS

E_K(GEV)	Radial Bin	ν Flux per K	Mean E_ν(GEV)	Sensitivity to ΔE_K (%/GEV)
284	0-20"	6.19×10^{-3}	262	-0.6
	20-28"	5.22×10^{-3}	245	-0.5
	28-36"	6.07×10^{-3}	229	-0.4
	36-43"	5.63×10^{-3}	213	-0.3
	43-50"	5.67×10^{-3}	197	-0.2
196	0-31"	9.70×10^{-3}	180	-0.9
	31-47"	10.64×10^{-3}	165	-0.7

B. PION NEUTRINOS

E_π(GEV)	Radial Bin	ν Flux per π	Mean E_ν(GEV)	Sensitivity to ΔE_π (%/GEV)
281	0-12"	5.17×10^{-3}	106	-0.4
	12-17"	3.21×10^{-3}	83.1	-0.1
	17-25"	4.19×10^{-3}	63.4	+0.3
	25-37"	3.87×10^{-3}	42.0	+0.9
194	0-13"	4.65×10^{-3}	76.7	-0.8
	13-20"	4.50×10^{-3}	64.7	-0.4
	20-27"	4.32×10^{-3}	53.4	0.0
	27-35"	4.10×10^{-3}	42.7	+0.5
	35-45"	3.79×10^{-3}	32.6	+0.9

momentum bite, and second, a real beam has some angular divergence. A finite momentum bite changes the results very little. A beam with a gaussian momentum spectrum centered at p_0, and with $\sigma/p_0 = 8\%$, changes the fluxes shown in table 2-4 by less than 1%. The angular divergence of our beam is more significant. The effective angular divergence comes from the intrinsic angular divergence of each beam pulse and from steering errors that we are unable to correct on a pulse to pulse basis.

B. NEUTRINO BEAM MONTE CARLO

In an attempt to understand the details of the dichromatic train, a monte carlo computer program was written to imitate the experiment from the production of secondary particles at the target to the interaction of neutrinos at the detector. This program has four separate parts. The first models the production of pions and kaons at the target. The second propagates particles produced at the target through the dichromatic train to determine the train acceptance. The third generates 2-body decays in the decay pipe and calculates neutrino fluxes at the neutrino detector. The fourth generates neutrino interactions in the detector.

Particle production

To generate secondary particles, we use a parameterization of pion and kaon production developed by Stefansky and White[13]. The values of some of the parameters have been adjusted slightly to give better agreement to preliminary yield measurements made by E616[18]. The parameters used in this program are given in table 2-5.

Train acceptance

A beam transport program to model the dichromatic train was written using thin lens beam optics. Rays are generated uniformly in phase space at the target. Each ray is propagated through the train one element at a time. The ray is discarded if it is blocked by an aperture at any point in the train. The magnetic fields of the magnets in the train are determined by currents that were monitored continuously while running the experiment. The locations of the train elements initially were taken to be the design values. This part of the program was used to generate 5000 rays at the front of the decay pipe to be used for calculating neutrino fluxes.

TABLE 2-5: HADRON PRODUCTION MODEL

The production of pions and kaons at the target is assumed to have the form

$$\frac{d^2N}{dpd\cos\theta} = \frac{ABC^2p^2T}{10E}$$

where

	π^+	K^+
A =	5.0	.43
B =	8.0	5.0
C_0 =	6.0	5.0

and $C = C_0 - 1.43e^{-X-2X^2/3}$

$T = e^{-BX-C(p\sin\theta)}$

θ = production angle

X = p/E

p = secondary energy

E = incident proton energy

Pion and kaon decay

Equation 2-10 can be put into a more convenient form for generating decays by noting that

$$d\cos\theta_{cm} = \frac{2}{p(1-m_\mu^2/M^2)} dE_\nu . \qquad (2\text{-}16)$$

The decay is isotropic in the rest frame of the decaying particle, so neutrinos are produced uniformly in energy in the lab frame up to a maximum energy $E_0 = p[1-(m_\mu/M)^2]$. Letting z measure the distance down the decay pipe from the front, equation 2-10 becomes

$$dN_\nu = BN_s\left(e^{-z/\lambda}\frac{dz}{\lambda}\right)\left(\frac{d\phi}{2\pi}\right)\left(\frac{dE_\nu}{E_0}\right). \qquad (2\text{-}17)$$

Define the variable u by

$$u = \frac{1-e^{-z/\lambda}}{1-e^{-L/\lambda}}, \qquad (2\text{-}18)$$

where L is the length of the decay pipe. Now u ranges from 0 to 1 and equation 2-17 becomes

$$dN_\nu = BN_s(1-e^{-L/\lambda})du\left(\frac{d\phi}{2\pi}\right)\left(\frac{dE_\nu}{E_0}\right). \qquad (2\text{-}19)$$

A decay now can be generated for each ray with three random

numbers, R_1, R_2, and R_3, ranging from 0 to 1. First generate a neutrino energy,

$$E_\nu = E_0 R_1. \tag{2-20}$$

This also defines a decay angle θ with respect to the ray from

$$E_\nu = \frac{p[1-(m_\mu/M)^2]}{1 + (p\theta/M)^2}. \tag{2-21}$$

Next determine a point in the decay pipe by generating

$$u = R_2. \tag{2-22}$$

Finally, generate an azimuthal angle,

$$\phi = 2\pi R_3. \tag{2-23}$$

Now the energy and trajectory of the neutrino have been defined. When calculating neutrino fluxes per secondary at the detector, this decay must be weighted by F_ν,

$$F_\nu = W_p B(1-e^{-L/\lambda}). \tag{2-24}$$

The factor W_p is the relative production probability for

the secondary ray with respect to all the rays in the decay pipe, determined by the production model given in table 2-5. To determine neutrino fluxes, at each beam setting 100 neutrino decays are generated in this manner for each of the 5000 secondary rays.

Neutrino interactions

When studying the energy calibration and the acceptance of the detector, it is convenient to use a model of neutrino interactions to generate an interaction for every neutrino hitting the target in the monte carlo. For this purpose a very simple model is used. It is assumed that the neutrino differential cross section has the form

$$\frac{d\sigma^2}{dxdy} = \frac{G^2 ME_\nu}{\pi}[Q(x)+\bar{Q}(x)(1-y)^2]. \qquad (2\text{-}25)$$

The quark and antiquark distributions Q and $\bar{Q}$ are parameterized by

$$\bar{Q}(x) = (1/2)F_2(x)e^{-\lambda x}, \qquad (2\text{-}26a)$$

$$Q(x) = F_2(x)-\bar{Q}(x). \qquad (2\text{-}26b)$$

The shape of F_2 is taken to be the SLAC-MIT[19] fit to e-d experiments, given in table 2-6. The parameter λ is taken

TABLE 2-6: PARAMETERIZATION OF F_2

$$F_2(x) = \sum_{n=3}^{7} c_n (1-x)^n$$

where $c_3 = 3.276$

$c_4 = -7.168$

$c_5 = 31.22$

$c_6 = -44.56$

$c_7 = 18.384$

to be 6.07, which corresponds to a 17% antiquark component. Nothing that this program is used to compute is very sensitive to the details of this model, primarily because of the very good acceptance of the detector.

C. PROBLEMS WITH THE DICHROMATIC TRAIN

Differences between the performance of the dichromatic train and the properties predicted by the beam monte carlo were discovered as soon as we began running the experiment. The most serious of these problems was the transmission of the train, which was about 50% of the predicted value. Eventually the cause was traced to a number of misaligned magnets. In at least one case surveyors had used an incorrect reference point to align a magnet. In some cases the magnets were not adequately secured to the train. Apparently they shifted, either when the train moved into position or when it moved out, so that surveys taken before and after the run could not determine with certainty the location of the magnets during the run. Greater care was taken in aligning the train for E616, after which the train functioned as predicted. A detailed study of the dichromatic train as it existed during the E356 run came to two conclusions. First, the predicted neutrino fluxes were very sensitive to the degree of misalignment present.

Second, it was impossible to reconstruct accurately the positions of all the magnets and beam apertures.

Fortunately, the only characteristic of the secondary beam to which the neutrino fluxes are very sensitive is the momentum spectrum. This is measured directly by the Cherenkov counter for protons and kaons in the beam and can be estimated accurately for pions (see section 2.6D). For this reason, we artificially adjusted the acceptance of the train until the predicted kaon momentum spectrum in the decay pipe matched the Cherenkov counter measurement. We did this in two different ways. First we adjusted the positions of train elements within the limits of our ignorance and found we could "fine tune" the train configuration to match the Cherenkov counter curve. Probably the solution found is not unique. Second, we left the train in its designed configuration and weighted the rays by an artificial acceptance function to get agreement. The two methods give identical neutrino fluxes, which reflects the fact that the mean secondary momentum by far is the most important parameter of the beam.

There is one significant second order effect we could not monitor precisely. The split plate ion chambers in the expansion port and in the target manhole are very sensitive

to the location of the secondary beam. When both are used to monitor the beam, the steering can be controlled very accurately. However, the target manhole ion chamber was not installed until near the end of the E356 run. Even though we kept the location of the secondary beam fixed at the expansion port, the beam location at the front of the decay pipe was sensitive to small changes in the primary beam tune upstream of the target. Instabilities in the accelerator resulted in small tuning shifts every several hours. Averaged over the entire run, effectively this increased the angular divergence of the beam.

The data that are most sensitive to this steering problem are the cross sections measured from 300 GEV pion neutrinos. The neutrino flux density varies rapidly as a function of radius in the detector, and if we try to divide the detector into several radial bins the flux in each bin is sensitive to steering error. If we choose a bin large enough to contain most of the pion neutrinos the error from steering becomes negligible compared with other errors in the experiment. A comparison of the 300 GEV pion neutrino event distributions with the monte carlo predictions indicates that the average steering error at the target was less than 4", and the distributions are consistent with no steering error. The uncertainty this introduces to cross

sections obtained from the rest of the data is small compared with statistical errors.

D. PION MOMENTUM DISTRIBUTIONS

The kaon momentum distributions are measured by the Cherenkov counter. To determine the pion momentum distributions we have to rely on our knowledge of the relative production of pions and kaons at the target and the acceptance of the train. We use the beam monte carlo to calculate the shift in momentum between pions and kaons, but a very simple calculation will illustrate the effect.

Suppose that one type of particle is delivered to the decay pipe with a gaussian momentum distribution with mean p_0 and standard deviation σ_p. If the production of a second particle type relative to the first is of the form

$$\frac{dN}{dx} = e^{-\alpha x} , \qquad (2\text{-}27)$$

where $x = p_{secondary}/p_{primary}$, then the mean momentum p of the second particle will be given by

$$p/p_0 = 1 - \alpha x (\sigma_p/p_0)^2 . \qquad (2\text{-}28)$$

Figure 2-31 shows that the relative production of

pions, kaon, and protons roughly has the form of equation 2-27. Assuming this form, the E356 particle fractions determine $\alpha_{\pi/K}$ =2.6±.3 and $\alpha_{K/P}$ =6.9±.2. The momentum spread σ_p/p_0 is about .084±.010 (see section 2.5H). Using these values and equation 2-28, we make the naive calculations shown in table 2-7. The calculated kaon/proton momentum shift agrees with the measured values to within 1% of p_0. The naive calculation of the pion/kaon momentum shift agrees with the beam monte carlo calculation to within 0.2% of p_0. The uncertainty in the pion/kaon momentum shift from uncertainties in α and σ_p/p_0 is less than 0.4% of p_0. Even if the calculated pion/kaon momentum shift is incorrect by as much as 1% of p_0 (which is an error as large as the calculated shift), the effect on the pion neutrino cross sections is small compared with other uncertainties.

E. NEUTRINO FLUXES AT THE DETECTOR

The neutrino fluxes are listed in table 2-8 for various radial bins in the detector. The center of these bins, R=0, is the center of the neutrino distribution, which differs slightly from the center of the detector (see section 4.5). In some cases the outer bin does not extend to R2 everywhere, because an additional fiducial cut is

TABLE 2-7: RELATIVE MOMENTA OF SECONDARY HADRONS

A. KAON/PROTON

$1-p_K/p_p$

Mean proton momentum	x	Naive calculation	Measurement
200 GEV	.50	.024	.015
297 GEV	.74	.036	.043

B. PION/KAON

$1-p_\pi/p_K$

Mean kaon momentum	x	Naive calculation	Beam monte carlo calculation
197 GEV	.49	.009	.010
284 GEV	.71	.013	.011

TABLE 2-8: NEUTRINO FLUXES

A. KAON NEUTRINOS

Beam Setting	Target Bin R1	R2	Mean E_ν (GEV)	ν Flux per K	Number of Kaons
300 GEV	0	20	261	6.02×10^{-3}	1.738×10^{13}
	20	28	246	5.16×10^{-3}	
	28	36	229	5.92×10^{-3}	
	36	43	214	5.57×10^{-3}	
	43	50	199	5.55×10^{-3}	
	50	60	182	5.76×10^{-3}	
200 GEV	0	31	180	9.62×10^{-3}	7.49×10^{12}
	31	47	166	10.56×10^{-3}	
	47	57	154	5.85×10^{-3}	

B. PION NEUTRINOS

Beam Setting	Target Bin R1	R2	Mean E_ν (GEV)	ν Flux per π	Number of Pions
300 GEV	0	12	101	4.08×10^{-3}	6.98×10^{13}
	12	17	86.3	2.91×10^{-3}	
	17	25	71.3	4.25×10^{-3}	
	25	37	52.7	4.44×10^{-3}	
200 GEV	0	13	73.5	4.04×10^{-3}	5.29×10^{13}
	13	20	64.7	4.15×10^{-3}	
	20	27	55.1	4.21×10^{-3}	
	27	35	45.9	4.21×10^{-3}	
	35	45	36.5	4.05×10^{-3}	
	45	57	27.4	2.83×10^{-3}	

made 6" from the edge of the detector.

The uncertainty in the neutrino flux per secondary comes from two sources. The first is an uncertainty in the mean secondary energy, which is ±1% for kaons and ±1.5% for pions. The sensitivity to this uncertainty is given in table 2.4. The second is the statistical uncertainty in the monte carlo run, which is less than 0.4%. The last column of table 2-8 gives the total number of secondary pions and kaons at the front of the decay pipe in the E356 data reported here.

CHAPTER 3

LAB E NEUTRINO DETECTOR

3.1 LAYOUT OF LAB E

Lab E contains the neutrino detector used in E356. The apparatus consists of two main parts, a 680 ton iron target followed by a 420 ton muon spectrometer. A floor plan of Lab E is shown in figure 3-1. The target is segmented into 6 target carts of dimension 10'X10'X10'. The muon spectrometer consists of three iron toroidal magnets, each 11.5' in diameter and 10' long. Each target cart and spectrometer magnet is on multiton rollers, so that they may be moved individually into a hadron beam line in Lab E for calibration.

The detector is designed to measure the following parameters of each neutrino interaction:

1. coordinates of the interaction vertex
2. total energy of the hadron shower
3. trajectories and momenta of muons.

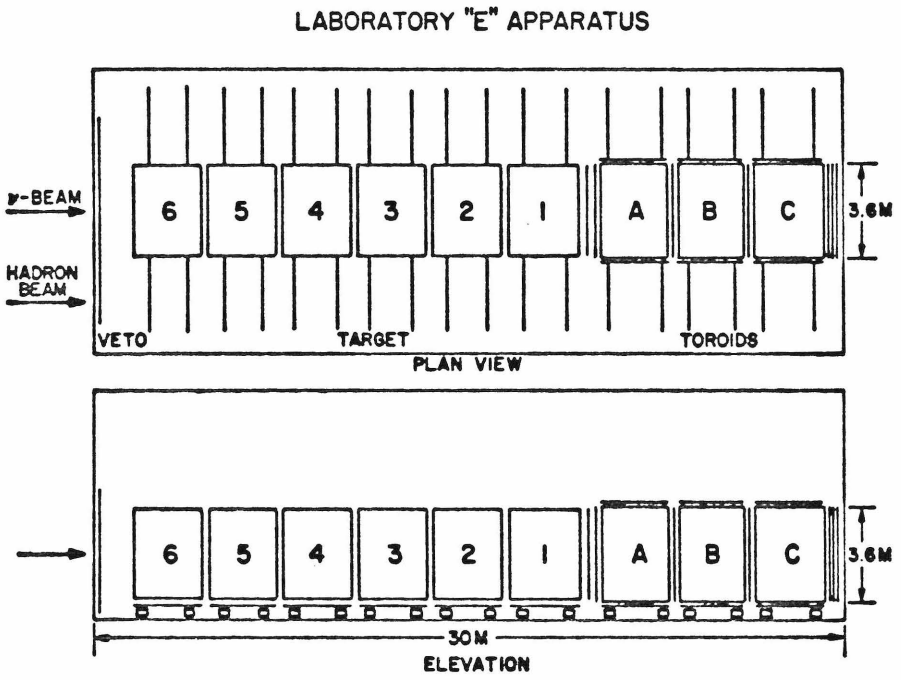

Figure 3-1: Lab E apparatus.

Most of the mass of each target cart is in 28 steel plates of dimension 10'X10'X2". A liquid scintillation counter is placed after every 2 plates. The arrangement is shown in figure 3-2. The steel plates and scintillation counters form a sampling calorimeter used to measure hadron energy. The spark chambers track charged particles traversing the target.

Each spectrometer magnet is instrumented with acrylic scintillation counters after every 8" of steel. Spark chambers are placed behind and in the middle of each magnet (see figure 3-3). The toroids can be used as a target for neutrino interactions, although this was not done for E356.

Planes of trigger counters with total area 10'X10' are placed between the first and second toroid (T2) and the second and third toroid (T3). A large plane of veto counters covers the front wall of Lab E but was not used in this experiment.

3.2 HADRON CALORIMETRY

A. SCINTILLATION COUNTERS

Details of the construction of the scintillation

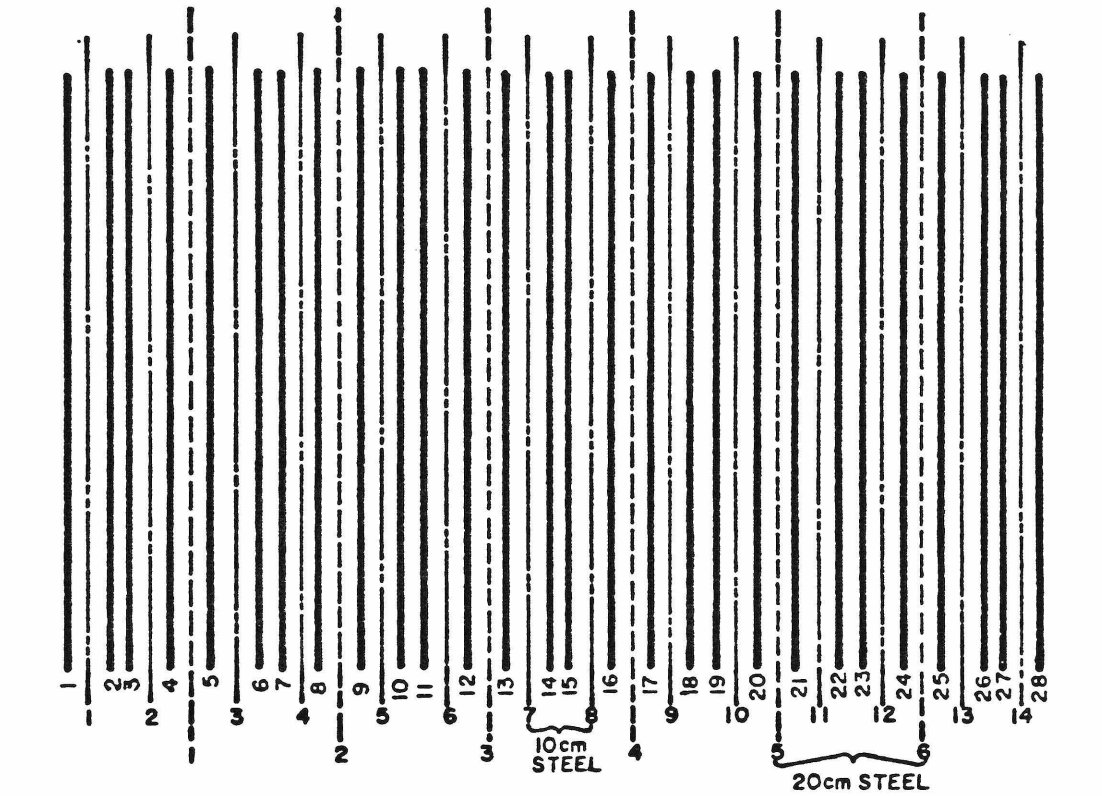

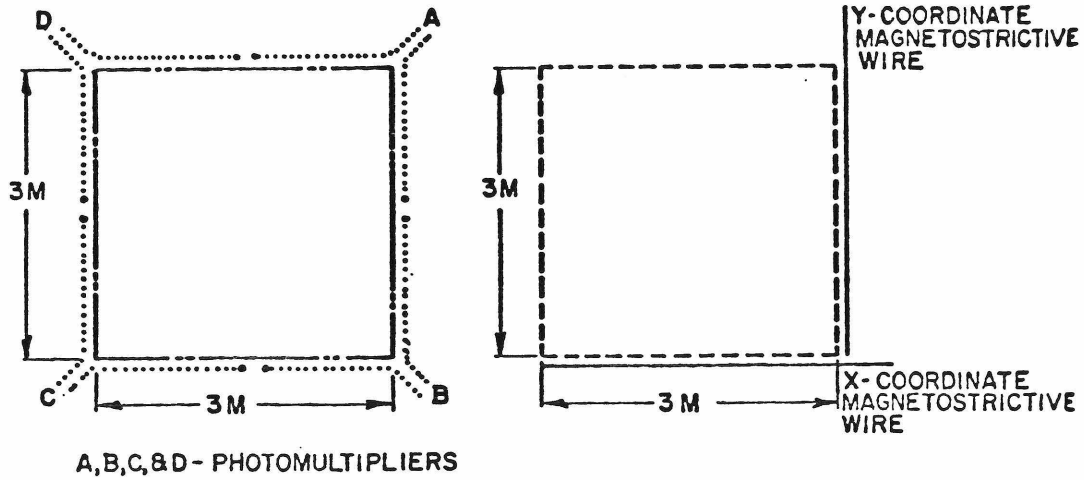

Figure 3-2: Arrangement of target cart scintillation counters and spark chambers.

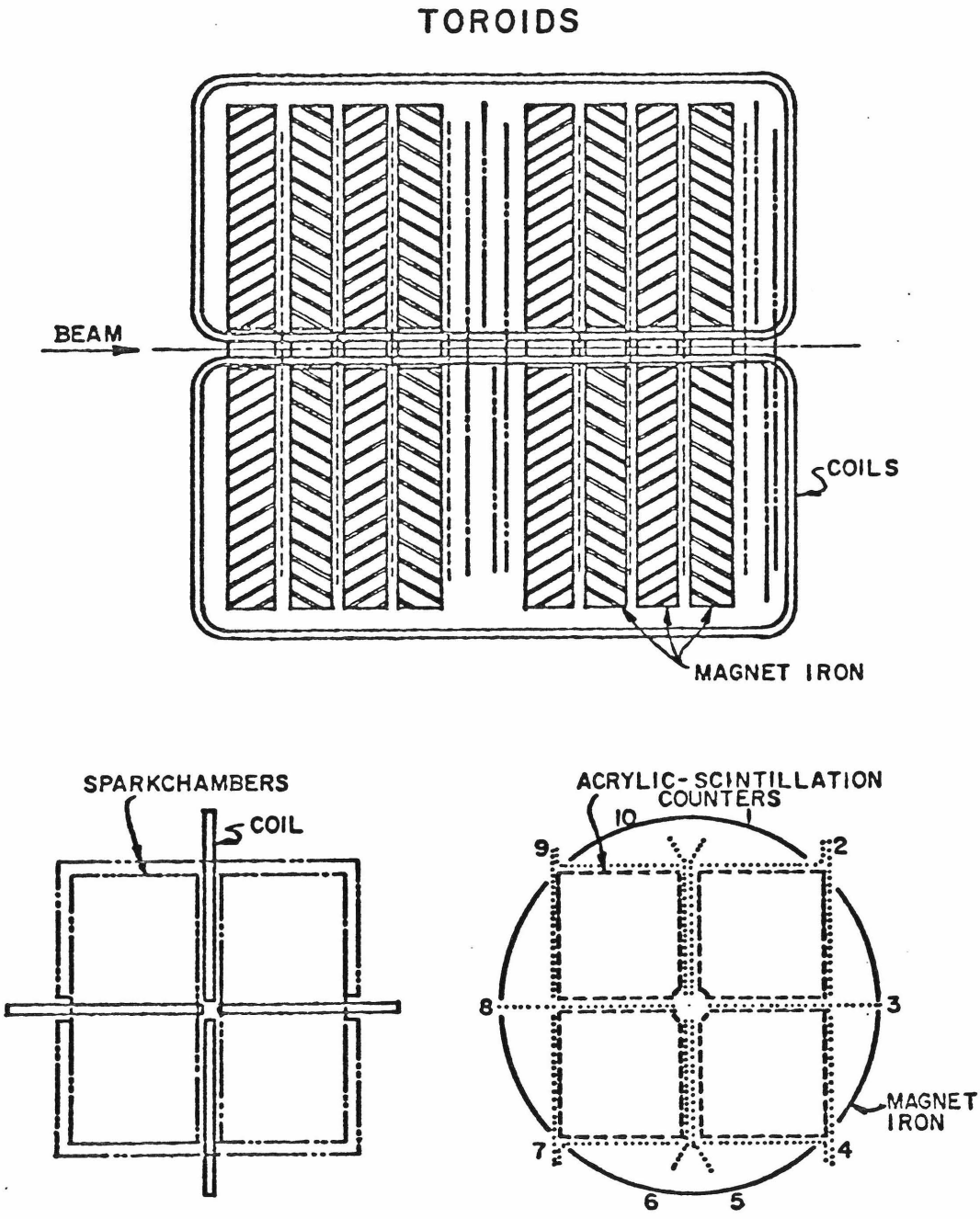

Figure 3-3: Arrangement of toroid scintillation counters and spark chambers.

counters used in E356 have been given elsewhere[20], so I will give only a brief description here.

The scintillation counters used in the target carts are acrylic tanks of dimension 10'X10'X1" filled with liquid scintillator. Around the outside of the counters are wavelength shifter bars (see figure 3-2). Ionizing radiation in the scintillator excites a primary fluor which emits ultraviolet light. A secondary fluor absorbs the UV light and reemits blue light, which has a much longer attenuation length in liquid scintillator. The wavelength shifter bars are acrylic bars doped with a fluor that absorbs blue light and reemits green light. The shifter bars are not in optical contact with the sides of the counter, so light produced in the bars can propagate to phototubes placed on the ends by total internal reflection (see figure 3-4).

The counters used in the toroidal magnets are made of plastic scintillator. Each counter is 5'X5'X1.5" with a notch cut in one corner to fit around the magnet coil. Four counters, 14 shifter bars, and 10 phototubes make up one plane, shown in figure 3-3.

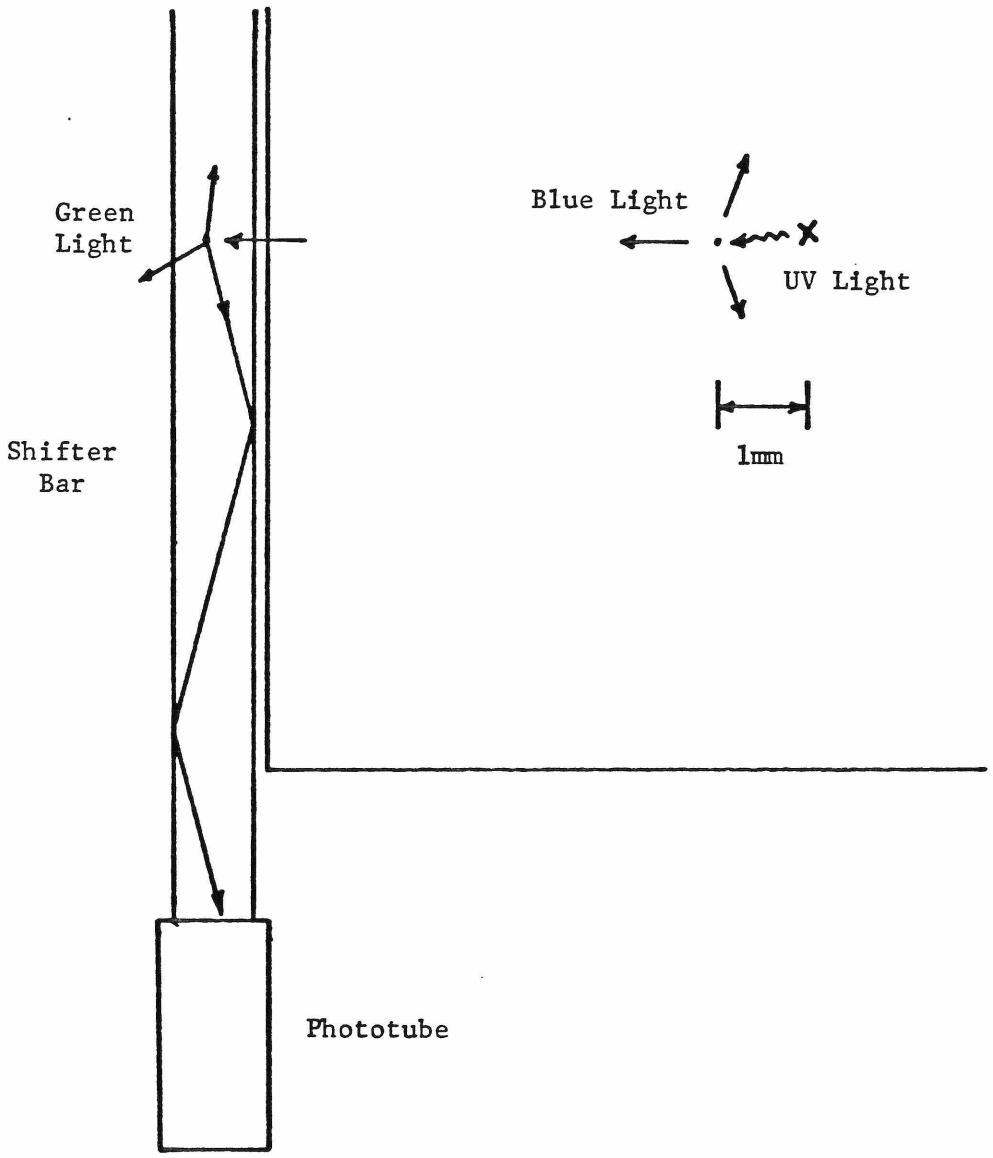

Figure 3-4: Principle of shifter bar.

B. PHOTOTUBE MONITORING SYSTEM

The large number of phototubes in the experiment (328 in the target, 250 in the toroid) makes an automatic system of monitoring phototube gains essential. This is accomplished with a light flasher system that is capable of delivering a controlled flash of light to the center of each counter.

Each counter is constructed with a 30' length of light fiber running to the center. The light fiber is mounted in a piece of plastic with a 45 degree edge (see figure 3-5). A 1/2" white spot is painted across from the light fiber mounting. A flash of light coming from the light fiber reflects off of the spot isotropically into the counter, so that the phototube gains can be balanced on each counter.

The light fibers from the 14 counters in each target cart (or the 16 counters in a half toroid) are brought together into a bundle, along with light fibers from two trigger tubes, a photodiode, and a monitoring phototube. A spark gap is used to illuminate the end of the bundle with light. A wheel of neutral density filters is used to attenuate the light by any desired amount (see figure 3-6(a)). The assembly is placed inside an aluminum box to

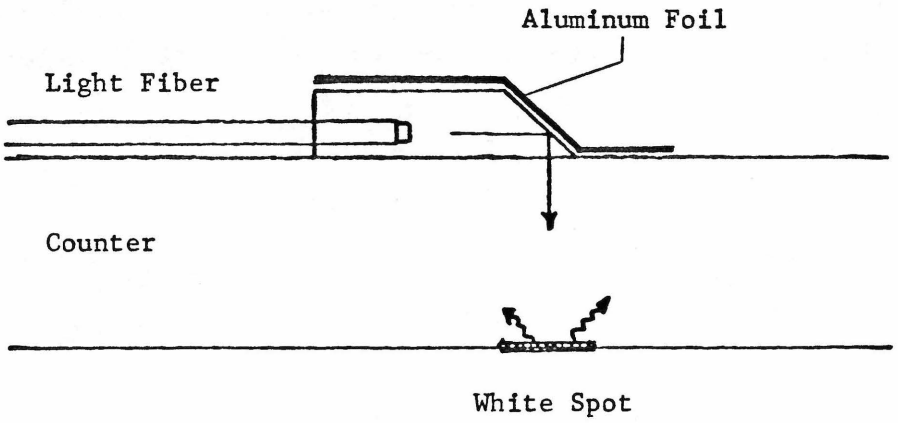

Figure 3-5: Light fiber mounting on counter.

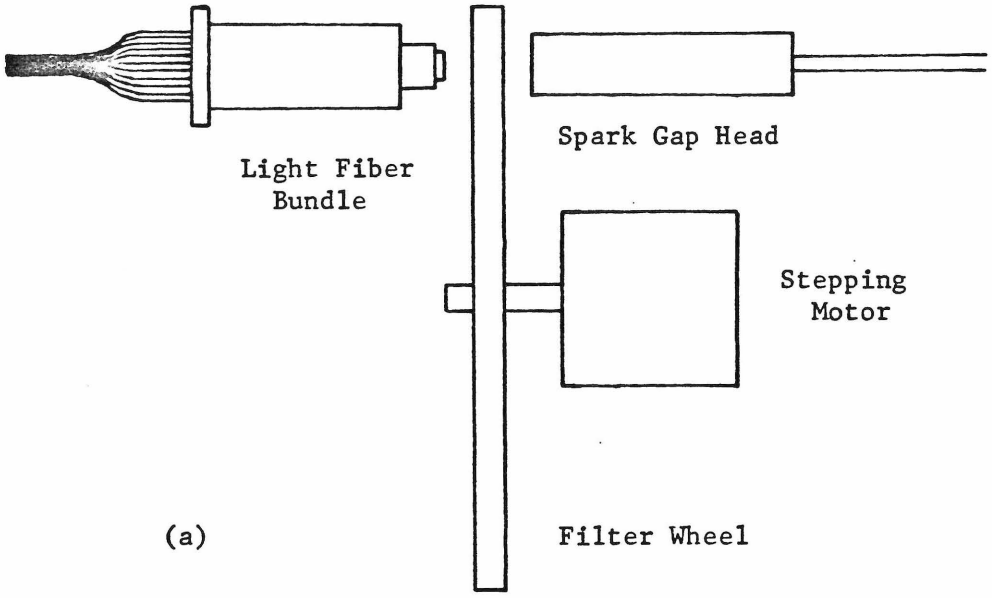

(a)

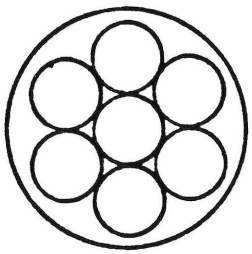

(b)

Figure 3-6: (a) Placement of light fiber bundle at spark gap.
(b) The light fiber from each counter consists of 7 separate strands. One strand from every counter goes into each of the 7 circles at the face of the fiber bundle.

shield the phototubes from RF noise produced by the flasher.

The spark gap does not uniformly illuminate the face of the fiber bundle, which has a diameter of about 1/4", and the distribution of light varies from pulse to pulse. However, the fiber from each counter consists of a bundle of 7 separate light fibers inside a plastic case. Inside the fiber bundle assembly is a ring with 7 holes in the pattern shown in figure 3-6(b). Each fiber is separated into its 7 strands, and then one strand is run through each of the 7 holes in the ring. After passing through the ring, all strands are brought back together into a tight bundle. Because the fiber from each counter collects light at 7 different positions in the bundle, the fraction of light seen by each counter varies much less from pulse to pulse than if the strands had not been separated. After the light fibers are strung, the entire fiber bundle assembly is filled with epoxy to form a rigid structure. The end of the bundle is cut with a fine toothed saw and polished to form a flat optical surface.

The light output of the spark gap typically varies by 30% from pulse to pulse. The fraction of light seen by an individual counter has pulse to pulse variations of about

4%. The intensity of the flash is monitored by a photodiode and a phototube, so in principle the absolute gain of each phototube in the experiment is measured by flashing the system. In practice, the monitoring photodiode and phototube proved to be the least stable part of the system. They have been redesigned for future use. It still was possible to compare the relative gain of each tube with respect to the rest of the 56 tubes in each target cart (40 in the case of a half toroid).

While taking neutrino data, one of the 12 flasher systems is fired in between each beam spill. The flasher data are analyzed by online software to provide a relative balance for the phototubes on each counter. This information is printed out at the end of each run (typically lasting 2 to 4 hours). The gain of a particular phototube rarely wanders by more than 5% unless something fails completely (e.g. a broken cable, connector, amplifier, etc.). The flasher system proved to be a useful diagnostic tool to alert operators to problems with the apparatus. Phototube gains were maintained at the 5% level during the running of E356. By adjusting phototube gains daily and fixing occasional component failures as they occur, it is possible with this system to maintain the gain of each phototube in the experiment to within $\pm$2%.

C. FRONT END ELECTRONICS

Our experiment required the calorimeter to be sensitive both to single minimum ionizing particles and to hadron showers up to 400 GEV. For the E356 running we had available only 10 bit ADCs, which made it necessary to split the signal from each phototube and separately integrate amplified and unamplified signals.

The front end scheme for one counter in the target is shown in figure 3-7. The "low" signal from each phototube is pulse height analyzed. This is necessary to calibrate and monitor the gain of each tube. The "high" signals from the 4 tubes on one counter are summed and sent to a X10 amplifier. The amplified signal is pulse height analyzed. The high channel is used to measure energy deposited by minimum ionizing particles and small hadron showers (up to about 10 minimum ionizing particles). When the high ADC overflows, the 4 low ADCs are summed in software and used to measure energy deposition. A scheme of superlow ADCs was designed to correct for rare cases in which low ADCs overflowed, but the superlows were not debugged in time for the run and were not used. This was a problem for events near the edge of the detector (see section 4.8).

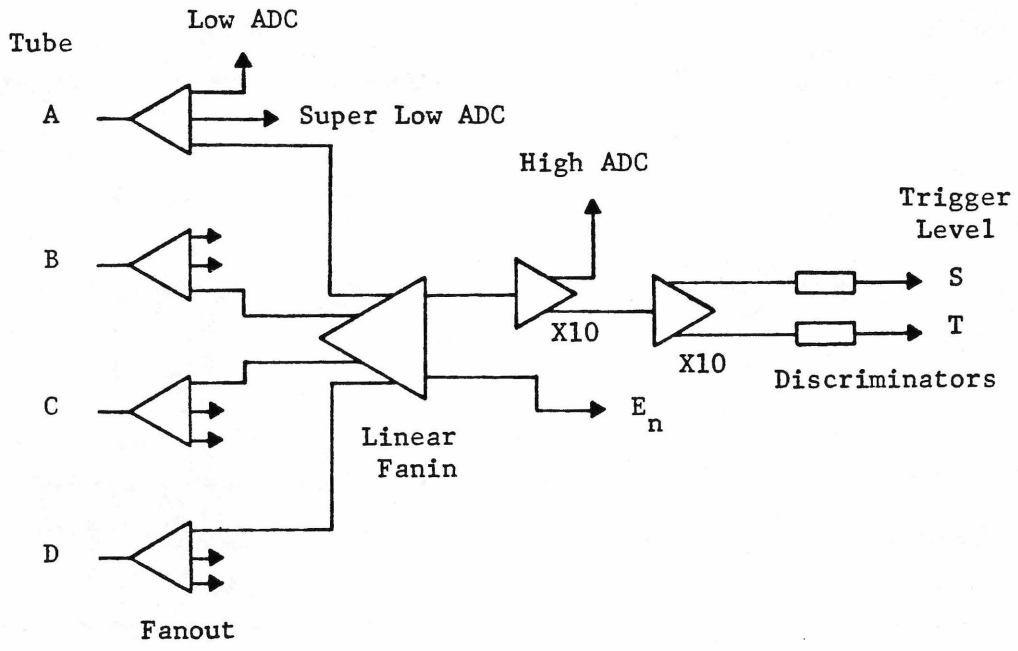

Figure 3-7: Front end electronics for one target cart scintillation counter.

One amplified output is amplified again and discriminated at two levels. The "S" trigger level is set at .5X minimun ionizing, and the "T" trigger level is set at 1.5X minimum ionizing. The outputs of these discriminators are used in various neutrino triggers. Latches on the "S" discriminators (S bits) are used in analyzing an event to find the interaction vertex and measure penetration in the counter. The output of the fanin and fanout labeled E_n also is used to trigger the apparatus.

The front end scheme for one plane in the toroids is similar and is shown in figure 3-8.

D. CALIBRATION

In Lab E we have available a beam line that can deliver either hadrons or muons of known energy (from 25 GEV to 300 GEV). Each target cart and toroid separately is moved into the hadron beam for calibration.

Calibrating a target cart is a two stage process. First muons are run through the center of the cart. For each counter the phototube voltage is adjusted so that the gains of each of the 4 tubes are equal when measured in a

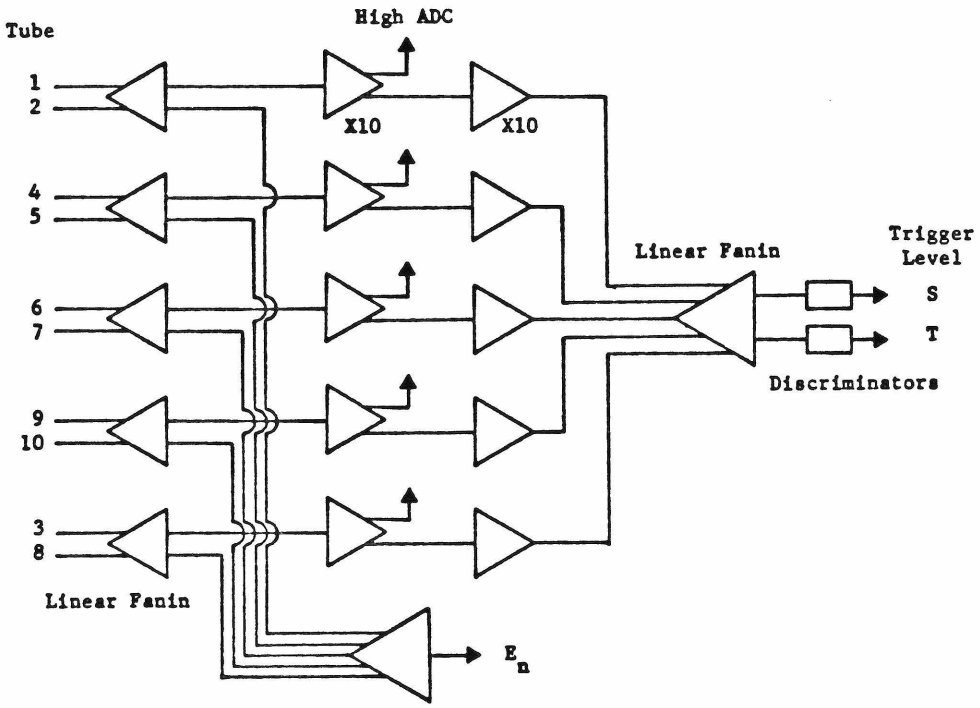

Figure 3-8: Front end electronics for one half plane of toroid scintillation counters.

light flasher run, and the mean of the muon distribution lies near channel 100 in the high ADC. The muon distribution for counter #58 is shown in figure 3-9.

After the phototube gains are set, hadrons are run into the front of the cart at a number of energies. The distribution for 100 GEV hadrons is shown in figure 3-10. The energy resolution can be computed from the width of the peak. Figure 3-11 shows mean pulse height (in units of minimum ionizing particles) versus hadron energy. The calorimeter is linear over the range from 25 GEV to 300 GEV, and the slope of the best fit line gives the energy calibration. The energy resolution of the target is shown as a function of hadron energy in figure 3-12.

The attenuation length of light in the liquid scintillation counters is about 1 meter, so the response of a counter varies as a function of position. The counters were mapped with staight-through muons while taking neutrino data. The hadron energy from a neutrino interaction is corrected by dividing the raw pulse height by the mapping function f(X,Y). Contour lines of f(X,Y) are shown in figure 3-13.

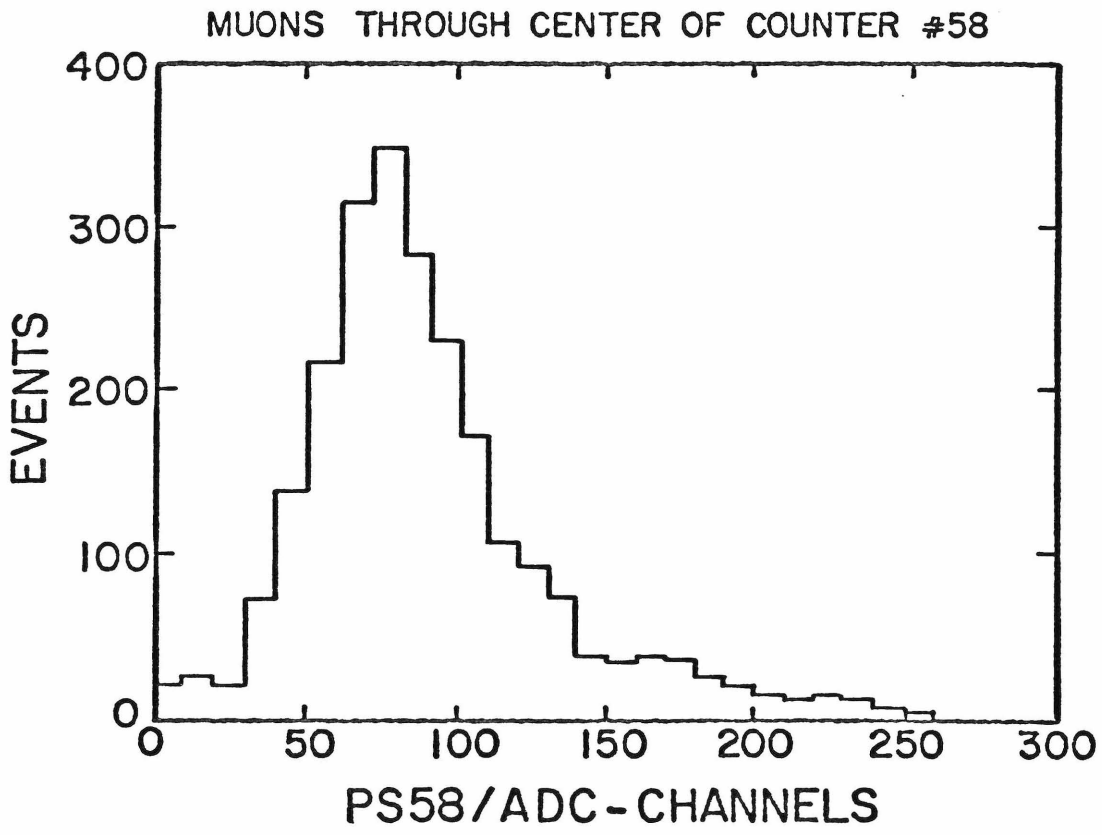

Figure 3-9: Pulse height distribution for muons hitting the center of a counter.

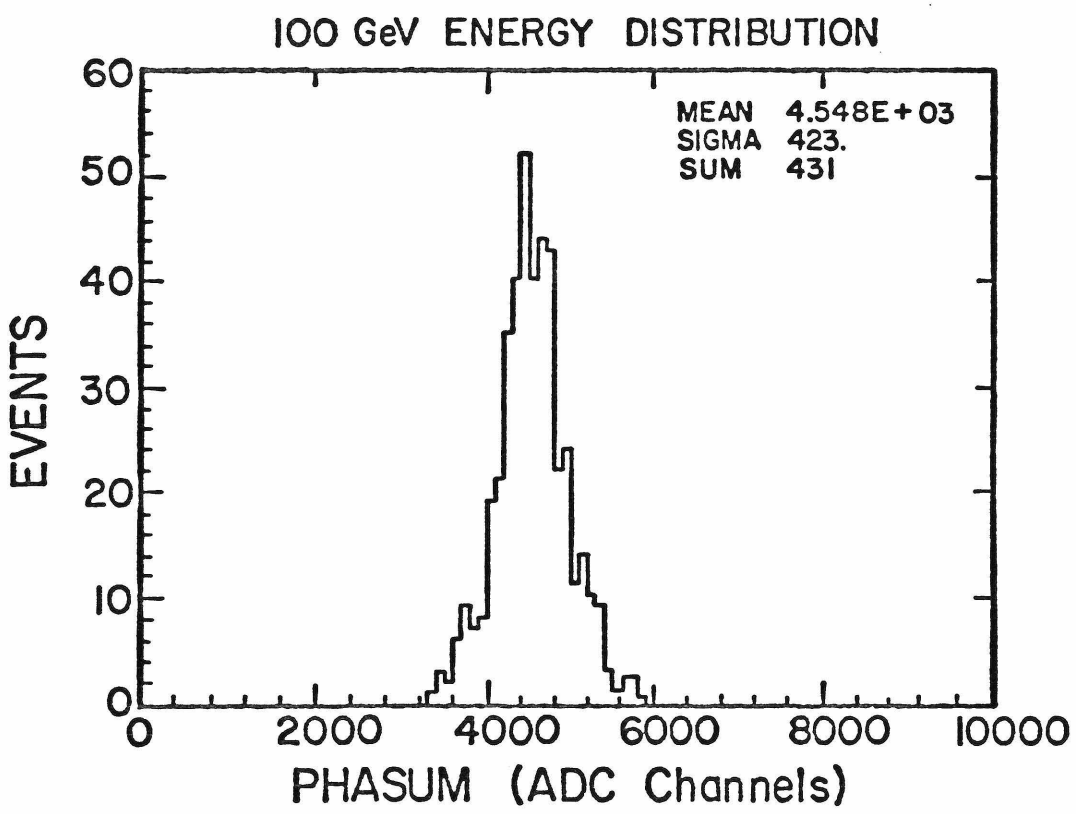

Figure 3-10: Pulse height distribution for 100 GEV hadrons in the center of a cart. The pulse height is summed over 14 planes (1 target cart).

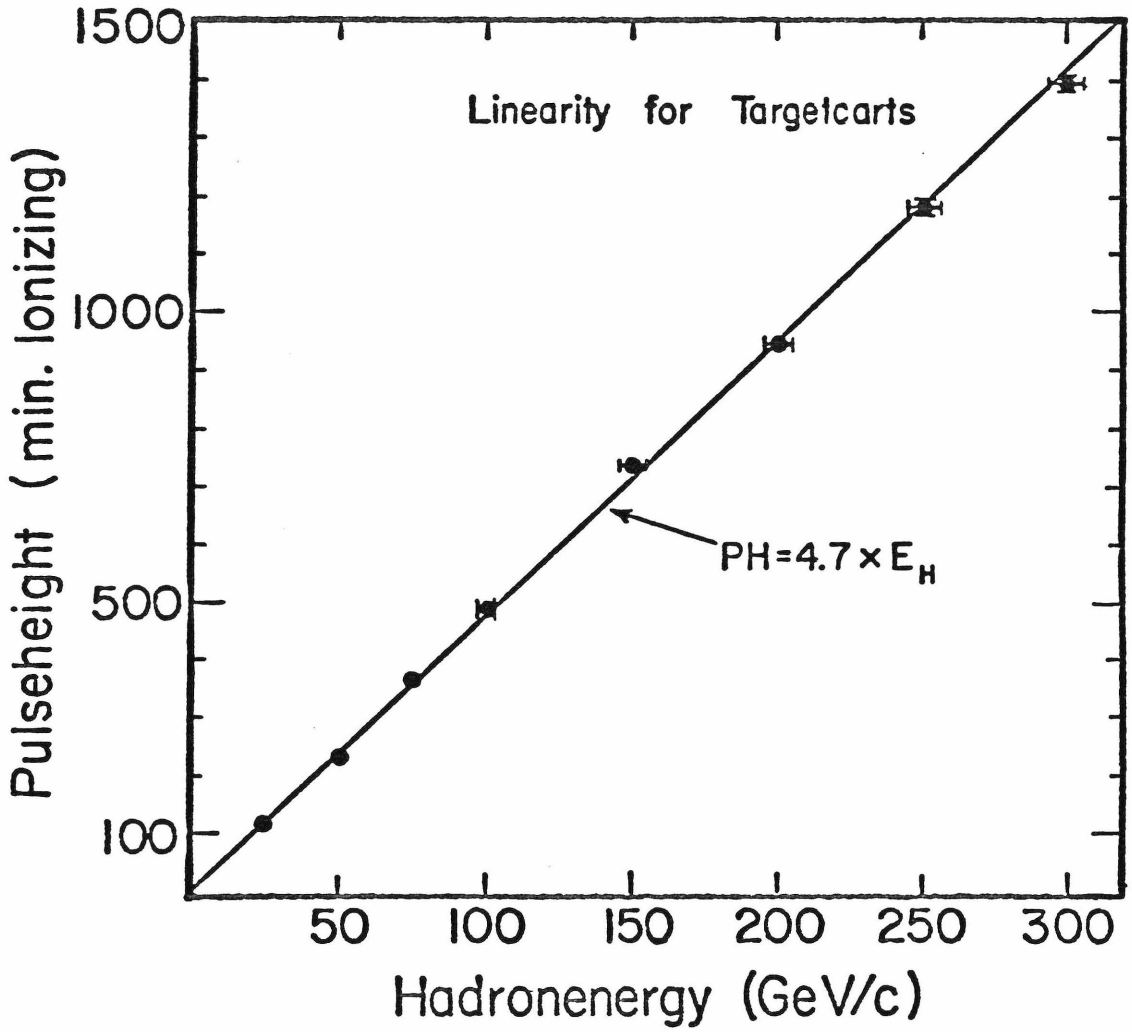

Figure 3-11: Linearity of pulse height with respect to hadron shower energy.

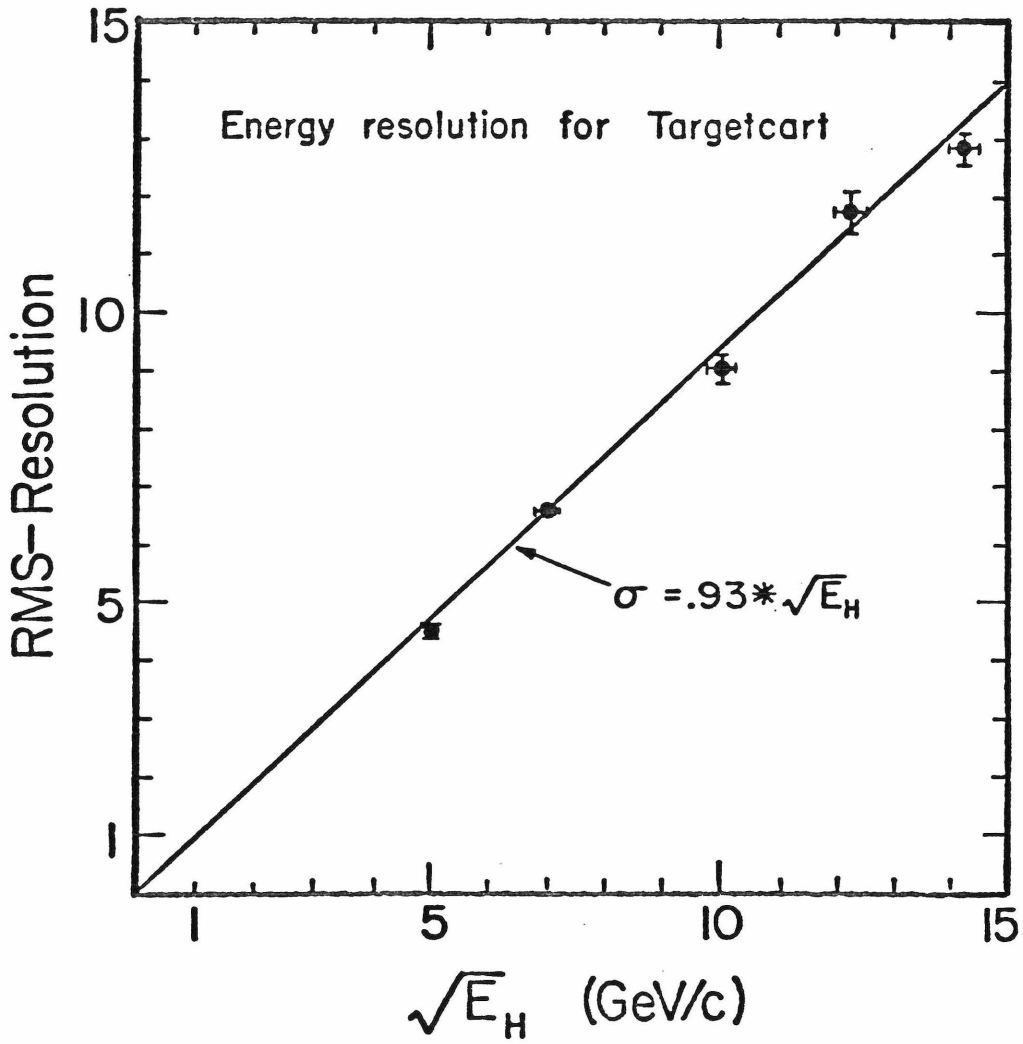

Figure 3-12: Energy resolution for hadron showers.

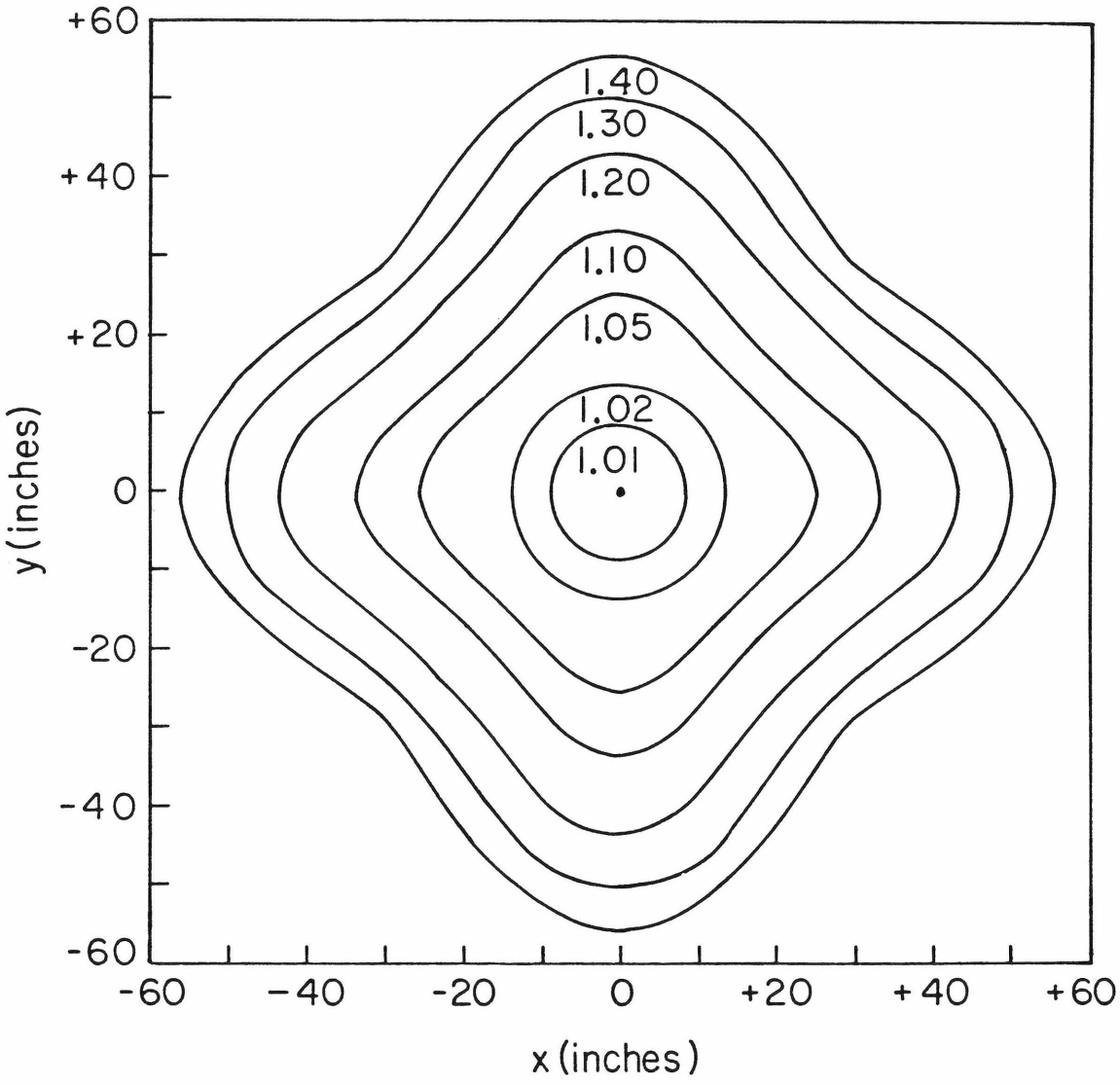

Figure 3-13: Target cart scintillation counter response normalized to signal at the center.

3.3 SPARK CHAMBER SYSTEM

Two different types of spark chamber are used in this experiment. In the toroids a plane of chambers is formed with two 5'X10' spark chambers. In the target a plane is a single 10'X10' chamber. See figure 3-2 and figure 3-3 for location in the apparatus. Both types of chamber work in a similar manner.

Each chamber has two planes of wires with 1 mm spacing for X and Y measurements. The interiors of the chambers are filled with neon-helium gas that is continuously recirculated through a liquid nitrogen purification system. When a chamber is pulsed, it sparks wherever a charged particle has ionized the gas. The magnetic field pulse created by a spark is picked up by a magnetostrictive readout wire at the edge of the wire plane (see figure 3-2). An acoustic pulse travels down the magnetostrictive wire to a transducer. Two fiducial pulses are generated near the two ends of the magnetostrictive wire when the chamber is pulsed.

Spark position is determined by measuring the time required for the acoustic pulse to travel to the transducer. The first fiducial pulse starts 16 20Mhz

scalars, and each succeeding pulse stops one of the scalars. The resolution of the system is about ±.5 mm.

The spark chambers were aligned with 1700 straight-through muon events. These events satisfied the following cuts: 1) the track had at least 10 sparks in the toroid, 2) p_μ>40 GEV , and 3) the χ^2 per degree of freedom for the momentum fit was less than 2. Two reference chambers were chosen near the front and back of the target. Each track was fitted using weights based on multiple scattering. In each chamber, the average deviation of the X and Y sparks from the fitted track determined the misalignment of the chamber. This procedure was iterated until the alignment became stable. The final alignment was insensitive to the choice of reference chambers and to the weighting scheme. The target chamber alignment is accurate to 20 mil, and the toroid chamber alignment is accurate to 67 mil except for two very inefficient chambers.

3.4 MUON SPECTROMETER

A. MAGNETIC FIELD

Each of the three spectrometer magnets is constructed with 8 donut shaped slabs of steel 8" thick and 11.5' in

diameter. Each slab has a hole 10" in diameter for the 4 power coils, and the top and bottom halves of each slab are separated by a 3/8" air gap. The coils are run at 1250 amps, which almost saturates the iron to provide a nearly uniform azimuthal magnetic field. The field has been calculated assuming no z dependence. The result is shown in figure 3-14 as a function of radius along 4 different directions.

The magnetic field was measured along direction d by inserting a Hall probe in the air gap. The magnetic field is distorted by the air gap (see figure 3-15), so it was measured at several points in z to obtain $\int Bdz$. This was done for each lamination at three different radii. In addition, a detailed radial dependence was measured for one lamination. The measurements are compared to the prediction in figure 3-16. The average field of 17 kgauss over the 16' of steel in the 3 toroids gives a transverse momentum kick of 2.45 GEV. The direction of the current was chosen to focus negative muons while taking neutrino data. It may be reversed to focus positive muons for taking antineutrino data.

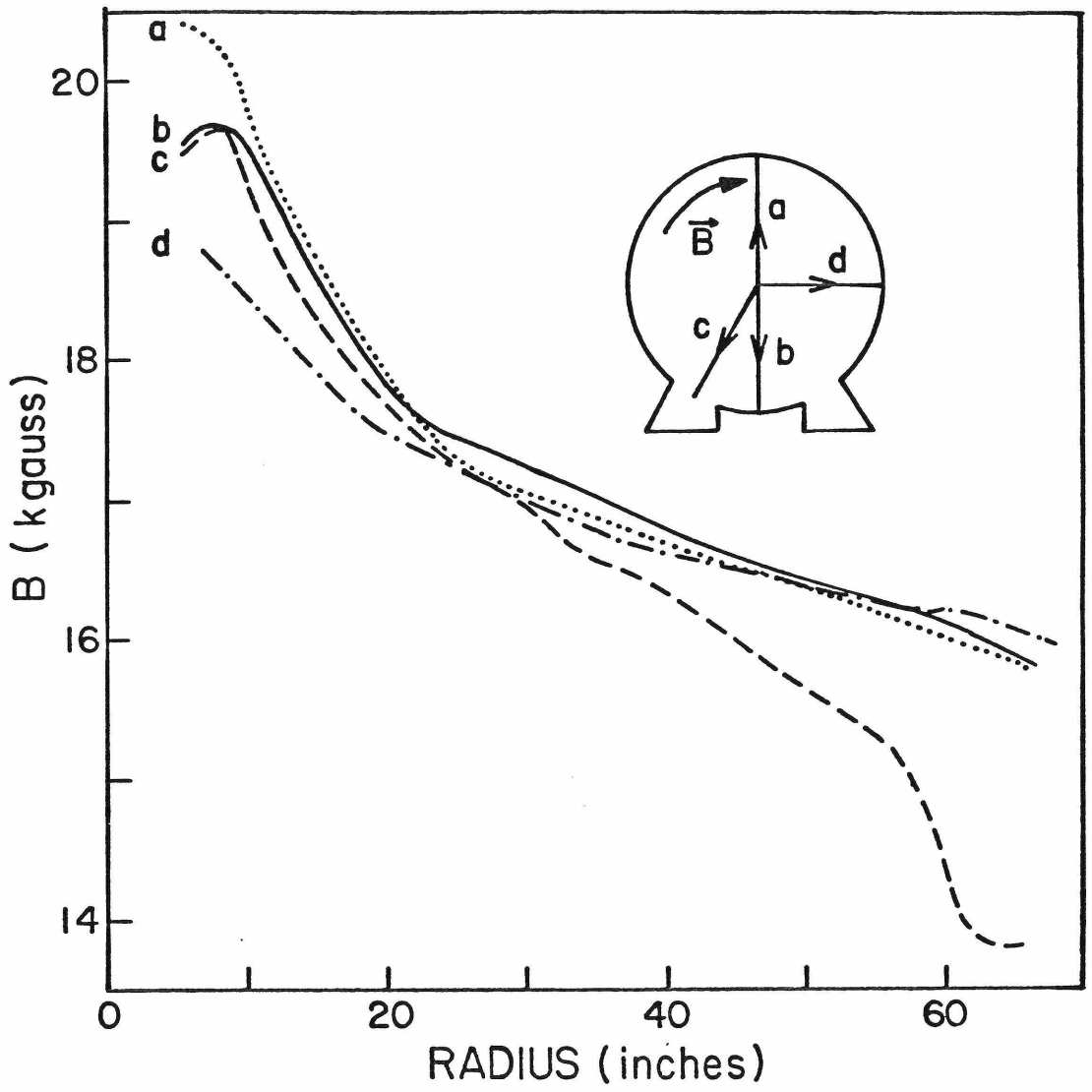

Figure 3-14: Calculated magnetic field in the toroid.

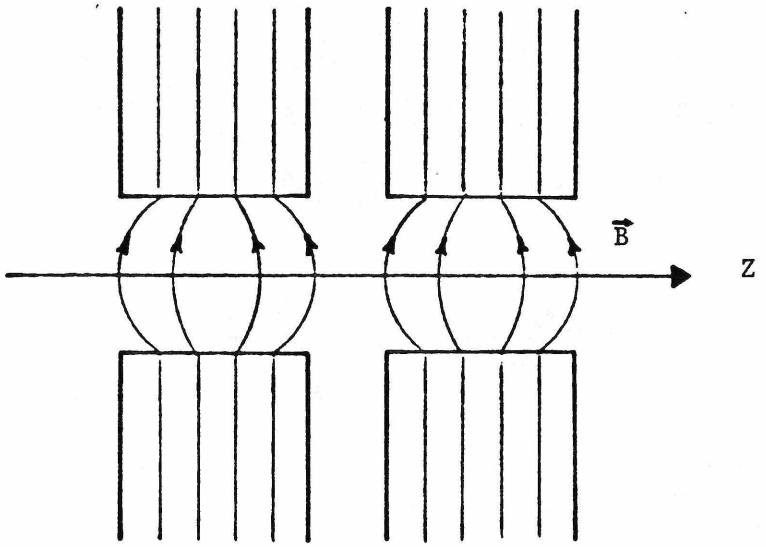

Figure 3-15: Magnetic field in the air gap.

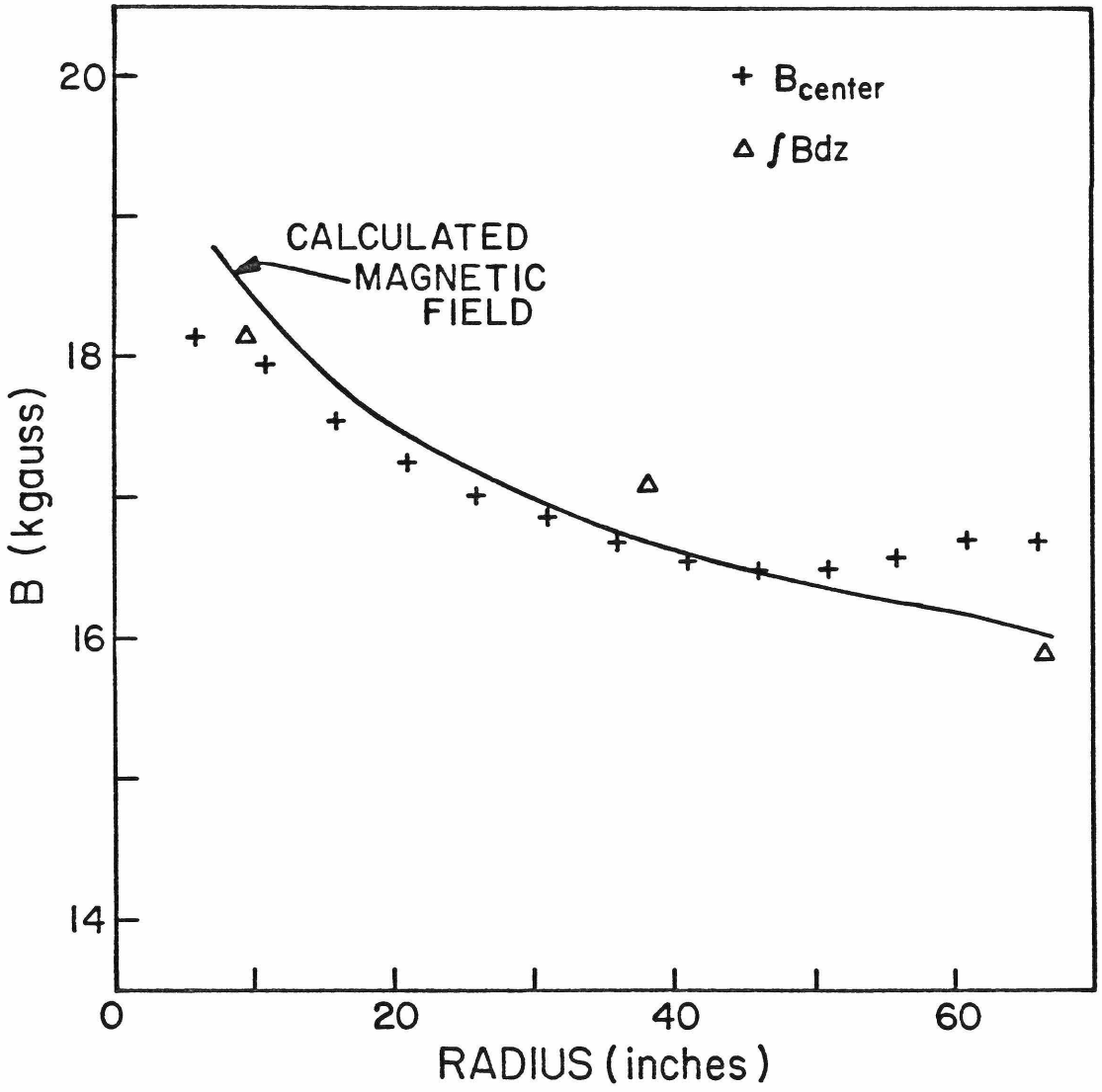

Figure 3-16: Magnetic field measurements in the air gap.

B. DETERMINING MUON MOMENTUM

The position of muons traversing the spectrometer is measured at the center and after each of the 3 magnets with 36 5'X10' spark chambers arranged in 18 10'X10' planes. The principal difficulty in determining the momentum of a muon lies in adequately treating the multiple scattering of a muon in the steel.

First consider the problem of a muon traveling through a length of material sufficiently short so that only a single scatter is important. After a distance L, the muon has been deflected by an angle ϕ for a net displacement δ (see figure 3-17). Ignoring nongaussian tails on the multiple scattering distribution, the probability of a deflection ϕ in this plane is

$$P(\phi) = \frac{1}{\sqrt{2\pi}\sigma_\phi} e^{-\phi^2/2\sigma_\phi^2} , \qquad (3\text{-}1)$$

where $$\sigma_\phi^2 = \left(\frac{.014}{p}\right)^2 \frac{L}{L_R}\left[1+\frac{1}{9}\log_{10}\left(\frac{L}{L_R}\right)\right].$$

L_R is the radiation length of the material. It is trivial to compute the correlation matrix σ of ϕ and δ,

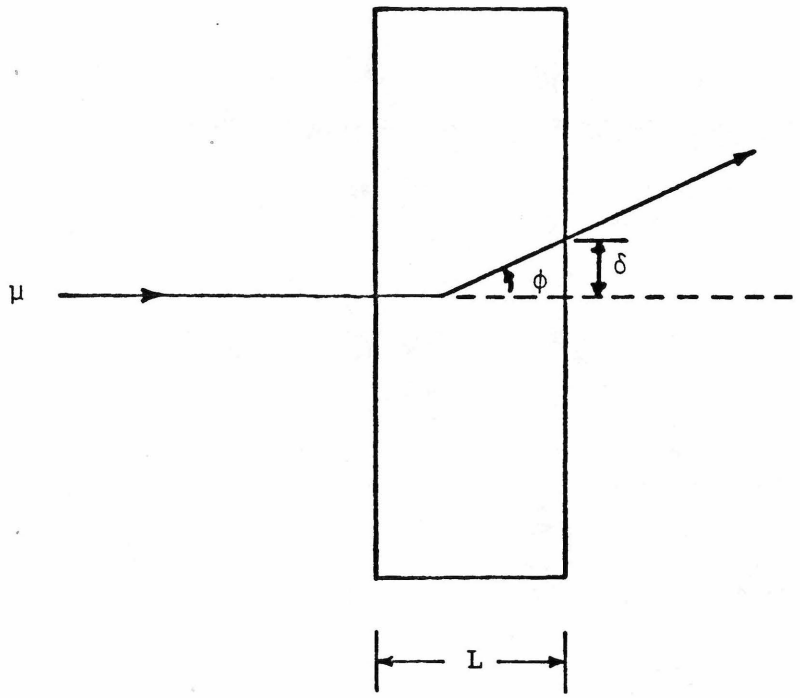

Figure 3-17: A single scatter in material.

$$\sigma = \begin{pmatrix} \langle \phi^2 \rangle & \langle \phi\delta \rangle \\ \langle \delta\phi \rangle & \langle \delta^2 \rangle \end{pmatrix} \tag{3-2a}$$

$$= \sigma_\phi^2 \begin{pmatrix} 1 & L/2 \\ L/2 & L^2/3 \end{pmatrix}. \tag{3-2b}$$

Now consider several blocks of material with one or more spark chambers placed after each. A muon is scattered in the i^{th} block with angle ϕ_i and displacement δ_i. Let the end of the m^{th} block be at $z=Z_m$, and the position of the i^{th} chamber be z_i (see figure 3-18). The displacement at chamber i due to a scatter at block m in front of chamber i is

$$y_m^i = \delta_m + (z_i - Z_m)\,\phi_m. \tag{3-3}$$

The total displacement at chamber i from all scatters is

$$Y^i = \sum_{\substack{m \\ Z_m < z_i}} [\,\delta_m + (z_i - Z_m)\,\phi_m\,]. \tag{3-4}$$

The correlation between ϕ_i and δ_j is given by

$$\langle \phi_i \phi_j \rangle = \sigma_i^2 \delta_{ij} \tag{3-5a}$$

$$\langle \delta_i \delta_j \rangle = (L_i^2/3)\,\sigma_i^2 \delta_{ij} \tag{3-5b}$$

$$\langle \phi_i \delta_j \rangle = (L_i/2)\,\sigma_i^2 \delta_{ij} \tag{3-5c}$$

where $$\sigma_i^2 = \left(\frac{.014}{p}\right)^2 \frac{L_i}{L_R} \left\{ 1 + \frac{1}{9} \log_{10} \left(\frac{L_i}{L_R}\right) \right\}.$$

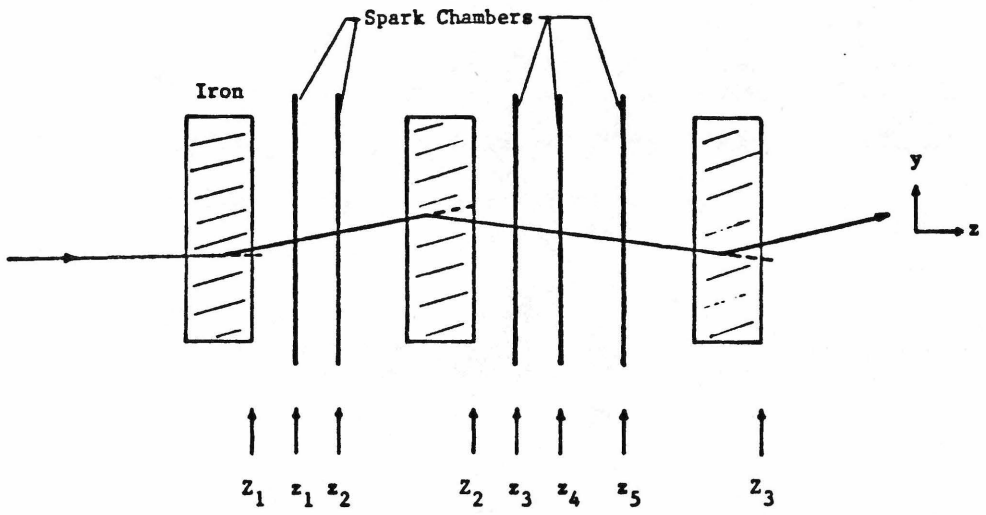

Figure 3-18: Multiple scattering in material.

The total correlation matrix from multiple scattering now can be computed.

$$\sigma_{ms}^{ij} = \langle Y^i Y^j \rangle \qquad (3\text{-}6a)$$

$$= \sum_{\substack{m \\ Z_m<z_i \\ Z_m<z_j}} \sigma_m^2 \left\{ \begin{array}{l} (L_m^2/3)+(z_i-Z_m)(z_j-Z_m) \\ +(L_m/2)[(z_i-Z_m)+(z_j-Z_m)] \end{array} \right\} . \qquad (3\text{-}6b)$$

In addition to the error from multiple scattering, there is error caused by finite spark chamber resolution. The total error matrix becomes

$$\sigma^{ij} = \sigma_{ms}^{ij} + \sigma_{sc}^2 \delta^{ij} \qquad (3\text{-}7)$$

where σ_{sc} = spark chamber resolution.

For a given event, sparks in the target are fit first, where there is no magnetic field. A multiple scattering fit is done to determine the slope and intercept of the track at the front of the magnet. For the rest of the fitting it is assumed that these parameters are known exactly. This approximation considerably simplifies the fitting procedure.

To find the momentum of a muon, an initial trial momentum is chosen. The trajectory of the particle through the magnet is computed from the incident track and the

trial momentum. This gives a projected position Y_i^{proj} at the i^{th} spark chamber. A χ^2 then is computed from the measured positions Y_i. The χ^2 is given by

$$\chi^2 = (Y_i - Y_j^{proj}) S_{ij} (Y_j - Y_j^{proj}) \qquad (3\text{-}8)$$

where $S = \sigma^{-1}$.

Then the trial momentum p is varied to minimize χ^2. The value of p where χ^2 is minimized is taken to be the particle momentum.

This procedure must be iterated because the error matrix σ is a function of momentum. If the value of p that minimizes χ^2 differs from the initial guess by more than 2%, σ is recomputed using the new value of p and χ^2 is minimized again. Also, energy loss by the muon in the magnet must be taken into account when calculating σ. For events used in this analysis, the distribution of χ^2/N_{DF}, where N_{DF} is the number of degrees of freedom in the fit, is shown in figure 3-19.

The error in measuring momentum is dominated by multiple scattering at the energies of this experiment. The total fractional error is shown as a function of

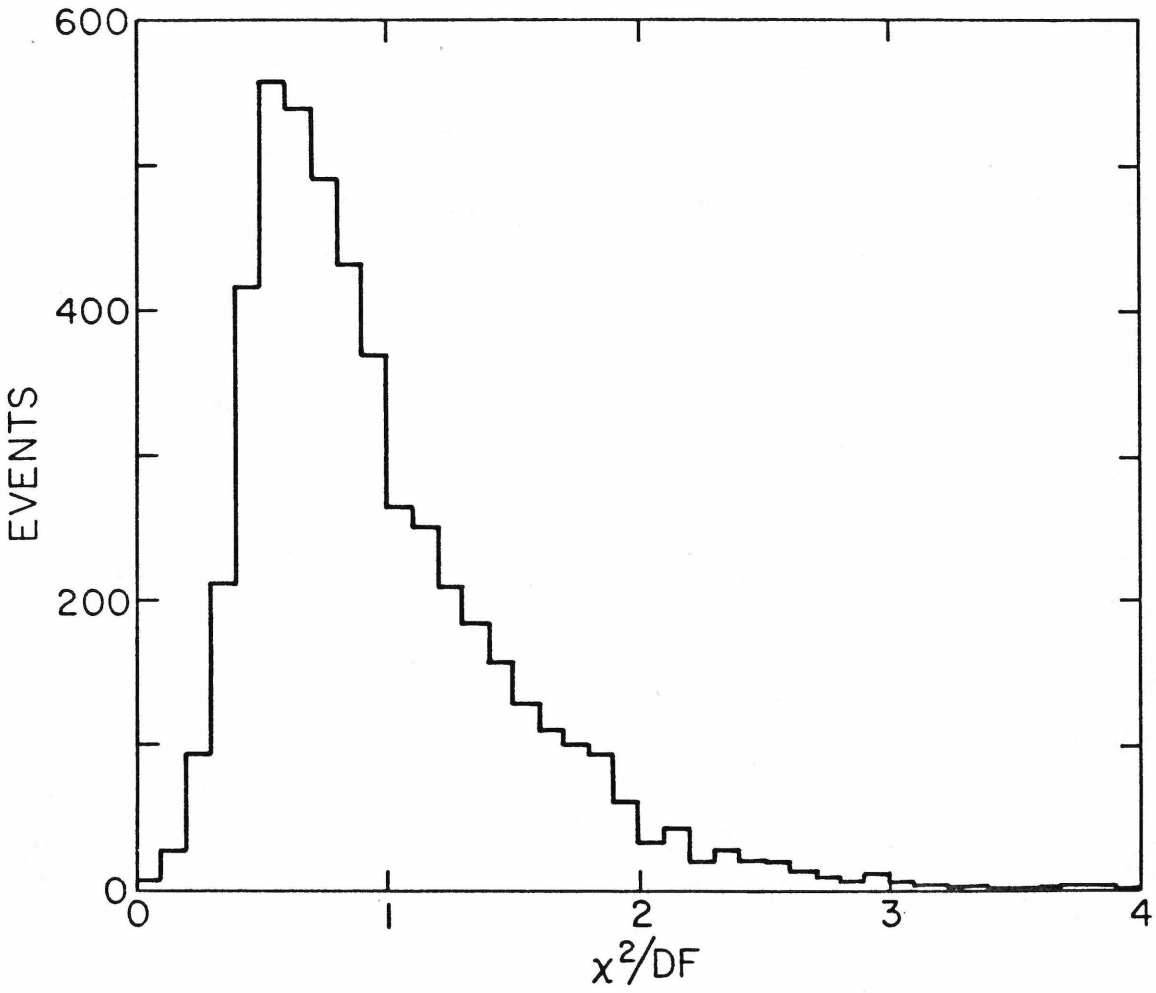

Figure 3-19: χ^2 per degree of freedom for momentum fit.

momentum in figure 3-20.

3.5 NEUTRINO TRIGGERS

The sensitivity of the scintillation counters to a single minimum ionizing particle allows great flexibility in designing electronic triggers for neutrino interactions. A high energy charged current neutrino interaction is characterized by a neutral incident particle, the production of a penetrating muon, and the deposition of energy by hadrons over a few collision lengths of the target material. Both the presence of a single penetrating particle and the deposition of energy in the calorimeter can be used to trigger the apparatus. Events with an incident charged particle are vetoed. The data reported here were taken with two triggers that are optimized for charged current interactions.

The first charged current trigger we called the muon trigger (MT). The logic for this trigger is shown in figure 3-21(a). The muon trigger required that an interaction take place in the target and that a muon hit at least one of the trigger counters between the toroids. Events that satisfied this trigger are particularly useful because the muon momentum is measured for muons going

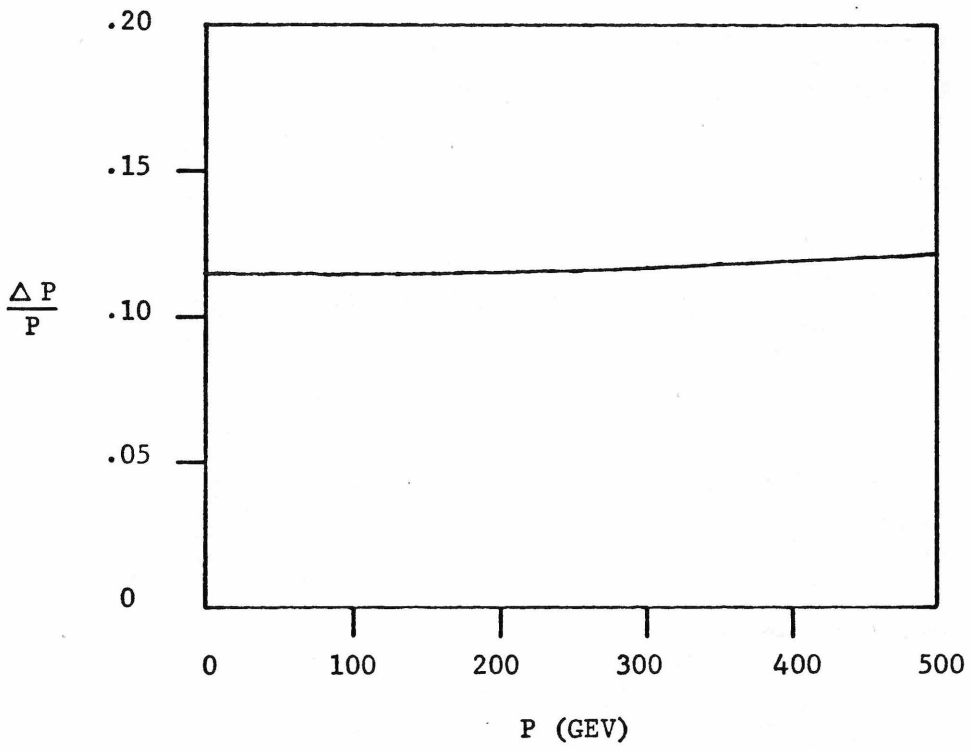

Figure 3-20: Muon momentum resolution.

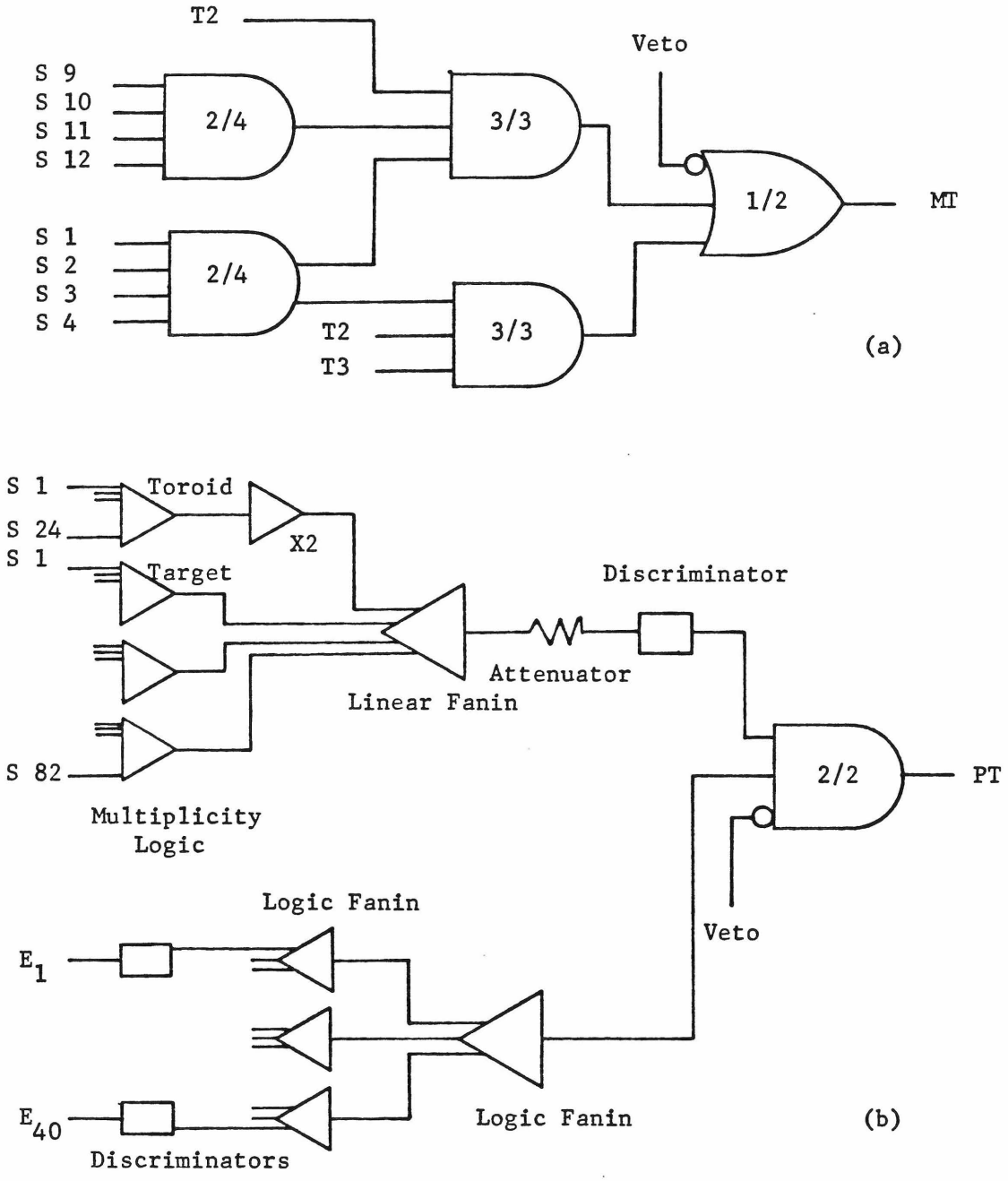

Figure 3-21: Charged current trigger logic
(a) muon trigger
(b) penetration trigger

through the toroids.

The second charged current trigger we called the penetration trigger (PT). The trigger logic is shown in figure 3-21(b). This trigger was designed to accept muons that may leave the apparatus at wide angles, but still penetrate enough steel to be identified as muons. The attenuator was adjusted so that the discriminator accepted an event that set 14 or more of the S bits. Cosmic ray muons could satisfy this part of the penetration trigger, so the trigger also required some energy deposition in the calorimeter. This did not reject neutrino events with wide angle muons, because these events produce large hadron showers.

In addition, we ran with a neutral current trigger and a straight through muon trigger. A neutral current interaction is characterized by hadronic energy deposition and the absence of a penetrating particle. The neutral current trigger was very unrestrictive, requiring penetration of only two or more counters along with energy deposition in the calorimeter. The energy threshold was set higher than for the penetration trigger to avoid an intolerable trigger rate from cosmic ray muons. The straight through muon trigger required a muon to hit the

veto and T2 and T3. Muons that satisfied this trigger were used to align the spark chambers and map the scintillation counters. Both the neutral current trigger and the straight through muon trigger were prescaled so that they did not significantly impact the collection of charged current data. I do not report on the analysis of the neutral current data in this thesis.

It is desirable to veto charged particles entering the front or sides of the detector. A large, very efficient wall of veto counters was built at the front of Lab E for this purpose, but phototube noise and cosmic ray muons that triggered the veto introduced a significant amount of dead time into the beam spill. The straight through muon rate was small enough that we decided to use a simple coincidence of the S discriminators on the first two counters in the target as the veto. This veto was not completely efficient, but it introduced a negligible amount of dead time into the experiment. Straight through muons that failed to fire the veto are removed from the data sample by making a fiducial cut.

We can use the substantial overlap in acceptance of the various triggers to measure the trigger efficiency. The penetration trigger is inefficient for an event with

short penetration or small hadron energy. We measured the efficiency of the penetration trigger as a function of penetration length by looking at events that satisfied the neutral current trigger. The result is shown in figure 3-22(a). The penetration trigger efficiency as a function of hadron energy was measured by looking at events accepted by the muon trigger. The result is shown in figure 3-22(b). The penetration trigger is used to measure cross sections only in a kinematic region where it is very close to being 100% efficient (for events with hadron energy > 10 GEV and penetration length > 20 counters).

The muon trigger efficiency was measured by examining penetration trigger events that had muons satisfying the geometrical requirements of the muon trigger. The measured trigger efficiency is .985±.017.

3.6 DATA COLLECTION

For E356, protons were delivered to the neutrino lab in 1 msec spills containing about 10^{13} protons. A 1 msec spill is short enough to reduce the trigger rate from cosmic ray muons to an acceptable level, but long enough to easily measure the fluxes. The apparatus can accept only one trigger per beam spill since the spark chambers take

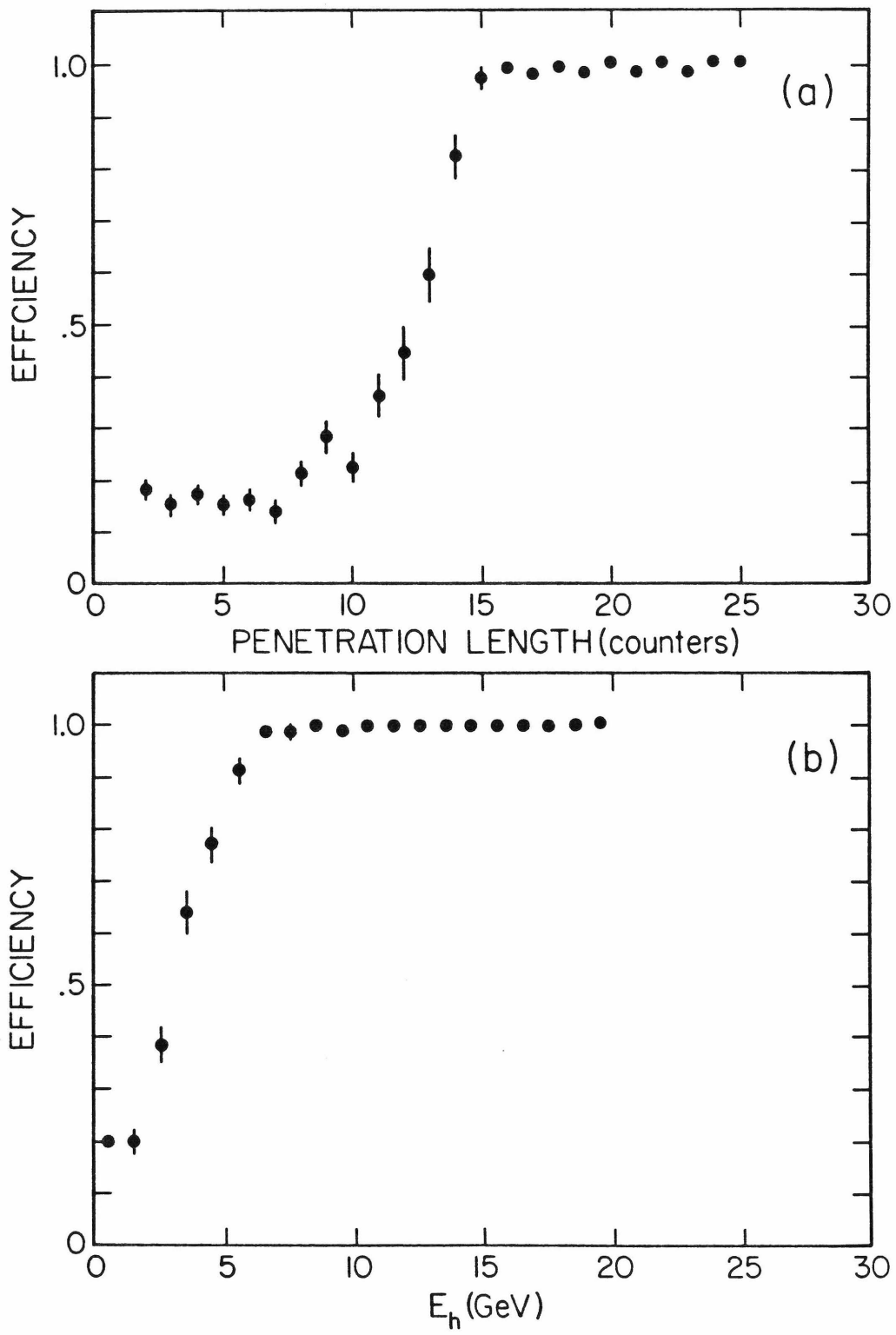

Figure 3-22: Penetration trigger efficiency
(a) versus penetration length
(b) versus hadron shower energy

longer than 1 msec to recover after being fired. The total trigger rate while running at the 200 GEV beam setting was about 1.3 triggers/10^{13} livetime protons. The rate at the 300 GEV beam setting was about .7 triggers/10^{13} livetime protons. Roughly 70% of the triggers came from neutrino interactions in the target. The duty cycle of the accelerator typically was about 10 seconds.

Between beam spills a variety of useful information is collected. A gate is opened to collect cosmic ray triggers, which are essential to study the backgrounds in neutral current data since they can fake neutral current interactions. These are not needed to analyze charged current events because cosmic ray triggers do not have the characteristics of charged current interactions and can be separated easily from the charged current data.. The ADC pedestals are measured once each beam cycle. Also, one of the spark gaps in the phototube monitoring system is fired each cycle, so that every 12 cycles the gain of each phototube is monitored.

Data collection is controlled and monitored by a PDP-11/50, and data from both the neutrino detector and the beam monitors are written onto magnetic tape. Figure 3-23 shows an event display for a typical neutrino interaction.

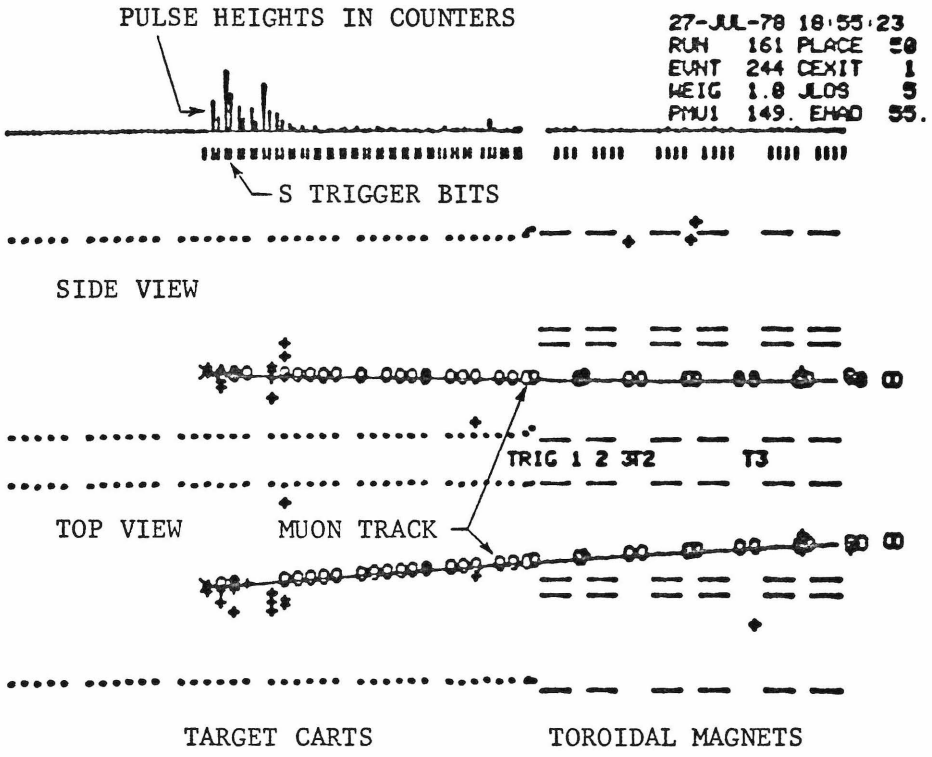

Figure 3-23: Event display.

This display can be drawn on a Tektronix 4010 online while taking data. The event display gives a visual overview of the detector and is useful in alerting operators to equipment failures.

CHAPTER 4

EVENT ANALYSIS

4.1 DETERMINING INTERACTION PARAMETERS

For each neutrino interaction we measure the coordinates of the interaction vertex, the total hadron energy, the penetration of the hadron shower, and the trajectories and momenta of final state muons. We have written a computer program to extract these parameters from the data tapes.

The longitudinal position of the interaction vertex is determined from the S bits on the scintillation counters. An interaction is characterized by a string of consecutive bits that have fired. Large hadron showers can have particles that backscatter one or two counters, so the vertex position is determined by an abrupt increase in pulse height near the front of the bit string. For hadron showers less than 10 GEV, we define the vertex at the first counter in the bit string having a signal greater than 1/3 of a minimum ionizing particle. For larger showers we

increase the minimum required signal by $2\ln(E_h/10\ \text{GEV})$ mip. In our calorimeter 1 mip=.21 GEV.

The transverse coordinates of the interaction vertex first are estimated by averaging the coordinates of sparks in spark chambers near the front of the hadron shower. Then a track finding program searches for sparks that line up on tracks going through this vertex. Once a track has been found, a filtering program removes bad sparks and searches for good sparks that were missed in the first search. A least squares fit to the sparks on the track determines the trajectory of the muon in the target. The intercepts of the longest track at the longitudinal position of the interaction vertex give the transverse coordinates of the vertex.

If a track goes into the toroid, a search is made for sparks on a curved track in the magnetic field of the toroid. If a track is found in the toroid, the sparks are filtered and the momentum is calculated in the manner described in section 3.4B. The total momentum of a final state muon is the sum of its momentum at the front of the toroid and the energy it deposits in the target.

The total penetration of an event is determined from

the S bits. Once the pulse height in the counters drops to three times miminum ionizing, it is assumed that the hadron shower has stopped and the remaining energy is deposited by a penetrating muon. The average energy deposited by a muon traveling the length of the hadron shower is used to correct the measurement of hadron energy and muon momentum. The measurement of hadron energy is described in section 3.2.

The event analysis program accurately reconstructed neutrino events more than 90% of the time. On the remaining events, the most common problem was with the momentum fitting. Sometimes random sparks near a track would be included in the track by the spark selection algorithm. These extra sparks came from random breakdowns in the spark chambers, multiple sparking near the muon trajectory, or hadrons near the interaction vertex. Tracks with spark selection problems had anomalously large χ^2 s and so could be flagged. In virtually all cases, good fits could be obtained by reselecting sparks by hand. Also, the analysis program failed to find tracks about 1% of the time, and frequently dimuon events (~1% of the charged current events) were reconstructed incorrectly. An event scanning project was undertaken to identify and fix problem events. An event that fired the penetration trigger was

scanned by hand if the penetration length of the event was longer that 15 counters and a track was not found in both views. A muon trigger event was scanned if the program did not converge to a reasonable momentum, if the χ^2 per degree of freedom of the momentum fit was greater than 2, or if there were less than 5 sparks on the track in either view in the toroid. Any event with more than one track in either view was scanned. Spark selection problems did not systematically affect the mean measured muon momentum, which shifted by less than 1% after scanning the entire data sample.

4.2 FIDUCIAL AND PENETRATION CUTS

Very conservative fiducial and kinematic cuts are placed on these data to eliminate problems with backgrounds and deficiencies in the event analysis program.

One background we must eliminate comes from muons that enter the front of the target without being vetoed. They can be found by looking at muon trigger events that have hadron energy less than 2 GEV. Figure 4-1(a) shows the longitudinal position distribution of the interaction vertex of these events. The large increase in events at the front of the target comes from straight through muons

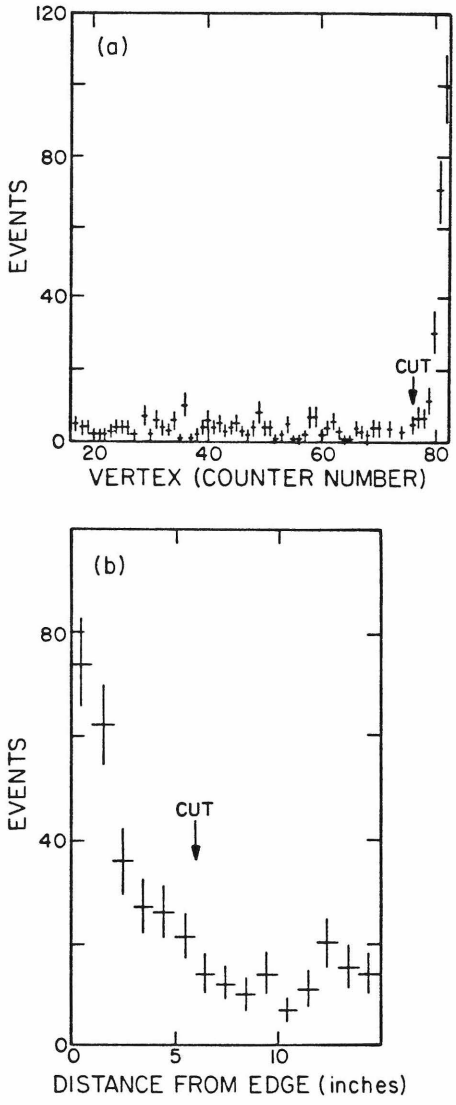

Figure 4-1: Fiducial cuts
(a) Longitudinal position of vertex for events with E_h<2 GEV. The large number of triggers at the front of the detector is from straight through muons.
(b) Distance of vertex from the edge of detector for events with E_h<5 GEV. The large number of triggers at the edge is from cosmic ray muons.

(counter 82 is located at the front of Lab E). Making a fiducial cut in front of counter 76 removes this background.

The analysis program presently cannot handle events that occur just in front of the toroids. The momentum analysis program requires that the trajectory of a muon be well determined before it enters the first toroid. This is difficult for events that take place in the target cart closest to the toroids because the hadron shower can swamp sparks on the muon track for a few chambers after the interaction vertex. Also, a large fraction of the hadron showers in these events penetrate into the toroids. The scintillation counters in the toroid were not calibrated for this run, so we are unable to measure energy deposited in the toroids. Therefore we make a longitudinal fiducial cut that excludes events in the first target cart.

Cosmic ray muons can trigger the apparatus, but the analysis program finds a vertex near the edge of the target for these events. Figure 4-1(b) shows the distribution of penetration trigger events with E_h<5 GEV near the edge of the detector. A transverse fiducial cut 6" from the edge of the target removes cosmic rays from the data sample. We also must exclude the corners of the target because muons

produced at zero degrees will miss the muon spectrometer if the vertex is more than 66" radially from the center of the detector. The fiducial volume after making all cuts includes 62 scintillation counters and 420 tons of material.

Neutral current interactions with large hadron showers can fire the penetration trigger. These events are indistinguishable from charged current events with very low muon momentum. In analyzing charged current data we require that a muon penetrate at least 20 counters. This places a 2.9 GEV muon momentum cut on the data.

It is difficult to measure the momentum of muons that miss part of the magnetic field of the toroids. We place a cut on muon trigger events if more than 35% of the length of the track lies in the center hole in the toroid, if the muon is more than 66" from the center of the toroid at the back of the toroid, or if the muon hits T2 within 5" of its edge.

4.3 GEOMETRICAL EFFICIENCY

A neutrino interaction that produces a wide angle muon can fail to trigger the apparatus or cannot be analyzed if

the muon exits from the detector too rapidly. The neutrino target is not polarized, so the azimuthal angle at which a muon is produced is completely random. Events with wide angle muons can be divided into 2 classes. One class has muons produced at such extreme angles that they never can be detected, regardless of their azimuthal angles. Neutrino cross sections must be corrected for these events in a model dependent way. This correction is discussed in section 4.6C. The other class has muons that cannot be detected if they are produced at some azimuthal angles but can be detected at other angles. We use the events in this class that we detect to correct for the events we do not detect in a model independent way.

For each event that satisfies our software cuts, we rotate the muon trajectory in ϕ to determine angles at which we would not have detected the event. This rotation is illustrated in figure 4-2 for a penetration trigger event, where the requirement on the muon trajectory is that it not exit the target until the muon penetrate 20 counters. The efficiency for seeing events identical to this one except for a random azimuthal angle is $\varepsilon = \Delta\phi/2\pi$. We correct for events we do not detect by weighting this event by $1/\varepsilon$.

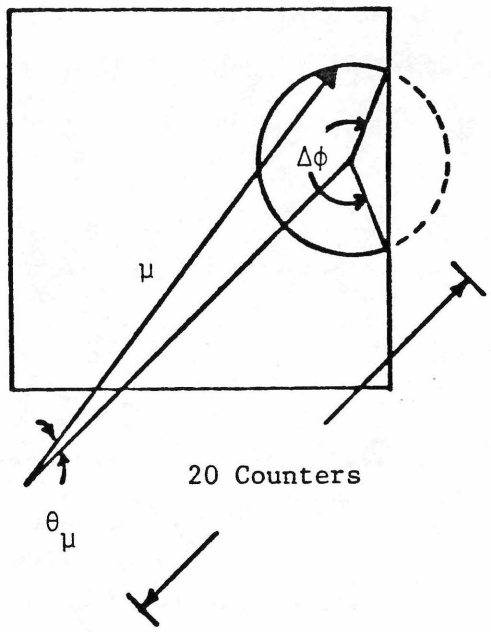

Figure 4-2: Azimuthal rotation of a penetration trigger event.

The constraints on muon trigger events are much more complicated. The muon trajectory must satisfy the fiducial cut on trigger counter T2, it must not be inside the hole for more than 35% of the length of the toroid, and it must pass through a circle with 66" radius at the end of the toroid. The muon also must have sufficient momentum to penetrate the detector to T2. The principle of the efficiency correction is the same as for the penetration trigger. The trajectory of each muon is rotated in ϕ to determine angles at which the event would be rejected. This depends on the z position of the interaction vertex, which also is random, so the efficiency is averaged over z within the fiducial volume. The event then is weighted by the inverse of the average efficiency.

Scatter plots of the efficiency versus muon production angle θ_μ are shown in figure 4-3 for muon trigger events and penetration trigger events within the fiducial volume of the detector. At each angle, the efficiency is a function of the transverse position of the interaction. In determining total cross sections, we use muon triggers only for events with θ_μ<100 mrad. In each radial bin, we reject penetration triggers above an angle θ that guarantees that the efficiency will be greater than 20%. When measuring x distributions we use all muon trigger

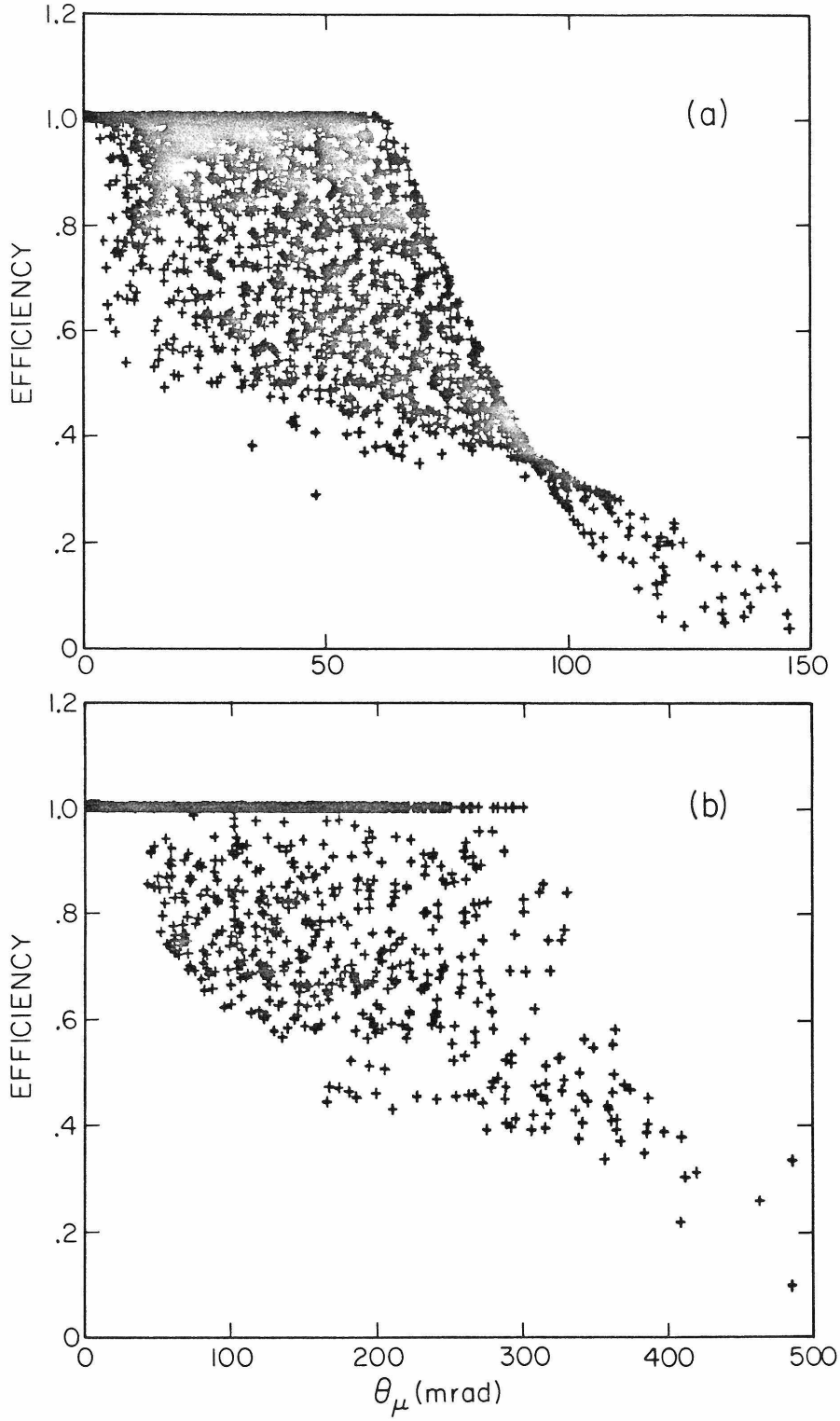

Figure 4-3: Efficiency of events under azimuthal rotation.
(a) muon triggers
(b) penetration triggers

events for which the geometrical efficiency is greater than 20%.

4.4 WIDE BAND BACKGROUND

Pions and kaons that decay upstream of the decay pipe contribute to the neutrino flux at the detector. The energy spectrum from these decays peaks at low neutrino energy, and the flux is roughly uniform over the area of the detector.

We measure the neutrino spectrum produced upstream of the momentum slit by taking data with the momentum slit closed. At the 300 GEV setting, the ratio of livetime protons on target taken with the slit closed to protons on target with the slit open is .348. At 200 GEV the ratio is .878. Neutrino events detected with the slit closed are weighted by the inverse of these ratios and subtracted from the slit open events.

Figure 4-4 shows neutrino event energy distributions from slit open running and the wide band background subtractions. These distributions are corrected for geometrical efficiency.

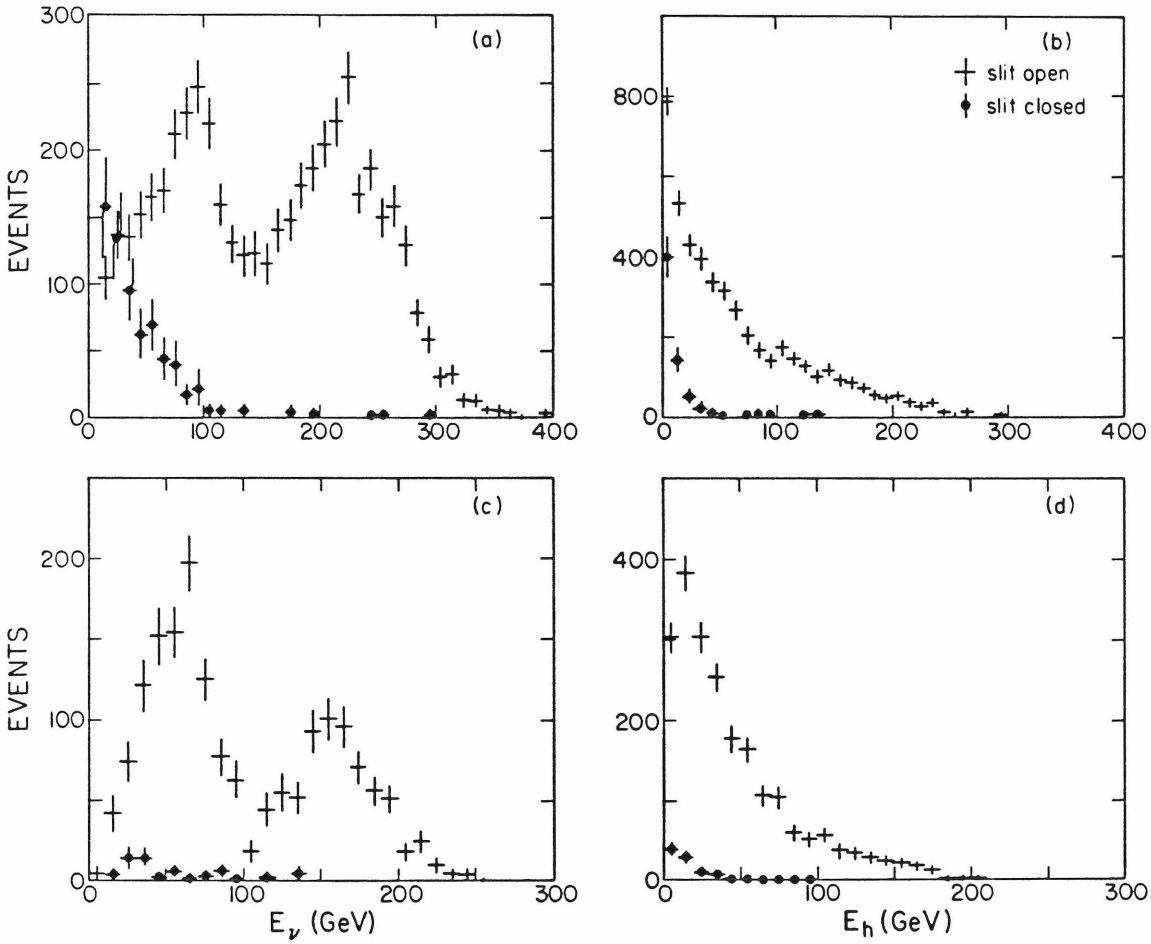

Figure 4-4: Wide band background subtraction
(a) muon trigger events at 300 GEV
(b) penetration trigger events at 300 GEV
(c) muon trigger events at 200 GEV
(d) penetration trigger events at 200 GEV

4.5 FINDING THE BEAM CENTER

We find the center of the neutrino beam by using neutrinos from pion decay, which have a flux distribution that peaks sharply in the center. Figures 4-5 and 4-6 show horizontal (X) and vertical (Y) event distributions, where X and Y are measured with respect to the beam center, X_0 and Y_0. At the 300 GEV setting, $(X_0,Y_0)=(.89",-5.18")$ with respect to the center of the target. At 200 GEV, $(X_0,Y_0)=(5.26",-6.50")$. The center of the beam is determined to about $\pm.5"$ in each dimension.

When dividing data into bins of different radii, the radius always is measured from the center of the neutrino distribution.

4.6 SEPARATION OF PION AND KAON NEUTRINOS

To measure cross sections separately for pion neutrinos and kaon neutrinos, we must determine the origin of a neutrino from the parameters of its interaction. This is possible because of the dichromatic nature of the beam and the kinematic constraints on the interaction. The method of separating pion neutrino events from kaon neutrino events depends on the angle of the final state

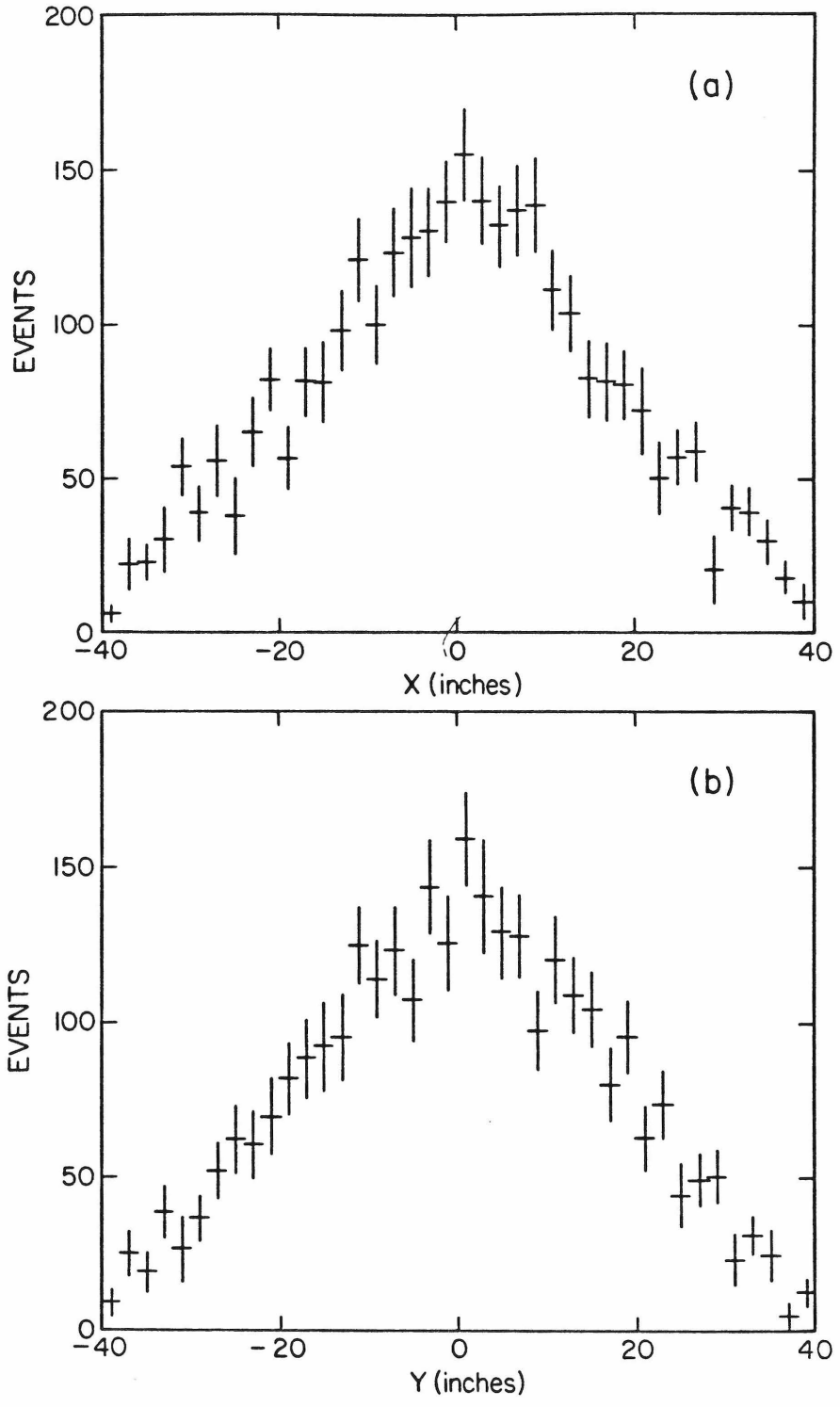

Figure 4-5: Position of ν_π events at 300 GEV with respect to the beam center.
(a) horizontal
(b) vertical

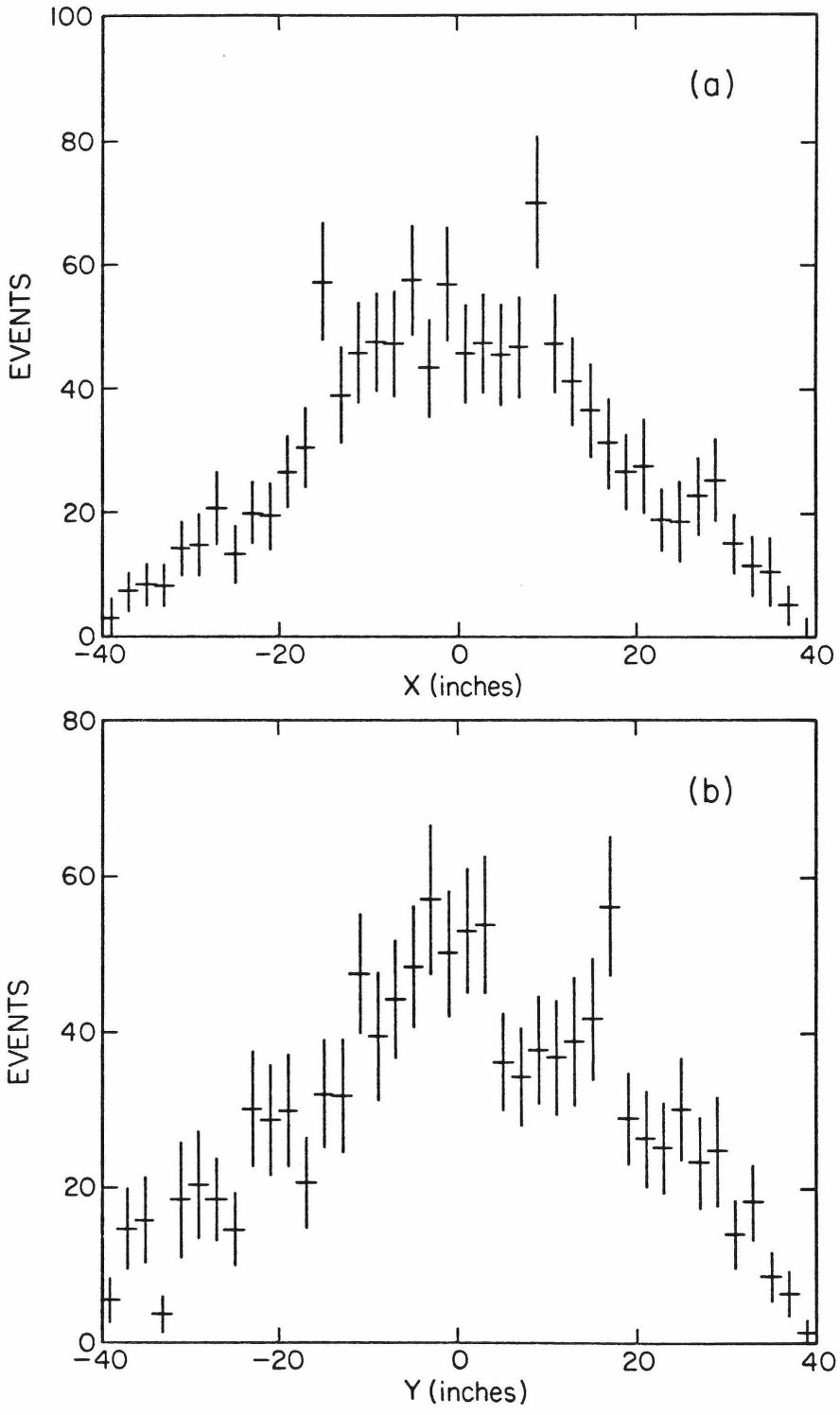

Figure 4-6: Position of ν_π events at 200 GEV with respect to the beam center.
(a) horizontal
(b) vertical

muon.

A. SMALL ANGLE MUONS

Muons with θ_μ <100 mrad are detected efficiently by the muon trigger. For these events we measure both the hadron energy and the muon momentum of each interaction, so we can separate pion neutrino events from kaon neutrino events using the total observed energy.

Figure 4-7 shows scatter plots of E_ν versus radius from the center of the neutrino distribution. The dichromatic nature of the beam at each radius is clearly visible. Energy distributions in various radial bins after weighting the events to correct for efficiency and subtracting the closed slit data are shown in figure 4-8 for the 300 GEV data and figure 4-9 for the 200 GEV data. Interactions are assumed to come from kaon neutrinos if the measured E_ν is greater than the cuts shown in these figures. The rest of the events are assumed to come from pion neutrinos.

B. LARGE ANGLE MUONS

We must use the penetration trigger to study

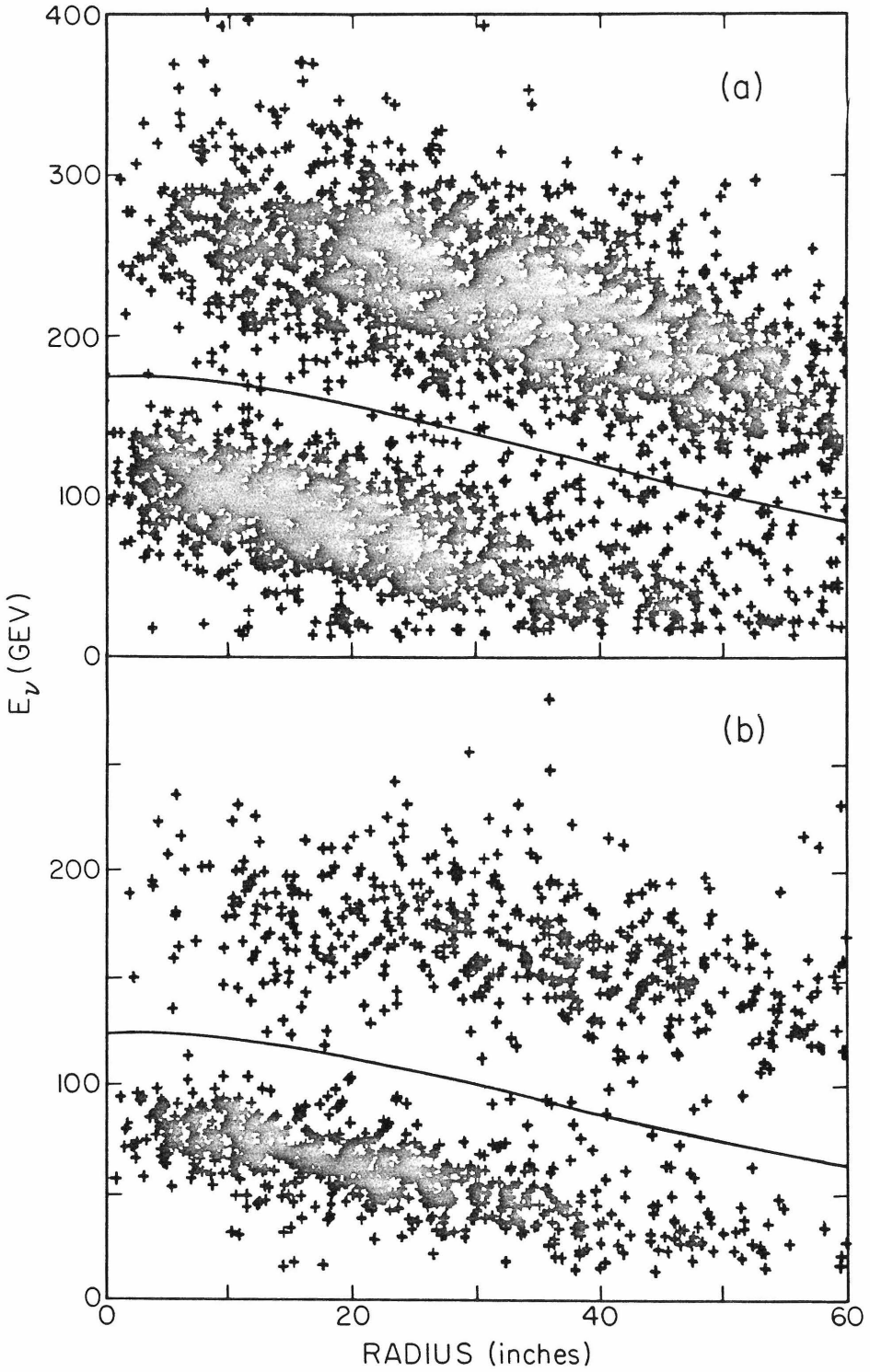

Figure 4-7: E_ν versus radius for events with E_μ>10 GEV and θ_μ<100 mrad.
(a) 300 GEV beam setting
(b) 200 GEV beam setting

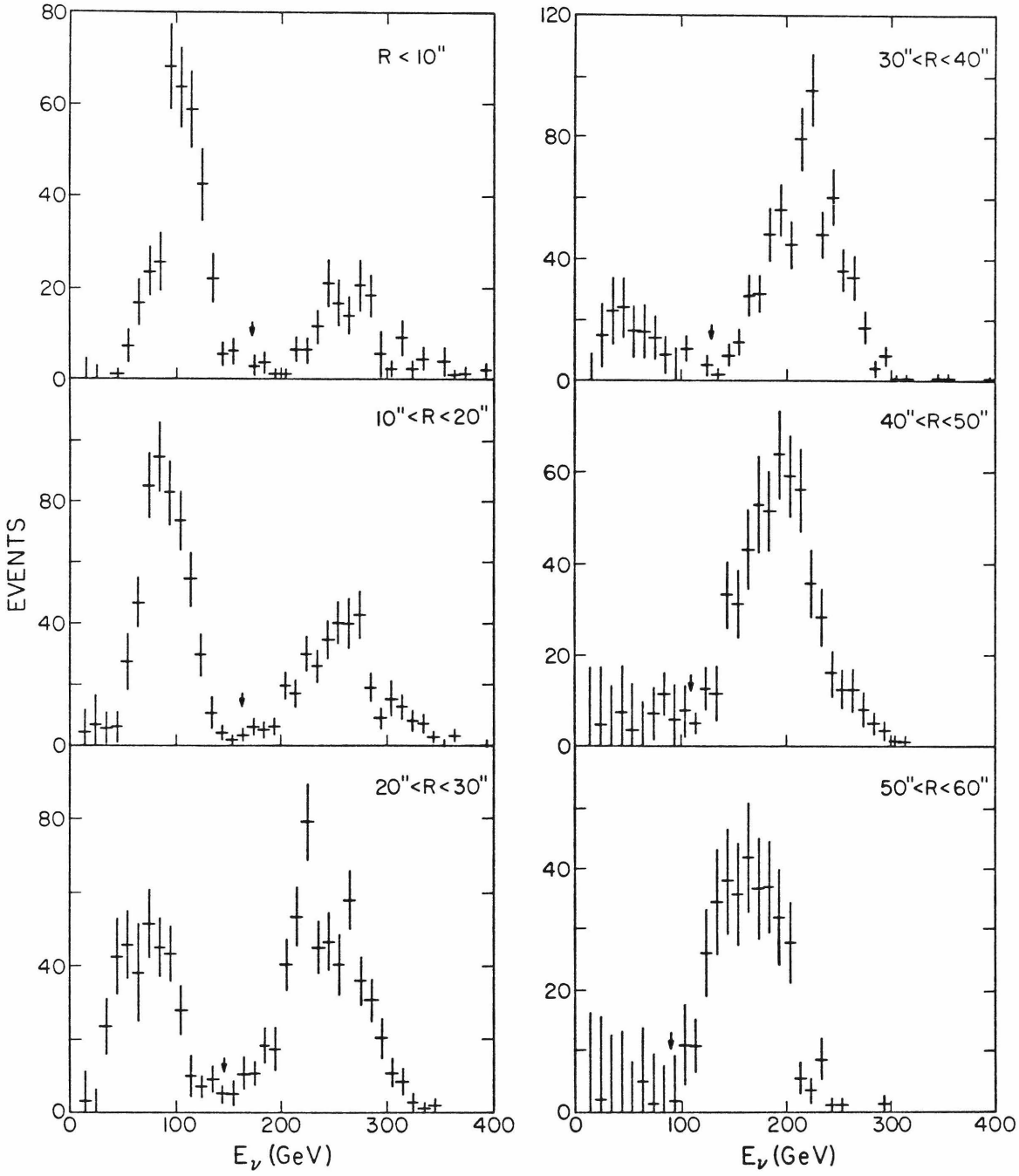

Figure 4-8: E_ν distributions at 300 GEV beam setting for events with E_μ >10 GEV and θ_μ <100 mrad.

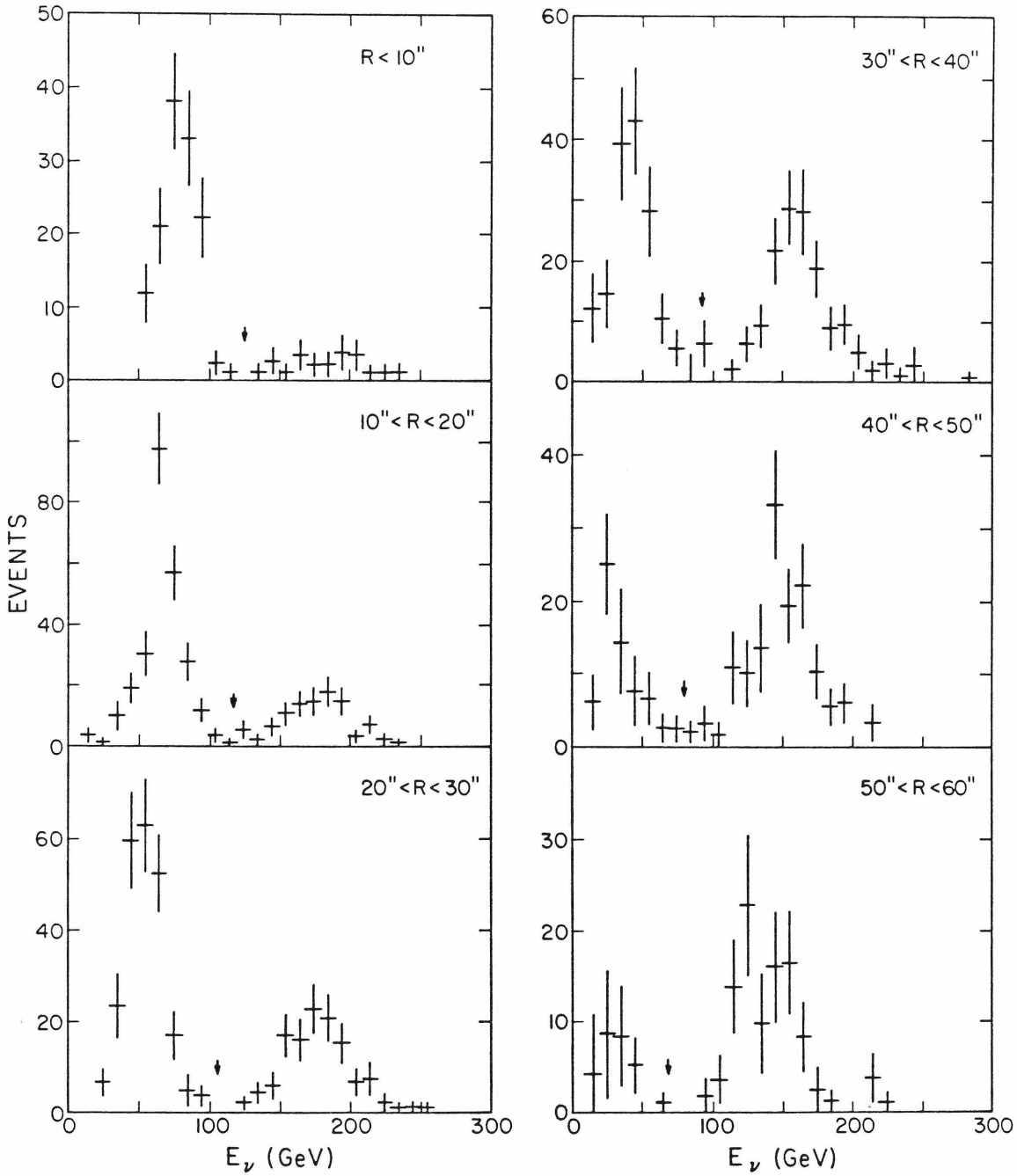

Figure 4-9: E_ν distributions at 200 GEV beam setting for events with E_μ >10 GEV and θ_μ <100 mrad.

interactions with θ_μ>100 mrad. For most of these events we do not measure the muon momentum, so we cannot use the previous method to separate pion neutrino events from kaon neutrino events. However, in interactions with wide angle muons, most of the neutrino energy gets converted into hadron energy. The hadron energy E_h can be written in terms of E_ν, x, and θ_μ,

$$E_h = \frac{E_\nu}{1+\frac{M_N x}{2E_\nu}\left(\frac{1}{\sin^2(\theta_\mu/2)}\right)}. \qquad (4\text{-}1)$$

Since x ranges from 0 to 1, at a given θ_μ the minimum hadron energy is

$$E_{h(min)} = \frac{E_\nu}{1+\frac{M_N}{2E_\nu}\left(\frac{1}{\sin^2(\theta_\mu/2)}\right)}. \qquad (4\text{-}2)$$

The mean x is below .25, so a typical hadron energy is much closer to E_ν. We can separate pion neutrino events from kaon neutrino events using only E_h for sufficiently large

θ_μ .

Figure 4-10 shows scatter plots of E_h versus radius for events with θ_μ >100 mrad. Hadron energy disributions are shown in various radial bins in figures 4-11 and 4-12 after correcting for acceptance and subtracting the closed slit distributions. The cuts between pion neutrino events and kaon neutrino events are shown in these figures.

4.7 PROCEDURE FOR EXTRACTING CROSS SECTIONS

A. BINNING THE EVENTS

We measure neutrino cross sections at several energies at each beam setting by dividing the target into several bins of different radius. Each bin is an annulus centered on the neutrino beam.

The inner and outer radius of each bin and the neutrino fluxes are summarized in table 2-9 for both beam settings.

B. SUMMING THE EVENTS

The muon trigger and the penetration trigger each have

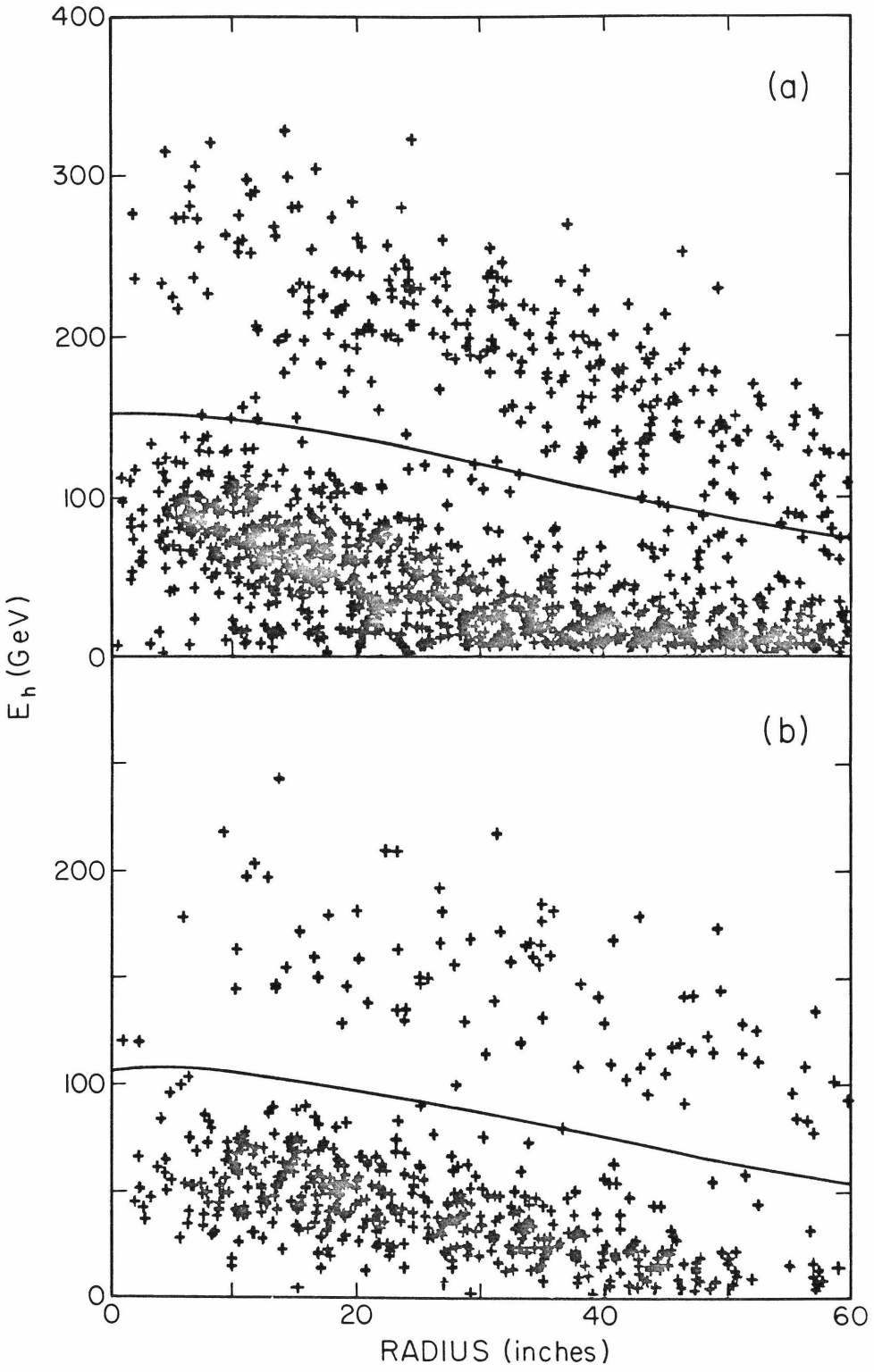

Figure 4-10: E_h **versus radius for events with** θ_μ **>100 mrad**
(a) 300 GEV beam setting
(b) 200 GEV beam setting

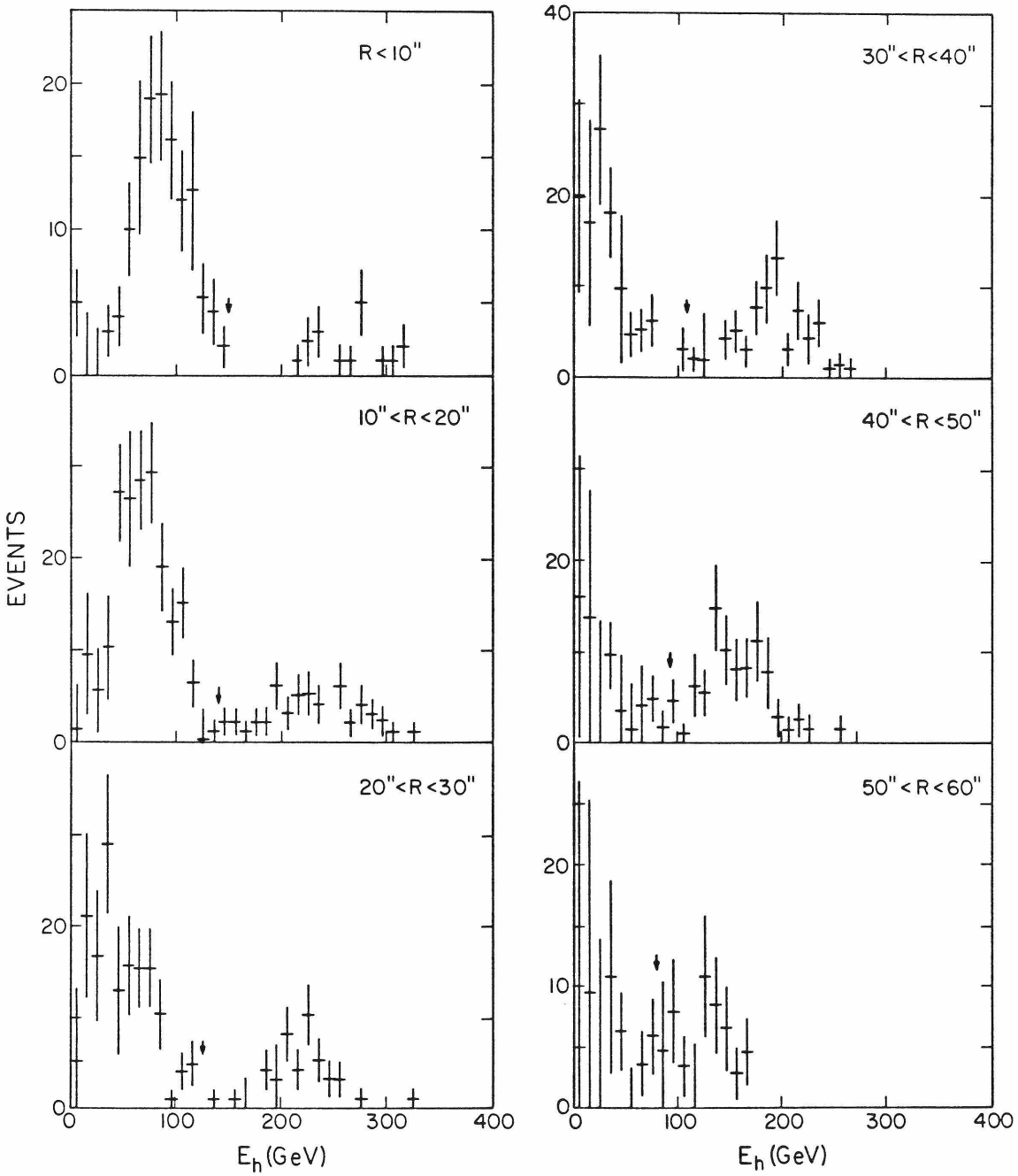

Figure 4-11: E_h distributions at 300 GEV beam setting for events with θ_μ >100 mrad.

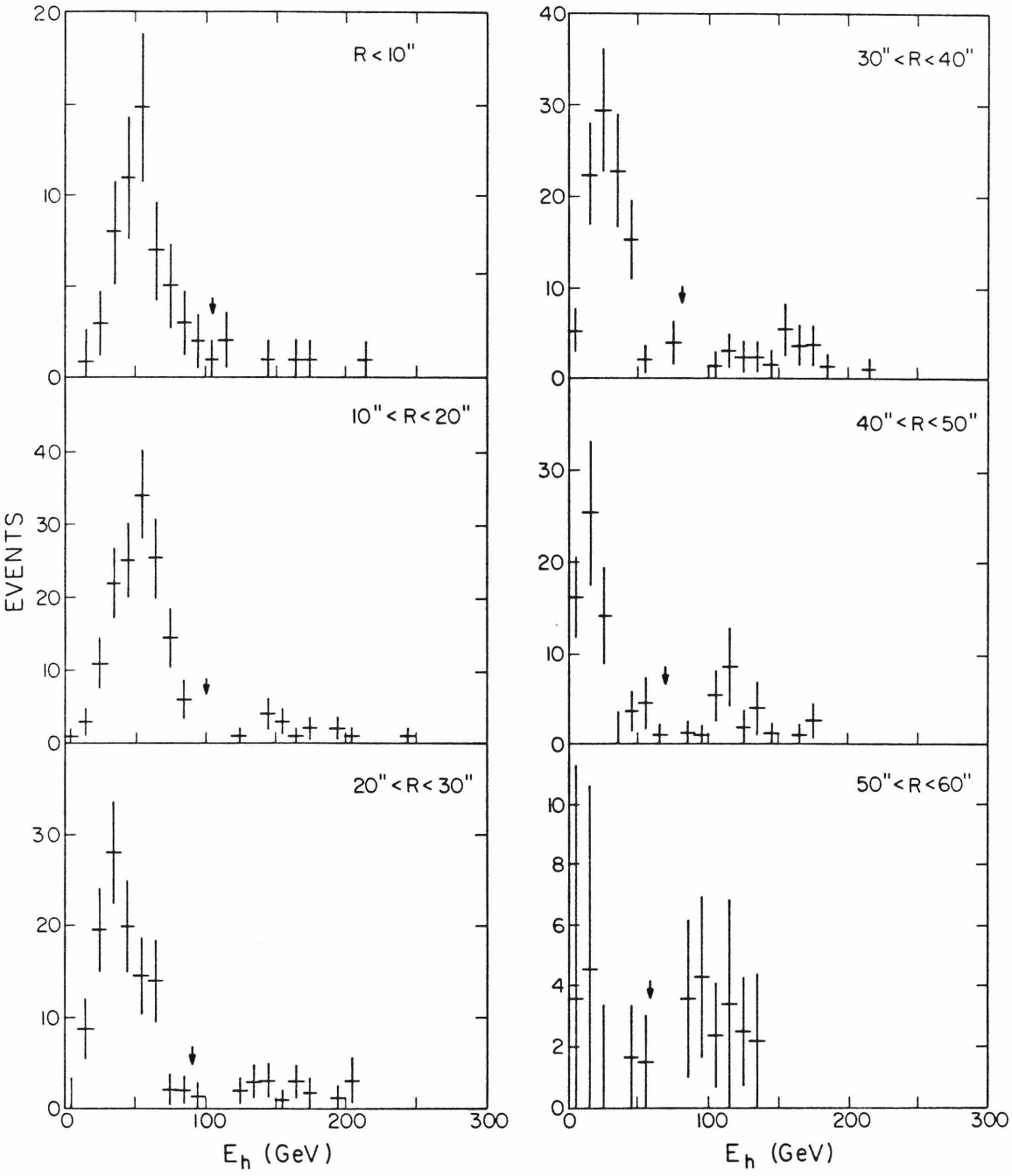

Figure 4-12: E_h distributions at 200 GEV beam setting for events with θ_μ>100 mrad.

inefficiencies in certain kinematic regions, but together they accept nearly all charged current interactions. We have two methods of determining the number of neutrino interactions in each target bin. The two methods differ in how the two triggers are combined to cover the kinematic range. This is possible because of the considerable overlap between the triggers. The method of separating pion neutrino events from kaon neutrino events and the ϕ rotation efficiency calculation differ for the two triggers, so it is a useful consistency check to sum the events in two different ways.

The kinematic acceptance of the two triggers is shown in figure 4-13 for 100 GEV neutrino interactions at the center of the target. The muon trigger cannot detect muons of too low a momentum to make it into the toroid or too wide an angle to hit the toroid. We make cuts at p_μ=10 GEV and θ_μ=100 mrad. The penetration trigger is inefficient for events with low hadron energy. Also, we cannot identify muons with too low a momentum or too wide an angle to penetrate 20 counters in the target. We make cuts at E_h=10 GEV, p_μ=2.9 GEV, and θ_μ=310 mrad (at the center of the target). We can accept larger angles for the penetration trigger in the outer target bins. The acceptance improves for both triggers as the neutrino

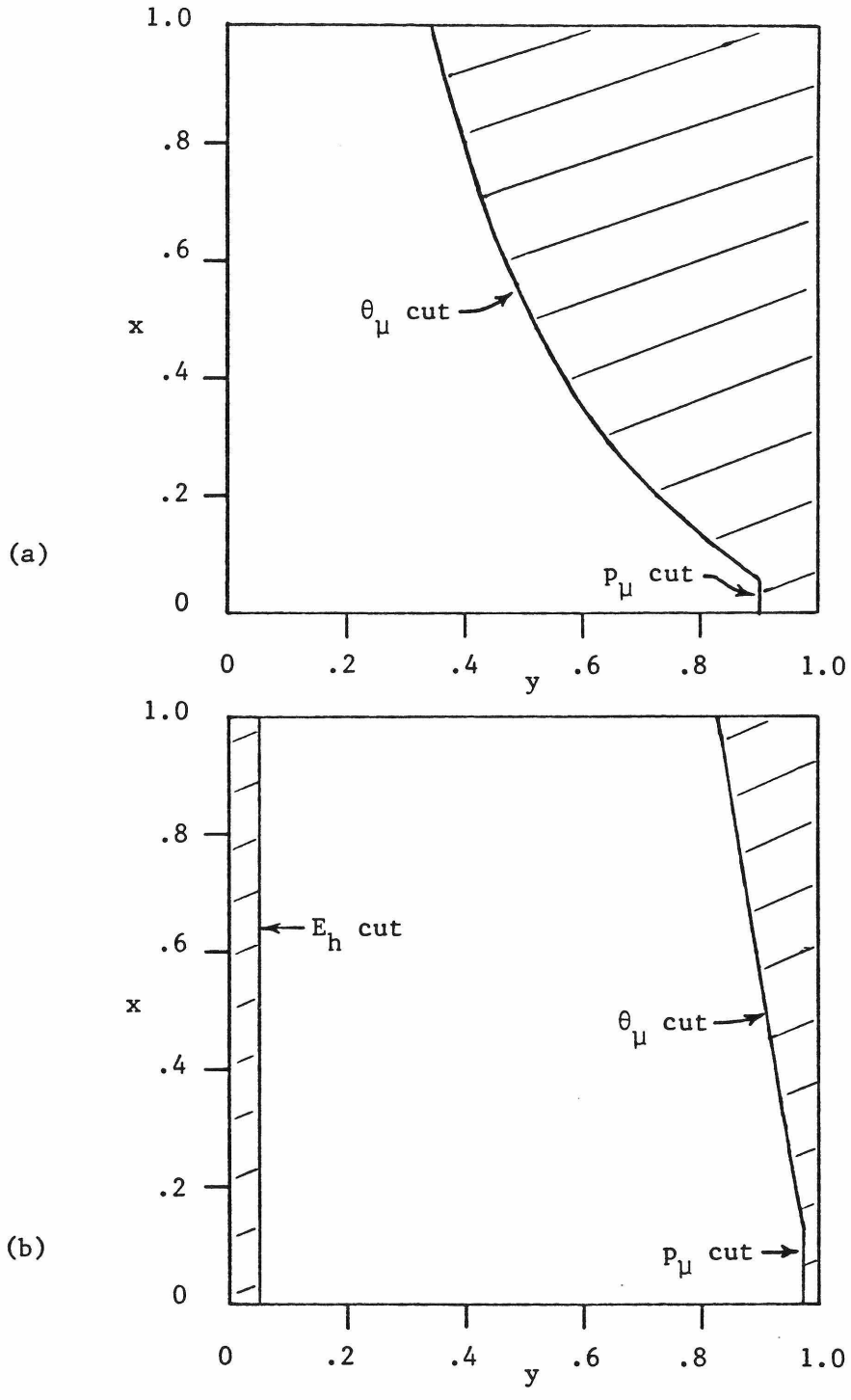

Figure 4-13: Kinematic acceptance for a 100 GEV ν.
(a) muon trigger
(b) penetration trigger

energy increases.

Method 1: Separating events with different θ_μ

The most straightforward way to sum the events is to use the muon trigger for interactions with θ_μ <100 mrad, and to use the penetration trigger for interactions with θ_μ >100 mrad. Each interaction is unambiguously identified as either a pion neutrino event or a kaon neutrino event in the manner described in section 4.6.

The combined kinematic region covered in this manner is shown in figure 4-14(a) for a 100 GEV neutrino event at the center of the target.

Method 2: Separating events with different E_h

This method exploits the greater acceptance of the penetration trigger to improve the statistical accuracy of the cross sections.

In interactions with E_h<10 GEV, the muons are kinematically constrained to have θ_μ <100 mrad at the neutrino energies of this experiment. We use the muon trigger in this region.

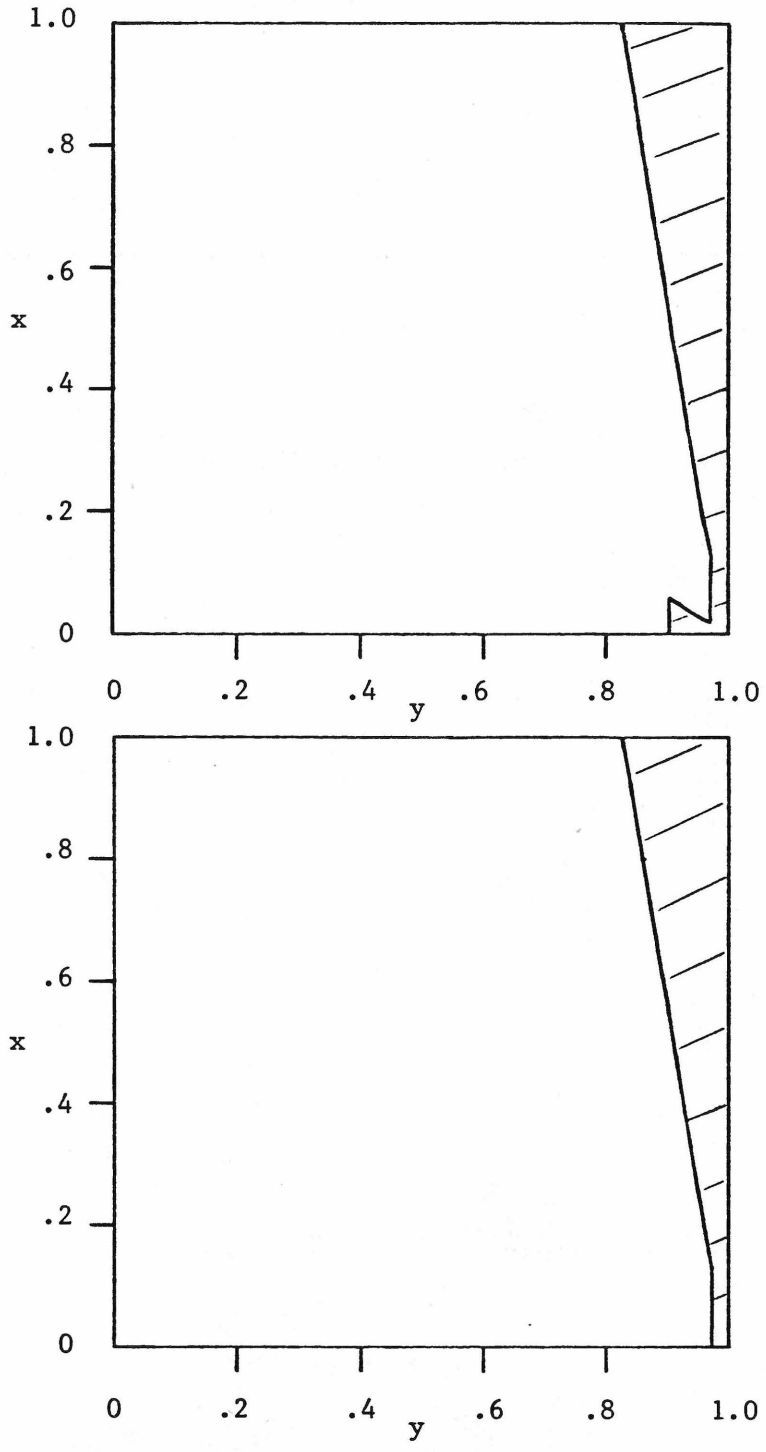

Figure 4-14: Kinematic region covered when summing events for total cross sections.
(a) method 1
(b) method 2

The total number of events with hadron energies greater than 10 GEV are determined with the penetration trigger. Events with E_h greater than the possible neutrino energy from pion decay must come from kaon decay. Below this energy pion neutrino events cannot be distinguished from kaon neutrino events with the penetration trigger. The number of kaon neutrino events in this region is determined with the muon trigger. Subtracting the kaon neutrino events from the total number of events leaves the pion neutrino events. This method works because kaon neutrino interactions with E_h below the maximum E_ν from pion decay must have muons with θ_μ <100 mrad.

The kinematic region covered with method 2 is shown in figure 4-14(b) for a 100 GEV neutrino.

Event distributions in θ_μ and E_h are shown in figures 4-15 through 4-18 for each target bin. When quoting cross sections, we use method 2 to obtain the number of neutrino events because it gives greater statistical accuracy and covers a slightly greater portion of the kinematic region.

C: KINEMATIC ACCEPTANCE CORRECTION

We correct charged current cross sections to account

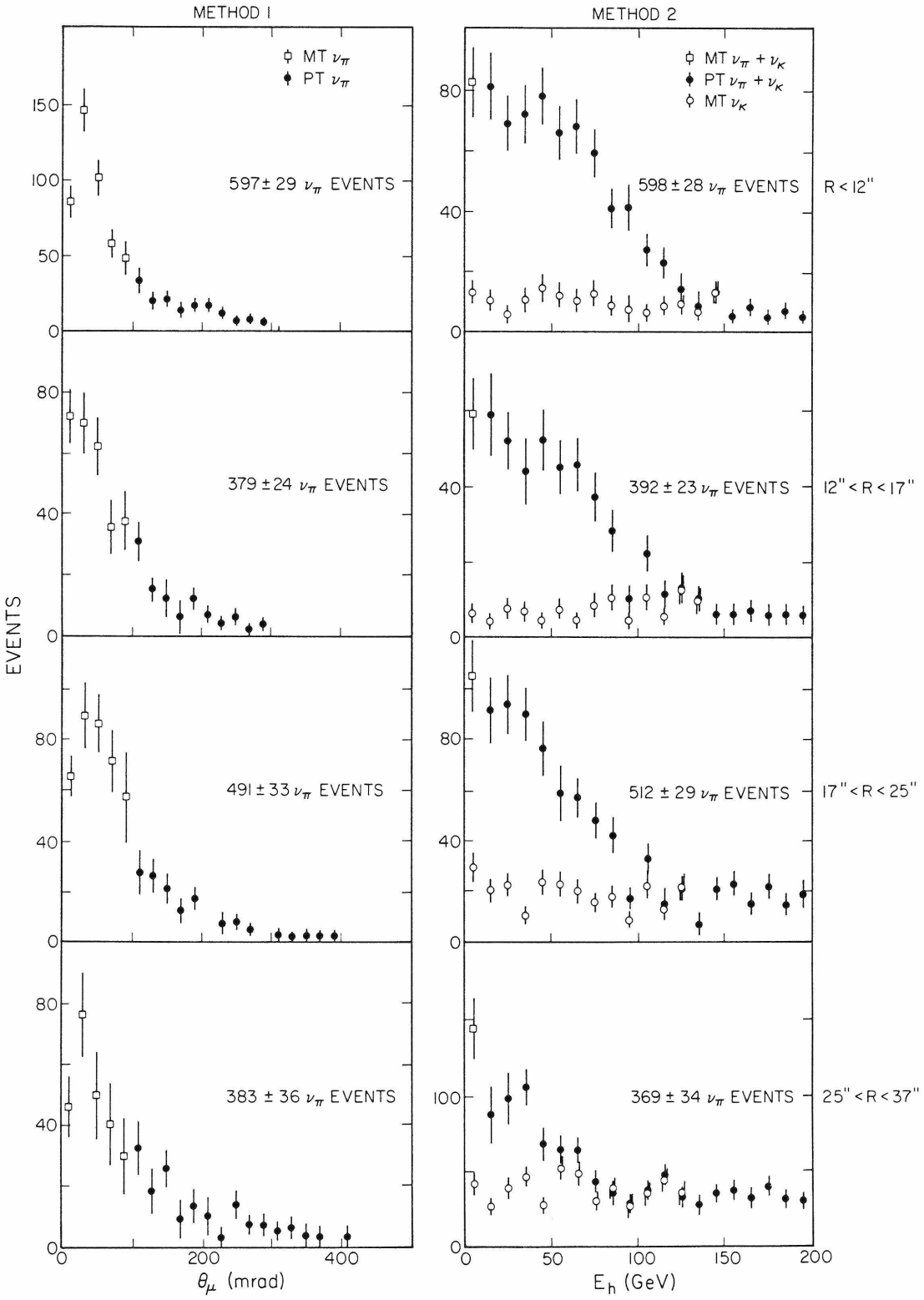

Figure 4-15: Number of ν_π interactions at 300 GEV beam setting.

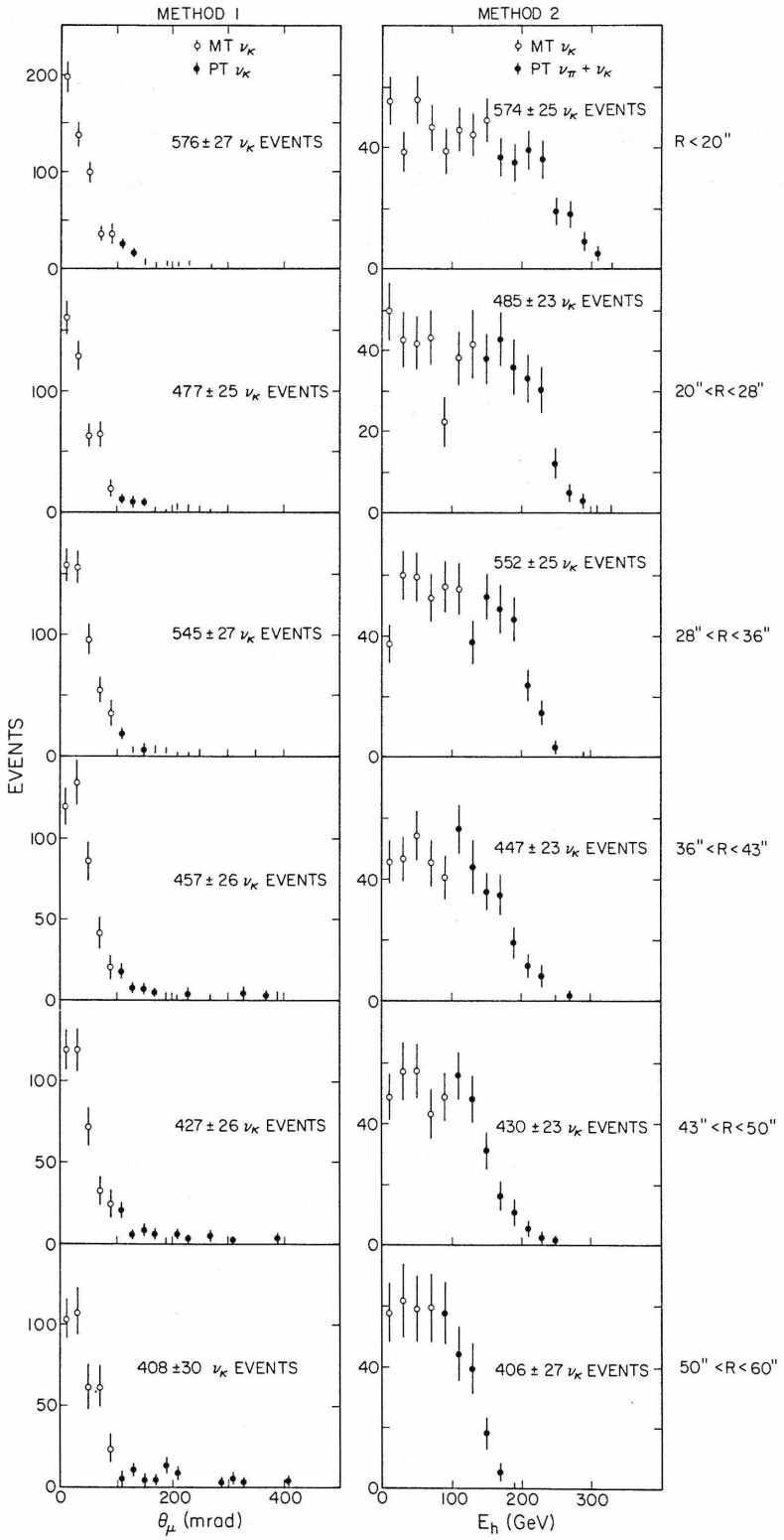

Figure 4-16: Number of ν_K interactions at 300 GEV beam setting.

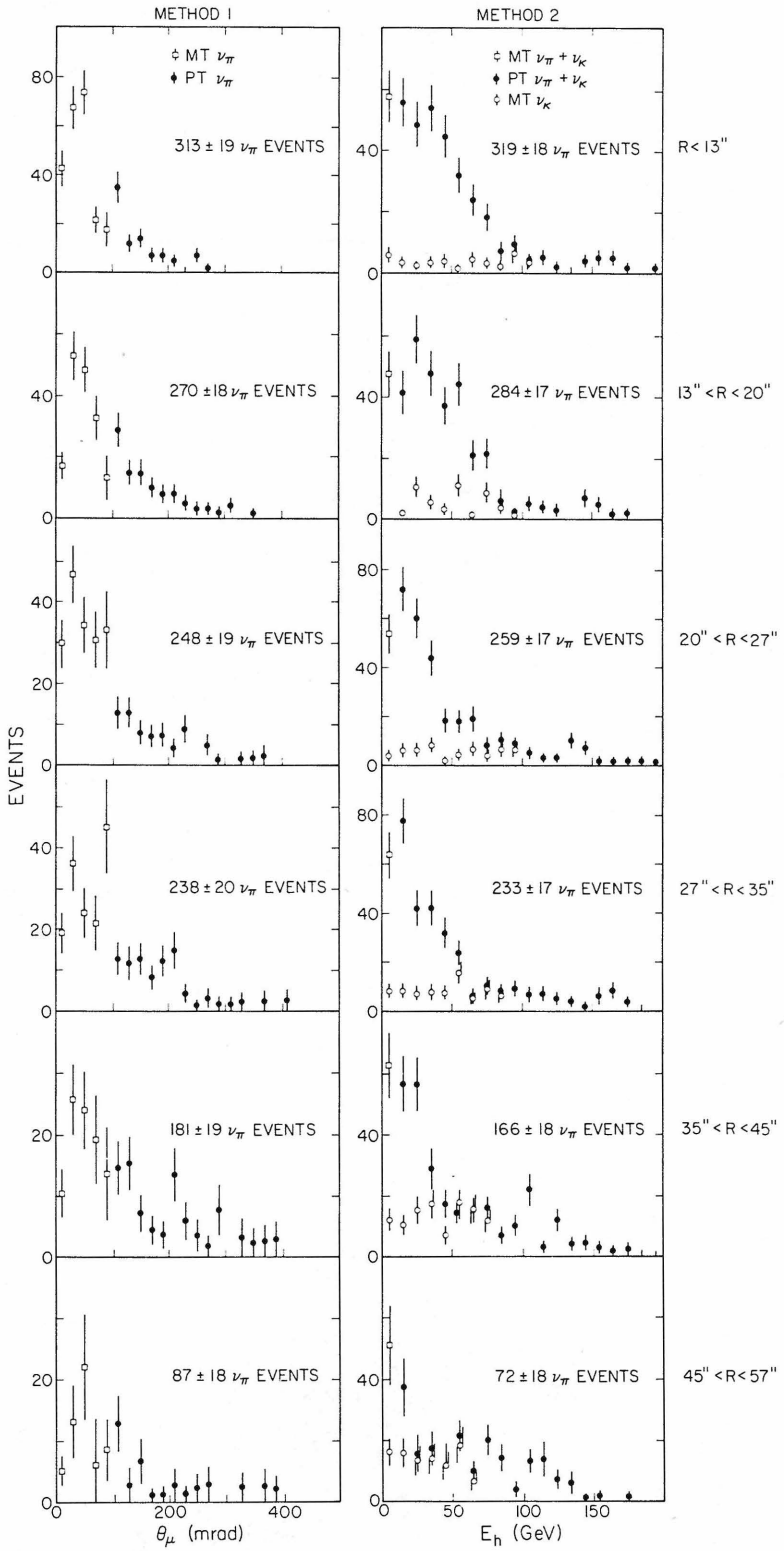

Figure 4-17: Number of ν_π interactions at 200 GEV beam setting.

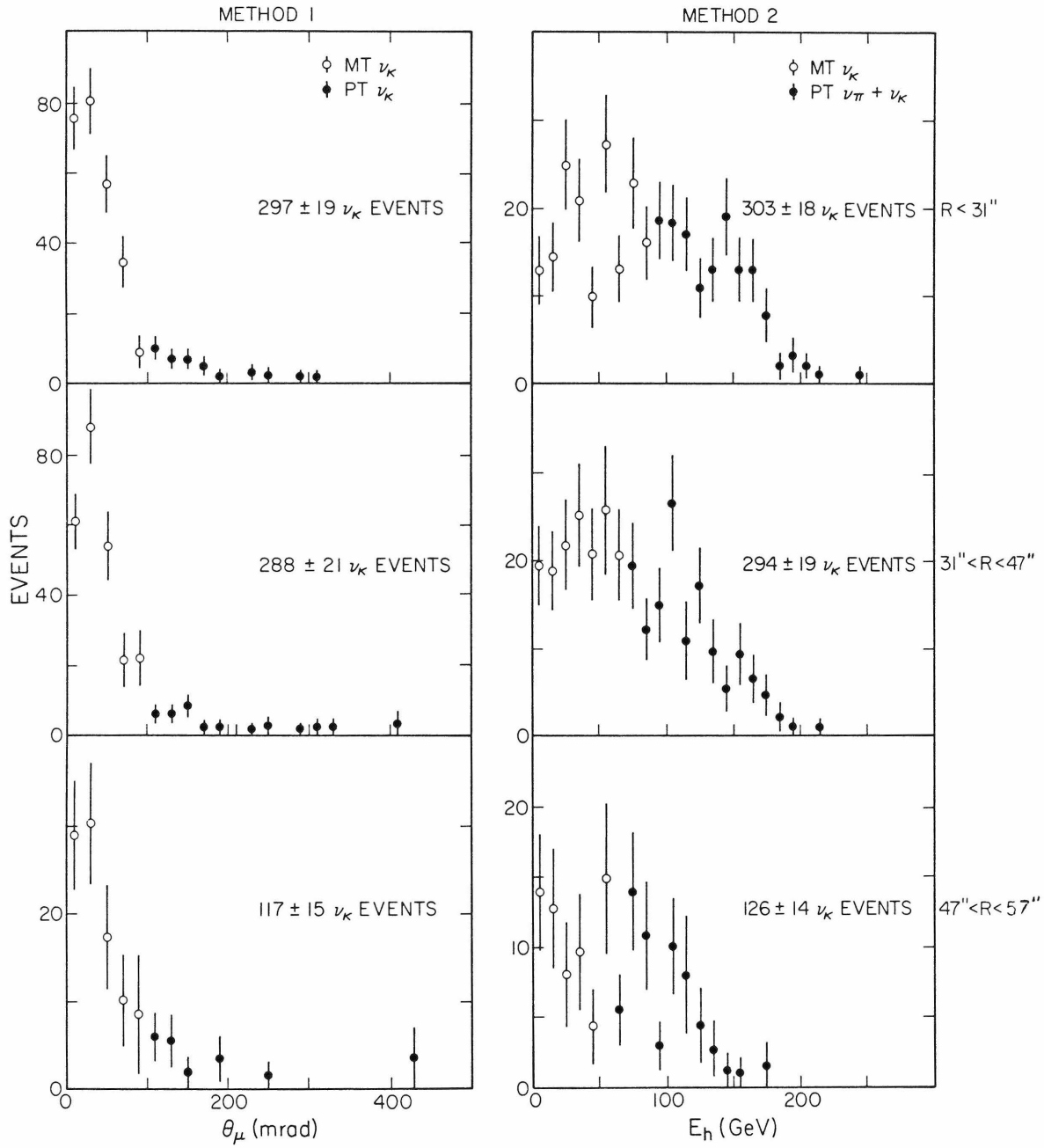

Figure 4-18: Number of ν_K interactions at 200 GEV beam setting.

for events with very large θ_μ or muon momentum less than 2.9 GEV. We must rely on a model of neutrino interactions to make this correction.

To make this correction we use the model of neutrino interactions in the beam monte carlo. Equation 2-25 is integrated over the region of missing acceptance to give the fraction δ of events that we miss. The number of events measured then is multiplied by a correction factor $f=1/(1-\delta)$. The angle cut and correction factor for each measurement is shown in table 4-1.

D: $K_{\mu 3}$ DECAYS

The decay mode $K^+ \rightarrow \mu^+ \nu \pi^0$ contributes to the neutrino flux at the detector. The energy spectrum for these neutrinos is a broad spectrum of much lower energy than neutrinos from $K^+ \rightarrow \mu^+ \nu$. Events from $K_{\mu 3}$ decay will contribute primarily to the pion neutrino signal.

To correct the pion neutrino cross sections for the flux from $K_{\mu 3}$ decays, we assume that the neutrino cross section rises linearly with energy. At any radius, the mean neutrino energy from $K_{\mu 3}$ decays is .50 times the neutrino energy from kaon two body decays. In any target

TABLE 4-1: CORRECTING FOR MISSING ACCEPTANCE

A. KAON NEUTRINOS

Beam Setting	Target Bin R1	R2	Mean E_ν (GEV)	Maximum θ_μ (mrad)	f
300 GEV	0	20	261	310	1.020
	20	28	246	397	1.015
	28	36	229	427	1.014
	36	43	214	454	1.015
	43	50	199	476	1.015
	50	60	182	494	1.016
200 GEV	0	31	180	310	1.029
	31	47	166	437	1.019
	47	57	154	487	1.019

B. PION NEUTRINOS

Beam Setting	Target Bin R1	R2	Mean E_ν (GEV)	Maximum θ_μ (mrad)	f
300 GEV	0	12	101	310	1.049
	12	17	86.3	364	1.043
	17	25	71.3	384	1.049
	25	37	52.7	416	1.053
200 GEV	0	13	73.5	310	1.069
	13	20	64.7	368	1.059
	20	27	55.1	397	1.063
	27	35	45.9	423	1.068
	35	45	36.5	451	1.077
	45	57	27.4	481	1.093

bin, the number of events from $K_{\mu 3}$ neutrinos will be be .50B times the number of events from $K_{\mu 2}$ neutrinos, where B=.05 is the $K_{\mu 3}$ branching ratio divided by the $K_{\mu 2}$ branching ratio.

The estimated fraction of $K_{\mu 3}$ events in the pion neutrino event sample for each target bin is given in table 4-2.

E: CALCULATING CROSS SECTIONS

For the fiducial target length used in this analysis, neutrino cross sections are given by

$$\sigma = \frac{N_{events}}{N_\nu (N_{nucleons}/Area)} \qquad (4\text{-}3a)$$

$$= \frac{N_{events}\,(3.13\times10^{-28}\,cm^2)}{N_\nu}. \qquad (4\text{-}3b)$$

The raw number of events is corrected to account for missing acceptance and events from $K_{\mu 3}$ decay neutrinos.

4.8 TARGET CALIBRATION CHECKS

To extract total cross sections from these data, the

TABLE 4-2: CORRECTION FOR $K_{\mu 3}$ DECAY

Beam Setting	Target Bin R1	R2	Mean E_ν(GEV)	Fraction of events in ν_π event sample from $K_{\mu 3}$ decays
300 GEV	0	12	101	1.0%
	12	17	86.3	1.6%
	17	25	71.3	2.6%
	25	37	52.7	7.7%
200 GEV	0	13	73.5	0.5%
	13	20	64.7	0.9%
	20	27	55.1	1.2%
	27	35	45.9	1.8%
	35	45	36.5	3.5%
	45	57	27.4	5.8%

energy calibration of the target only must be good enough to separate pion neutrino events from kaon neutrino events. The clean separation shown in figures 4-7 through 4-12 indicates that the calibration is sufficient for this purpose everywhere in the target.

The energy calibration must be known much more accurately to measure x and y distributions. The target calorimeter was calibrated directly in a hadron beam of known energy, but the calibration was done only at the center of the target. Away from the center we have to rely on maps of the counters made with muons. Also, near the edge of the apparatus a significant fraction of the hadron showers saturate the electronics for at least one counter. The muon momentum calibration relies on magnetic field calculations and on measurements of the magnetic field made in the magnet gaps. To check both the hadron energy calibration and the muon momentum calibration, we use the beam monte carlo program to generate energy distributions for neutrinos interacting in the target.

A: TOTAL ENERGY CALIBRATION

The total energy of a neutrino event is measured for events satisfying the muon trigger. We make total energy

distributions with the monte carlo for each target bin we use to obtain a total cross section, and we compare these distributions with the data in each bin. Cuts of $\theta_\mu < 100$ mrad and $p_\mu > 10$ GEV are placed on both the monte carlo distributions and the data.

The mean energy of the measured distribution divided by the mean energy of the monte carlo distribution is plotted in figure 4-19 for each bin. The average ratio for all bins with mean radius less than 43" from the center is $.979 \pm .004$.

The discrepancies between data and monte carlo distributions near the edge of the target correspond to known problems with the calorimeter. The probability that an event at a given radius will saturate at least one counter is shown in figure 4-20(a) for all the events in this experiment. The probability of saturation as a function of energy is shown in figure 4-20(b) for three radial bins. Counter saturation at low energy is more serious than at high energy, because a low energy shower penetrates fewer counters and the saturated counter samples a larger fraction of the energy. Also, the muon map varies more rapidly with position and is less well understood at large radii than near the center of the target.

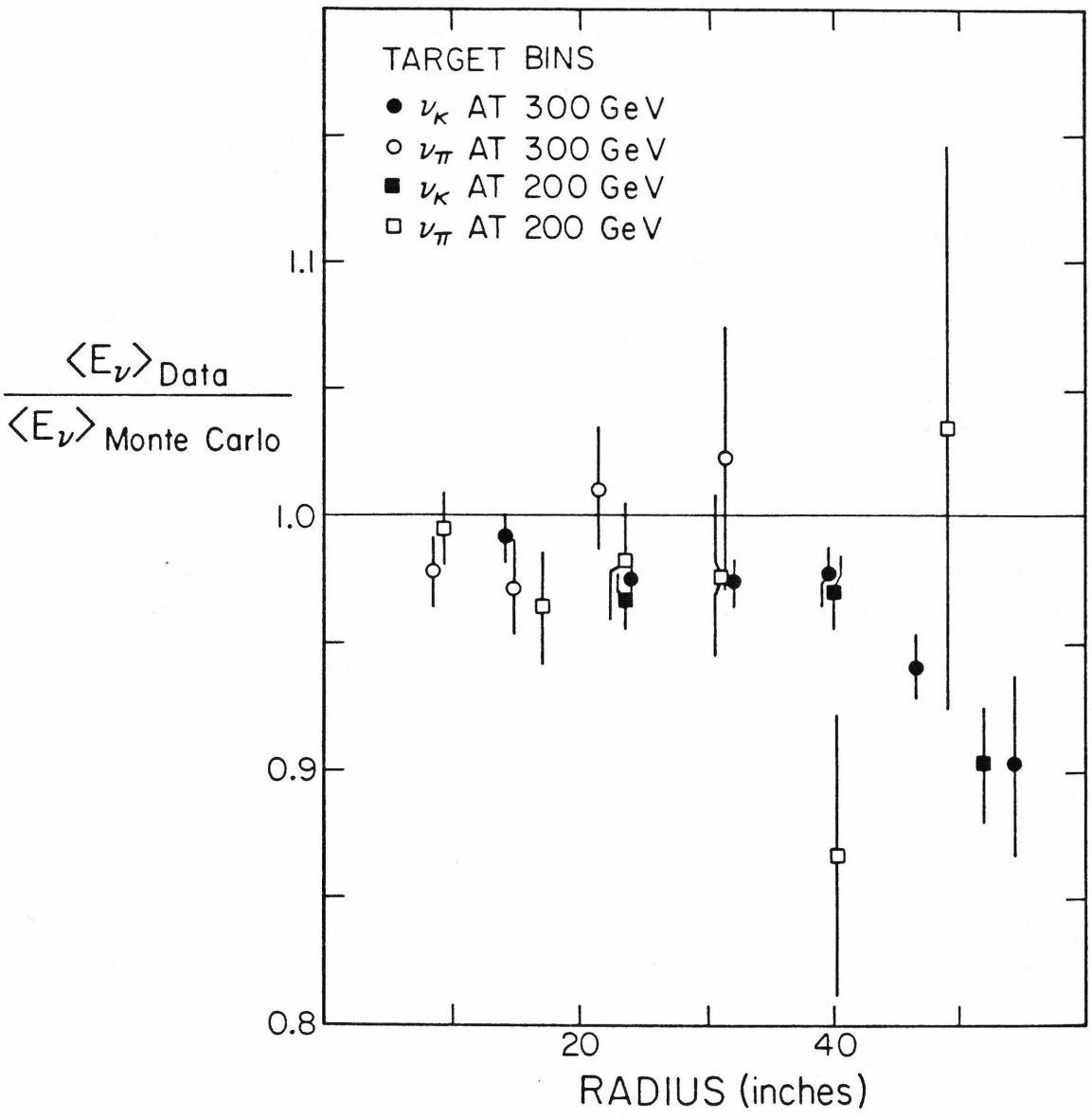

Figure 4-19: $\langle E_\nu \rangle_{data} / \langle E_\nu \rangle_{MC}$ **in each target bin.**

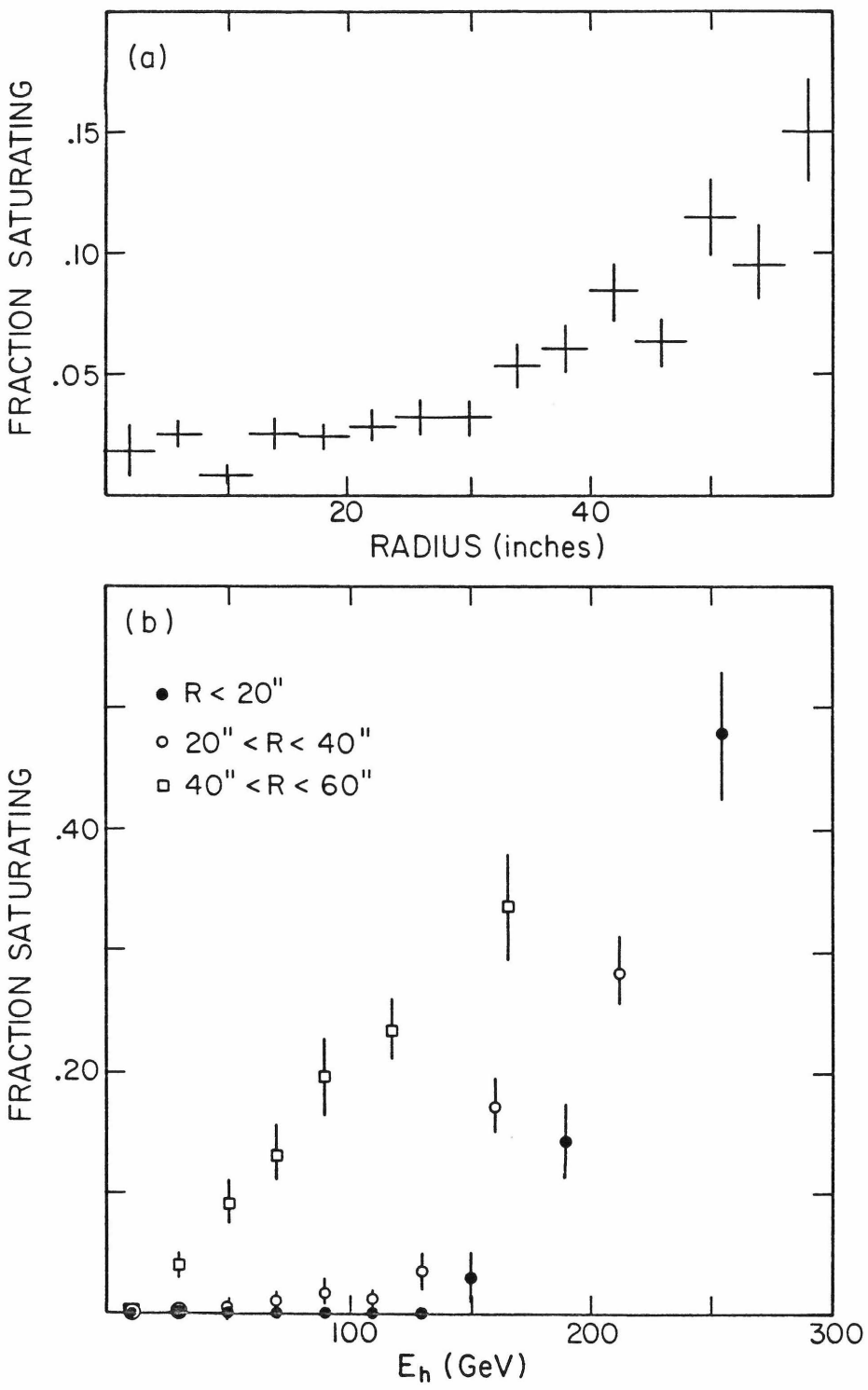

Figure 4-20: Fraction of events with one or more counters saturating
(a) versus radius
(b) versus E_h in three radial bins

To avoid problems with the hadron energy calibration near the edge of the target, we make a fiducial cut 43" from the center when extracting x and y distributions and mean elasticity.

B: CONSISTENCY OF HADRON AND MUON ENERGY CALIBRATIONS

To investigate the 2% discrepancy between data and monte carlo near the center of the target, we separate all events with radius less than 43" into bins of different y and compare the measured total energy with the monte carlo. This was done separately for pion neutrinos and kaon neutrinos at both energy settings. The ratios of E_ν^{data} to E_ν^{MC} in each y bin are averaged, and the result is shown in figure 4-21(a). The variable y is defined experimentally by

$$y = \frac{E_h}{E_h + E_\mu} . \qquad (4-4)$$

At y near 0, $E_\nu \sim E_\mu$, and at y near 1, $E_\nu \sim E_h$. Therefore, the y=0 intercept of the curve in figure 4-21(a) tests the muon momentum calibration, and the y=1 intercept tests the hadron energy calibration. The muon momentum calibration and the hadron energy calibration are

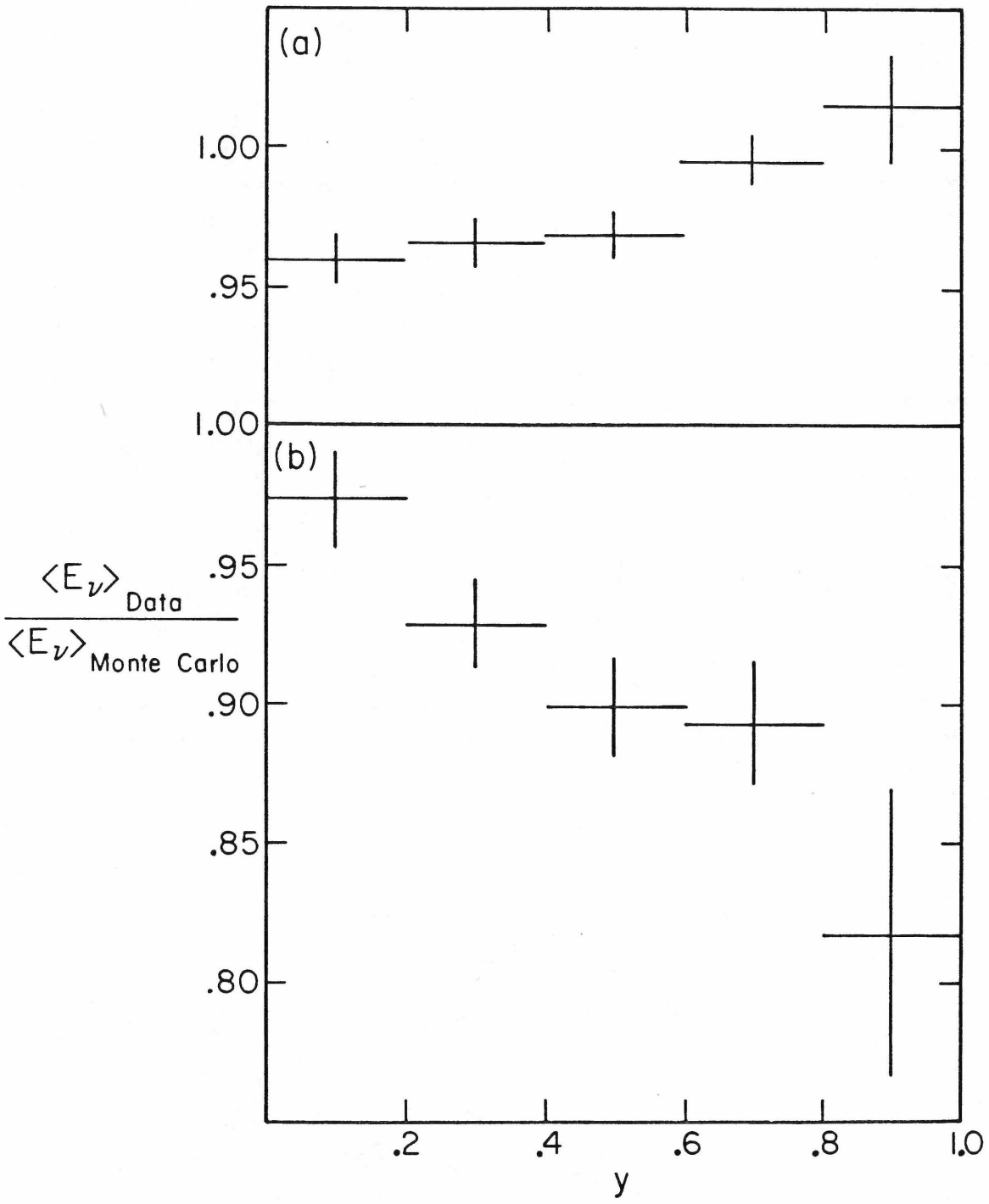

Figure 4-21: $\langle E_\nu \rangle_{data} / \langle E_\nu \rangle_{MC}$ versus y
(a) all data with R<43"
(b) ν_K data with R>43"

inconsistent by about 4%. The same comparision for kaon neutrino events near the edge of the target is shown in figure 4-21(b), which verifies that the hadron energy calibration is incorrect at large radii.

At small y, the muon momentum for each event can be predicted from the mean neutrino energy E_ν^{MC} generated by the monte carlo and from the measured hadron energy E_h,

$$E_\mu^{predicted} = E_\nu^{MC} - E_h. \qquad (4\text{-}5)$$

The measured muon momentum was compared with the predicted muon momentum for events with y<.2 and radius less than 43". The average ratio of E_μ to $E_\mu^{predicted}$ was .96±.01, which is equivalent to the first bin in figure 4-21(a). This comparison then was made in bins of different E_μ. The ratio was found to be independent of E_μ to within 3%. The radius of the muon at T2 also was used to bin the events, and the ratio was independent of position in the magnet to within 3%.

When extracting x and y distributions, we make an overall correction to the momentum calibration of 4%. We make no adjustment to the hadron energy.

CHAPTER 5

RESULTS

5.1 TOTAL CROSS SECTIONS

The neutrino charged current total cross sections obtained from all of the E356 data are shown in figures 5-1 and 5-2 and tables 5-1 and 5-2. The cross sections are presented in two ways. Figure 5-1 shows σ/E_ν versus the average energy of the incident neutrinos in each radial target bin. The errors shown are statistical errors only. The systematic uncertainties are not shown in this plot because they are highly correlated from bin to bin. In figure 5-2 the events from the entire target are summed together to obtain an average cross section for pion neutrinos and kaon neutrinos at each beam setting. Using the entire target as one bin minimizes the systematic uncertainties in the neutrino flux. Here the inner error bars are statistical and the outer error bars combine the statistical and all systematic uncertainties except the uncertainty in the ion chamber calibration. Presented in this manner, the systematic uncertainties are almost

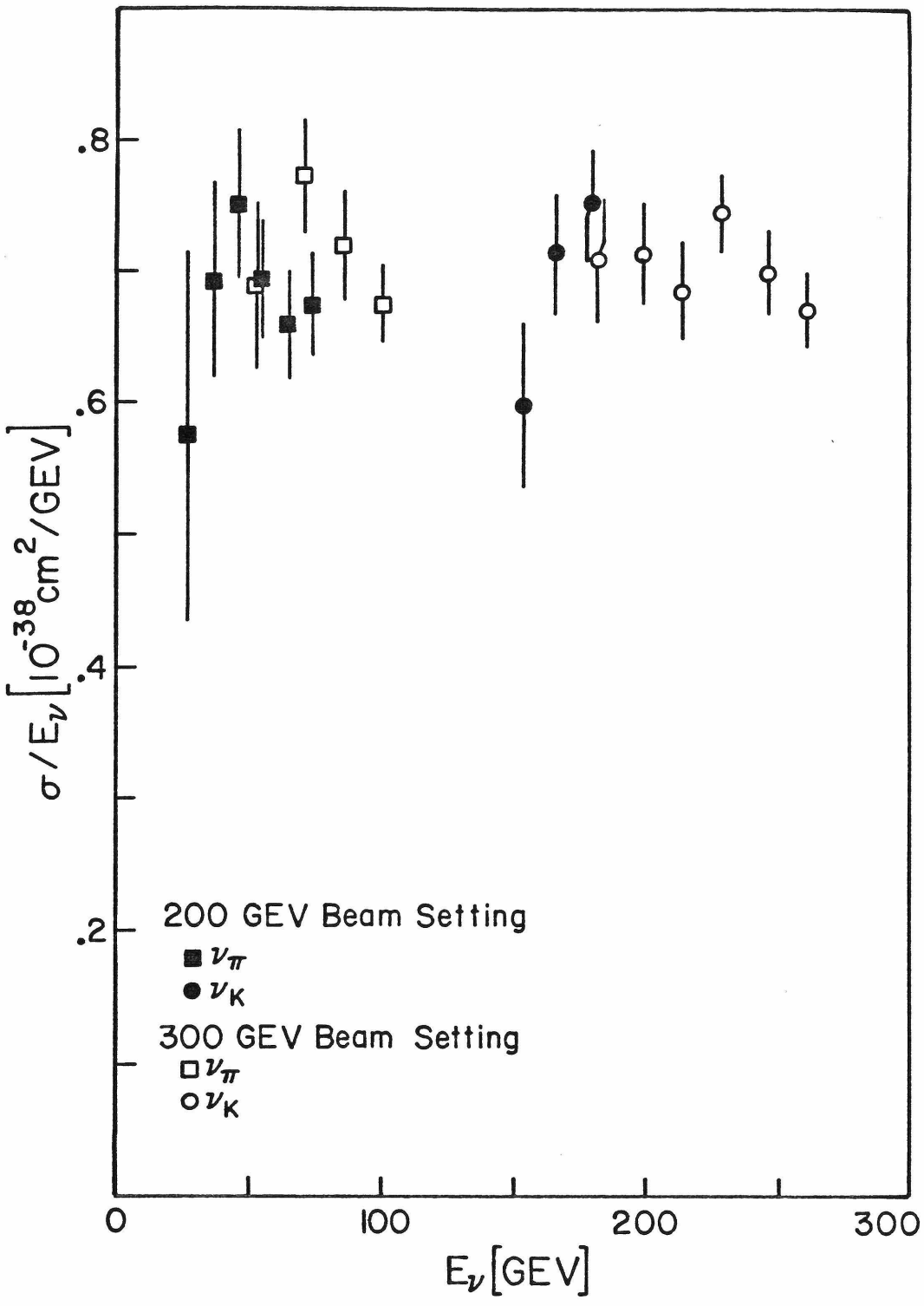

Figure 5-1: Total cross section per nucleon for $\nu N \to \mu^- X$. Error bars are statistical uncertainties only.

TABLE 5-1: TOTAL CROSS SECTIONS - FINE BINNING

A. KAON NEUTRINOS

Beam Setting	Mean E_ν (GEV)	σ/E_ν (10^{-38} cm^2/GEV)
300	261	.671±.029
	246	.699±.033
	229	.744±.033
	214	.685±.036
	199	.713±.039
	182	.709±.048
200	180	.752±.044
	166	.714±.047
	154	.598±.064

B. PION NEUTRINOS

Beam Setting	Mean E_ν (GEV)	σ/E_ν (10^{-38} cm^2/GEV)
300	101	.675±.031
	86	.719±.042
	71	.772±.044
	53	.690±.063
200	74	.675±.039
	65	.659±.040
	55	.694±.045
	46	.751±.056
	37	.693±.074
	27	.577±.141

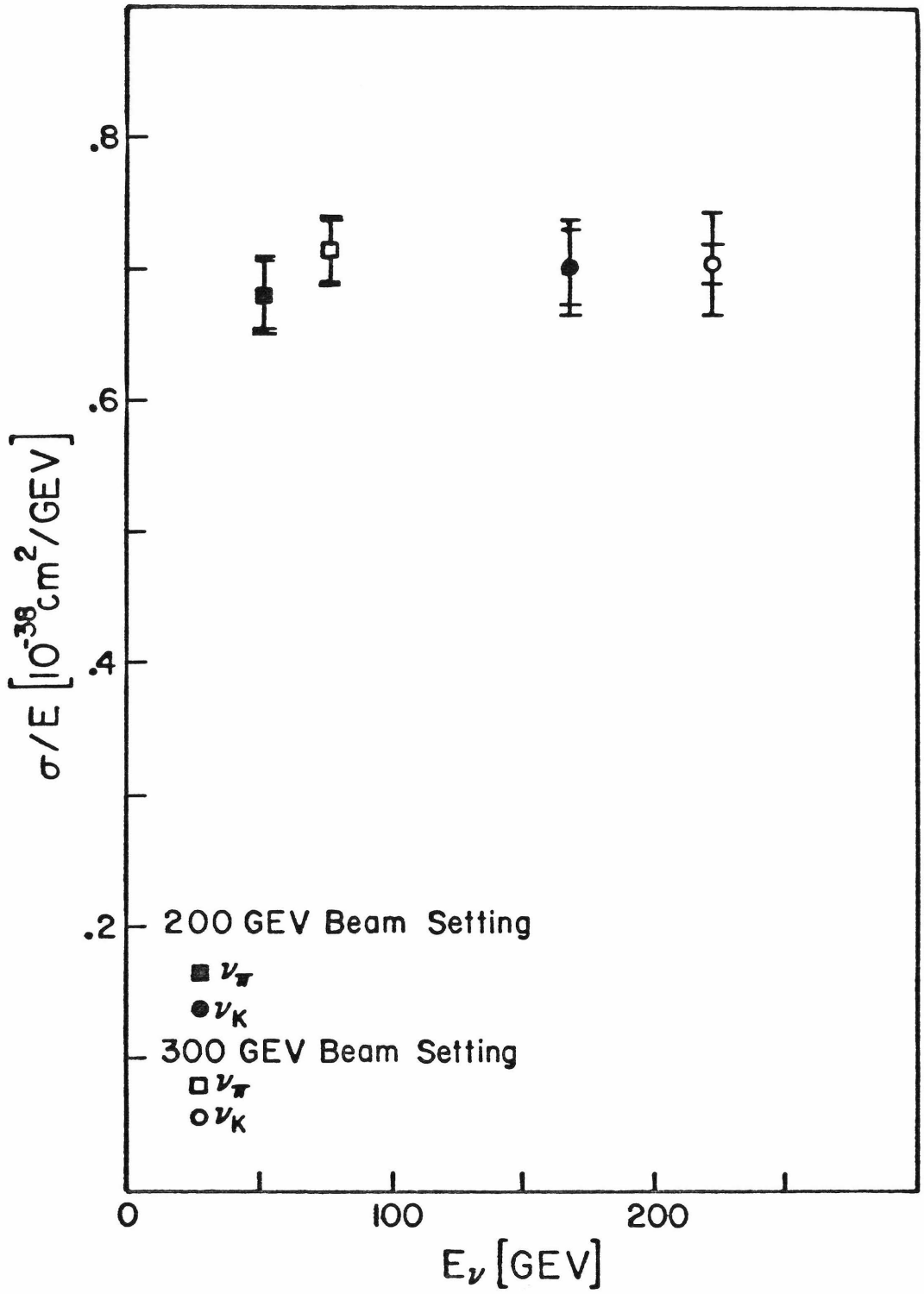

Figure 5-2: Total cross section per nucleon for $\nu N \to \mu^- X$. There is an additional 5% scale uncertainty.

TABLE 5-2: TOTAL CROSS SECTIONS - COARSE BINNING

Beam Setting	Mean E_ν (GEV)	σ/E_ν (10^{-38} cm^2/GEV)
300 GEV	222	.704±.015±.039
200 GEV	168	.702±.029±.036
300 GEV	77	.714±.024±.026
200 GEV	52	.680±.027±.029

independent from point to point. The ion chamber calibration introduces an additional 5% uncertainty common to all points.

5.2 MEAN ELASTICITY

We measure the mean elasticity of neutrino interactions by measuring the mean hadron energy separately for kaon neutrino events and pion neutrino events at each beam setting. The mean inelasticity is defined experimentally by

$$\langle y \rangle = \frac{\langle E_h \rangle}{\langle E_\nu \rangle}. \qquad (5\text{-}1)$$

$\langle E_h \rangle$ is the mean of the hadron energy distribution used to extract the total cross section. $\langle E_\nu \rangle$ is the mean energy of neutrino interactions and is calculated by the beam monte carlo. The results are shown in figure 5-3 and table 5-3. A correction is made to account for missed events at high y and large θ_μ. The size of the correction ranges from 2% at the highest energy to 8% at the lowest energy.

The inner error bars are statistical uncertainties only. The outer error bars combine statistical uncertainties with uncertainties in the beam energy and the

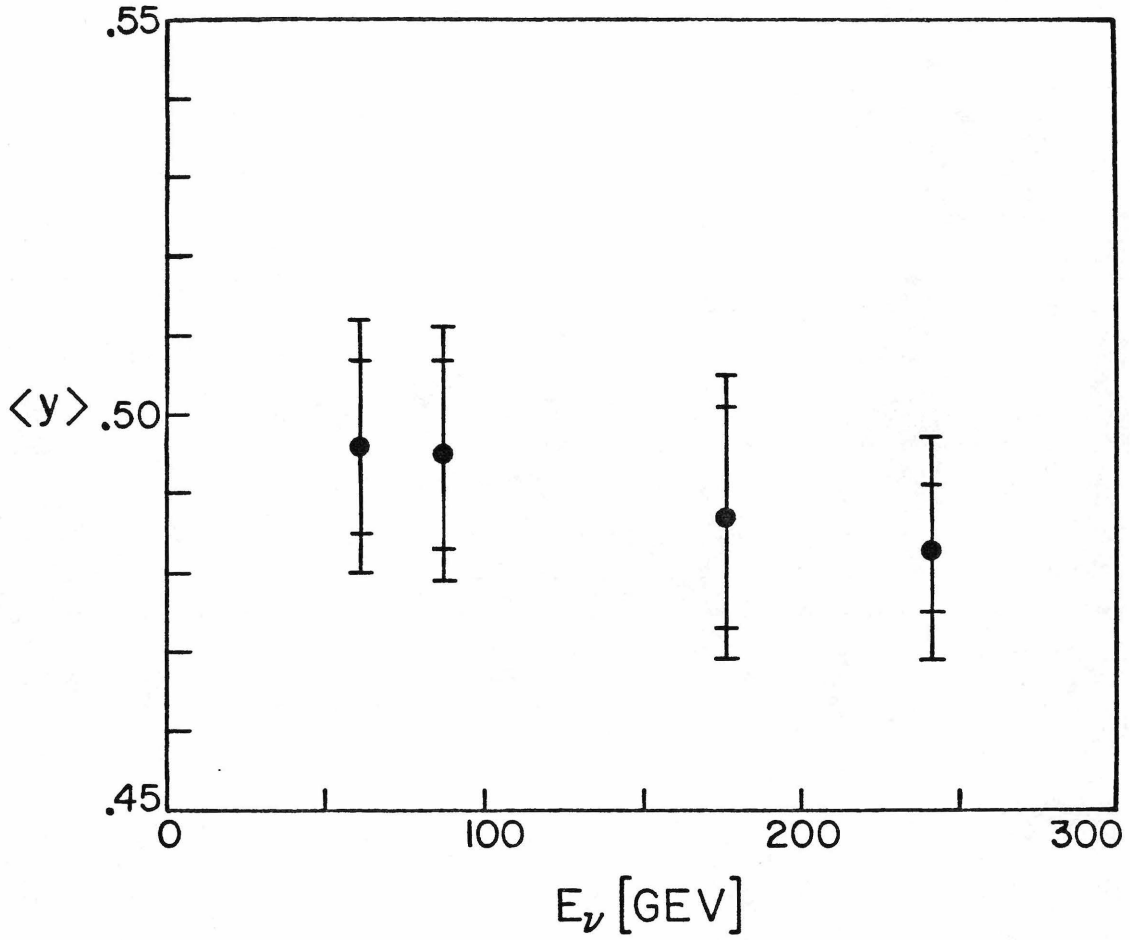

Figure 5-3: Mean y for $\nu N \to \mu^- X$.

TABLE 5-3: MEAN INELASTICITY

Mean E_ν (GEV)	<y>
241	.483±.008±.014
176	.487±.014±.018
87	.495±.012±.016
61	.496±.011±.016

hadron energy calibration. The average of the four points is .489±.005±.012.

5.3 CROSS SECTIONS AT SMALL y

The muon trigger has complete kinematic acceptance for events with y<.2 and E_ν>40 GEV. Even at E_ν=20 GEV, the acceptance is complete for x<.5. We use muon trigger events to measure $d\sigma/dy$ for y<.2 for pion neutrinos and kaon neutrinos at both energy settings. We determine y experimentally for these events by using the measured hadron energy and muon energy,

$$y = \frac{E_h}{E_h + E_\mu} . \qquad (5\text{-}2)$$

The results are shown in figure 5-4 and table 5-4. The inner error bars show the statistical uncertainties, and the outer error bars show the combined statistical and systematic uncertainties. There is an additional 5% calibration uncertainty common to all points.

5.4 KAON NEUTRINO y DISTRIBUTION

At neutrino energies above 150 GEV, the muon trigger and penetration trigger together have complete kinematic

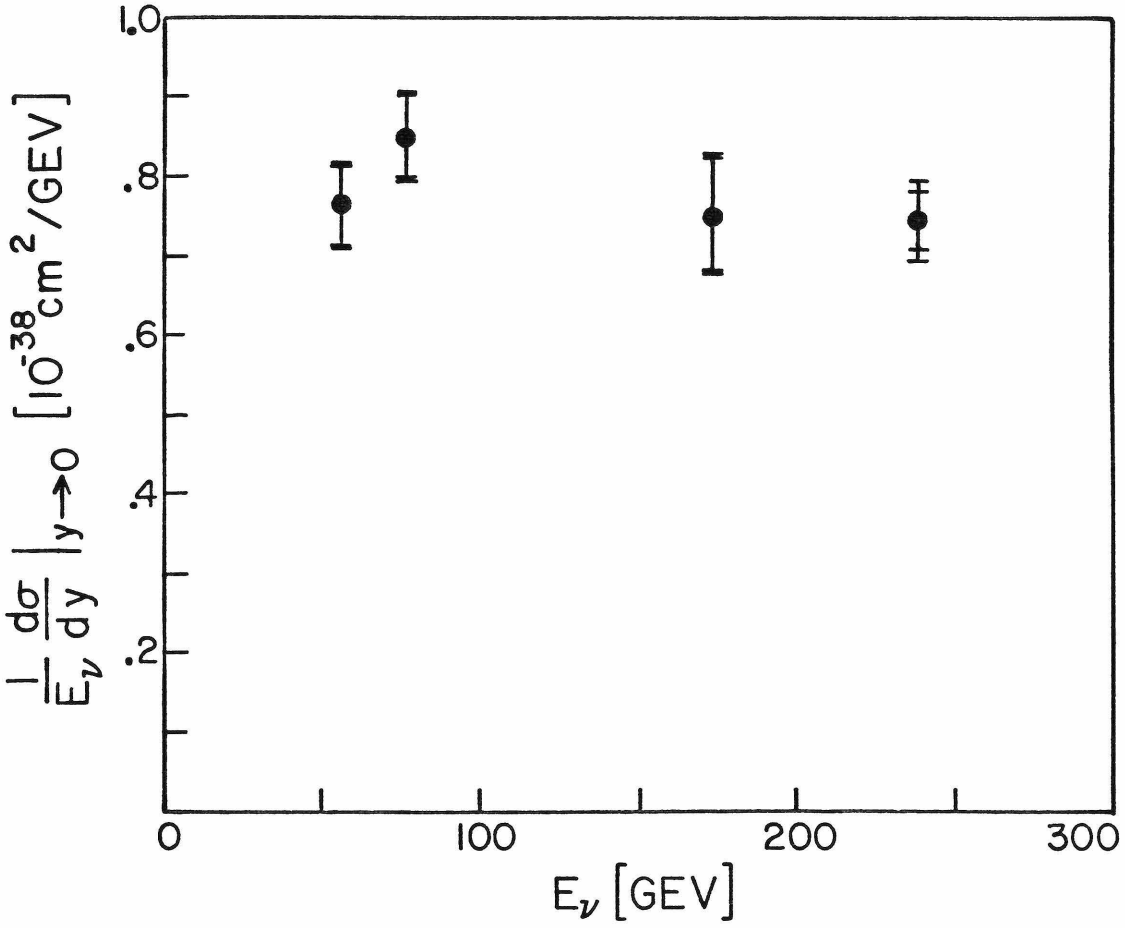

Figure 5-4: Cross section at small y for $\nu N \to \mu^- X$. There is an additional 5% scale uncertainty.

TABLE 5-4: CROSS SECTIONS FOR y<.2

Mean E_ν (GEV)	$\frac{1}{E_\nu}\frac{d\sigma}{dy}$, y<.2 (10^{-38} cm^2/GEV)
238	.745±.036±.052
174	.751±.073±.077
77	.851±.055±.056
56	.767±.051±.052

acceptance for events with y<.88. The muon momentum is not measured for penetration triggers, so we rely on our knowledge of the incident neutrino spectrum to measure y. At a given position in the target, the uncertainty in E_ν for a kaon neutrino event is ±10%. We determine y experimentally by

$$y = \frac{E_h}{\langle E_\nu \rangle}, \qquad (5\text{-}3)$$

where E_h is the measured hadron energy and $\langle E_\nu \rangle$ is the mean energy of neutrino events computed by the beam monte carlo at the radius of the event. The data taken at 200 GEV and 300 GEV are combined to produce a y distribution for kaon neutrinos.

The results are shown in figure 5-5 and table 5-5. The mean incident neutrino energy for this distribution is 226 GEV. The last bin includes events for which the measured y is greater than 1. The smearing of the distribution caused by experimental resolutions must be taken into account since $\sigma_y \propto \sqrt{y}$. This will distort a flat distribution into one that is greater at low y than at high y. We include this effect by generating monte carlo events with a "true" y distribution, smearing the experimentally measured parameters for each event, and then calculating a

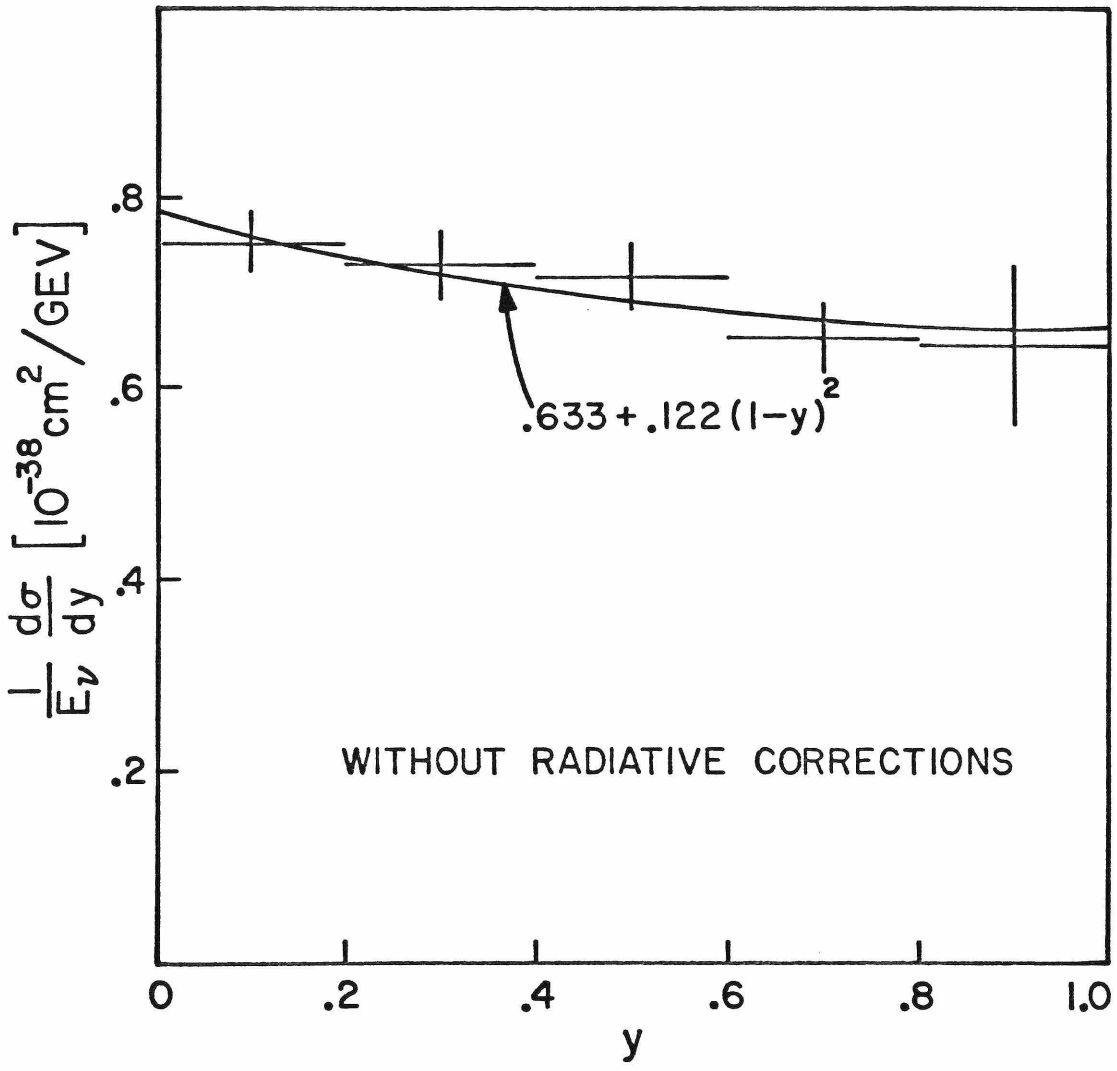

Figure 5-5: y distribution for $\nu N \to \mu^- X$. Mean E_ν=226 GEV. There is an additional 7% scale uncertainty.

TABLE 5-5: KAON NEUTRINO y DISTRIBUTION

NO RADIATIVE CORRECTIONS

Mean E_ν = 226 GEV

y	$\frac{1}{E_\nu}\frac{d\sigma}{dy}$ (10^{-38} cm^2/GEV)
0-.2	.754±.033
.2-.4	.731±.036
.4-.6	.718±.036
.6-.8	.655±.037
.8-1.0	.647±.081

"smeared" y distribution. In each y bin, the number of "true" events divided by the number of "smeared" events determines the correction to be applied to the data. This correction is less than 2% in each bin for y<.8. A 4% correction is made to the last bin. In addition, a correction is made for events with θ_μ>310 mrad in the same way the correction is made to the total cross sections. The missed events are only 2.4% of the total cross section, but all of the missed events have y>.8, so the correction increases the signal in the last bin by 15%. There is an overall scale uncertainty of 7% for this distribution.

Radiative corrections have not been made to the y distribution presented here. This will be done in section 6.2B so that the fraction of antiquarks in the nucleon can be extracted from this distribution.

5.5 A TEST OF SCALING: x DISTRIBUTIONS FOR .1<y<.4

To obtain x distributions we can use only muon trigger events. To insure nearly complete acceptance and good resolution in x, we limit the range in y to .1<y<.4. We determine x experimentally by

$$x = \frac{E_\nu E_\mu \theta_\mu^2}{2M_N E_h}, \qquad (5\text{-}4)$$

where E_μ, E_h, E_ν, and θ_μ are measured values and the nucleon mass M_N=.94 GEV. Data taken at both 200 GEV and 300 GEV are combined to get x distributions separately for kaon neutrinos and pion neutrinos. The mean incident pion neutrino energy is 67 GEV, and the mean incident kaon neutrino energy is 226 GEV. We correct for smearing caused by experimental resolutions with our monte carlo in the manner described in the previous section. The correction becomes very large for x>.75, so we do not present data in this region. The corrections are less than 20% elsewhere. Because we have restricted the range in y, the correction is nearly independent of neutrino energy. The results are shown in figure 5-6 and table 5-6. The kaon neutrino distribution clearly peaks at smaller x than the pion neutrino distribution.

It is interesting to examine the effect of changing the scaling variable. Suppose we define the variable x' by

$$x' = \frac{x}{1 + (M_N^2 / Q^2)}. \qquad (5\text{-}5)$$

The x' distribution is indistinguishable from the x distribution for kaon neutrinos, but there is a striking change for pion neutrinos. The results are shown in figure 5-7 and table 5-7. The relative scale uncertainty between

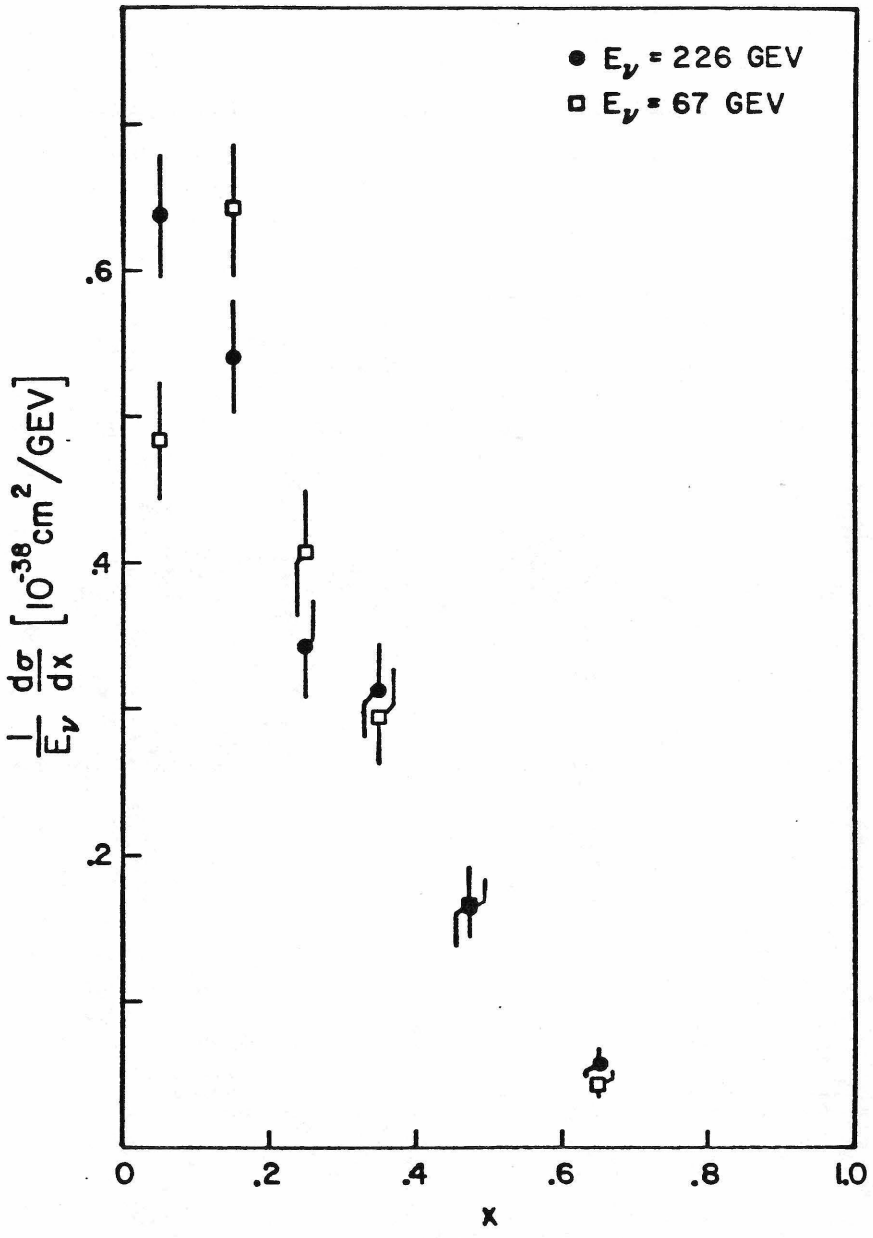

Figure 5-6: x distribution for $\nu N \to \mu^- X$ in the region $.1 < y < .4$.

TABLE 5-6: x DISTRIBUTIONS FOR .1<y<.4

x	E_ν=226 GEV $\frac{1}{E_\nu}\frac{d\sigma}{dx}$	E_ν=67 GEV $\frac{1}{E_\nu}\frac{d\sigma}{dx}$
0-.1	.638±.042	.484±.041
.1-.2	.541±.039	.642±.045
.2-.3	.342±.034	.408±.043
.3-.4	.313±.032	.295±.033
.4-.55	.164±.020	.166±.027
.55-.75	.058±.009	.044±.009

Cross sections are in units of 10^{-38} cm^2/GEV.

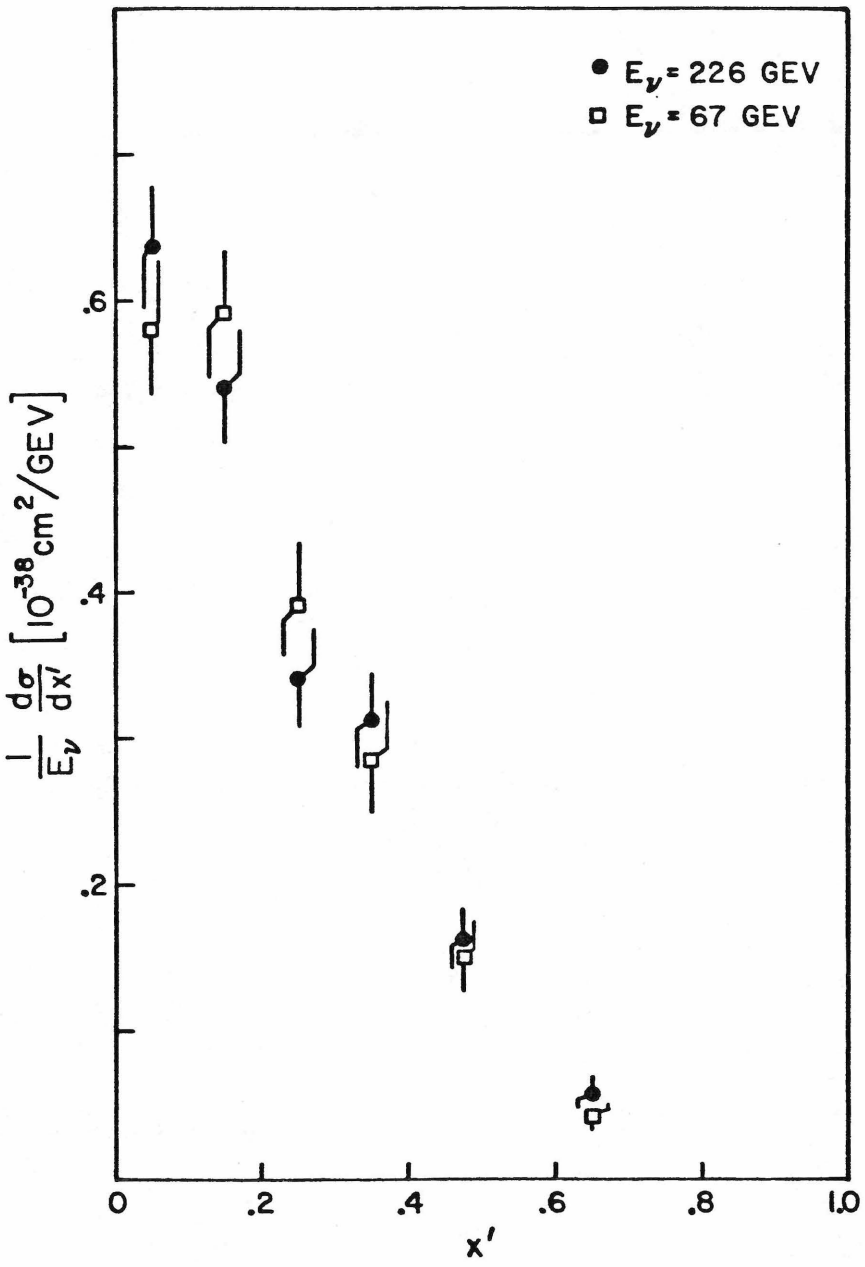

Figure 5-7: x' distribution for $\nu N \to \mu^- X$ in the region .1<y<.4, where $x' = x/(1+M_N^2/Q^2)$.

TABLE 5-7: x' DISTRIBUTION FOR .1<y<.4

x'	E_ν=226 GEV $\frac{1}{E_\nu}\frac{d\sigma}{dx'}$	E_ν=67 GEV $\frac{1}{E_\nu}\frac{d\sigma}{dx'}$
0-.1	.637±.042	.581±.047
.1-.2	.541±.039	.592±.044
.2-.3	.342±.034	.392±.044
.3-.4	.313±.032	.287±.037
.4-.55	.164±.020	.152±.023
.55-.75	.058±.009	.043±.009

Cross sections are in units of 10^{-38} cm^2/GEV.

the kaon neutrino distributions and the pion neutrino distributions is 5%. There is an additional 5% scale uncertainty common to both.

CHAPTER 6

DISCUSSION AND CONCLUSIONS

6.1 THEORETICAL PERSPECTIVE

A. MOTIVATION

The study of high energy νN interactions addresses two general physical questions.

1. What is the behavior of the weak interactions?
2. What is the structure of the nucleon?

Neutrinos are chargeless, massless (or nearly so), and interact only via the weak force. At low energies, charged current weak interactions can be described by the phenomenological Lagrangian[21]

$$\mathcal{L}_{eff} = \frac{G}{\sqrt{2}} J^{\dagger} \cdot J, \qquad (6\text{-}1)$$

where $J = J^{lepton} + J^{hadron}$ and Fermi's constant

$G = (1.023 \pm .001 \times 10^{-5})/M_p^2$. The lepton current is given by

$$J_\alpha^{\text{lepton}} = \bar{\psi}^l \gamma_\alpha (1-\gamma_5) \psi^{l'} \qquad (6\text{-}2)$$

where $l = e, \mu, \tau, \ldots,$ and $l' = \nu_e, \nu_\mu, \nu_\tau, \ldots$. Equation 6-1 represents a point interaction that cannot be correct at high energies. For instance, equation 6-1 predicts cross sections that rise linearly with energy and eventually violate the unitarity limit. This and other problems are solved in the Weinberg-Salam[22,23] model by introducing heavy W bosons to mediate the weak interaction. The WS model has had many successes, such as the observation of neutral current neutrino interactions[1,9] and parity violation in polarized electron scattering[24]. All experimental evidence to date is consistent with the WS model with a $\gamma - Z_0$ mixing angle of $\sin^2\theta_W = .23$. To first order, an intermediate vector boson modifies equation 6-1 by requiring the substitution[21]

$$G \rightarrow \frac{G}{1+Q^2/M_W^2}, \qquad (6\text{-}3)$$

which damps linearly rising νN cross sections at energies of $E_\nu \sim M_W^2/2M_N$. The WS model predicts M_W in terms of $\sin\theta_W$,

$$M_W = \sqrt{\frac{\pi\alpha}{G\sqrt{2}}} \frac{1}{\sin\theta_W} \simeq 78 \text{ GEV.} \qquad (6\text{-}4)$$

The existence of the intermediate bosons has not yet been verified.

If the lepton vertex in νN scattering is well understood, then neutrinos can be used to probe the structure of the nucleon. Over the last two decades there has emerged a picture of hadrons being made up of point-like, fractionally charged spin 1/2 objects. This picture, though still incomplete, encorporates the quarks of Gell-Mann[25] and Zweig[26], the partons of Feynman[27], and the idea of scaling introduced by Bjorken[28]. These general concepts have been supported by a large number of electron, muon, and neutrino scattering experiments. More recently, a candidate field theory has been developed, quantum chromodynamics (QCD). In this theory the quarks have a color quantum number and are held together by spin 1 gluons. QCD predicts small violations of scaling that vary with $\ln Q^2$. Three jet events in e^+e^- annihilations have been reported as evidence of gluon bremsstrahlung[29], and scaling violations have been seen in a number of νN [15,30], μN [31,32], and eN [33,34] experiments, but we are still far from having a definitive test of QCD.

B. QUARK-PARTON MODEL

In this model the constituents of nucleons that have weak and electromagnetic interactions are assumed to be spin 1/2, left handed quarks with third integral charges. Each nucleon has 3 valence quarks plus a sea of quark-antiquark pairs. The valence quarks for the proton are (uud), and for the neutron are (udd). The weak interactions of quarks are assumed to be identical to lepton weak interactions.

Deep inelastic lepton-nucleon scattering is pictured as the incoherent sum of point-like scatters from individual quarks (see figure 6-1(a)). The struck quark initially carries the fraction x of the total momentum P_i of the nucleon. In the Lorentz frame where the momentum has only spacelike components (see figure 6-1(b)),

$$\frac{-q^2}{2P_i \cdot q} = \frac{(2x\vec{P}_i)^2}{2(\vec{P}_i \cdot 2x\vec{P}_i)} . \qquad (6\text{-}5a)$$

$$= x. \qquad (6\text{-}5b)$$

Evaluating the Lorentz invariant $P_i \cdot q$ in the Lab frame,

$$x = \frac{-q^2}{2ME_h} , \qquad (6\text{-}6)$$

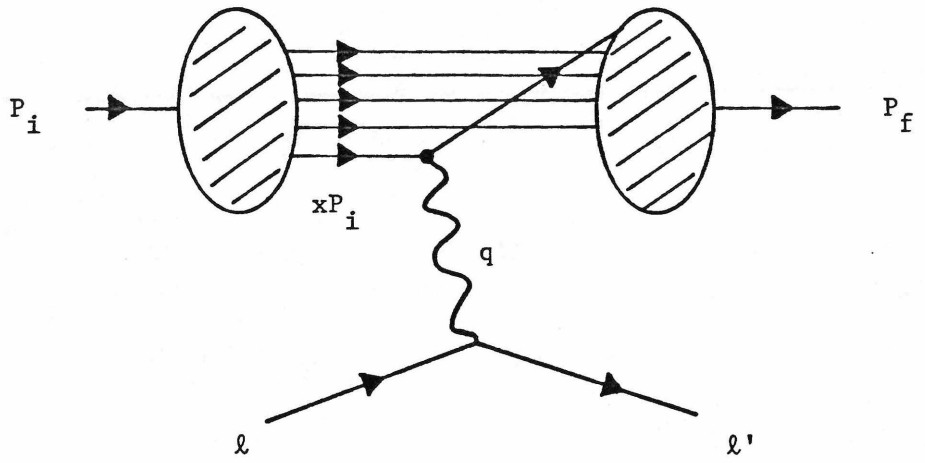

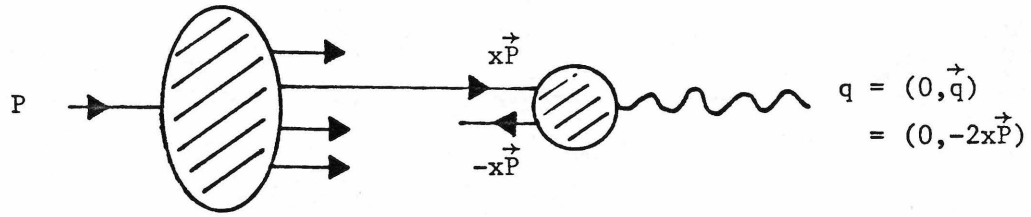

$$\frac{-q^2}{2MP\cdot q} = \frac{(2x\vec{P})^2}{2M(\vec{P}\cdot 2x\vec{P})} = x$$

Figure 6-1: Deep inelastic lepton-nucleon scattering in the quark-parton model.

which is the same as equation 1-4. At some time long after the lepton-quark scatter has taken place, the quarks recombine into the hadronic final state.

The helicities of the interacting particles are not changed by a purely V-A interaction, so νq and $\bar{\nu}\bar{q}$ scattering can be distinguished from $\nu\bar{q}$ and $\bar{\nu}q$ scattering. This is illustrated in figure 6-2. In νq and $\bar{\nu}\bar{q}$ scattering the spins add to $J_z=0$, so $d\sigma/d\cos\theta_{cm} \propto 1$, where θ_{cm} is the angle of the scattered muon. In $\nu\bar{q}$ and $\bar{\nu}q$ scattering, the helicities add to a J=1 spin state. In this case, $d\sigma/d\cos\theta_{cm} \propto (1+\cos\theta_{cm})^2$. In terms of the variable y,

$$y = \frac{P_f \cdot P_i}{P_i \cdot P_\nu} \qquad (6\text{-}7a)$$

$$= \frac{1}{2}(1-\cos\theta_{cm}). \qquad (6\text{-}7b)$$

Therefore νq and $\bar{\nu}\bar{q}$ interactions have flat y distributions,

$$\frac{d\sigma}{dy} \propto 1, \qquad (6\text{-}8)$$

while $\nu\bar{q}$ and $\bar{\nu}q$ interactions have

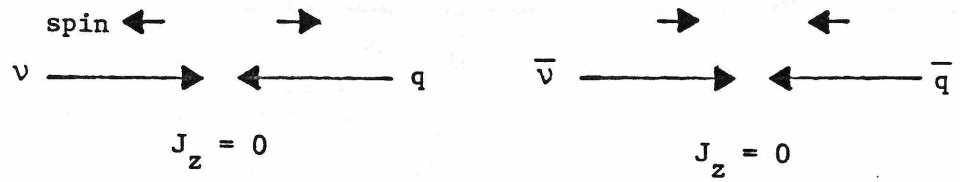

(a) $d\sigma/d\cos\theta \propto 1$ in the CM frame for νq and $\bar{\nu}\bar{q}$ scattering.

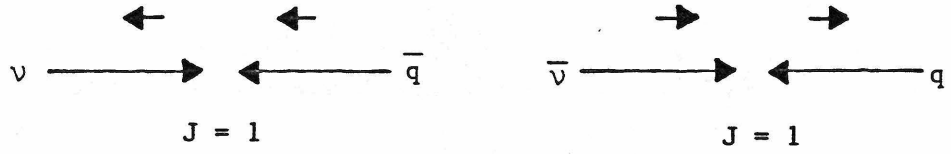

(b) $d\sigma/d\cos\theta \propto \frac{1}{2}(1+\cos\theta)^2$ in the CM frame for $\nu\bar{q}$ and $\bar{\nu}q$ scattering.

Figure 6-2: Helicities for neutrinos and antineutrinos scattering off quarks and antiquarks.

$$\frac{d\sigma}{dy} \propto (1-y)^2. \qquad (6\text{-}9)$$

Assuming only 4 quark flavors, the scattering diagrams and amplitudes for the possible neutrino-quark charged current interactions are shown in figure 6-3.

The functions $u(x)$, $d(x)$, $s(x)$, $c(x)$, and $\bar{u}(x)$, $\bar{d}(x)$, $\bar{s}(x)$, $\bar{c}(x)$ are the distributions of the fractional momentum carried by the respective quarks and antiquarks in the proton. The proton and neutron are related by isospin symmetry, so the cross sections for scattering from an isoscalar target can be written in terms of the proton quark distributions. The charged current cross sections per nucleon for scattering from an isoscalar target are given by

$$\frac{d^2\sigma^{\nu N}}{dxdy} = \frac{G^2 M E_\nu}{\pi}\left\{\begin{array}{l} u(x)+d(x)+2s(x) \\ \quad +(1-y)^2[\bar{u}(x)+\bar{d}(x)+2\bar{c}(x)]\end{array}\right\}, \qquad (6\text{-}10a)$$

$$\frac{d^2\sigma^{\bar{\nu}N}}{dxdy} = \frac{G^2 M E_\nu}{\pi}\left\{\begin{array}{l} [u(x)+d(x)+2c(x)](1-y)^2 \\ \quad +\bar{u}(x)+\bar{d}(x)+2\bar{s}(x)\end{array}\right\}. \qquad (6\text{-}10b)$$

Iron is not quite an isoscalar target, with 26 protons and 30 neutrons.

The strange and charm seas are expected to be small

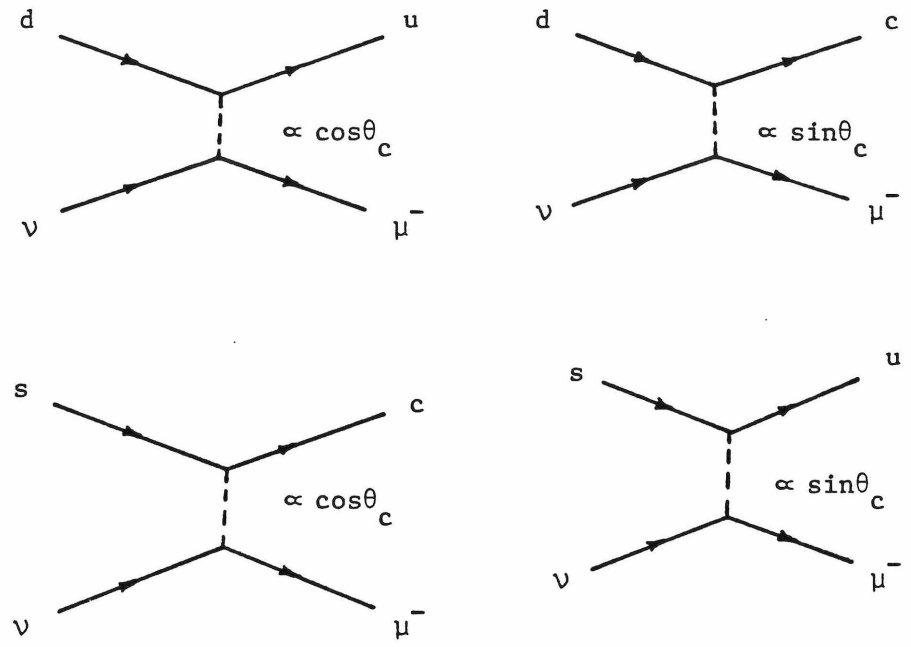

Process	$\frac{G^2 ME}{\pi} \frac{d\sigma}{dy}$
$\nu \begin{pmatrix} d \\ s \end{pmatrix} \rightarrow \mu^- X$	$2x$
$\bar{\nu} \begin{pmatrix} u \\ c \end{pmatrix} \rightarrow \mu^+ X$	$2x(1-y)^2$
$\nu \begin{pmatrix} \bar{u} \\ \bar{c} \end{pmatrix} \rightarrow \mu^- X$	$2x(1-y)^2$
$\bar{\nu} \begin{pmatrix} \bar{d} \\ \bar{s} \end{pmatrix} \rightarrow \mu^+ X$	$2x$

Figure 6-3: Scattering diagrams and amplitudes for neutrinos and antineutrinos scattering off quarks and antiquarks.

because s and c quarks are heavy compared with u and d quarks. Defining $q(x)=u(x)+d(x)$ and $\bar{q}(x)=\bar{u}(x)+\bar{d}(x)$, and ignoring the strange and charm seas, the sum of the ν and $\bar{\nu}$ cross sections measures the total quark and antiquark function $q(x)+\bar{q}(x)$:

$$\frac{\pi}{G^2 ME_\nu}\left(\frac{d^2\sigma^{\nu N}}{dxdy}+\frac{d^2\sigma^{\bar{\nu}N}}{dxdy}\right) = [1+(1-y)^2][q(x)+\bar{q}(x)]. \qquad (6\text{-}11)$$

The valence quark distribution is obtained from the difference of the ν and $\bar{\nu}$ cross sections:

$$\frac{\pi}{G^2 ME_\nu}\left(\frac{d^2\sigma^{\nu N}}{dxdy}-\frac{d^2\sigma^{\bar{\nu}N}}{dxdy}\right) = [1-(1-y)^2][q(x)-\bar{q}(x)]. \qquad (6\text{-}12)$$

Taking the limit $y\to 1$ gives $q(x)$ and $\bar{q}(x)$ directly:

$$\frac{\pi}{G^2 ME_\nu}\frac{d^2\sigma^{\nu N}}{dxdy}\bigg|_{y\to 1} = q(x), \qquad (6\text{-}13a)$$

$$\frac{\pi}{G^2 ME_\nu}\frac{d^2\sigma^{\bar{\nu}N}}{dxdy}\bigg|_{y\to 1} = \bar{q}(x). \qquad (6\text{-}13b)$$

Integrating equation 6-11 gives the total fractional momentum carried by quarks and antiquarks in the nucleon:

$$\int_0^1 [q(x)+\bar{q}(x)]dx = \frac{3\pi}{4G^2 ME_\nu}\left(\sigma_{TOT}^{\nu N}+\sigma_{TOT}^{\bar{\nu}N}\right). \qquad (6\text{-}14)$$

C. SCALING VIOLATIONS

Assuming charge symmetry, a V-A interaction, and M_W large, the most general form for neutrino charged current cross sections on an isoscalar target is

$$\frac{d^2\sigma^{\nu,\bar{\nu}}}{dxdy} = \frac{G^2 ME}{\pi}\nu\left\{\begin{array}{l}(1/2)[2xF_1(x,Q^2)\pm xF_3(x,Q^2)] \\ +[F_2(x,Q^2)-2xF_1(x,Q^2)](1-y) \\ +(1/2)[2xF_1(x,Q^2)\mp xF_3(x,Q^2)](1-y)^2\end{array}\right\}. \tag{6-15}$$

In the quark model, the term proportional to (1-y) vanishes as $Q^2\rightarrow\infty$ (Callan-Gross relation[31]). Then if we ignore the Q^2 dependence of xF_1 and xF_3, we recover the quark-parton model by defining

$$q(x) = (1/2)(2xF_1+xF_3), \tag{6-16a}$$

$$\bar{q}(x) = (1/2)(2xF_1-xF_3). \tag{6-16b}$$

The structure functions F_i are expected to have Q^2 dependence in models with gluons (such as QCD). These arise from processes such as those shown in figure 6-4. In diagram (a), a quark radiates a gluon before scattering from the W with $x'<x$. In diagram (b), a gluon converts into a $q\bar{q}$ pair, one of which is struck by the W. The mean

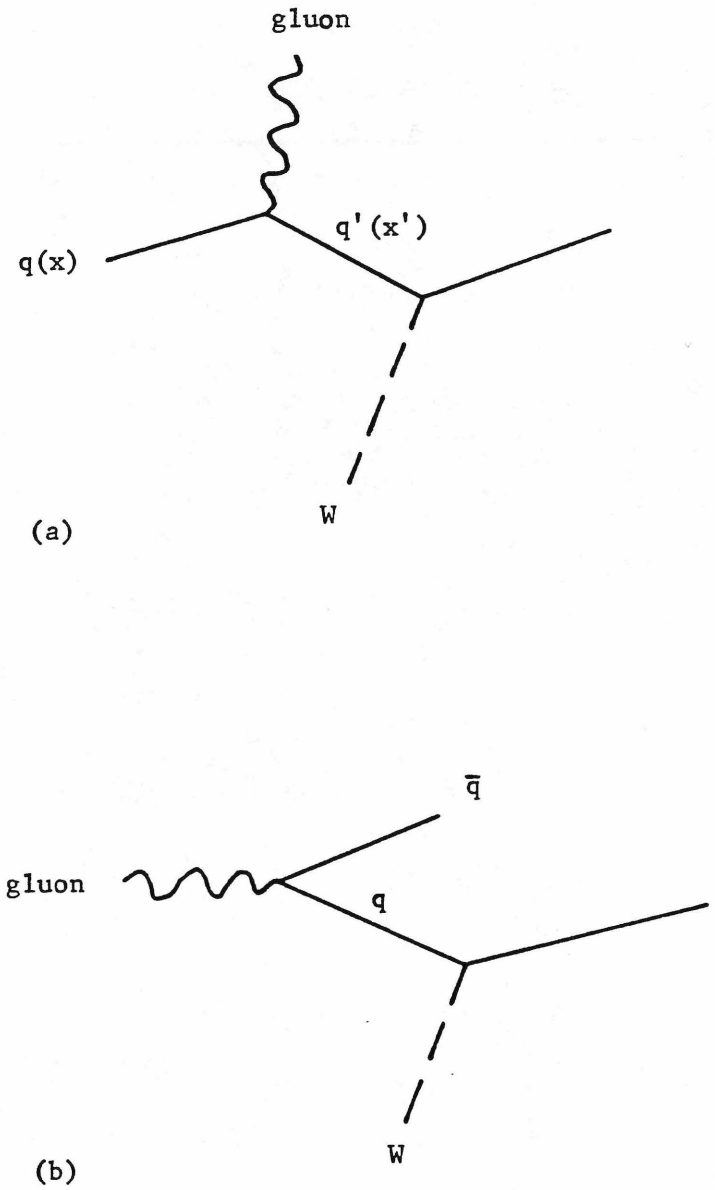

Figure 6-4: Examples of processes that lead to scaling violations.
(a) gluon bremsstrahlung
(b) gluon resolved into $q\bar{q}$ pair

x of the sea quarks is small compared with the valence quarks. Both of these processes become more important at large Q^2 and result in a shrinkage of the structure functions toward small x. Diagram (b) also should increase the antiquark component of the nucleon at high Q^2.

6.2 INTERPRETATION OF DATA

A. TOTAL CROSS SECTIONS

Charged current total cross sections for νN scattering have been reported by several groups at neutrino energies up to 200 GEV. In each experiment the results are consistent with a constant σ/E_ν, but there are discrepancies in overall normalization among the measurements. This is summarized in table 6-1, where the uncertainties in σ/E_ν include all systematic uncertainties reported by each group.

The theoretical expectation is that σ/E_ν should scale nearly exactly in the energy range of E356 (σ/E_ν should not vary by more than 5% between E_ν=50 GEV and E_ν=500 GEV [32,33]) unless the W is light. An unexpected rise in σ/E_ν might indicate the production of new quark states. A

TABLE 6-1: TOTAL CROSS SECTION MEASUREMENTS

GROUP	ENERGY RANGE	$\sigma/E_\nu(\nu N \to \mu^- X)$ [10^{-38} cm^2/GEV]
CFRR	25-260 GEV	.700 ±.038
CFR	45-205 GEV	.609 ±.030 [6]
CDHS	30-200 GEV	.62 ±.03 [15]
CHARM	20-200 GEV	.594 ±.027 [16]
BEBC	20-200 GEV	.58 ±.05 [38]
	10-50 GEV	.73 ±.08 [39]
IHEP-ITEP	3-30 GEV	.72 ±.07 [40]
GGM	2-10 GEV	.72 ±.07 [38,41]
	6 GEV	.61 ±.06 [42]
	1.5 GEV	.69 ±.05 [42]
ANL	0.3-4 GEV	.87 ±.09 [43]

fall in σ/E_ν might be caused by a light W boson. The CFRR results are consistent with exact scaling and test scaling at the 5% level.

If we assume that any deviation in σ/E_ν from scaling is caused by a light propagator, then to first order the cross section is

$$\frac{\sigma}{E_\nu} = \frac{\sigma_0/E_\nu}{\left(1+\langle Q^2\rangle/M_W^2\right)^2} \qquad (6\text{-}17a)$$

$$= \frac{\sigma_0/E_\nu}{\left\{1+\left(\frac{2M_N E_\nu \langle xy\rangle}{M_W^2}\right)\right\}^2} \quad , \qquad (6\text{-}17b)$$

where σ_0/E_ν is the slope at small E_ν. The antiquark component of the nucleon is small compared with the quark component, so equation 6-10(a) nearly factorizes into a function of x and a function of y. Then $\langle xy\rangle \simeq \langle x\rangle\langle y\rangle$. If we use figure 5-6 to determine $\langle x\rangle$ in the region $.1<y<.4$, we slightly underestimate $\langle x\rangle$ for all y since $\bar{q}(x)$ peaks at lower x than q(x). Therefore we take $\langle xy\rangle=(.23)(.49)=.113$. The effect of a propagator is shown in figure 6-5, where the overall level is fit to the data. A lower bound can be placed on M_W by comparing the ν_K cross sections with the ν_π cross sections. The lower limit on M_W as a function of confidence level is shown in figure 6-6. At the 90%

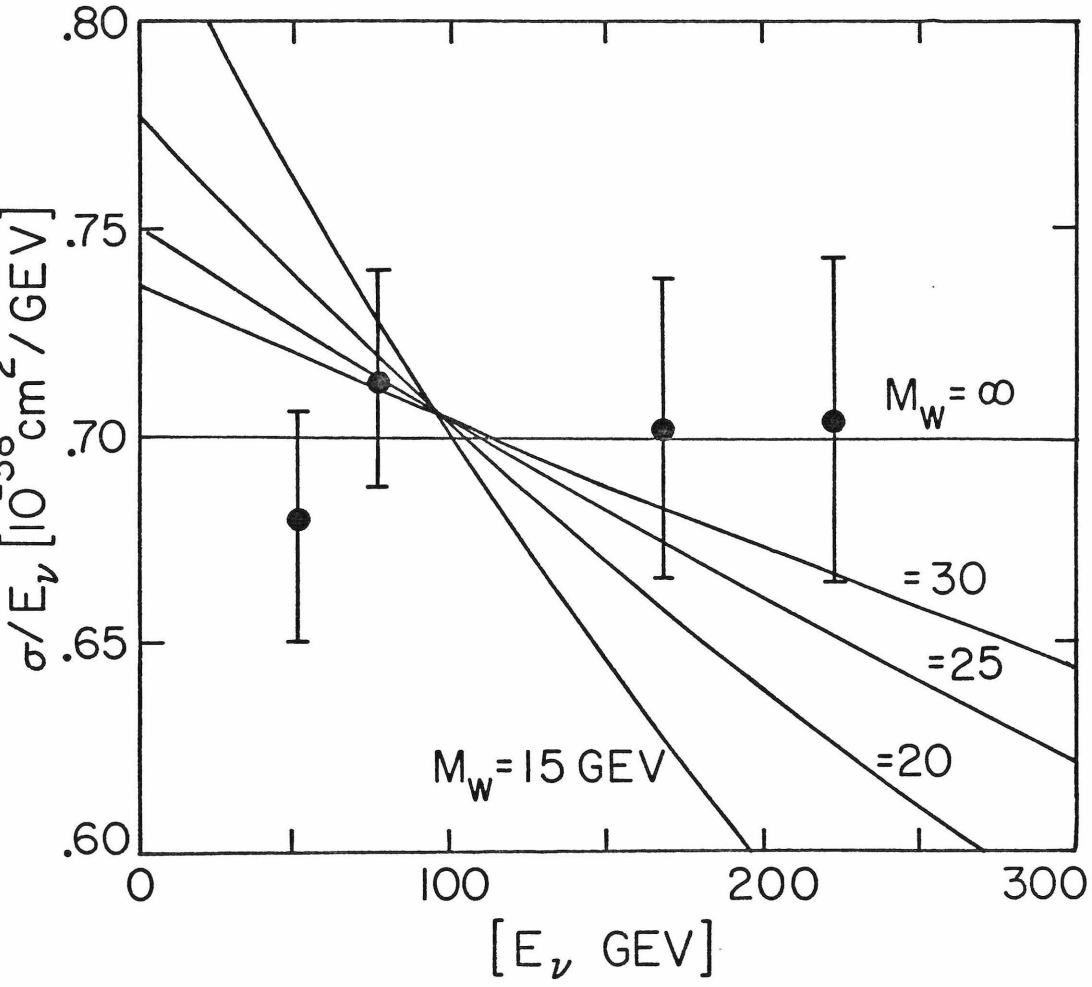

Figure 6-5: Effect of a massive propagator on the total cross section for $\nu N \to \mu^- X$.

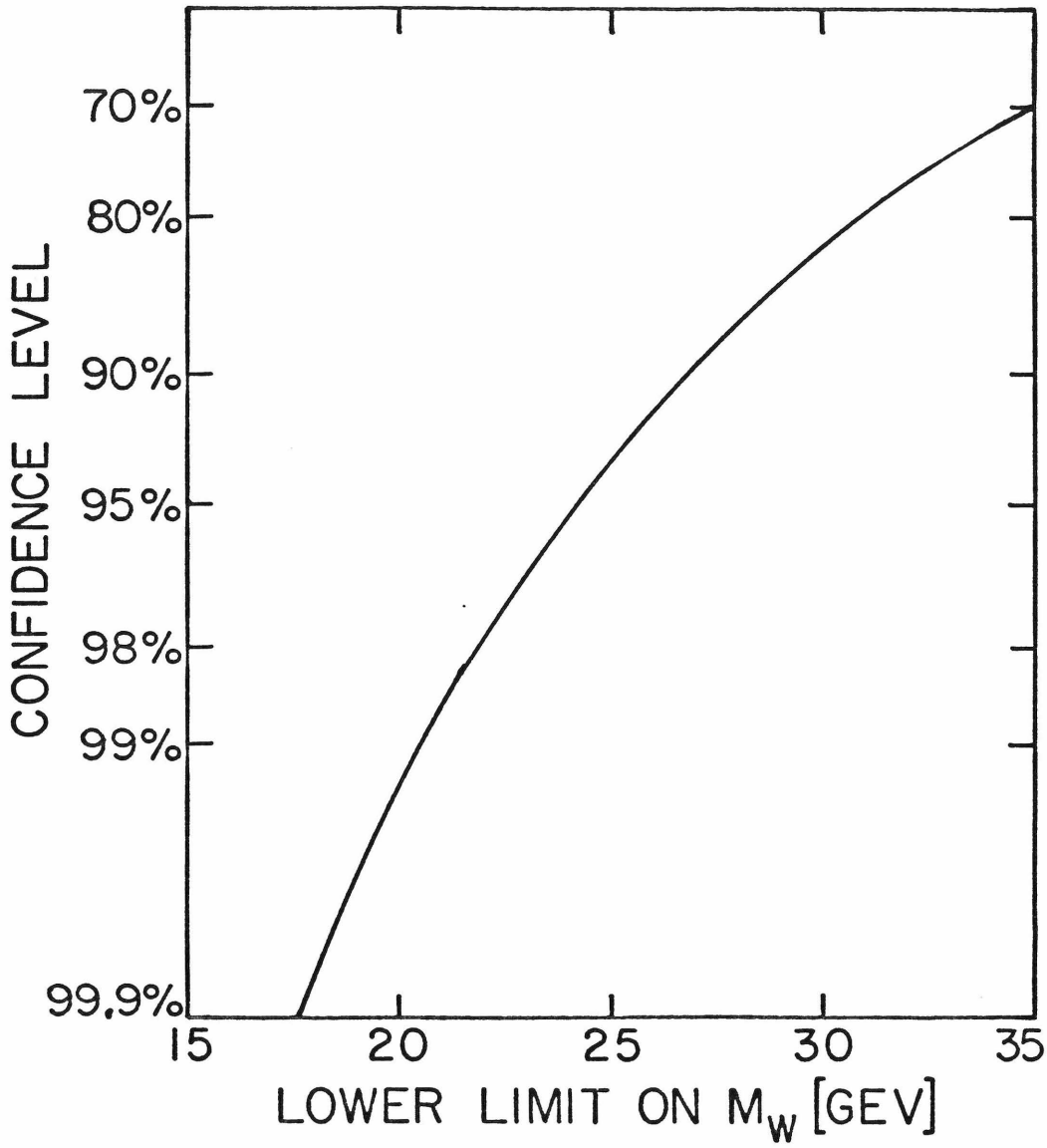

Figure 6-6: Lower bound on M_W versus statistical confidence level.

confidence level, $M_W > 27$ GEV.

The total fraction of the nucleon momentum that is carried by quarks is given by

$$Q + \bar{Q} = \frac{3\pi}{4G^2 M_N}\left(\frac{\sigma^{\nu}}{E_{\nu}}\right)\left\{1+\left(\frac{\sigma^{\bar{\nu}}}{\sigma^{\nu}}\right)\right\}, \qquad (6\text{-}18)$$

where $Q = \int_0^1 q(x)dx$ and $\bar{Q} = \int_0^1 \bar{q}(x)dx$. Assuming that the discrepancies in normalization among experiments do not effect $\sigma^{\bar{\nu}}/\sigma^{\nu}$, we can use previous measurements of this ratio to determine $Q+\bar{Q}$. The value $\sigma^{\bar{\nu}}/\sigma^{\nu} = .50 \pm .05$ encompasses previous measurements[8,15,16] and probably overestimates the uncertainty. Using the average CFRR value of $\sigma^{\nu}/E_{\nu} = .700 \pm .038$, we obtain

$$Q + \bar{Q} = .50 \pm .03. \qquad (6\text{-}19)$$

This compares with the CDHS results of $Q+\bar{Q} = .44 \pm .02$ for $30 \text{ GEV} < E_{\nu} < 90$ GEV and $Q+\bar{Q} = .45 \pm .03$ for $90 \text{ GEV} < E_{\nu} < 200$ GEV[15].

B. y DISTRIBUTIONS

The νN y distributions provide information on the relative fraction of antiquarks and quarks in the nucleon.

The y distribution is given by

$$\frac{d\sigma^{\nu}}{dy} = \frac{G^2 ME_{\nu}}{\pi}[Q + \bar{Q}(1-y)^2]. \qquad (6\text{-}20)$$

The CFRR measurements of <y> are compared with other recent experiments in figure 6-7. The error bars on the CFRR points include all systematic uncertainties. There is good agreement among these experiments, and the data show no significant departure from scaling.

In terms of <y>, the antiquark fraction $\alpha = \bar{Q}/(Q+\bar{Q})$ is given by

$$\alpha = \frac{6 - 12\langle y\rangle}{5 - 8\langle y\rangle} . \qquad (6\text{-}21)$$

Using the CFRR average value of $\langle y\rangle = .489 \pm .012$ gives $\alpha = .12 \pm .12$.

A more precise determination of α can be made at a mean E_{ν} of 226 GEV by using the measured y distribution for kaon neutrino interactions. To do this we first make radiative corrections following de Rujula et al.[44]. The y distribution after making radiative corrections is shown in figure 6-8 and table 6-2. The best fit of equation 6-20

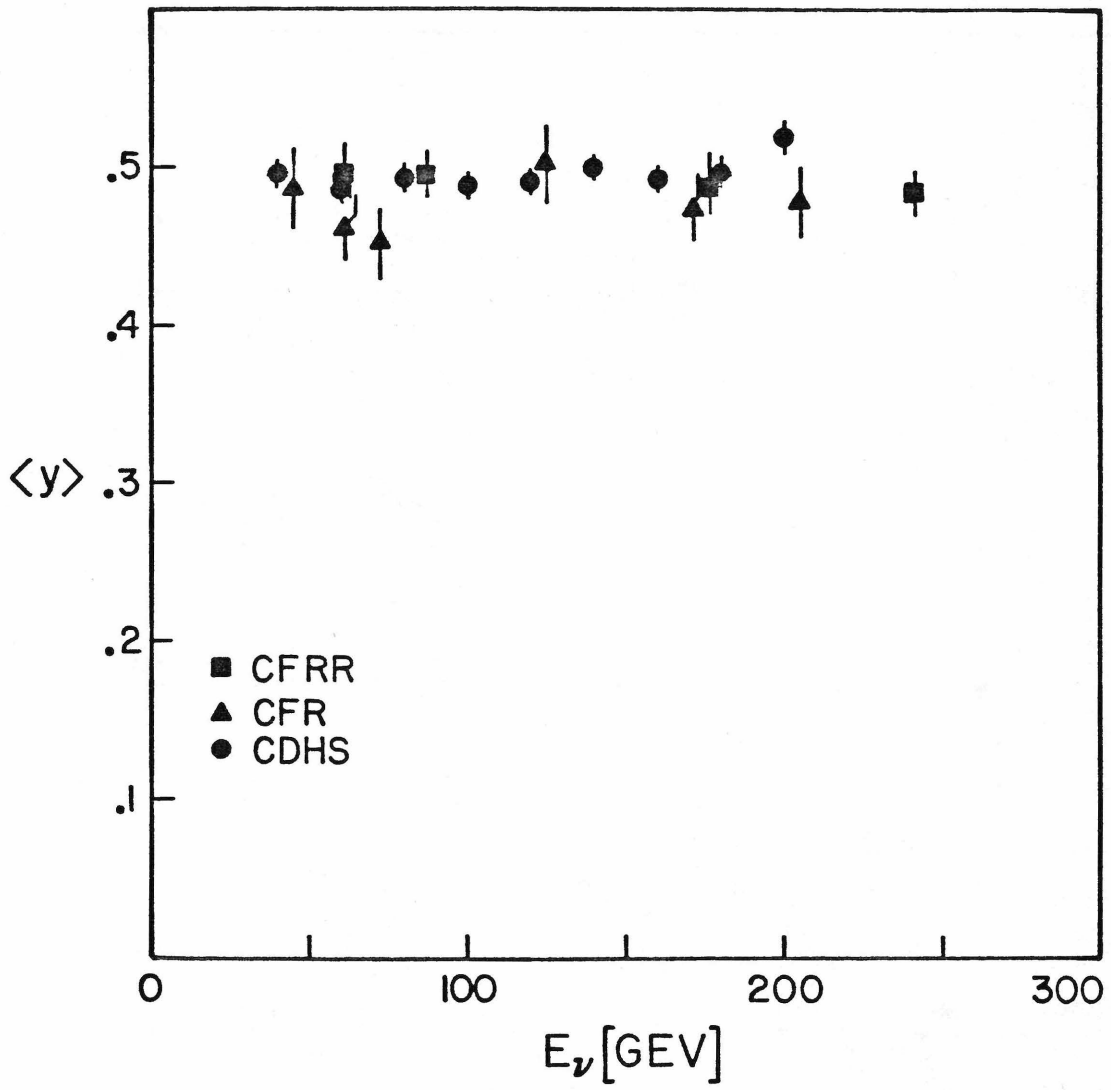

Figure 6-7: Comparison of CFRR measurements of mean y with previous results.

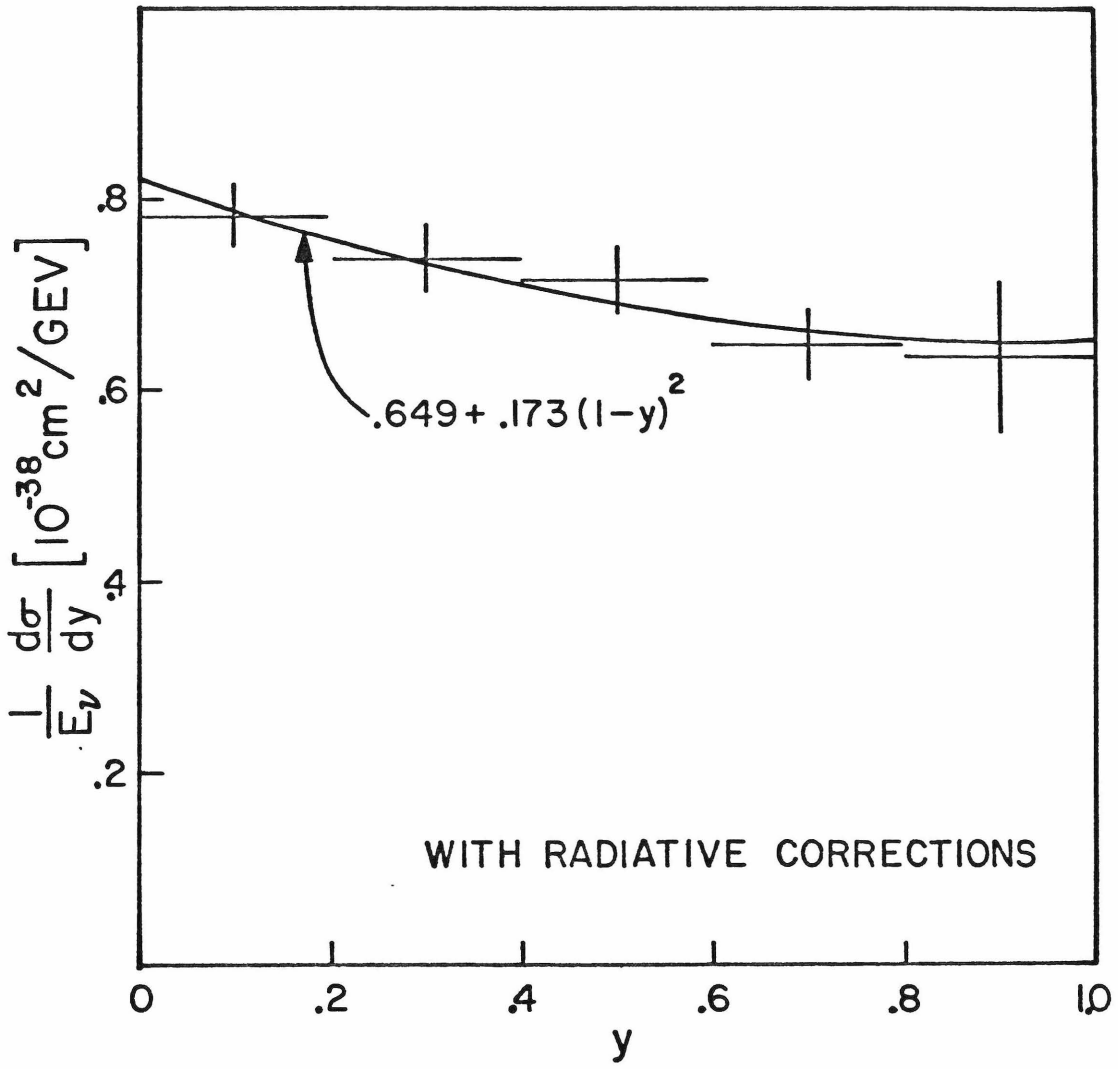

Figure 6-8: Kaon neutrino y distribution after making radiative corrections.

TABLE 6-2: KAON NEUTRINO y DISTRIBUTION

WITH RADIATIVE CORRECTIONS

Mean E_ν = 226 GEV

y	$\frac{1}{E_\nu}\frac{d\sigma}{dy}$ (10^{-38} cm^2/GEV)
0-.2	.782±.034
.2-.4	.738±.036
.4-.6	.716±.036
.6-.8	.647±.037
.8-1.0	.635±.079

to the data is shown in figure 6-6 and gives $\alpha = .21 \pm .07$. If we fit the data without making radiative corrections (see figure 5-5), the result is $\alpha = .16 \pm .07$. This is consistent with the CDHS results of $\alpha = .15 \pm .04$ (with radiative corrections) and $\alpha = .08 \pm .04$ (without radiative corrections)[15], which were obtained by fitting both ν and $\bar{\nu}$ data at energies between 30 and 200 GEV. A value of $\alpha = .11 \pm .03$ is reported by BEBC[30].

Previous groups have made tests of charge symmetry by comparing $d\sigma^{\nu}/dy$ with $d\sigma^{\bar{\nu}}/dy$ as $y \rightarrow 0$ [7,15,34]. This is not feasible with the current CFRR data sample since E356 did not obtain any antineutrino data. The 15% discrepancies in normalization among experiments precludes any meaningful comparison of our neutrino data with previously published antineutrino data.

C. x DISTRIBUTIONS

The simple parton picture of deep inelastic scattering can be valid only if the momentum transfered in the collision is much larger than the mass of the nucleon. At present it is not known how to accurately describe scattering at low Q^2, but presumably corrections to the

naive parton model will be of order M_N^2/Q^2. Empirically, it was discovered that eN data from SLAC[19] scaled much better in the variable $x/(1+M_N^2x/Q^2)$ than in x.

The variable $x'=x/(1+M_N^2/Q^2)$ used in section 5.5 is simply a phenomonological variable that illustrates the sensitivity of the x distribution to effects of order M_N^2/Q^2. The observed violations of scaling in x are in a Q^2 region where the naive parton picture cannot be expected to be exact.

Radiative corrections have not been applied to the x and x' distributions presented in section 5.5. Radiative corrections could be as large as 10%, but the difference in the correction between E_ν=20 GEV and E_ν=200 GEV is never more than 2% and is less than 1% for x<.5 [44]. Therefore a test of scaling can be made at the statistical level of this experiment without making radiative corrections.

6.3 CONCLUSIONS

The νN charged current data of this experiment can be consistently interpreted within the framework of the quark-parton model.

The total cross sections are consistent with exact scaling from E_ν=25 GEV to E_ν=260 GEV. The overall level of σ/E_ν=.700±.038 is about 15% higher than reported in previous experiments. The total cross sections determine a lower bound of M_W>27 GEV at the 90% confidence level.

The measurements of <y> agree with previous experiments and also are consistent with exact scaling. Averaged over E_ν, <y>=.484±.012. The kaon neutrino y distribution measures the antiquark fraction of the nucleon to be α =.21±.07 at E_ν=226 GEV.

Scaling violations are seen in $d\sigma/dx$ in the interval .1<y<.4. The x distribution shrinks toward small x at E_ν=226 GEV compared with E_ν=67 GEV, which is the direction predicted by QCD. However, the effect disappears if the scaling variable is changed to $x'=x/(1+M_N^2/Q^2)$. A stringent test of QCD must be careful to separate $\ln Q^2$ behavior from mass effects of order M_N^2/Q^2.

We expect to learn a great deal more with the E616 data recently taken by our group. This data sample contains more than 100,000 neutrino and antineutrino events. The primary goal of E616 is to make high precision measurements of xF_1, F_2, and xF_3 as functions of x and Q^2.

We believe it is possible to make meaningful tests of QCD with the E616 data sample. In the future, the Tevatron holds promise of extending our measurements above E_ν=750 GEV.

REFERENCES

1. B. C. Barish et al., Phys. Rev. Lett., 34, 538 (1975).
2. B. C. Barish et al., Phys. Rev. Lett., 36, 939 (1976).
3. B. C. Barish et al., Phys. Rev. Lett., 39, 981 (1977).
4. B. C. Barish et al., Phys. Rev. Lett., 38, 577 (1977).
5. B. C. Barish et al., Phys. Rev. Lett., 35, 1316 (1975).
6. B. C. Barish et al., Phys. Rev. Lett., 39, 1595 (1977).
7. B. C. Barish et al., Phys. Rev. Lett., 39, 741 (1977).
8. B. C. Barish et al., Phys. Rev. Lett., 40, 1414 (1978).
9. F. S. Merritt, et al., Phys. Rev. D17, 2199 (1978).
10. D. Edwards and F. Sciulli, "A Second Generation Narrow Band Neutrino Beam", Fermilab TM-660 (1976).
11. D. Edwards, S. Mori, and S. Pruss, "350 GEV/c Dichromatic Neutrino Target Train", Fermilab TM-661 (1976).
12. H. Stredde, "Mechanical Design of the 350 GEV/c Dichromatic Train", Fermilab TM-810 (1978).
13. R. J. Stefansky and H. B. White, "Neutrino Flux Distributions", Fermilab No. 2060.000 (1976).
14. B. C. Barish et al., CALT 68-714, Fermilab No. 7410.021, published in the Proceedings of the Third International Conference on New Results in High Energy Physics, Vanderbilt University, Nashville, Tennessee (1978).
15. J. G. H. de Groot et al., Z. Phys. C1, 143 (1979).
16. M. Jonker et al., "Experimental Study of Neutral and Charged Current Neutrino Cross Sections", paper contributed to the XX International Conference on High Energy Physics, Madison, Wisconsin (1980).

17. W. F. Baker et al., "Production of $\pi^{\pm}$, $K^{\pm}$, p and $\bar{p}$ by 40 GEV/c Protons", Fermilab No. 7110.104 (1978).

18. F. J. Sciulli, private communication.

19. A. Bodek, Ph. D. Thesis, Mass. Institute of Technology, Report No. COO-3069-116, 1973 (unpublished).

20. B. C. Barish et al., IEEE Trans. Nucl. Sci. NS-25, 532 (1978).

21. C. H. Llewellyn Smith, Physics Reports, 3C, 261, (1972).

22. S. Weinberg, Phys. Rev. Lett. 19, 1264 (1967).

23. A. Salam, Elementary Particle Theory, ed. N. Swartholm (Almquist and Forlag, Stockholm, 1968).

24. C. Y. Prescott et al., Phys. Lett. 77B, 347 (1978); Phys. Lett. 84B, 524 (1979).

25. M. Gell-Mann, Phys. Lett. 8, 214 (1964).

26. G. Zweig, CERN preprints TH401 and TH412 (1964).

27. R. P. Feynman, Phys. Lett. 23, 1415 (1969); Photon-Hadron Interactions (Benjamin, Reading, Mass., 1972).

28. J. D. Bjorken, Phys. Rev. 179, 1547 (1969).

29. R. Brandelik et al., Phys. Lett. 86B, 243 (1979).

30. P. C. Bosetti et al., Nucl. Phys. B142, 1 (1978).

31. H. L. Anderson et al., Phys. Rev. Lett. 38, 1450 (1977); Phys. Rev. Lett. 37, 4 (1976).

32. B. A. Gordon et al., Phys. Rev. D20, 2645 (1979); Phys. Rev. Lett. 41, 615 (1978).

33. W. B. Atwood et al., Phys. Lett. 64B, 479 (1976).

34. E. M. Riordan et al., SLAC-PUB-1634 (1975).

35. C. G. Callan and D. Gross, Phys. Rev. Lett. 22, 156 (1969).

36. I. Hinchliffe and C. H. Llewellyn Smith, Phys. Lett. 70B, 247 (1977).

37. A. J. Buras and K. J. F. Gaemers, Phys. Lett. 71B, 106 (1977).

38. B. C. Bosetti et al., Phys. Lett. 70B, 273 (1977).

39. D. C. Colley et al., Z. Phys. C2, 187 (1979).

40. A. E. Asratyan et al., Phys. Lett. 76B, 239 (1978).

41. T. Eichten et al., Phys. Lett. 46B, 274 (1973).

42. C. Ciampolillo et al., Phys. Lett. 84B, 281 (1979).

43. S. J. Barish et al., Phys. Rev. D19, 2521 (1979).

44. A. de Rujula et al., Nucl. Phys. B154, 394, (1979).